MOUNTAIN-PLAINS CONSORTIUM

MPC 24-570 | P. Vaikasi and M.W. Halling

IMPLEMENTATION OF PRECAST CONCRETE SEGMENTS FOR ELECTRIFIED ROADWAY

MOUNTAIN-PLAINS CONSORTIUM REGION 8

A University Transportation Center sponsored by the U.S. Department of Transportation serving the Mountain-Plains Region. Consortium members:

Colorado State University
North Dakota State University
South Dakota State University
University of Colorado Denver
University of Denver
University of Utah
Utah State University
University of Wyoming

Technical Report Documentation Page

1. Report No.	2. Government Accession No.	3. Recipient's Catalog No.
MPC-580		

4. Title and Subtitle	5. Report Date
Implementation of Precast Concrete Segments for Electrified Roadway	October 2024
	6. Performing Organization Code

7. Author(s)	8. Performing Organization Report No.
Pilaiwan Vaikasi Marvin W. Halling	MPC 24-570

9. Performing Organization Name and Address	10. Work Unit No. (TRAIS)
Department of Civil and Environmental Engineering Utah State University Logan, UT 84321	11. Contract or Grant No.

12. Sponsoring Agency Name and Address	13. Type of Report and Period Covered
Mountain-Plains Consortium North Dakota State University PO Box 6050, Fargo, ND 58108	Final Report
	14. Sponsoring Agency Code

15. Supplementary Notes

Supported by a grant from the US DOT, University Transportation Centers Program

16. Abstract

Maintaining sufficient charge during the duration of travel along with the time required to recharge the vehicle are major concerns for electric vehicle (EV) owners. This project focuses on in-motion, inductive power transfer (IPT) embedded in roadways to ensure charge duration and replace stationary charging units for EVs. This research is a collaboration between civil, electrical, and mechanical engineers from Advancing Sustainability through Powered Infrastructure for Roadway Electrification (ASPIRE) at Utah State University.

Using a 3D finite element analysis (FEA) model in ANSYS and load-bearing tests performed in a lab, electrified precast concrete pavement (EPCP) was examined. The EPCP was subjected to two testing loads: 1) thermal load created by the IPT and 2) a cyclic structural load created by a heavy truck. EPCP panel specimens were constructed and embedded with temperature gauges and fiber optic strain gauges to collect data regarding the heat generated by IPT and the durability of the concrete slabs. The results of the FEA models, such as strain and crack patterns on the concrete, were calibrated with experimental data from strain and temperature readings. The models were then updated to develop reasonable mechanical behavior of the entire structure.

17. Key Word	18. Distribution Statement
electric vehicle charging, electric vehicles, energy transfer, implementation, intelligent vehicles, precast concrete pavements	Public distribution

19. Security Classif. (of this report)	20. Security Classif. (of this page)	21. No. of Pages	22. Price
Unclassified	Unclassified	200	n/a

Form DOT F 1700.7 (8-72) Reproduction of completed page authorized

IMPLEMENTATION OF PRECAST CONCRETE SEGMENTS FOR ELECTRIFIED ROADWAY

Pilaiwan Vaikasi
Marvin W. Halling

Department of Civil and Environmental Engineering
Utah State University
Logan, Utah 84321

October 2024

Acknowledgments

This project is funded by the National Science Foundation (NSF) Engineering Research Center and Mountain-Plains Consortium (MPC).

Disclaimer

ABSTRACT

Maintaining sufficient charge during the duration of travel along with the time required to recharge the vehicle are major concerns for electric vehicle (EV) owners. This project focuses on in-motion, inductive power transfer (IPT) embedded in roadways to ensure charge duration and replace stationary charging units for EVs. This research is a collaboration between civil, electrical, and mechanical engineers from Advancing Sustainability through Powered Infrastructure for Roadway Electrification (ASPIRE) at Utah State University.

Using a 3D finite element analysis (FEA) model in ANSYS and load-bearing tests performed in a lab, electrified precast concrete pavement (EPCP) was examined. The EPCP was subjected to two testing loads: 1) thermal load created by the IPT and 2) a cyclic structural load created by a heavy truck. EPCP panel specimens were constructed and embedded with temperature gauges and fiber optic strain gauges to collect data regarding the heat generated by IPT and the durability of the concrete slabs. The results of the FEA models, such as strain and crack patterns on the concrete, were calibrated with experimental data from strain and temperature readings. The models were then updated to develop reasonable mechanical behavior of the entire structure.

TABLE OF CONTENTS

LIST OF TABLES

LIST OF FIGURES

LIST OF ABBREVIATIONS

ASPIRE	Advancing Sustainability through Powered Infrastructure for Roadway Electrification
BEVs	Battery electric vehicles
EVs	Electric vehicles
EPCP	Electrified precast concrete pavement
FEA	Finite element analysis
GFRP	Glass fiber reinforced polymer
IPT	Inductive power transfer
INTIS	Integrated infrastructure solution
KAIST	Korea Advanced Institute of Science & Technology
PATH	Partners for Advanced Transit and Highway
PCM	Phase change material
PHEVs	Plug-in hybrid electric vehicles
RPEVs	Roadway-powered electric vehicles
SCEVs	Stationary charging electric vehicles

EXECUTIVE SUMMARY

Two main concerns with electric vehicles (EVs) are maintaining a sufficiently charged battery to reach a destination and the time required to charge the vehicle. In-motion, inductive power transfer (IPT) embedded in roadways addresses both concerns. This project focuses on the function and durability of IPT electronics integrated in concrete pavements. This research is a collaboration between civil, electrical, and mechanical engineers from the Advancing Sustainability through Powered Infrastructure for Roadway Electrification (ASPIRE) at Utah State University.

A 3D finite element analysis (FEA) model in ANSYS was used to simulate electrified precast concrete pavement (EPCP) and to observe the structural behavior of the concrete. The models considered two load cases: 1) thermal load from the IPT operation and 2) cyclic structural load from a heavy truck.

The EPCP panel specimens were constructed for the physical test. The instrumentation plan was determined from the results of the FEA model. For thermal testing, embedded fiber optic strain and temperature gauges were used to monitor the heat while the IPT system ran. The cyclic wheel load testing was performed to investigate the structural behavior of the panels. Strain readings were obtained from the internal embedded fiber optic and external strain gauges. The external gauges were attached to the surface of the concrete to measure high-level stresses associated with concrete cracking.

In thermal testing analysis, the models were consistent with the experimental results for thermal strain and temperature by an 8% – 15% difference. In cyclic loading analysis, the crack patterns in the models were consistent with the experiment. The ultimate failure loads in the models aligned with the experiment for an estimated 5% error. Glass fiber reinforced polymer (GFRP) reinforcement was recommended for future improvement in high-cycle fatigue and reducing power loss of the IPT system.

1. INTRODUCTION

This section introduces the research and discusses the scope, objectives, and limitations of the project.

1.1 Background and Motivation

EVs' increasing popularity is due to their use of clean energy. Replacing traditional gas-powered vehicles with EVs reduces CO_2 emission and improves air quality. However, the existing battery technology limits EVs' driving range. Inductive power transfer (IPT) systems embedded in concrete roadways could charge EVs' batteries in transit and improve long-range driving capability. Also, IPT systems address the challenges of inconvenient distribution of charging stations and the wait times associated with EV charging.

1.2 Project Definition and Scope

This research focused on the constructability and performance of a dynamic wireless charging system embedded in precast concrete panels. Full-sized concrete panels were constructed, embedded with electrical coils, and subjected to two testing phases. The testing included 1) thermal testing and 2) repeated cyclic load and statically applied load testing. Data were collected using embedded and attached instruments. Following the studies, finite element models were created. Modeling and analysis were performed using commercially available ANSYS software. Three-dimensional (3D) finite element analysis (FEA) models were created by comparing output from the thermal and structural load studies. The models can then be used to predict behavior of the panels under combined loading situations as well as additional load cases that can be expected from this system.

1.3 Objective

The objective of this work is to develop a functioning, full-sized electrified precast concrete pavement (EPCP). Future IPT systems will consist of a primary coil (the transmitter) embedded in concrete and a secondary coil (the pick-up coil) installed in a vehicle. Using a magnetic field, the transmitter will transfer power from the source to the pick-up coil without physically contacting the source.

This research has four objectives:

1. Determine the cyclic thermal stresses in the concrete created from the IPT system.
2. Determine the structural stresses in the concrete from the cyclic load of heavy traffic applied on the surface of EPCP.
3. Determine the fatigue crack growth under cyclic traffic load.
4. Predict the durability of the concrete and the survivability of the embedded electronics.

1.4 Limitation

The research is limited to two load cases: 1) the internal thermal load from the heat generated by the IPT system and 2) the structural loads from the moving traffic. These two load cases can cause the most critical stresses, which result in concrete failure. The concrete durability and performance under these two load cases are considered by critical stresses, cracking, and residual service life. Strength capacity testing is conducted to determine the load limit of the EPCPs. The primary focus of this study is to investigate structural solutions that can be used to accommodate the IPT architectures embedded in concrete.

The civil, electrical, and mechanical research teams designed the embedded wireless charging systems. In civil engineering, concrete dimensions, such as thickness and concrete covering, follow the standard specification of ACI 318 code. The proposed concrete design allows the embedded electrical components to fit into the concrete structure. As a result, this research integrates concrete pavement and wireless charging systems.

This research does not address load cases other than the two mentioned above. Moreover, this research does not address the many IPT system configurations that could be considered.

2. LITERATURE REVIEW

This section provides an overview of previous research relevant to inductive power transfer and electrified roadways.

2.1 Development of Inductive Power Transfer (IPT) Systems for Roadway-Powered Electric Vehicles

Battery electric vehicles (BEVs), hybrid electric vehicles (HEVs), and plug-in hybrid electric vehicles (PHEVs) have batteries and run on electricity. There are two charging options: 1) stationary charging electric vehicles (SCEVs) and dynamic charging electric vehicles. This research focuses on full-sized IPT for dynamically charging electric vehicles. Dynamic charging utilizes electronics, which are integrated into the concrete pavement and charges vehicles on the move. In the future, EVs will be adapted to utilize IPT systems whether statically or dynamically. Researchers and industries around the world are interested in dynamic wireless charging for EVs.

The first roadway-powered electric vehicles (RPEVs) started in France in 1894 with the U.S. patent of the transformer systems for an electric railway by Hutin and Leblance (1894). In the past century, RPEV development has grown (Schladover 1988, Bolger 1989, Eghtesadi 1990, Klontz 1992, Empey 1994, Choi et al. 2015, Mi et al. 2016). Lawrence Berkeley National Laboratory began the RPEV project in 1976, and Partners for Advanced Transit and Highway (PATH) program started in 1992. Research teams around the world have recently been working on IPTs. These international teams include Korea Advanced Institute of Science & Technology (KAIST), University of Auckland, Bombardier, Oak Ridge National Laboratory, Korea Railroad Research Institute (KRRI), Endesa, Integrated Infrastructure Solution (INTIS), and Utah State University (ASPIRE) research team.

KAIST started with RPEVs in 2009 and created a sixth generation on-line electric vehicle (OLEV). KAIST's vehicle decreased battery size to 20 kWh and reduced construction costs of a power rail embedded roadway (Choi et al. 2015, Mi et al. 2016). The KAIST project resolved the problems of high-frequency and power transfer continuity, which were presented in the 1992 research conducted by PATH.

University of Auckland developed the configuration of the IPT. First, the IPT was made into a circular shape with 26 turns of Litz wire and 12-ferrite spokes (Budhia et al. 2011). Unfortunately, the circular pads created a non-uniform magnetic field, and the ferrite structure was fragile. (Covic and Boy 2013). Ferrite-less circular pads solved those issues, and a small scale IPT was embedded into the concrete pavement with steel and fiberglass reinforcement. The fiberglass reinforced pavement performed better than the steel reinforced pavement. Power loss decreased with the fiberglass reinforced pavement. (Tejeda et al. 2017). Robust ferrite-less double-D topology IPT improved magnetic field leakage (Pearce et al. 2019).

The KRRI team developed the IPT systems for a high-speed train in 2012. The IPT used a 1-MW inverter. The 128-m long IPT transmitter was placed on the railway and had four pick-ups. The efficiency at the 818-kW output power was 82.7% with a 5-cm air gap (Kim et al. 2015).

The Endesa team worked on a fast-charging station and developed dynamic charging lanes for electric buses (Endesa 2015). This team worked on a charger integrated into the ground for electric buses in Malaga, Spain (Endesa 2019). The contact charger was a 200-kW quick-charge station integrated into the

ground at the bus stop. Unfortunately, Endesa did not reveal much information about dynamic charging EVs.

INTIS, headquartered in Hamburg, Germany, developed both stationary inductive and dynamic inductive charging. INTIS focused on low-cost construction and durability (INTIS n.d.). The INTIS testing center in Emsland, Germany, tested the full range of the IPT. The 25-m long test track had a 1.2-m wide trench and double-D coil topology installed inside the trench. The IPT systems were designed for stationary and dynamic charging with 200 kW power at frequencies up to 35 kHz (INTIS 2014).

The Utah State University team tested dynamic IPT charging systems, which were installed in a test track at the Electrified Vehicle Roadway (EVR) in Logan, Utah. The IPT system was embedded in concrete pads, which were placed in a trench. This project tested the efficiency of the embedded IPT regarding different coil materials. The purpose was to investigate proper coating for the coil. The embedded IPT pads were tested at USU's Systems, Materials, and Structural Health (SMASH) laboratory for fatigue testing. As a result, the 42 in. x 42 in. x 10 in. pad, which consisted of Litz wire, the ferrites, aluminum plate, and rebar, performed the best subjected to the cyclic load with tensile stress at cracking of 209.3 psi and 91 cycles to initial cracking (Gardner 2017).

2.2 Inductive Charging Pavement Test

The French Institute of Science and Technology for Transport (IFSTTAR) at LUNAM University (Nguyen et al. 2014) integrated electrified concrete slabs into a test track at its Accelerated Pavement Testing facility. Five different dimensions of slab prototypes were tested with a dual wheel load of 65 kN for one million cycles. Displacement (LVDT) and strain sensors were used to monitor the mechanical behavior in the concrete during the test.

Nguyen et al. (2015) conducted accelerated pavement testing. The test was performed for 500,000 load cycles, the measurement data were collected at 10,000, 50,000, 100,000, 260,000, and 500,000 load cycles. As a result, most deflections at the slab joint were small, about 0.05 – 0.15 mm. The critical strain of 9 μm/m at the bottom of the slab did not cause any damage to the structure. Measurement of the vertical strains on the subgrade demonstrated that the subgrade did not depend on the traffic load but was related to temperature changes. The power supply still exhibited a good performance after 500,000 load cycles. An FEA software, CESAR-LCPC, was used to predict the tensile stress in the electrified slabs and compared the measured result.

2.3 Cracking Failure in Electrified Concrete Pavement

Generally, failure in concrete pavement is caused by cracking due to high stress. The possible origins of the cracks include fatigue, shrinkage, movement of the subgrade soil, constructional defects, aging, and environmental exposure (ACI Control of Cracking 2001). These kinds of failures are external. In electrified pavements, cracks are similar to the traditional concrete pavements; however, electrified pavements have unique and inherent problems. The heat created by the IPT causes stress from inside the pavement.

No research has been conducted on the internal thermal stresses created by the IPT. However, studies show embedded electric heating pipes used to deice concrete pavements behave similarly to the IPT system by generating cyclic heat inside the concrete, thus causing damage (Joerger and Martinez 2006).

2.3.1 Thermal Cycle from IPT System Operation in Concrete Pavements

As EVs pass over the embedded IPT systems, the systems produce heat, which expands the pavement. When the EV leaves the IPT system, the power transfer is terminated, the heat discontinues, and the pavement cools. Consequently, the concrete is subjected to cyclic heating, or transient thermal analysis, from the heat generated by the IPT. The fluctuating heat creates internal stresses that can contribute to concrete cracking. The internal stresses are based on the nonlinear temperature gradient in the concrete (ACI Thermal and Volume 2007). The temperature difference inside and outside of the electrified pavements also accounted for this structural problem (Mackiewicz 2014). Therefore, the lifespan of electrified pavement rapidly decreases (Sharifi et al. 2020).

The breakdown of the pavement due to the heat fluctuations of the IPT system is like the pavement damage caused by embedded heating pipes (ASHRAE 2015; FAA 2001). Both the IPT system and the heating pipes emitted internal heat, which caused the damage (Joerger and Martinez 2006). Unlike the cyclic heat in an IPT system, the heat emitted from the pipes was steady and contingent upon expected snowfall rate, air temperature, relative humidity, and wind speed.

For the numerical simulation studies, 3D FEA models (Abdualla 2018, Nechnech et al. 2002) were used to improve the heated pavement design related to time-dependent variables. This model can efficiently evaluate the heat generated, temperature distribution, and thermal stress over operational time. Abdualla (2018) and Nechnech et al. (2002) conducted sensitivity analysis based on the following design variables: electricity resistivity, heating pavement configuration, and ambient temperature. Abdualla (2018) showed stress growth was subjected to the different heating times and cumulative stress damage models to predict residual life.

Thermal analysis models of traditional concrete were demonstrated in the studies related to unusual fire stresses (Nechnech et al. 2002, Luccioni et al. 2003, Gernay 2013, Gernay and Franssen 2015). Using elastic-plastic concrete behavior, Liu et al. (2017) modeled reinforced concrete pavements that had internal thermal loads to determine stress damage and crack patterns. Xu and Cebon (2021) created FEA models of jointed plain concrete pavements (JPCPs) to predict the cracks subjected to vehicle load, foundation voiding, and environmental effect. The loads resulted in stressed and curling profiles.

Dere et al. (2006) conducted research on premature transverse cracks in a section of skewed JPCPs on Indiana State Route 49. Dere et al. (2006) used 3D FEA in ANSYS to investigate the failure in the JPCPs and cracking orientation. Three different subgrade materials were simulated in the FEA models by applying the traffic load and nonlinear thermal load. The actual temperature gradient was determined by comparing linear and nonlinear temperature gradients. As a result, the actual temperature gradient was nonlinear.

2.3.2 Traffic Damage of Concrete Pavements

Traffic load, which causes fatigue cracking on the electrified concrete pavement, poses a challenge to the pavement's structural design. Fatigue damage is a concern because it can lead to structural failure. Fatigue testing is used to determine pavement performance. Also, fatigue cracking is related to concrete pavement stiffness, strain level, temperature, and wheel loading frequency. Miller (1945) proposed the concept of cumulative damage for fatigue cracking prediction. The fatigue model predicted the number of repetitions to the pavement failure related to tensile strains.

Fatigue testing for traditional concrete pavement design can be applied to the electrified concrete pavement design. There are two methods for analyzing the fatigue resistance of concrete material. The first utilizes a fatigue crack propagation formulation. The second utilizes varying stress levels and load frequencies. The second method generates S-N curves to determine the beam's service life under the fatigue load. Fatigue life is derived from the S-N relationship between the stress ratio and cyclic loading number at failure.

Recent studies demonstrate how an FEA model of concrete pavement responded to moving truck loads. Pavement damage caused by the dynamic response of the moving load depended on the frequency and amplitude of the loads. Zhao and Wang (2020) developed the FEA model by focusing on the dynamic load effect of the traffic. The traffic frequency response under harmonic excitation was compared with field measurement from previous studies. The modeling results agreed with the field tests. The dynamic moving load was applied to concentrated or distributed moving loads with harmonic shape. Time-dependent moving loads were used in the model (Al-Qadi et al. 2008, Beskou and Theodorakopoulos 2011, Wang and Al-Qadi 2011, Chen et al. 2016, Wu et al. 2020).

Darestani et al. (2007) studied the dynamic responses of moving truck loads on concrete pavements. Strain and displacement sensors were used to measure the data at a site. An FEA model in ANSYS was used to simulate the pavement compared to the measuring data. Therefore, the 3D FEA model of the concrete pavement (Kuo et al. 1995) was an excellent tool for simulating complicated models of the foundation support, base thickness, friction, and dowel load transfer.

3. THERMAL LOAD, CYCLIC LOAD, AND ULTIMATE STRENGTH TESTING

The purpose of the research was to determine the behavior of embedded inductive coils in concrete pavement. Three full-scale concrete panels were constructed with embedded electronic components and various reinforcing schemes. External sensors were placed on the concrete during the testing phases.

The testing for each panel included 1) thermal testing as the coils were powering, 2) cyclic testing using a servo-controlled hydraulic ram with a simulated tire load to represent repeated traffic, and 3) ultimate flexural load testing until failure.

This chapter discusses the construction of each panel, including 1) the material properties, 2) reinforcement type and position, and 3) details of the instrumentation placed in each specimen. Additionally, the testing setups and procedures are described followed by the results from the three testing programs.

3.1 Specimen Design and Construction

This section lays out the construction procedures, the material properties, the thermal tests, the cyclic load tests, and the ultimate load tests.

3.1.1 Construction Procedure

Figure 3.1 shows the top view, and Figure 3.2 shows the cross-section A of a typical EPCP panel. The drawings include the reinforcement and IPT system elevation. Three wood forms were constructed to cast the large-scale 4 ft x 8 ft x 1 ft thick EPCP panels at the EVR (Figure 3.3). A #4 glass fiber reinforced polymer (GFRP) rebar and a #4 steel rebar were used for the two layers of reinforcement on each panel. Panels 1 and 3 were reinforced with top and bottom mats of GFRP rebar, and Panel 2 used a steel rebar for the two reinforcement mats. Phase-changing material (PCM) was placed on top of the ferrite for thermal management inside the concrete structure. Circular holes were drilled later to insert conduit pipes (2 in. diameter) to store the Litz wires and sensor cables reaching to the outside of the concrete panels for future connections.

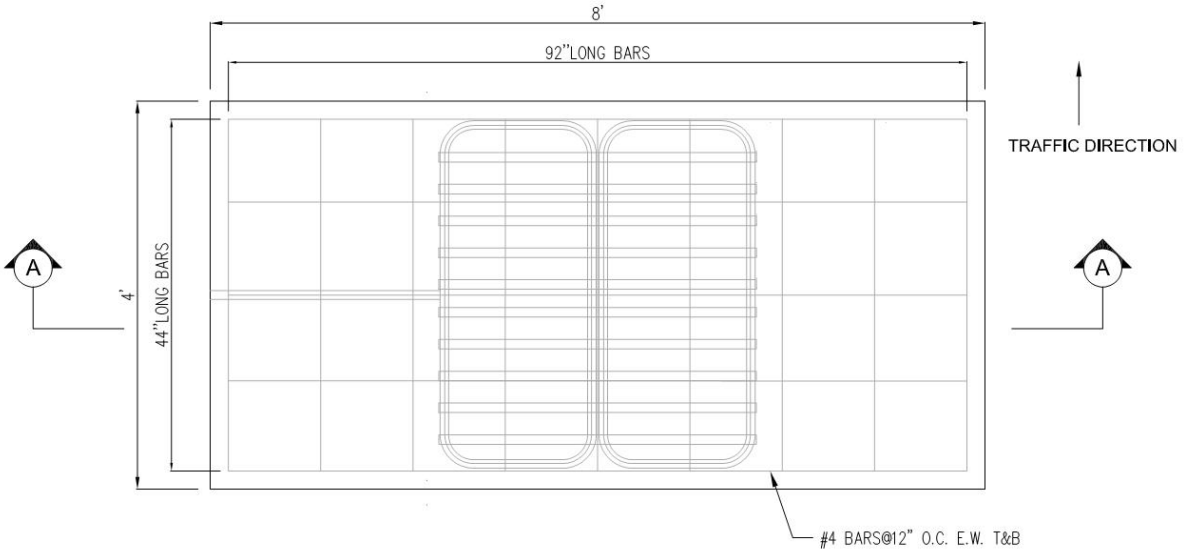

Figure 3.1 Top view of typical electrified precast concrete slab

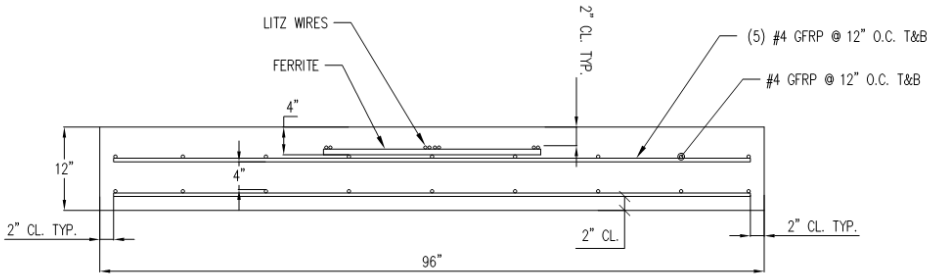

Figure 3.2 Cross-section detail-A of typical electrified precast concrete slab

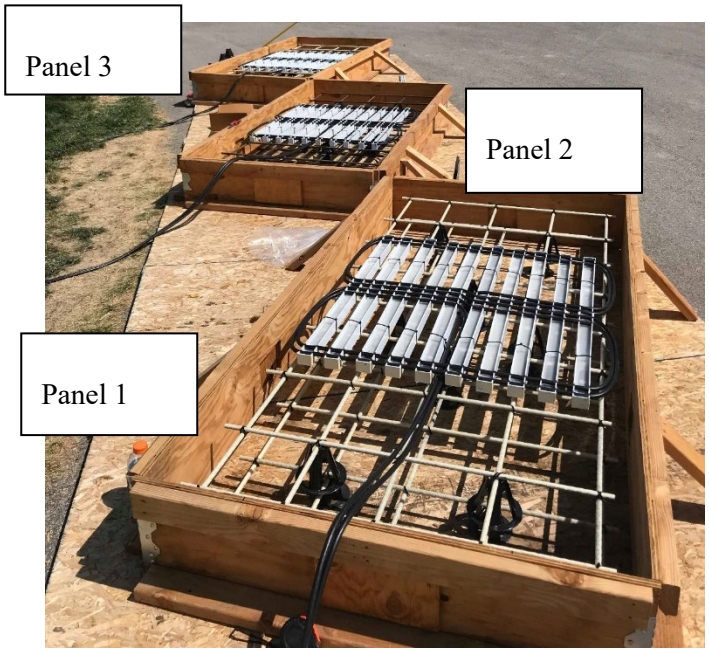

Figure 3.3 IPTs placed on the top reinforcement mats

Large-scale precast concrete electrified pavement design

Panel 1: #4 GFRP rebar was used for the reinforcement at 12-in. spacing each way and phase change material (PCM) filling on top of the ferrite with dimensions of 4 ft x 8 ft x 1 ft thick (Figure 3.4).

(a)

(b)

Figure 3.4 Panel 1 design (a) configuration and (b) embedded IPT system with PCM

Panel 2: #4 steel rebar was used for the reinforcement at 12-in. spacing each way and no phase change material (Non-PCM) with dimensions of 4 ft x 8 ft x 1 ft thick (Figure 3.5).

(a)

(b)

Figure 3.5 Panel 2 design (a) configuration and (b) embedded IPT system without PCM

Panel 3: #4 GFRP rebar was used for the reinforcement at 12-in. spacing each way and no phase change material (non-PCM) with dimensions of 4 ft x 8 ft x 1 ft thick (Figure 3.6).

(a) (b)

Figure 3.6 Panel 3 design (a) configuration and (b) embedded IPT system without PCM

3.1.2 Material Properties

The panels consisted of various materials: concrete, steel, GFRP, Litz wire, and ferrite bars.

Concrete

A 28-day concrete compressive strength of 4.5 ksi was considered for this research, and the quality of materials was similar to that of the Illinois Tollway (Class TL concrete). However, the mix did not include slag cement because of electromagnetic conditions, so the slag cement was replaced by Portland cement. For the EPCP construction, 4 in. x 8 in. (100 mm x 200 mm) concrete cylinders were cast to test for concrete properties such as compressive strength, tensile strength, and young modulus.

According to ASTM C39, three 4 in. x 8 in. (100 mm x 200 mm) concrete cylinders aged for 28 days were tested in compression at a rate of 440 lb/min (1960 N/min) by using the compression testing machine, as shown in Figure 3.7. The average 28-day concrete compressive strength of the three cylinders was 3,225 psi (Table 3.1).

The spilt tensile-strength tests were conducted in accordance with ASTM C496. Three 4 in. x 8 in. (100 mm x 200 mm) 28-day concrete cylinders were placed horizontally, and perpendicular forces were applied to the specimen's longitudinal axis. The testing caused vertical cracks along the cylinders' diameters, as seen in Figure 3.8. As presented in Table 3.2, the average tensile strength of three 28-day

concrete cylinder specimens was 424 psi (based on the average values from tests performed on 4 in. x 8 in. (100 mm x 200 mm) cylinders).

The static modulus of elasticity of concrete test was performed on three 4 in. x 8 in. (100 mm x 200 mm) 28-day concrete cylinders on ASTM C469 by using an axial deflectometer, as shown in Figure 3.9. The loads were applied to specimens at the rate of 10%, 20%, and 40% of the expected peak cylinder compressive strength (ASTM C469). Based on these tests, the stress-strain of elastic range was plotted (Figure 3.10). The slope of a line was created in the stress-strain plot from the 10% of stress value to 40% of the compressive stress values. The modulus of elasticity of concrete of 3,417 ksi was obtained from the slope of the plot.

Figure 3.7 concrete compressive strength test of cylinder

Figure 3.8 concrete split tensile strength test of cylinder

Figure 3.9 concrete Young's modulus test of cylinder

Table 3.1 Compressive strength test data of each concrete cylinder specimen

Test	f'_c (psi)
1	3116.652
2	3425.412
3	3130.578
avg	3224.214

Table 3.2 Split tensile strength test data of each concrete cylinder specimen

Test	f_t (psi)
1	349.3849
2	493.2212
3	428.3058
avg	423.6373

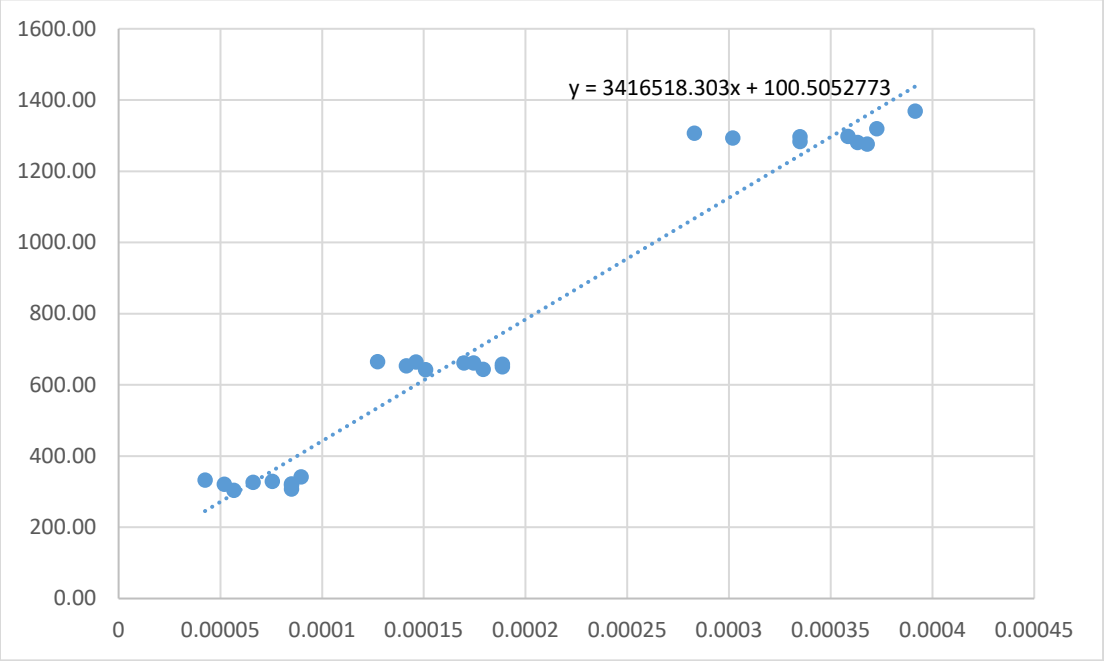

Figure 3.10 stress-strain plot for concrete in elastic range

Steel

One of the three concrete pavements was reinforced with steel bars (Size 4) grade 60, which had a specified yield strength of 60 ksi and elastic modulus of 29,000 ksi.

GFRP

GFRP rebars (Size 4 with 0.5 in. nominal diameter) were used as reinforcement for two concrete panels. These bars had a guaranteed tensile strength of 110 ksi and low tensile modulus of elasticity of 6,700 ksi with low unit weight/length of 0.189 lb/ft. (138.86 pcf density).

Litz Wire

Litz wire had a specified elastic modulus of 15.8 ksi and yield strength of 2.072 ksi.

Ferrite Bars

Mn-Zn Ferrite bar for power supplies had an elastic modulus of 17,500 ksi and yield strength of 4.35 ksi.

3.1.3 Construction and Experiment

Concrete was poured into the three panels on 07/30/2019 at 8:30 a.m. For thermal analysis, the tests were first conducted on 12/16/2019. The concrete panels were cured for 137 days, and the tests of all three panels were completed for the data collection on 02/14/2020. For Panels 1 and 2, the cyclic loading test occurred from 03/03/2021 – 03/11/2021, the concrete age was approximately 1 year and 8 months. In ultimate strength testing, the experiments occurred from 04/09/2021 – 04/10/2021 for Panels 1 and 2.

3.1.4 Instrumentation Installation

Fiber optic strain gauges were mounted on the prepared dog-bone acrylic samples using strain gauge adhesive in the sensor area (Figure 3.11a). The strain gauges were installed in critical areas of high-level stresses, as determined from the FEA modeling simulation (Figure 3.11b). The strain gauges were embedded in the concrete with the following directions:

- Panel 1 and Panel 3 were reinforced with GFRP. The strain gauges were attached to the rebar on the top (both x and y directions) and bottom (x direction) mats located at the center of the slabs. An area near the mid-slab edge also had two gauges at the top mat installed in x and y directions.
- Panel 2 was reinforced with steel rebar. Two gauges were attached to only the top mat rebar in horizontal x and y directions at the center of the slab.

Small PVC tubes were placed on the ferrites and Litz wires, so temperature sensors could be inserted after the concrete cured (Figure 3.12).

(a) (b)

Figure 3.11 (a) Fiber optic strain gauges mounted on a dog bone of acrylic and (b) Fiber optic strain gauges attached to rebar in two directions

Figure 3.12 PVC tubes installed on IPTs system

3.2 Thermal Test and Procedure

This section describes the thermal testing performed on the three concrete panels. Heat was generated through powering the IPT.

3.2.1 Test Setup

The test was conducted outside the EVR building during winter (Figure 3.13). The fiber-optic strain sensors were embedded inside the concrete pavement panels to measure the critical strain data. The temperature sensors were inserted into the tube to reach the coil area for the measurement (Figure 3.14 and Figure 3.15). To protect the temperature sensors from the wind and avoid measurement uncertainties, the sensors were covered with insulation. All gauges were connected to a data acquisition system to display and store data on a computer. The coils were connected to the power supply inside the building (Figure 3.16) to generate transfer energy in the thermal test.

Figure 3.13 Pavement test setup

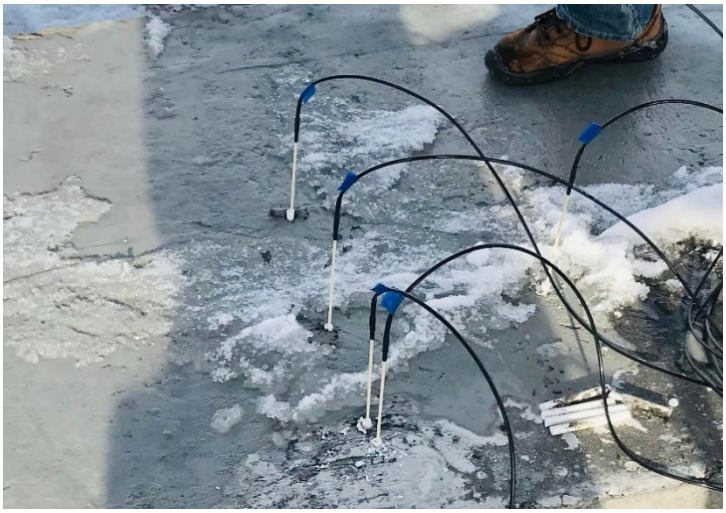

Figure 3.14 Temperature sensors inserted into the tubes

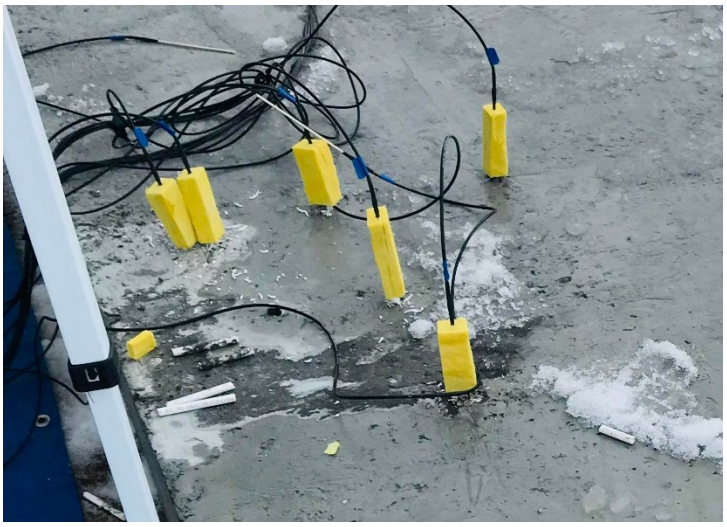

Figure 3.15 Temperature sensors, covered by insulation, inserted into the tubes

Figure 3.16 Power supply

3.2.2 Instrumentation Plan

On each panel, the fiber optic strain gauges (Figure 3.17 and Figure 3.18) were attached to the top and bottom reinforcement mats, and the six fiber optic temperature gauges were installed where the high temperature and strain would occur. As shown in Figure 3.17, Panel 1 had four strain gauges (SI1, SI2, SI5, and SI6) attached to the top reinforcement mat. Six temperature gauges were inserted into the tubes to measure the heat from the coil components. For instrumentation plans, *S* indicates strain gauges, *T* indicates temperature sensors, *I* indicates an internal gauge embedded in the concrete.

For Panel 3, four strain gauges (SI3, SI4, SI5, and SI6) were installed on the top mat. The center coil was shifted from the middle of the panel, which affected the position of the strain gauges (SI3 and SI4) differently from Panel 1. For Panel 2, two strain gauges (SI1 and SI2) were placed on only the top mat (Figure 3.17). As seen in Figure 3.18, Panel 1 had a strain gauge (SI8) attached to the bottom mat and a strain gauge (SI7) for Panel 3.

When the concrete was poured, tubes were placed on the IPT at critical points to leave spaces for inserting the temperature gauges. The temperature gauges were inserted during the test. The instrument labels are listed in Table 3.3.

Table 3.3 Instrumentation for each panel

	Temperature sensors	Fiber optic strain sensors
Panel 1	T1, T2, T3, T4 (broken), T5, and T6	SI1, SI2, SI5, SI6, and SI7
Panel 2	T1, T2, T3, T4, T5, and T6	SI1 and SI2
Panel 3	T1, T2, T3, T4, T5, and T6	SI3, SI4, SI5, SI6, and SI8 (broken)

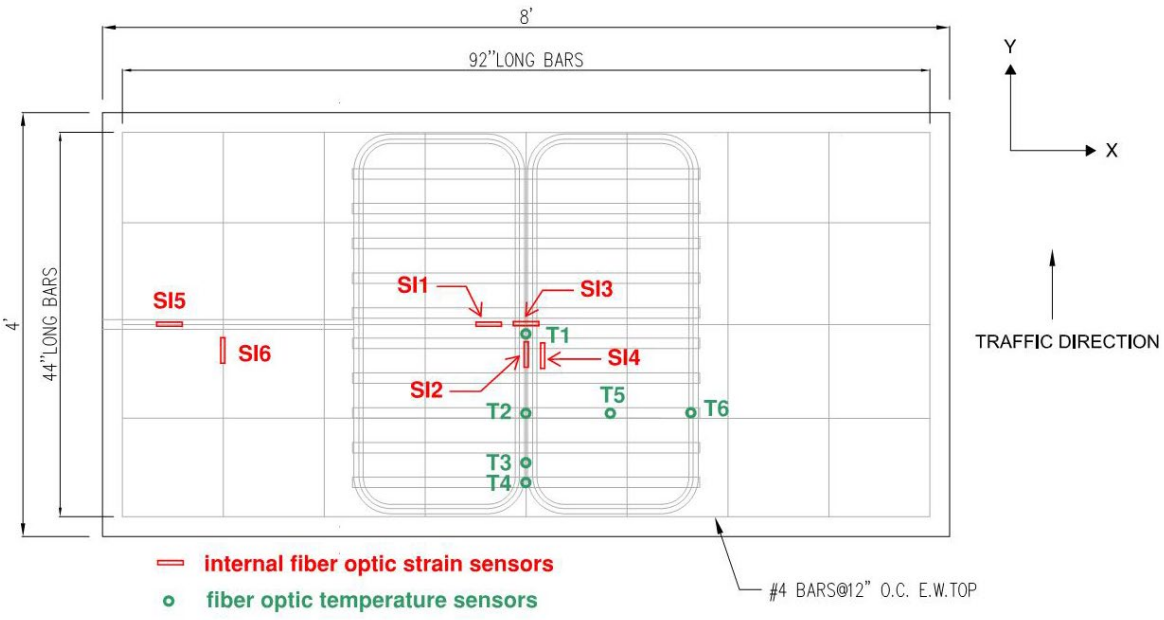

Figure 3.17 Instrumentation plan for typical panels – top mat of reinforcement, plan view

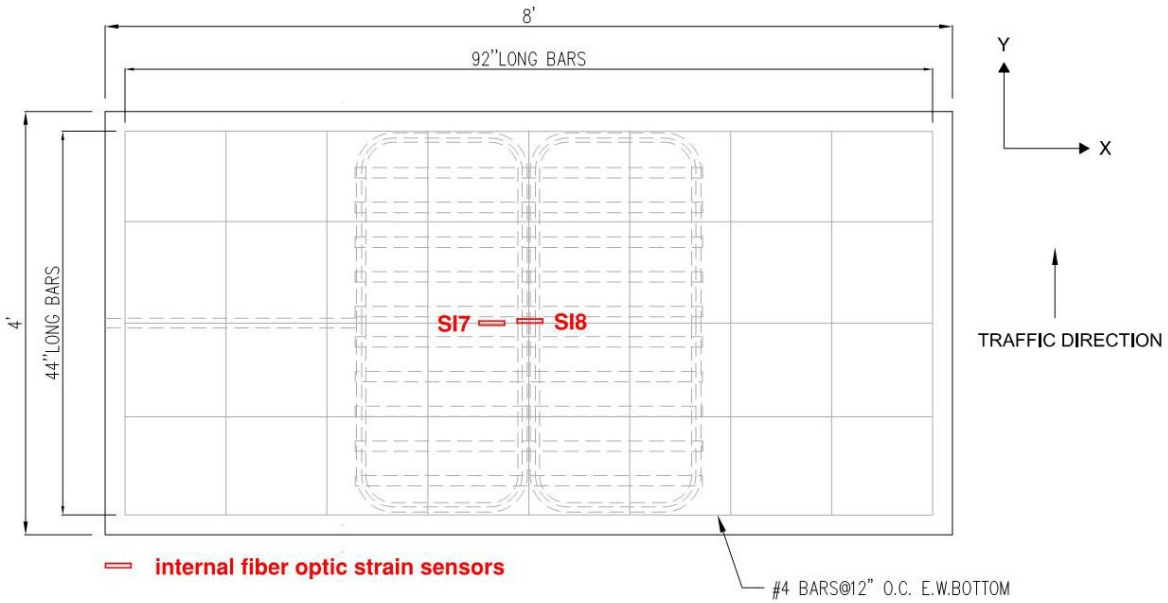

Figure 3.18 Instrumentation plan for typical panels – bottom mat of reinforcement, plan view

3.2.3 Measurement

The experiments on Panels 1, 2, and 3 were conducted on the same day and their performances were compared with and without PCM. The thermal testing on Panels 1, 2, and 3 was attempted a couple of times but failed because the IPT power supply could not run for an hour. Eventually, the IPT power source was corrected, and the IPT generated continuous power to accommodate the long period of measurements.

The embedded inductive coils were powered for approximately an hour (63 minutes) for Panel 1 and two hours (119 minutes) for Panel 3. Strain readings of the two panels were recorded while the coil was in operation. The recording continued for an hour after turning off the power. This test studied the heating and cooling rate in concrete materials. However, Panel 2 was tested for only 30 minutes due to power loss from the steel reinforcement (mentioned in the next chapter). Consequently, the researchers are concerned with using GFRP bars as the final design of the EPCP instead of the steel bars.

3.3 Cyclic Load Test

This section describes the mechanical loading applied to each panel using a hydraulic actuator.

3.3.1 Test Setup and Instrumentation

Two of the three EPCP panels (Panels 1 and 2) were transported from the EVR to the SMASH laboratory for this testing**.** After the thermal test, cyclic testing was conducted on the panels. The slab was placed directly on the top of a 4-in. thick gravel subbase in a wood frame (Figure 3.19). A hydraulic actuator applied a cyclic load defined as a sinusoidal load with a 32,000 lbs. maximum and 4,000 lbs. minimum amplitudes with 2 hertz of certain load frequency (Figure 3.20). The cyclic load simulated as AASHTO HS20 was applied on a spreader beam to split the load in half at each support (roller and pin supports). There was 6-ft. spacing between each wheel. Using 12 in. x 12 in. steel plates represented a tire pressure area.

Two types of strain gauges were used for the instrumentation: the internal (fiber optic) strain gauges and the external (foil strain transducers) strain gauges. The external strain gauges (SE) were mounted with epoxy at the same locations as the internal strain gauges (SI). As shown in Figure 3.21 and Figure 3.22, the external strain gauges SE1, SE3, SE4, SE6, and SE8 measured the strain in the x direction, and the gauges SE2, SE5 and SE7 captured data in the y direction. The internal strain gauges SI1 and SI3 measured the strain in the x direction and SI2 and SI4 for the strain in the y direction (Figure 3.21). The internal strain gauges SI1 measured the strain in the x direction and SI2 measured strain in the y direction.

The FEA models had similar mechanical properties and dimensions as Panels 1 and 2 to be a guideline for the instrumentation plan. As a result, the critical strain, which caused cracking, was expected to occur at the center of the panel in the x direction. The gauges were installed in the x and y directions spreading from the center of the panel to the IPTs system's location. In addition, a few strain gauges were placed at the outer area of the IPT system to monitor additional damage from the test. Thus, the gauges were used to investigate the concrete behaviors subjected to the structural load. The instrument labels are indicated in Table 3.4.

Figure 3.19 Cyclic loading test setup

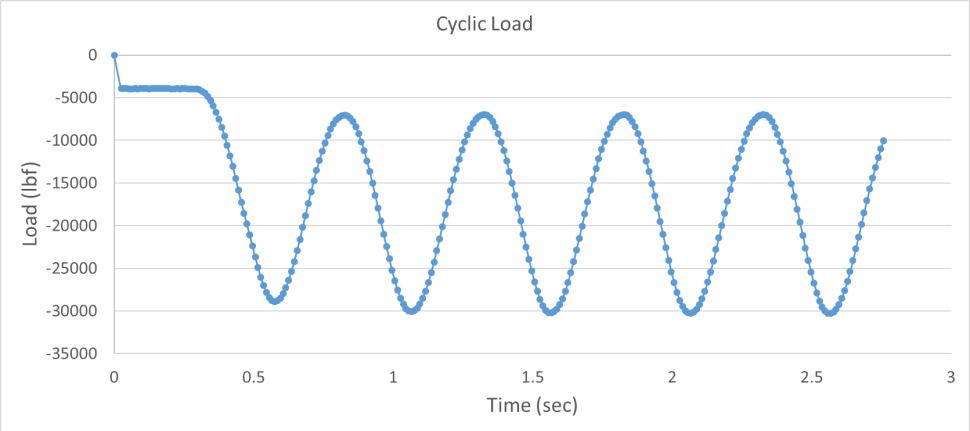

Figure 3.20 Cyclic load pulse

Table 3.4 Instrumentation of each panel

	External BDI strain sensors	Internal fiber optic strain sensors
Panel 1	SE1, SE2, SE3, SE4, SE5, SE6, SE7, and SE8	SI1, SI2, SI5, SI6, and SI7
Panel 2	SE1, SE2, SE3, SE4, SE5, SE6, SE7, and SE8	SI1 and SI2

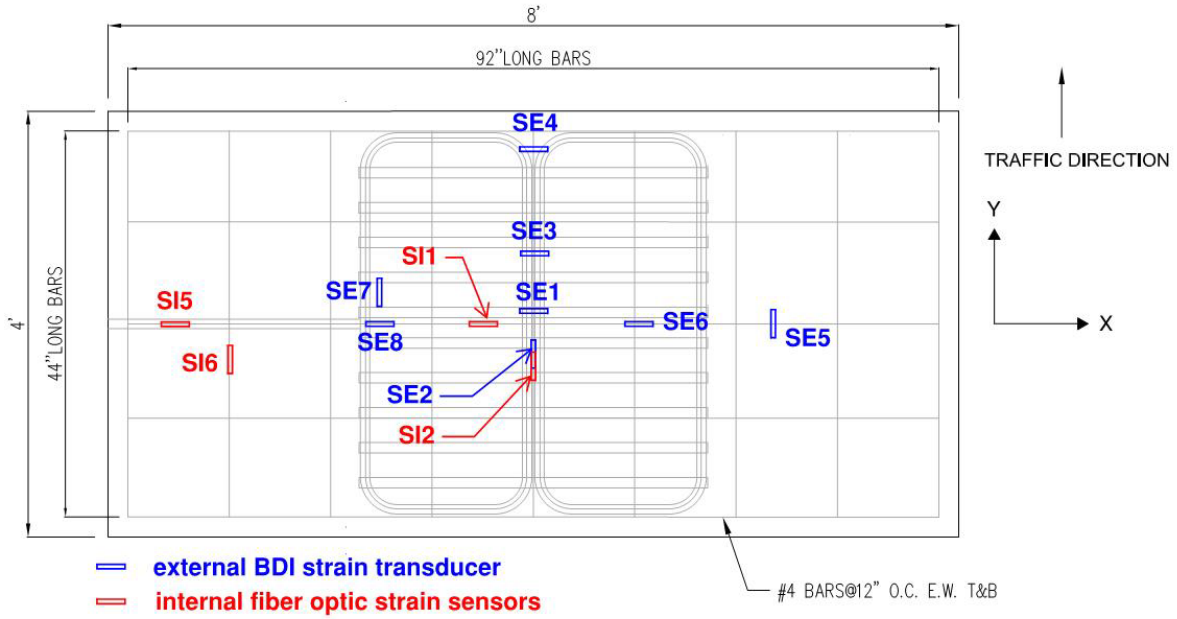

Figure 3.21 Instrumentation plan for typical panels – top mat of reinforcement, plan view

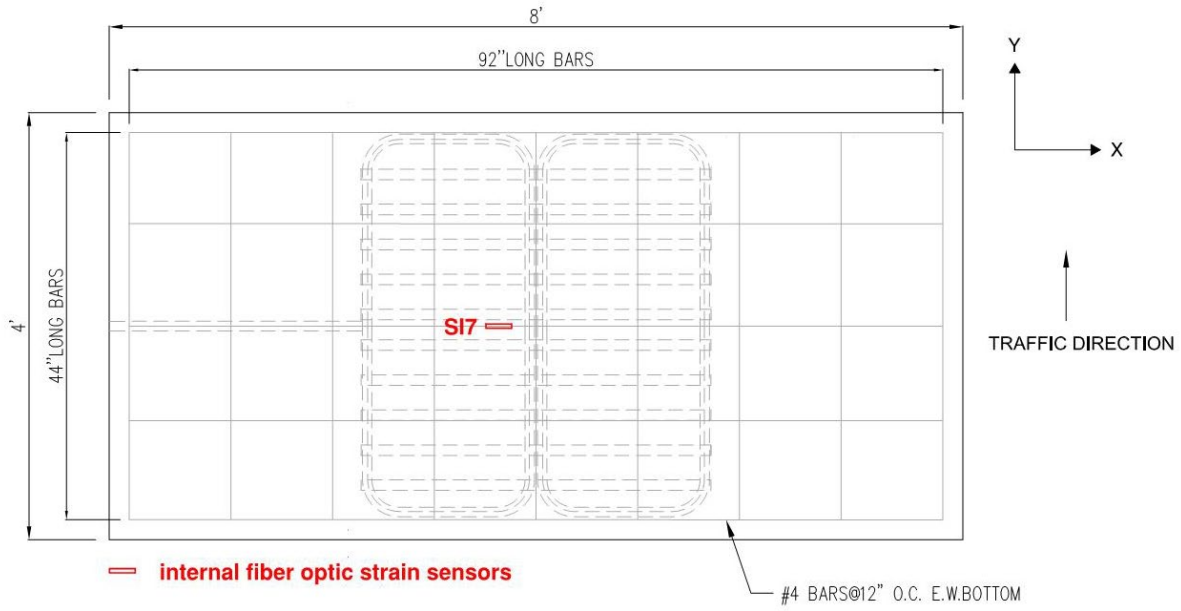

Figure 3.22 Instrumentation plan for typical panels – bottom mat of reinforcement, plan view

3.4 Ultimate Load Test

This section describes the application of a monotonically applied load until failure occurs.

3.4.1 Laboratory Procedure and Setup

To achieve an efficient service life, the EPCPs must have adequate strength to resist traffic and bending loads. The EPCPs were designed for the ultimate load for structural safety. The center-point loading test (as per ASTM C 293) was performed on the EPCPs to determine the modulus of rupture, known as flexural strength.

After completing the cyclic loading test, Panels 1 and 2 were turned upside down. They were placed under a simple support boundary condition (pin and roller supports), as shown in Figure 3.23 and Figure 3.24. Flexural tests were conducted on the panels. The tensile strengths of the panels were measured from the modulus of rupture. As seen in Figure 3.23, during the experiment, the beam was raised to the maximum height the SMASH lab equipment could accommodate, which affected the load setup. The space was inadequate to insert a roller under the head of the hydraulic actuator for transferring the applied load to the structure.

Only the steel plate with a dimension of 18 in. x 18 in. x 2 in. was inserted under the head of the machine. Therefore, the applied load did not meet the idealized center-point loading. The pressure load (18 in. x 18 in. pressure area) was applied at the center of the panel's span length instead. As a result, the maximum stress could be less than the actual stress of approximately 9% based on the maximum bending moment formulas of a simply supported one-span beam. Figure 3.25 presents the spacing such as span length and pressure-loading length in the center point loading test.

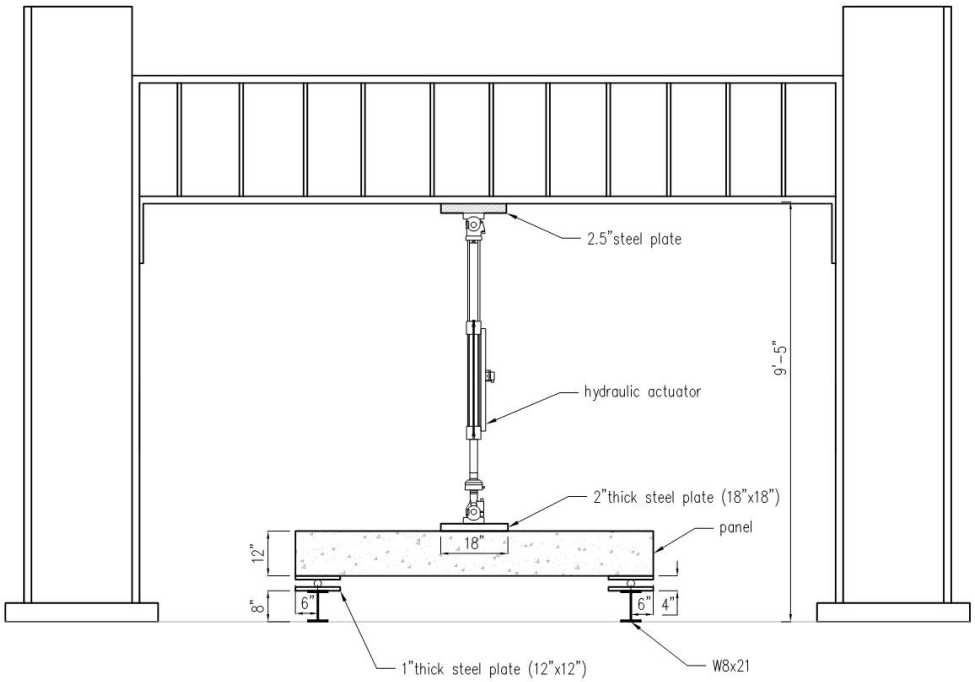

Figure 3.23 Failure load test setup dimension

Figure 3.24 Failure load test setup

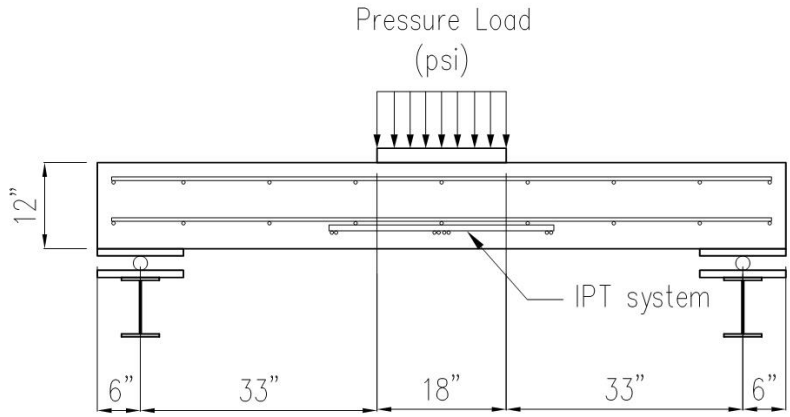

Figure 3.25 Center point loading test on the upside down panel, turning the IPT system at the bottom side

3.5 Summary

The physical tests were divided into three types: thermal, cyclic, and ultimate load testing to determine the durability of the EPCPs. The construction of the panels and material properties were described. The internal embedded strains were used in the thermal and cyclic load tests. In addition, external strain transducers were attached to the top surface of the concrete for crack pattern investigation in the fatigue test. Finally, the ultimate strength test was performed on the panels. The panels were turned upside down for the new boundary condition.

4. NUMERICAL MODELING

This chapter describes a 3D-FEA approach to model the electrified precast concrete pavements (EPCPs) under two load cases: 1) the internal thermal load from the embedded IPT systems and 2) the cyclic load representing the heavy vehicle on the roadway. The ultimate strength of the panels was determined through the maximum load and crack pattern result. As noted in Chapter 3, the analyses were conducted using concrete physical testing to obtain a realistic result. For thermal testing, experimental results were used as input parameters for a numerical solution using the ANSYS software. For the cyclic load case, the FEA models were calibrated to correct the results. Some unknown physical parameters, concrete stiffness, and boundary conditions were estimated from the real data.

4.1 ANSYS Modeling

The ANSYS mechanical FEA software (ANSYS 2021) was used to simulate the EPCPs' complex models. The mechanical behavior of the structure was investigated in terms of both elasticity and plasticity. To determine the robustness of the panels, nonlinear analysis was performed using ANSYS to obtain crack pattern and damage results.

4.1.1 Nonlinear Solution

The nonlinear analysis was performed in several steps. The step end-time was defined at each individual step. Automatic time stepping was defined by either time or sub step to control load step size, which was applied to the FEA models. The maximum and minimum load step sizes were also needed for the automatic time stepping to converge results. In the ANSYS program (ANSYS 2021), the Newton-Raphson method was used for solution convergence. In other words, the stiffness matrix was adjusted to impact nonlinear changes at each converged solution after equilibrium iteration.

The small load step sizes were required for the fatigue failure of the concrete pavement panel models to ensure that the solution would converge. The failure mode occurred when the solution did not converge. The ANSYS program then displayed a warning message indicating that a large deflection effect was active.

Newton-Raphson Procedure

The Newton-Raphson method was used to solve nonlinear static structural analysis in ANSYS mechanical (ANSYS 2021). Eq. (4.1) was a simultaneous equation of the finite element discretization process:

$$[K]\{u\} = \{F^a\} \tag{4.1}$$

Where $[K]$ = coefficient matrix, $\{u\}$ = vector of unknown degree of freedom (DOF) values, and $\{F^a\}$ = vector of applied loads.

Eq. (4.1) was rewritten by using an iterative process of the Newton-Raphson method to solve the nonlinear equation as:

$$[K_i^T]\{\Delta u_i\} = \{F^a\} - \{F_i^{nr}\} \tag{4.2}$$

$$\{u_{i+1}\} = \{u_i\} + \{\Delta u_i\} \tag{4.3}$$

Where $[K_i^T]$ = Jacobian matrix (tangent matrix), i = subscript representing the current equilibrium iteration, and $\{F_i^{nr}\}$ = vector of restoring loads corresponding to the element internal loads.

The FEA models were conducted through structural and thermal analyses in this research. In the static structural analysis, $[K_i^T]$ was the tangent stiffness matrix, $\{u_i\}$ was the displacement vector, and $\{F_i^{nr}\}$ was the restoring force vector calculated from the element stresses. In a transient thermal analysis, $[K_i^T]$ was the conductivity matrix, $\{u_i\}$ was the temperature vector, and $\{F_i^{nr}\}$ was the resisting load vector calculated from the element heat flows. Figure 4.1 explains that the Newton-Raphson iteration was proceeded until the problem converged. First, $\{u_0\}$ was assumed. Then, the updated tangent matrix $[K_i^T]$ and the restoring load $\{F_i^{nr}\}$ were determined related to the vector $\{u_i\}$. $\{\Delta u_i\}$ was computed from Eq. (4.2). Next, $\{u_{i+1}\}$ was obtained from the sum of $\{\Delta u_i\}$ and $\{u_i\}$. The next iteration continued until reaching the load level $\{F^a\}$, the solution converged in equilibrium.

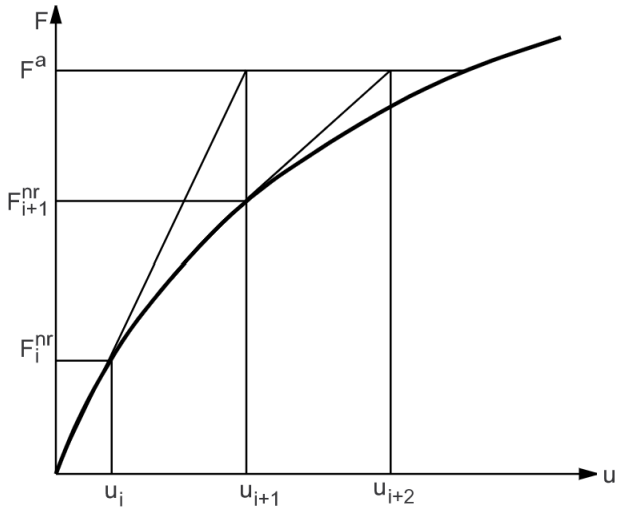

Figure 4.1 Newton-Raphson solution (ANSYS 2021)

In the case of the analysis considering path-dependent nonlinearities such as plasticity, a step-by-step analysis was required to meet the load path. Load increment and the Newton-Rapson iteration was used as:

$$\left[K_{n,i}^{T}\right]\{\Delta u_i\} = \{F_n^a\} - \left\{F_{n,i}^{nr}\right\} \tag{4.4}$$

Where $[K_{n,i}]$ was tangent matrix for time step n, iteration I $\{F^a{}_n\}$ was total applied force vector at time step n, and $\{F^{nr}{}_{n,i}\}$ was restoring force vector for time step n, iteration i.

This process was called the incremental Newton-Raphson procedure, as shown in Figure 4.2. The Newton-Raphson nonlinear solution contained full, modified, unsymmetric, and initial, and program-controlled options to control the updating of the stiffness matrix. Full and unsymmetric options made the stiffness matrix updated in every iteration, but less updated in the stiffness with using a modified procedure. Using initial-stiffness, Newton-Raphson restricted any stiffness matrix updates.

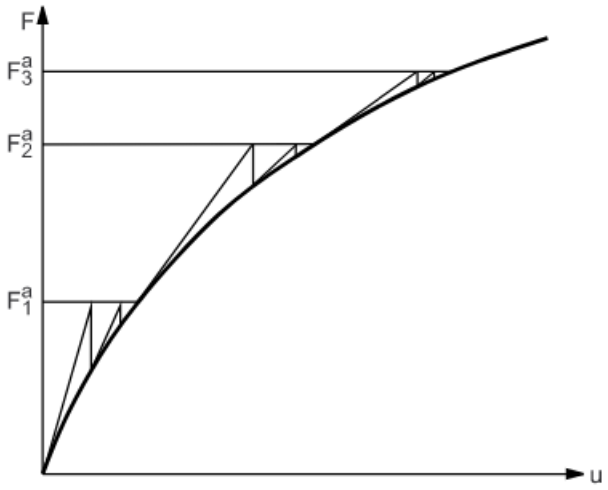

Figure 4.2 Incremental Newton-Raphson procedure (ANSYS 2021)

The Drucker-Prager material model was used for concrete to study the nonlinear plastic behavior. Reinforcement was bilinear plasticity to create the hardening module.

Computation Resources

In this study, a computer workstation with an Intel(R) Core (TM) i9-10980XE CPU processor with 192 GB of RAM was used. Disk space of up to 700 GB was required for the fatigue analysis of each pavement panel. The computational time was up to 72 hours.

4.2 Thermal Load Finite Element Analysis

The 3D FEA models of the full-sized EPCPs were simulated using ANSYS software (ANSYS 2021) to investigate any structural behavior or damage during the IPT system operation inside the concrete structure. All dimensions, material properties, and boundary conditions were similar to the experiment to obtain the same results. The models were subjected to thermal-structural analysis to determine the temperature, strain, and stress of the EPCPs.

4.2.1 Principle of Analysis for Thermal Load Case

The thermal analysis on the EPCP models was performed first to obtain the temperature data from heat transfer. The transient thermal analysis depended on the time of heating and cooling of the IPT. The previous temperature results were then imported into the static structural analysis to determine the mechanical behavior, such as strains and stresses of the EPCPs.

Thermal Analysis

The transient thermal analysis was used to determine temperature profile versus time. The FEA models predicted the heating and cooling rate when heat generation started and stopped in the IPT system. In 3D FEA models, the Panel 1 model was performed in two steps. During the first step, the IPT generated heat for about an hour. In the second step, the heat was turned off for an hour. The Panel 3 model was performed in two steps as well. The first step, with the IPT generating heat, ended after two hours; the second step, with the heat turned off, ended after one hour.

Static Structural Analysis

The temperature load from the thermal analysis was imported into the structural analysis to determine the thermal strain in the concrete. Thermal effect was derived from the temperature changes in the concrete pavement, which caused damage to the EPCP. The expansion or contraction of a structure was generated by temperature changes, resulting in thermal strains and thermal stresses. Contraction or compression in the concrete was negative, and expansion or tension in the concrete was positive.

Composite materials were subjected to large stresses due to the differences in their coefficients of thermal expansion (α). Thermal strain (Eq. 4.5) is the change in a dimension compared with the original dimension from the temperature change, which can be expressed as

$$\varepsilon_T = \alpha \Delta T \tag{4.5}$$

where ε_T is the thermal deformation, α is the coefficients of thermal expansion ($^oF^{-1}$), and ΔT is the temperature gradient (^oF) and stress expresses in Eq. (4.6) as follows:

$$\{\sigma\} = [D](\{\varepsilon\} - \{\varepsilon_T\}) \tag{4.6}$$

where $\{\sigma\}$ is the stress vector, D is elasticity or elastic stiffness matrix, $\{\varepsilon\}$ is the total strain vector, and $\{\varepsilon_T\}$ is the thermal strain vector.

4.2.2 Material Properties

All materials in the EPCP had isotropic elasticity behavior. The plasticity properties of the IPT system and GFRP reinforcement were represented as bilinear isotropic hardening. Table 4.1 and Table 4.2 provide the material property data for thermal-structural analysis divided into transient thermal and static structural analysis material properties.

Transient Thermal Analysis Material Properties

Table 4.1 Mechanical material properties

Material	Thermal		Physical
	Thermal conductivity, (Btu/[h-ft-^{o}F])	Specific heat, (Btu/[lb-^{o}F])	Density, (lb-ft^3)
Concrete	1.45*	0.24	145
GFRP rebar	35	0.1	138.6
Ferrite	2.31	0.18	306
Litz wire	23.11	0.092	70
Subbase	1.04	0.215	100

*referred to ACI 207

Static Structural Analysis Material Properties

Table 4.2 Mechanical material properties

Material	Elasticity		Thermal	Physical
	Modulus of elasticity (E), (psi)	Poisson's ratio (ν)	Coefficients of thermal expansion, ($^oF^{-1}$)	Density, (lb-ft^3)
Concrete	$3x10^7$	0.3	$7.78x10^{-6}$	145
GFRP rebar	$6.7x10^6$	0.3	$3.3x10^{-6}$	138.6
Ferrite	$1.75x10^7$	0.2	$5.17x10^{-6}$	306
Litz wire	15,800	0.3	$9.33x10^{-6}$	70
Subbase	300	0.4	$4x10^{-6}$	100

4.2.3 Mesh and Element

In concrete and gravel support material, the element order of the mesh was defined as an eight-node element (hexahedral solid element) as solid 278 and solid 185 in thermal and structural analysis, respectively. The reinforcement was meshed to a two-node beam element.

In as much as the mesh size impacted the FEA solution accuracy, the mesh sensitivity analysis was undertaken prior to modeling to determine the most accurate mesh size. As presented in Table 4.3, the analysis was done by comparing the response of the model of Panel 2 under cyclic fatigue loading with various mesh sizes. The mesh sizes ranged from 1.4 in. to 2.0 in. When element sizes were less than 1.4 in., the model solution failed to converge.

If the mesh size was larger than 2.0 in., the FEA results were much different than the experiment. Figure 4.3 is created from tensile stresses in Table 4.3 to show the difference in mesh sizes corresponding to the stress. In Table 4.3, the absolute magnitudes of errors in tensile stresses for concrete in horizontal x direction were trivial at less than 1%. The tensile stresses from the mesh sizes of 1.6 in. and 1.7 in. differed by 0.08%. The 1.5 in. mesh size was chosen because the crack pattern most agreed with the actual failure from the physical tests. Therefore, for the two load cases, the 1.5 in. element size for all materials was used to yield the most accurate outputs with reasonable analysis time.

Table 4.3 Mesh sensitivity analysis

Mesh size (in.)	Tensile stress at x direction, (psi)	% difference
1.4	531	-
1.5	529	0.377
1.6	526	0.477
1.7	526	0.080
1.8	522	0.706
2.0	519	0.657

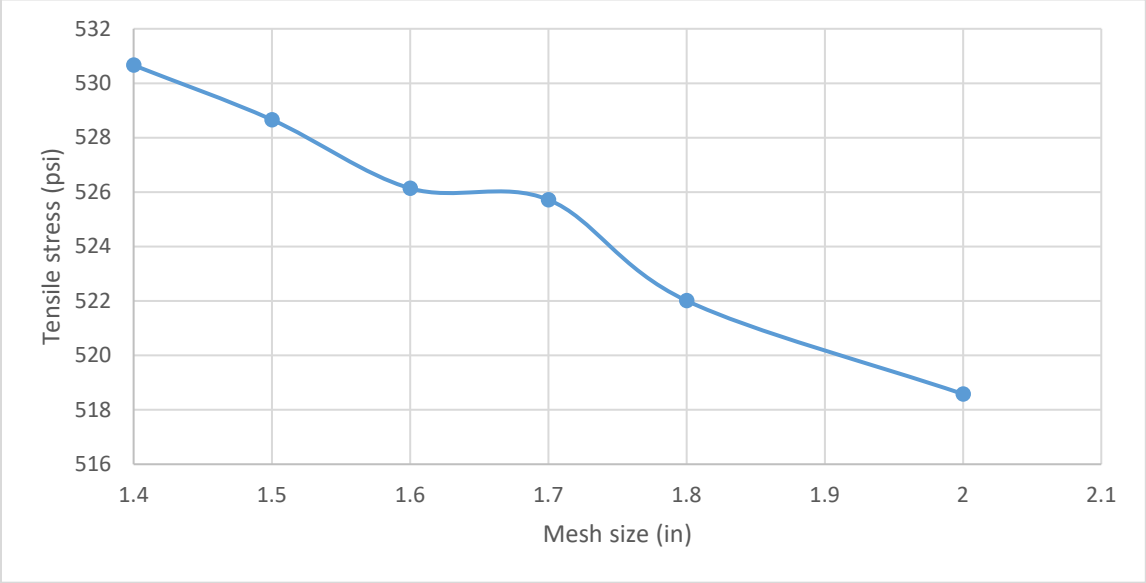

Figure 4.3 The relationship between mesh sizes (in.) and tensile stresses (psi) in concrete

Material Modeling

Concrete was modeled using a solid 278 element to support reinforcing-element generation (Figure 4.4). The solid 278 consists of 8 nodes in 3D with a single degree of freedom at each node. The element is also capable of thermal conductivity for steady-state or transient thermal analysis. In structural analysis, the solid 185 element was set as a default, which has eight nodes with three degrees of freedom: translations at each node in x, y, and z directions, as shown in Figure 4.4. This element contains plasticity, hyper elasticity, stress stiffening, creep, large deflection, and large strain capabilities.

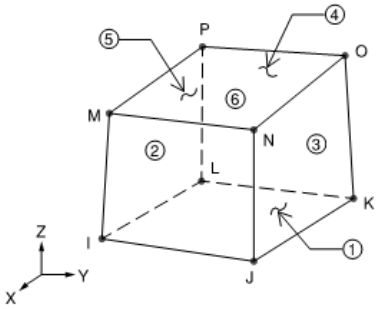

Figure 4.4 3D solid 278 or 3D solid 185

The gravel support was also modeled using a solid 278 element with the same capability as mentioned in the concrete material. Afterward, this element was switched to solid 185 in the structural analysis.

The IPT system consisted of Mn-Zn ferrite and Litz wire. The ferrite and wire were modeled using line bodies of REIN264 with standard 3D link elements reinforced to base element of the solid 278. The REIN264 has stress stiffening, large strain, plasticity, creep, and large deflection. Reinforcing fibers of REINF264 are oriented in spaces and had their intersection points of II and JJ for sharing nodes with the

solid 278 base element, as shown in Figure 4.5. In addition, each fiber contains only uniaxial stiffness or conductivity.

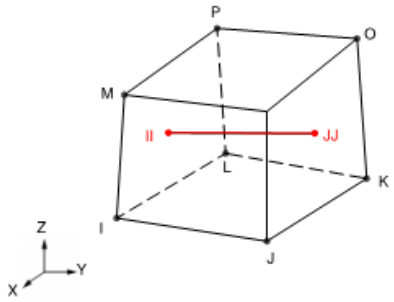

Figure 4.5 3D 8-Node Solid of REINF264

The GFRP rebar was modeled using the discrete reinforcing element REINF264 like the IPT system, as presented in Figure 4.5.

Geometry

In transient thermal analysis, the full-size model for all three EPCP panels was used with the dimensions of 96 in. x 48 in. x 12 in., as seen in Figure 4.6.

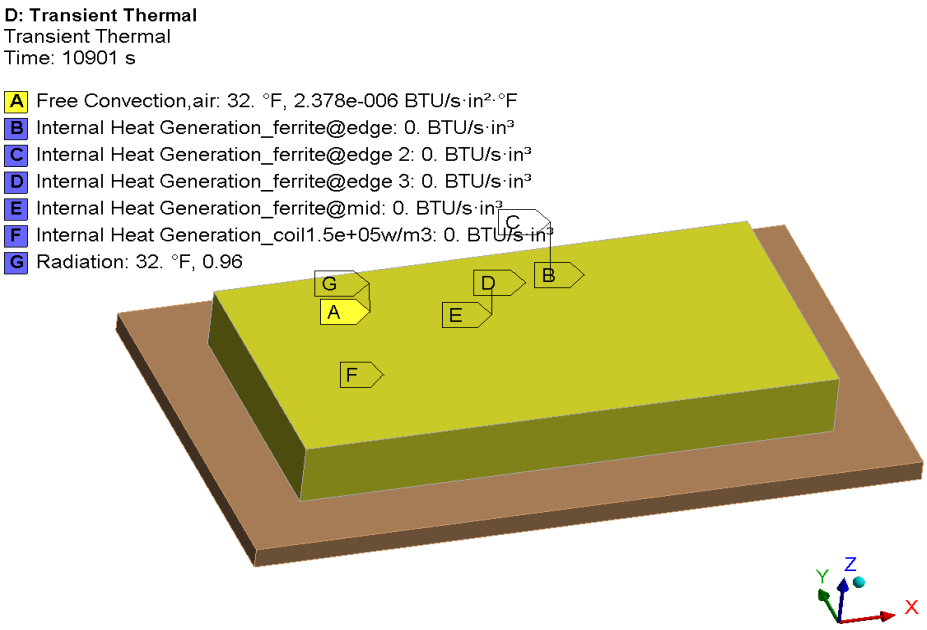

Figure 4.6 Geometry of a full panel model for typical panels

4.2.4 Connections and Contacts

The contact between the concrete body and the gravel support body was “frictional” with a friction coefficient of 0.1. ANSYS mechanical had specific functions for modeling the reinforcement into a structure in the thermal-structural analysis by selecting the model type property as “reinforcement.” The reinforcement was modeled as line bodies with assigned #4 GFRP rebar cross section via the discrete reinforcing element REINF264 mentioned above.

4.2.5 Boundary Conditions and Applied Loads

Transient Thermal Analysis

To demonstrate the boundary conditions, free convection was caused by heat transfer of the IPT charging system generating heat inside the concrete, and the EPCP was exposed to the ambient outdoor air. The initial temperature was set at 32°F (0°C). Thus, the concrete surfaces exposed to weather were assigned for the convection coefficient of 2.4×10^{-6} BTU/s·in^2·°F with the temperature of 32°F and the emissivity of 0.96. The heat from the IPT was exchanged from the concrete surface to ambient temperature (32°F) by radiation. The initial temperature was 32°F.

For all three panels, internal heat-generated loads in the ferrite were derived from expected loss contours in the ferrite bars (Varghese 2021). These derived heat flux results were then applied as contours and divided into individual elements of the ferrites, as shown in Figure 4.7 to Figure 4.10. The heat loads in the Litz wires were adjusted until the temperatures in the model coincided with the measured temperature from the physical thermal testing (Figure 4.11). The parameters of heat loads in the IPT are shown in Table 4.4, Table 4.5, and Table 4.6.

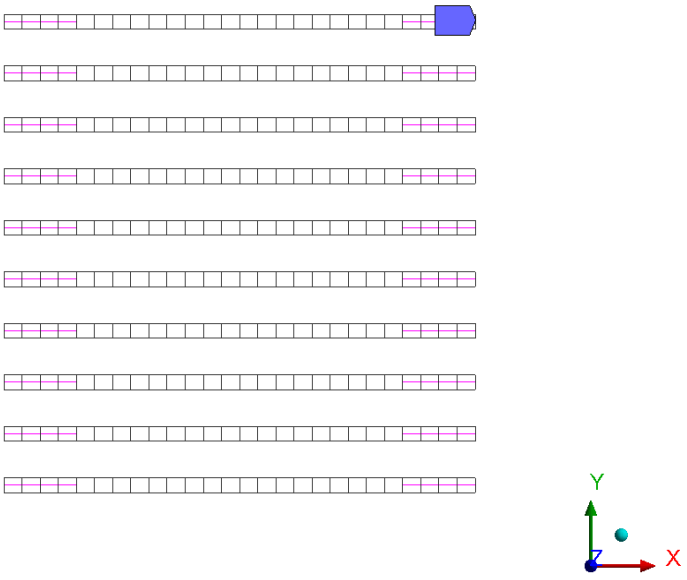

Figure 4.7 Internal heat generation in ferrite bars contour location @ edge 1

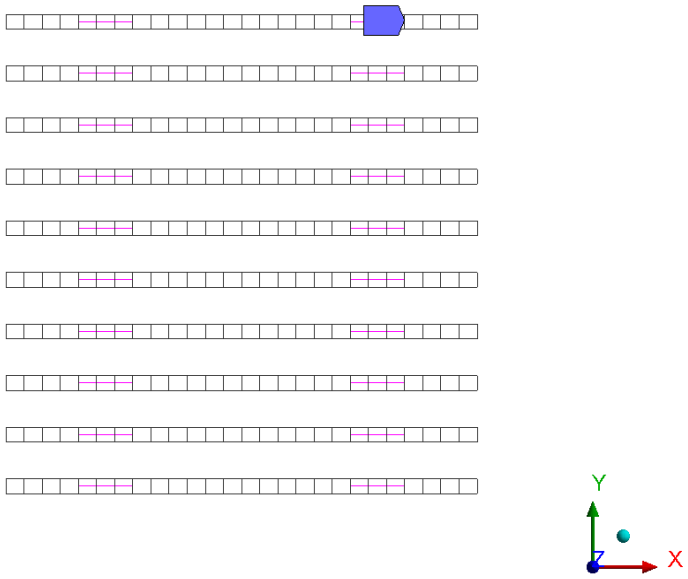

Figure 4.8 Internal heat generation in ferrite bars contour location @ edge 2

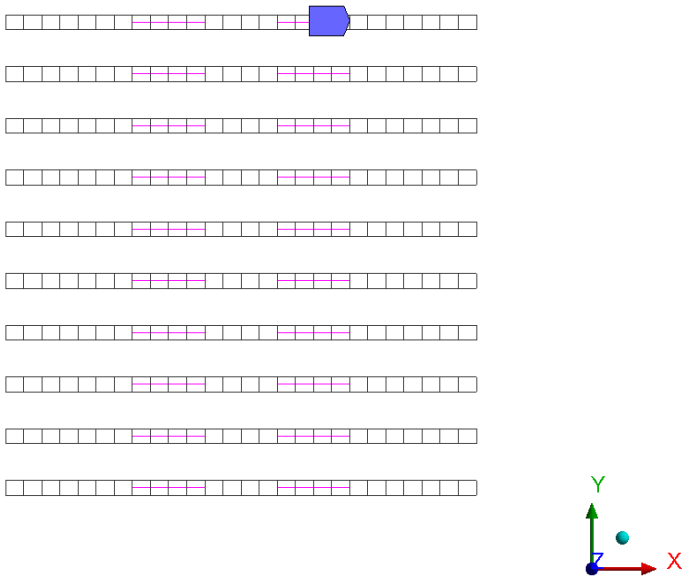

Figure 4.9 Internal heat generation in ferrite bars contour location @ edge 3

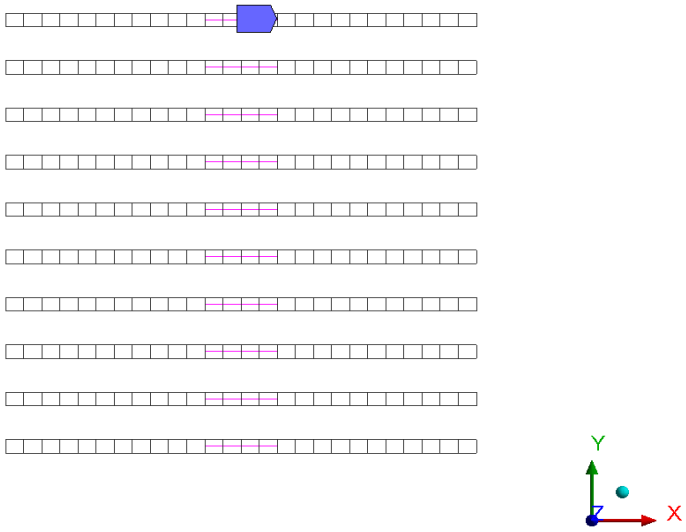

Figure 4.10 Internal heat generation in ferrite bars contour location @ mid

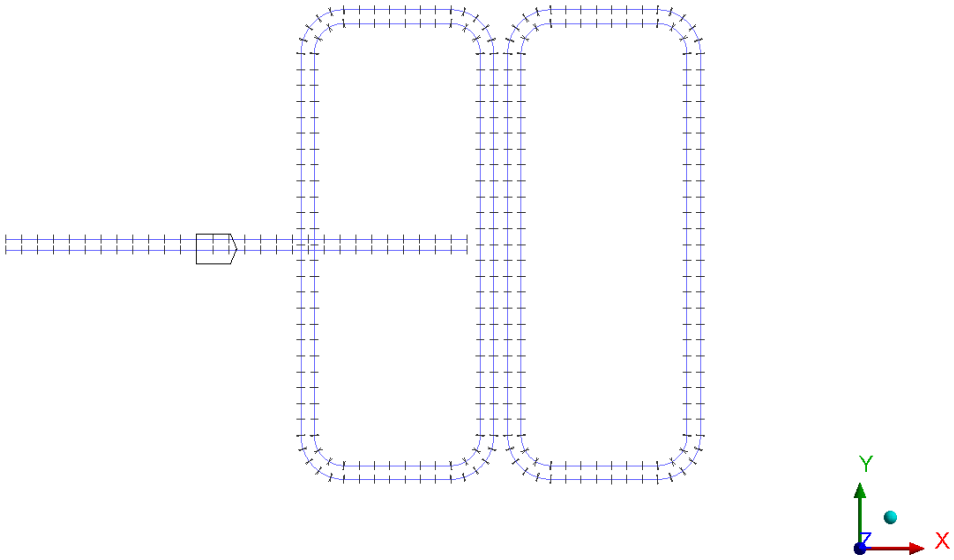

Figure 4.11 Internal heat generation in Litz wire

Table 4.4 Internal heat generation parameters in coil for Panel 1

Steps	Time (s)	Internal Heat Generation@ edge 1 (BTU/s·in^3)	Internal Heat Generation@ edge 2 (BTU/s·in^3)	Internal Heat Generation@ edge 3 (BTU/s·in^3)	Internal Heat Generation@ mid (BTU/s·in^3)	Internal Heat Generation@ wire (BTU/s·in^3)
1	0	0	0	0	0	0
1	1	2.5887×10^{-7}	1.1649×10^{-4}	4.1419×10^{-4}	9.0602×10^{-4}	3.1064×10^{-4}
2	601	2.5887×10^{-7}	1.1649×10^{-4}	4.1419×10^{-4}	9.0602×10^{-4}	3.883×10^{-4}
3	1801	2.5887×10^{-7}	1.1649×10^{-4}	4.1419×10^{-4}	9.0602×10^{-4}	3.883×10^{-3}
4	8001	0	0	0	0	0

Table 4.5 Internal heat generation parameters in coil for Panel 2

Steps	Time (s)	Internal Heat Generation@ edge 1 (BTU/s·in^3)	Internal Heat Generation@ edge 2 (BTU/s·in^3)	Internal Heat Generation@ edge 3 (BTU/s·in^3)	Internal Heat Generation@ mid (BTU/s·in^3)	Internal Heat Generation@ wire (BTU/s·in^3)
1	0	0	0	0	0	0
1	1	2.5887×10^{-7}	1.1649×10^{-4}	4.1419×10^{-4}	9.0602×10^{-4}	1.2426×10^{-5}
2	2001	2.5887×10^{-7}	1.1649×10^{-4}	4.1419×10^{-4}	9.0602×10^{-4}	3.1064×10^{-3}
3	4001	2.5887×10^{-7}	1.1649×10^{-4}	4.1419×10^{-4}	9.0602×10^{-4}	3.1064×10^{-3}
4	8001	0	0	0	0	0

Table 4.6 Internal heat generation parameters in coil for Panel 3

Steps	Time (s)	Internal Heat Generation@ edge 1 (BTU/s·in^3)	Internal Heat Generation@ edge 2 (BTU/s·in^3)	Internal Heat Generation@ edge 3 (BTU/s·in^3)	Internal Heat Generation@ mid (BTU/s·in^3)	Internal Heat Generation@ wire (BTU/s·in^3)
1	0	0	0	0	0	0
1	1	2.5887×10^{-7}	1.1649×10^{-4}	4.1419×10^{-4}	9.0602×10^{-4}	1.5532×10^{-3}
2	3601	2.5887×10^{-7}	1.1649×10^{-4}	4.1419×10^{-4}	9.0602×10^{-4}	3.3394×10^{-3}
3	4201	2.5887×10^{-7}	1.1649×10^{-4}	4.1419×10^{-4}	9.0602×10^{-4}	2.4851×10^{-3}
4	7301	2.5887×10^{-7}	1.1649×10^{-4}	4.1419×10^{-4}	9.0602×10^{-4}	2.4851×10^{-3}
5	8021	2.0968×10^{-7}	9.3191×10^{-5}	3.3135×10^{-4}	7.2482×10^{-4}	7.7659×10^{-4}
6	10901	0	0	0	0	0

Static Structural Analysis

The bottom face of gravel support was constrained in all x, y, and z directions as fixed support (Figure 4.12). Standard earth gravity of 386.1 in/s^2 was applied to the EPCP structure.

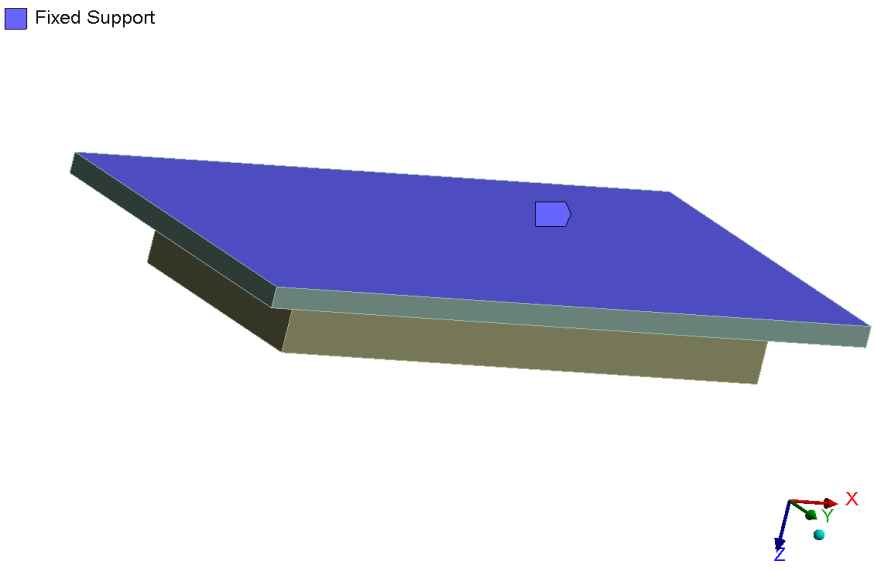

Figure 4.12 Fixed support applied at the bottom face of the gravel support

4.3 Cyclic Load Finite Element Analysis

The 3D FEA model in ANSYS software was used to study the mechanical behavior of the EPCP, which was embedded with an IPT system and subjected to cyclic load testing. In the FEA model, the cyclic load was a simulation of truck traffic, resulting in stresses and strains to the concrete structures and their performances during service life. This simulation was performed in Static Structural Analysis in ANSYS, which was suitable for long-duration loading, cyclic loading, and structural failure.

The FEA models were validated by the results of the experiment. Concrete stiffness, boundary condition imperfections, and default conditions assumed by the FEA simulation caused the differences between the model and experiment. Furthermore, the concrete stiffness was probably reduced due to cracks from the heat of the coil during thermal testing in Phase 1. In this process, all material properties in the models were calibrated to the real experimental data. The FEA models were properly developed. If the FEA simulation results did not coincide with the experimental test results, the FEA models were adjusted until the results were consistent. The laboratory test was done in the SMASH lab, and all results were shown in the previous section.

4.3.1 Material Properties and Element Types

Plasticity-Damage Microplane Model for Concrete

Bazant and Gambarova (1984 and 1985) conducted research on a brittle aggregate material behavior using the microplane model through stress-strain laws. Uniaxial tensile strain-softening behavior was studied and subjected to loading and unloading combination on individual microplanes. Coupled damage-plasticity and elastic damage are the microplane material model types. The coupled damage-plasticity has been used for concrete material that consists of aggregates and undergoes cyclic loading. Zreid and Kaliske (2014, 2016, and 2018) used this model to determine the modeling damage and strain-softening. The stress-strain relationship is used to formulate the microplane material as follows (EQ 4.7):

$$s = \frac{3}{4\pi}\int_{\Omega}\left(1 - d^{mic}\right)\ \left[K^{mic}V\left(e_V - e_V^{pl}\right) + 2G^{mic}Dev^T \times (e_D - e_D^{pl})\right]d\Omega \qquad (4.7)$$

where d^{mic} = the normalized damage variable $\{0 \le d^{mic} \le 1\}$, ε_V^{pl} = the volumetric microplane plastic strain, and ε_D^{pl} = the deviatoric plastic strain.

The nonlocal implicit gradient regularization, presented as *c* and *m* parameters in Table 4.7, is added to the model to accomplish numerical instabilities, convergence failure, and pathological mesh sensitivity. Furthermore, the outputs of this model are the homogenized total damage, homogenized tension damage, homogenized compression damage, and the split weight factor.

Smooth Three-Surface Microplane Cap Yield Function

A smooth three-surface microplane Drucker-Prager yield function, as shown in Figure 4.13, defines the plasticity. The yield function is determined within the undamaged stress space, which includes tension and compression caps located at the left and right sides, respectively, based on triaxial mechanical properties in the material, and is defined as shown in Eq 4.8 through 4.26.

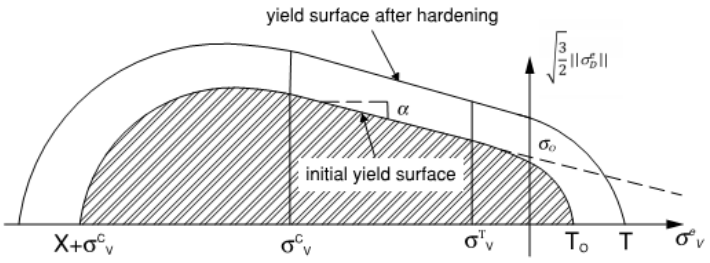

Figure 4.13 Microplane Drucker-Prager yield function

$$f^{mic} = \frac{3}{2}\mathrm{s}_D^e * \mathrm{s}_D^e - f_1^2 f_c f_t \tag{4.8}$$

where f_1 = the Drucker-Prager yield function with hardening, f_C = the compression cap, and f_t = the tension cap. The Drucker-Prager yield function is given by:

$$f_1 = \mathrm{s}_0 - \mathrm{a}\mathrm{s}_V^e + f_h \tag{4.9}$$

where σ_0 = the initial yield stress, α = a friction coefficient, and f_h = a hardening function. The compression cap expresses as follows:

$$f_C = 1 - H(\mathrm{s}_V^C - \mathrm{s}_V^e)(\frac{(\mathrm{s}_V^C - \mathrm{s}_V^e)^2}{X^2}) \tag{4.10}$$

$$X = Rf_1(\mathrm{s}_V^C) \tag{4.11}$$

where $H(\cdot)$ = the Heaviside step function for creating the cap only from the domain of the stress state, $\sigma^C{}_V$ = the abscissa of the intersection point between f_C and f_1·R is the ratio between the major (deviatoric) and minor (volumetric) axes of the cap. The tension cap is defined as:

$$f_t = 1 - H(\mathrm{s}_V^e - \mathrm{s}_V^T)(\frac{(\mathrm{s}_V^e - \mathrm{s}_V^T)^2}{(T - \mathrm{s}_V^T)^2}) \tag{4.12}$$

$$T = T_0 + R_T f_h \tag{4.13}$$

where σ_V^T = the abscissa of the intersection point between f_1 and $f_T \cdot T_0$ is the initial intersection of the cap with the volumetric axis, and R_T = a hardening parameter controlling the increase of the intersection point T due to hardening. The hardening is calculated as:

$$f_h = D\mathrm{k} \tag{4.14}$$

$$\dot{\mathrm{k}} = \dot{\lambda} \tag{4.15}$$

where D = a hardening parameter, and κ = a hardening variable.

Fifteen parameters were assigned for the coupled damage-plasticity microplane model of the concrete. The two Drucker-Prager yield function parameters (f_{uc} and f_{ut}) were derived from experimental tests, concrete cylinder compression testing, and split concrete cylinder testing, respectively. f_{bc} is defined as:

$$f_{bc} = 1.15 f_{uc} \tag{4.16}$$

The compression cap parameters were from triaxial experimental data, but they are determined as follows:

$$\mathrm{s}_V^C = -\frac{2}{3} f_{bc} \tag{4.17}$$

R parameter is the ratio between the major and minor axes of the cap and is calculated as 2, f_1 is the Drucker-Prager yield function with hardening as follows:

$$R = X_0 / f_1(\mathrm{s}_V^C) \tag{4.18}$$

Damage Evolution

The concrete damage under cyclic load considered two cases to make the model realistic. First, the difference between the initial and evolution of damage was in tension and compression. Concrete was weak in tension and had softening behavior happening immediately after the elastic limit. Whereas concrete hardening in compression was monitored before the softening. Second, the concrete stiffness was reduced during tensile cracking due to the transition from tension to compression. The damage split (Lee 1998) can explain this transition and is defined by:

$$1 - d^{mic} = (1 - d_c^{mic})(1 - r_w d_t^{mic}) \tag{4.19}$$

where the total damage d^{mic} is separated into two parts: compression d_c^{mic} and tension d_t^{mic} and the damage laws are calculated by:

$$d_t^{mic} = 1 - \exp\left(-\beta_t g_t^{mic}\right) \tag{4.20}$$

$$d_c^{mic} = 1 - \exp\left(-\beta_c g_c^{mic}\right) \tag{4.21}$$

where β_t and β_c = material constants, and the damage driving variable γ_t^{mic} and γ_c^{mic} is defined from equivalent strain by:

$$g_t^{mic} = \begin{cases} h_t^{mic} - g_{t0} & h_t^{mic} > g_{t0} \\ 0 & h_t^{mic} \le g_{t0} \end{cases} \tag{4.22}$$

$$g_c^{mic} = \begin{cases} h_c^{mic} - g_{c0} & h_c^{mic} > g_{c0} \\ 0 & h_c^{mic} \le g_{c0} \end{cases} \tag{4.23}$$

where γ_{t0} and γ_{c0} are the tension and compression damage thresholds, respectively.

The equivalent strain rate $\dot{h}_t^{mic}$ *and* $\dot{h}_c^{mic}$ is a function of the volumetric plastic strain rate as defined by:

$$\dot{h}_t^{mic} = \begin{cases} r_W \dot{e}_V^{pl} & \dot{e}_V^{pl} > 0 \\ 0 & \dot{e}_V^{pl} \le 0 \end{cases} \tag{4.24}$$

$$\dot{h}_c^{mic} = \begin{cases} (1 - r_W)\, \dot{e}_V^{pl} & \dot{e}_V^{pl} > 0 \\ 0 & \dot{e}_V^{pl} \le 0 \end{cases} \tag{4.25}$$

$$r_W = \frac{\sum_{I=1}^{3} \acute{a} e^I \tilde{n}}{\sum_{I=1}^{3} |e^I|} \tag{4.26}$$

where r_w = the split weight factor, ε^j = the principal strain values, and $\langle \varepsilon^j \rangle$ = the positive part of the strain tensor principal values.

The evolution of damage mentioned above is a condition to limit the accumulated damage in two cases. For the first $\dot{e}_V^{pl} > 0$ case, the concrete damage is controlled under high confining pressure for monitoring the hardening. For the second case, $\dot{e}_V^{pl} < 0$ happens when the stress state is within the compression cap subjected to plastic volumetric compaction. As seen in Figure 4.14, the equivalent strain is divided into compression and tension. The stiffness reduces during unloading and increases during applied compression.

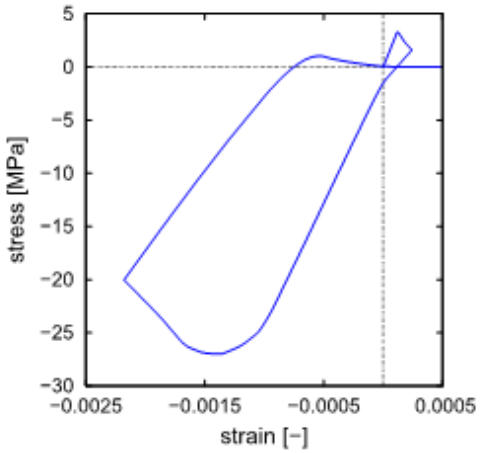

Figure 4.14 The effect of the damage split on the tension-compression cyclic loading response (Zreid and Kaliske 2018)

Concrete

The coupled pore-pressure-thermal mechanical solid element CPT215 (ANSYS, Inc. 2022) was used to simulate the concrete element of the electrified concrete pavement. As shown in Figure 4.15 (a), the CPT 215 has eight nodes with four (or five) degrees of freedom at each corner node: translations in x, y, and z direction at each node, one pore-pressure, and optional one temperature degree of freedom. Large deflection, large strain capacities, stress stiffening, and elasticity are included in the CPT215. The element CPT215 supports the couple damage-plasticity microplane model.

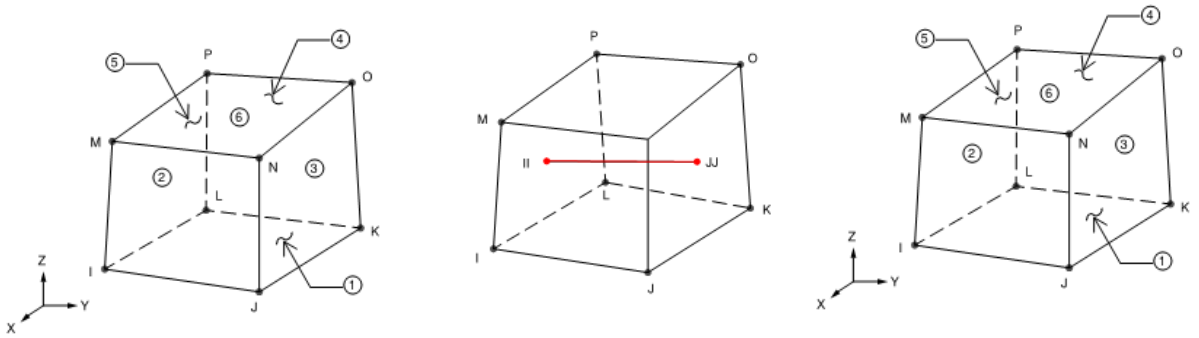

Figure 4.15 Element types: (a) CPT215 structural solid geometry, (b) 3-D 8 node solid or solid shell geometry, and (c) SOLID185 geometry

Table 4.7 Coupled damage-plasticity microplane model parameter for concrete material

Parameter Type	Parameter Subtype	Parameter	Value	Unit	Formula
Elasticity	--	Modulus of elasticity (E)	$3x10^6$	psi	Experimental
	--	Poisson's ratio (ν)	0.18	--	Experimental
Plasticity	Drucker-Prager yield function	Uniaxial compressive strength (f_{uc})	3,220	psi	Experimental
		Biaxial compressive strength (f_{bc})	3,703	psi	$=1.15\ f_{uc}$
		Uniaxial tensile strength (f_{ut})	370	psi	Experimental
	Compression cap	Intersection point abscissa between compression cap and Drucker-Prager yield function ($\sigma^C{}_V$)	-3,000	psi	$< -(2/3)\ f_{bc}$
		Ratio between the major and minor axes of the cap (R)	2	--	$X_0/f_1(\sigma^C{}_V)$
	Hardening	Hardening material constant (D)	$8.41x10^8$	psi^2	Experimental
		Tension cap hardening constant (R_T)	1	--	≈1
Damage	--	Tension and compression damage thresholds (γ_{t0}, γ_{c0})	0, $2x10^{-5}$	--	≥ 0, ≥0
	--	Tension and compression damage evolution constants (β_t,β_c)	3,000, 2,000	--	$\approx 1.5\beta_c$, ≥ 0
Nonlocal	--	Nonlocal interaction range parameter (c)	3	in^2	≥ 0
	--	Over-nonlocal averaging parameter (m)	2	--	≥ 1

Reinforcement

The steel rebar used the discrete reinforcing element REINF264, which includes large deflection, large strain capacities, stress stiffening, creep, and plasticity. The standard 3D link is used for the REINF264 depending on the base element of the concrete (CPT215). The REINF264 is modeled in reinforcing fibers oriented in spaces and has their intersection points of II and JJ with the CPT215, as shown in Figure 4.15 (b). The REINF264 and CPT215 are connected to the same nodes. Each fiber contains only uniaxial stiffness or conductivity. The plastic properties of the steel rebar were defined via bilinear isotropic hardening, which consisted of the yield strength and the tangent modulus, as presented in Table 4.8.

Table 4.8 Mechanical material properties

Material	Elasticity		Plasticity (Bilinear isotropic hardening)	
	Modulus of elasticity (E), psi	Poisson's ratio (ν)	Yield strength, psi	Tangent modulus, psi
Steel rebar	2.9×10^7	0.3	40,000	2.52×10^5
GFRP rebar	6.7×10^6	0.3	88,000	4.8×10^6
Ferrites	1.75×10^7	0.2	4,350	5×10^4
Litz wire	15,800	0.3	2,072	8512
Subbase	700	0.4	-	-

The GFRP rebar used the discrete reinforcing element REINF264 like the steel rebar, as illustrated in Figure 4.15 (b). The plastic properties of the GFRP rebar are determined by bilinear isotropic hardening, which consists of the yield strength and the tangent modulus, as seen in Table 4.8.

IPT System

The IPT system was created in double D topology consisting of ferrites and Litz wires. Mn-Zn ferrite bar was used for power supplies of this charging system. The discrete reinforcing element REINF264 was the elements of both ferrite and Litz wire, the same principle as the reinforcement. The material characteristics are shown in Table 4.8.

Subbase

Crushed gravel was used for the subbase. The SOLID185 element was used for this model and has eight nodes with three degrees of freedom: translations at each node in x, y, and z directions, as shown in Figure 4.15 (c). This element contains plasticity, hyper elasticity, stress stiffening, creep, large deflection, and large strain capabilities. The material properties are presented in Table 4.8.

Geometry

The full-size EPCPs dimensions were 96 in. x 48 in. x 12 in. Due to the symmetry of the beams, half of the full Panel 1 was used for modeling. This approach reduced computational time and computer disk space requirements in solving for high-cycle fatigue. Half of the entire model is shown in Figure 4.16. The full model of the EPCPs for Panel 2 was used for short-term analysis because the structure was expected to fail at the low number of cycles, as illustrated in Figure 4.17.

4.3.2 Connections and Contacts

The type of contact between a concrete body and a subbase body was "frictional" with a friction coefficient of 0.1. ANSYS mechanical had specific functions for modeling the reinforcement into a structure in the static structural analysis by selecting the model type property as "reinforcement." The reinforcement was modeled as line bodies with assigned #4 rebar cross section via the discrete reinforcing element REINF264, as mentioned above.

4.3.3 Mesh and Element Size

The element order of the mesh was defined as linear to make the solid elements (concrete and subbase) become eight-node elements (hexahedral solid element) as the CPT 215 and the SOLID185, respectively. The reinforcement meshed to a two-node beam element. The average element size of 1.5 in. for all materials was used based on the mesh sensitivity check that was mentioned earlier.

4.3.4 Boundary Condition and Loading

The 3D FEA model was expected to determine the desired crack pattern. Thus, the boundary condition was defined to allow for rotations and translations similar to cyclic load testing at the SMASH lab. For the two panels, the fix support (constrained all translation and rotation in the x, y, and z directions) was applied at the bottom of the 4-in. thick subbase (Figure 4.18 and Figure 4.19). This boundary condition simulated the subbase sitting on the floor as the experimental test in the SMASH lab.

Because using ideal boundary conditions did not fully reflect reality, downward displacement was applied to the model. Thus, the boundary condition, the displacement of the function -0.15–0.05 x sin (720 x [time–0.6]) in inches, was added to simulate the imperfection in the contact between the concrete slab and subbase, as presented in Figure 4.20 and Figure 4.21. In the experiment, the panel obviously bent during the cyclic load test, which may have been by the geometric imperfection of the concrete at the side facing the subbase. The displacement applied at the two edges of the slab varied between 0.1 in. and 0.2 ft in a downward direction (-z global direction).

For fatigue loading, the sinusoidal load was applied on the top of the concrete at the 12 in. x 12 in. pressure area. The cyclic load was simulated from the HS20 traffic vehicle, which had a 32,000-lb axle (two 16,000-lb wheel groups) with 6-ft axle spacing (center to center) from AASHTO Standard Specification for Highway Bridges. The cyclic load was applied by using the sinusoidal function of -18,000–14,000 x sin (720 x [time-0.6]) in lbs. with a 2 Hz loading rate similar to the cyclic load testing in the experiment for Panel 2 and -18000–14000 x sin (720 x [time-0.6])/2 in lbs., 2 Hz, which was a half fatigue force rate for Panel 1 due to a half panel model (Figure 4.22 and Figure 4.23). The cyclic load varied between 7,000 lbs. and 32,000 lbs. in the model.

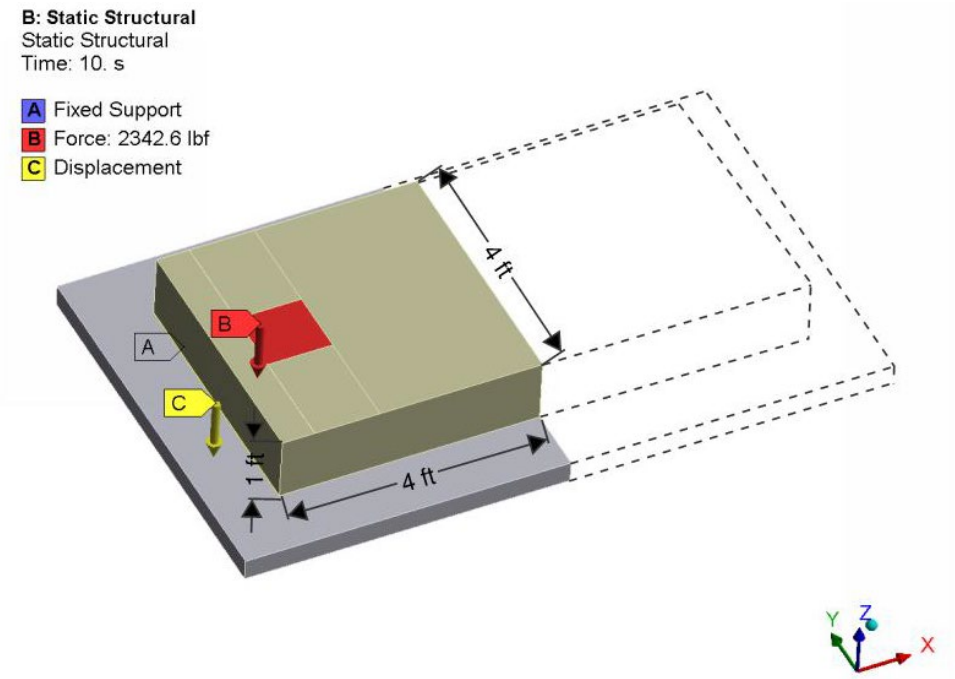

Figure 4.16 Geometry of a half panel model for Panel 1

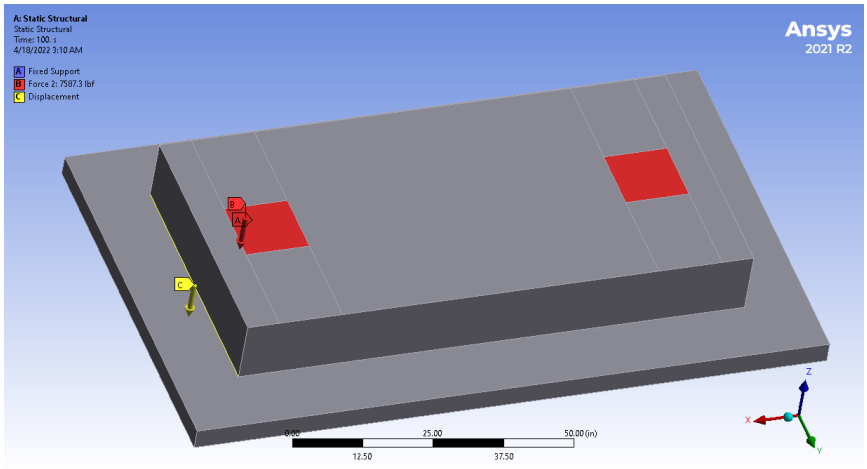

Figure 4.17 Geometry of a full panel model for Panel 2

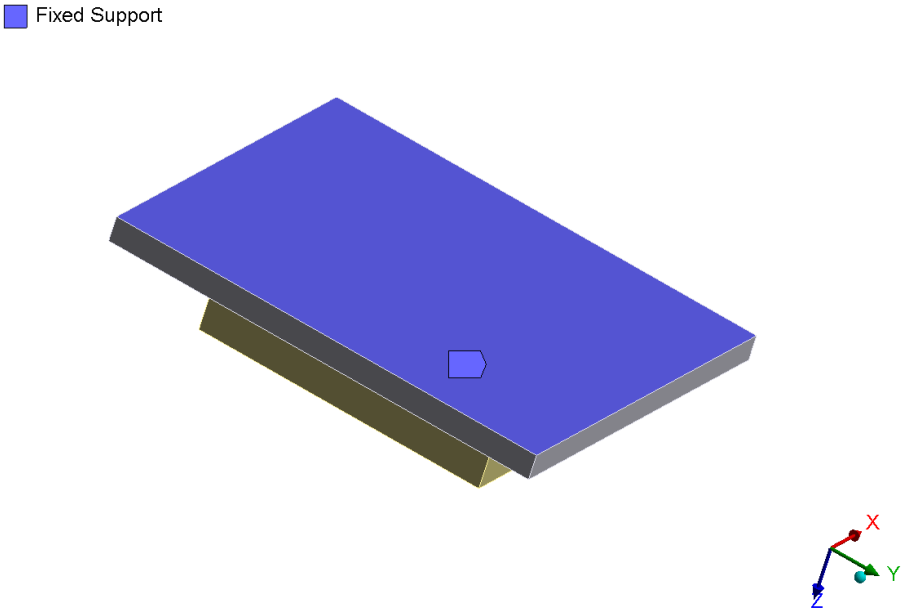

Figure 4.18 Boundary condition – fixed support for Panel 1

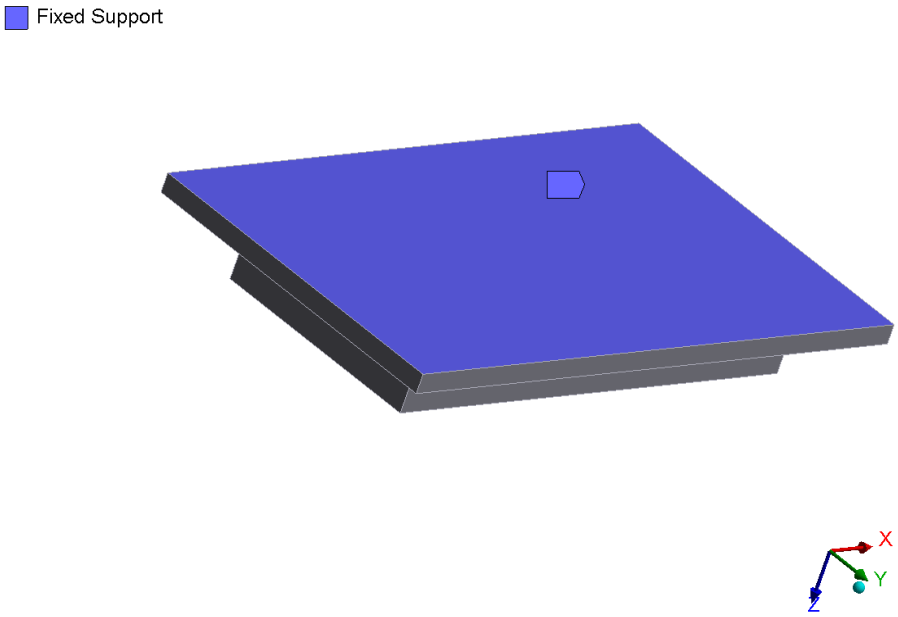

Figure 4.19 Boundary condition – fixed support for Panel 2

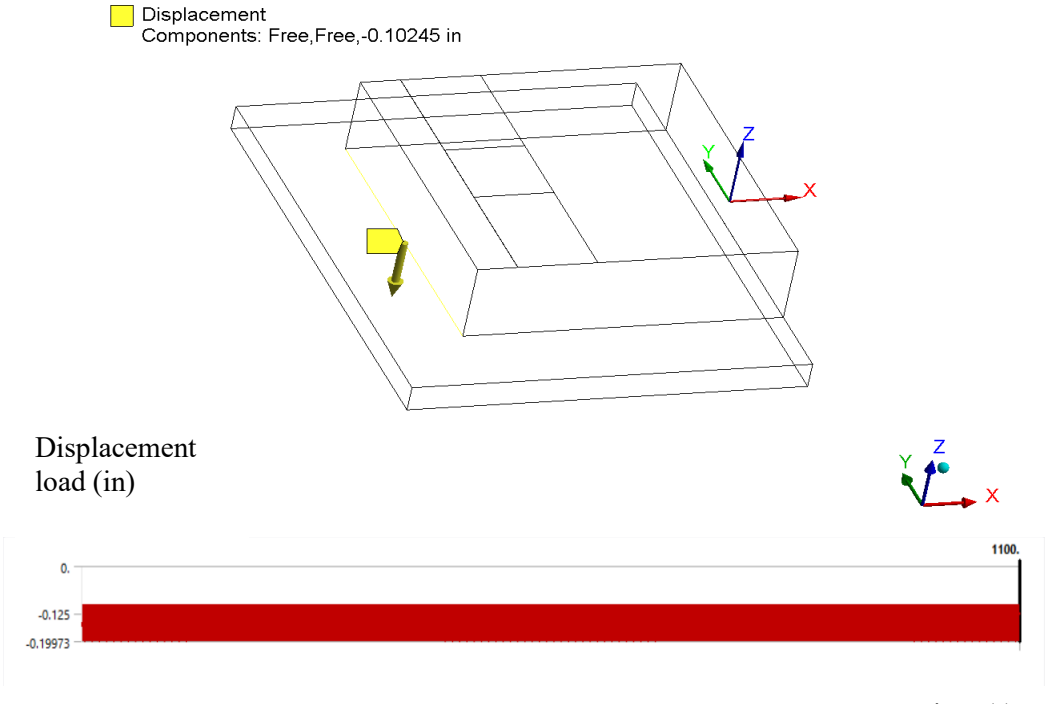

Figure 4.20 Boundary condition – displacement sinusoidal load for Panel 1

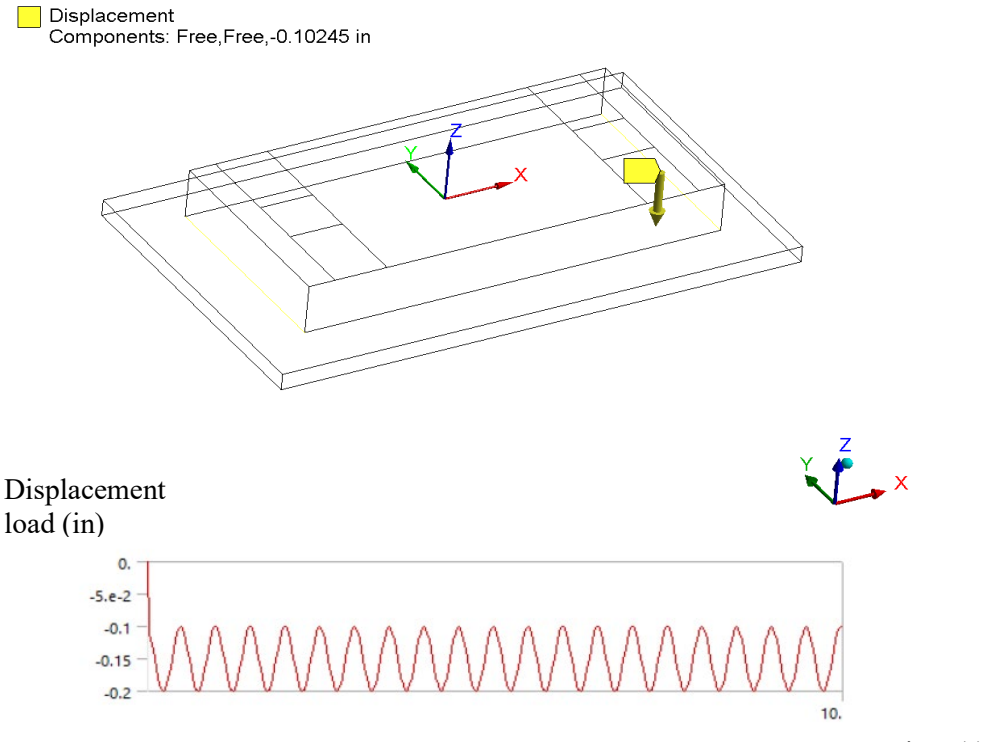

Figure 4.21 Boundary condition – displacement sinusoidal load for Panel 2

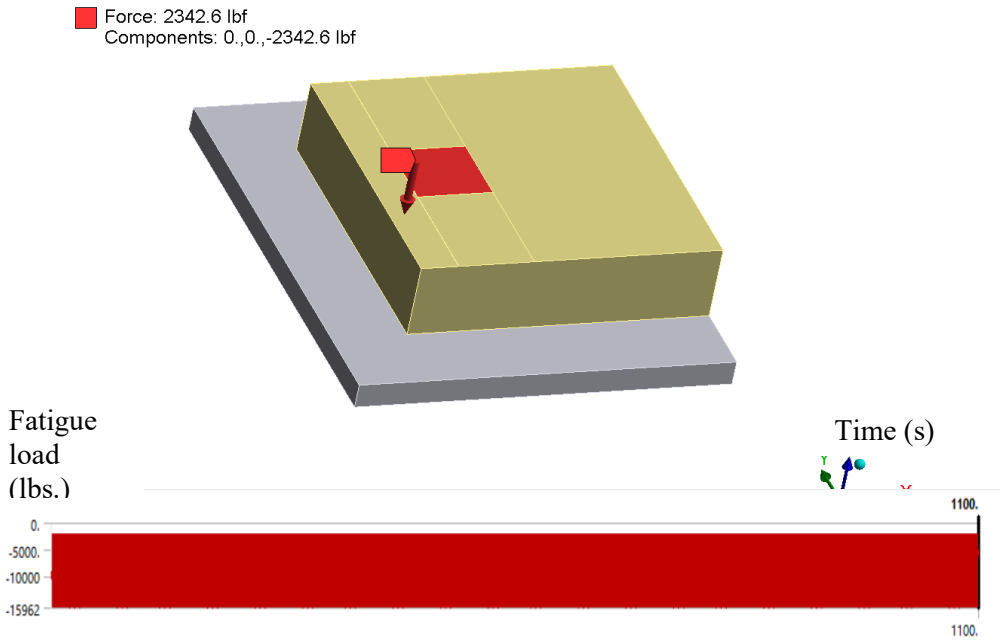

Figure 4.22 Applied load – sinusoidal loading for fatigue for Panel 1

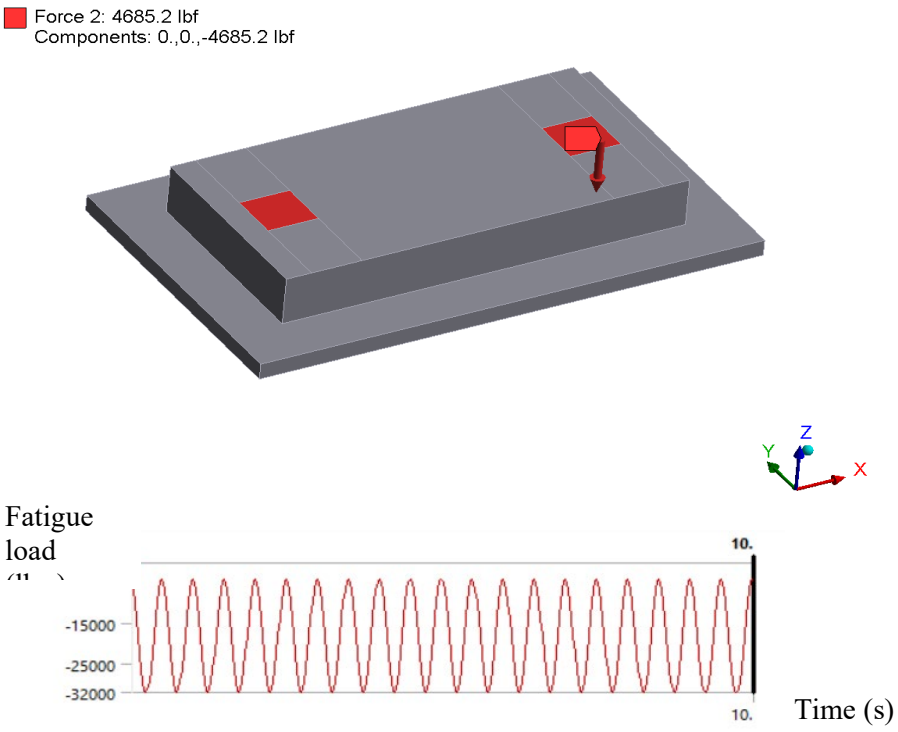

Figure 4.23 Applied load – sinusoidal loading for fatigue for Panel 2

4.4 Ultimate Failure Load Finite Element Analysis

Reinforced concrete was a composite material consisting of the base matrix material (concrete) and reinforcement (GFRP and steel). The concrete material was strong in compression but weak in tension. However, the reinforcing material was used to support tensile stresses in the composite material. In structural design, ultimate load was determined to indicate the maximum load the structure could resist before failure occurred. This research presented the load limit analysis for the electrified concrete panels based on a flexural loading test.

4.4.1 Problem Description and Geometry

The models were created in the full size of the concrete panels with 8 ft x 4 ft x 1 ft dimensions. The panels were tested upside down. To study the concrete behavior with the embedded coil, this setup allowed the top face, where the IPT system was located, to suffer tensile damage. The modeling geometry and loading were the same as the EPCPs in the experiment. The dead load of the panels and the surface-pressure load representing the center point load were applied to the FEA models. The models constrained in the vertical z direction as a simple support, as seen in Figure 4.24. The panels consisted of the IPT system and reinforcement embedded into the concrete structure. The panels absorbed compressive and tensile stresses under the center point loading test analysis.

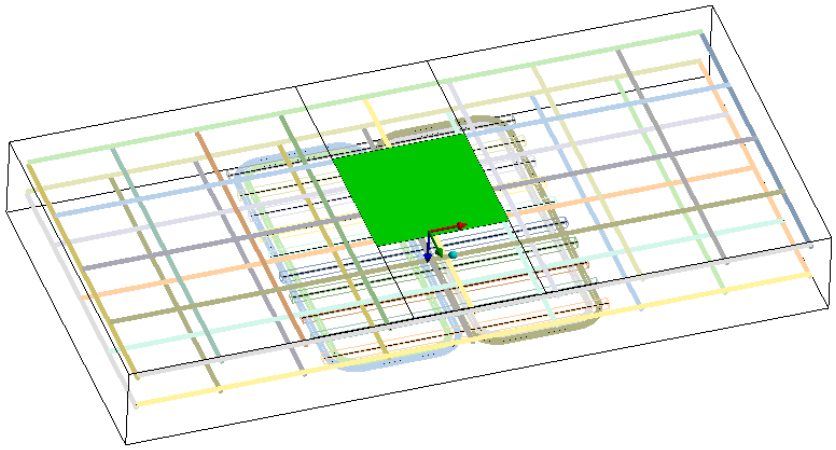

Figure 4.24 FEA model geometry

4.4.2 Modeling and Meshing

The 3D model consisted of concrete, reinforcing, and IPT system element types. The couple-pressure-thermal mechanical CPT 215 element was used for the concrete. The reinforcement and IPT system were created via the discrete reinforced element REINF264 by selecting the reinforcement option in the model type. The CPT 215 and REINF264 elements are connected at the nodes. The mesh size was 1.5 in. for all elements in the models.

4.4.3 Boundary Conditions and Loading

The boundary condition was defined as a simple support for one span as shown in Figure 4.25. The displacement condition was used as a pin support, which constrained the displacement at vertical z and horizontal y directions but allowed any rotations in all directions. The fixed support was applied on another side of the panel to constrain any displacement in all directions but rotate freely. Thus, these supports did not bear any reaction on the panel in the horizontal direction. This boundary condition was applied to nodes that were 6 inches away from the edge for both sides.

The load limit analysis was divided into two steps for the loading (Figure 4.26). For the first step, the model was subjected to only the dead load of the panel self-weight by applying a gravitational acceleration of 386.1 in/s^2 in the z direction. For the second step, 320 psi of the surface-pressure load (18 in. x 18 in. pressure area) was applied on the bottom surface of Panel 1 and then linearly increased until the structure failed. Panel 2 was applied by the pressure load of 160 psi. The load limit, or ultimate load, was determined from the last load step that caused the solution divergence. The load/displacement curve explains the concrete structure failure.

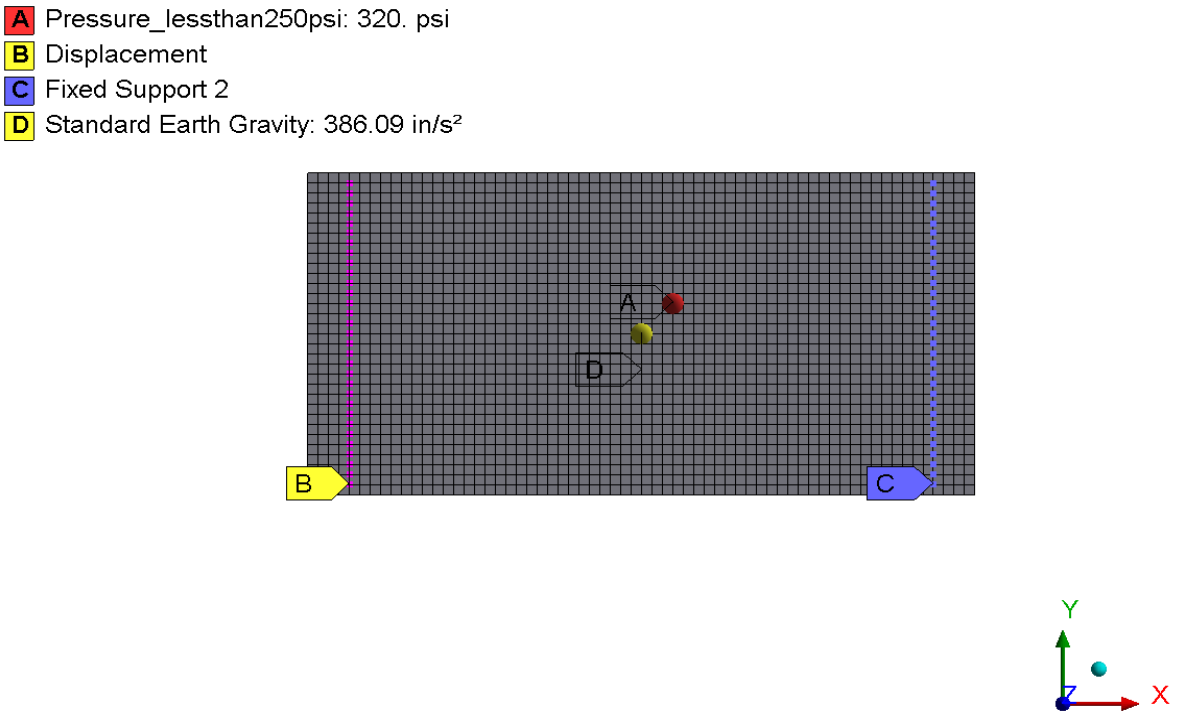

Figure 4.25 Boundary conditions at the top face of the panel

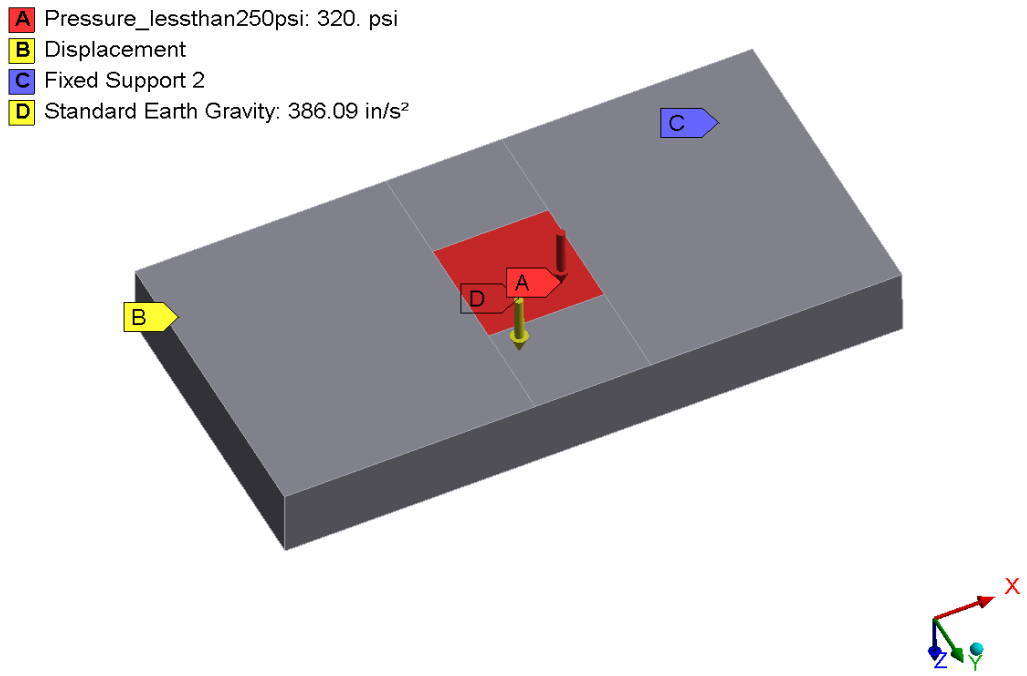

Figure 4.26 Applied loads on the bottom face of the panel

4.4.4 Material Properties

The Drucker-Prager concrete material model (CPT215) was considered in the load limit analysis of the concrete, as presented in Table 4.7, which was suitable for aggregate material like concrete to perform plasticity and softening behavior. The reinforcement and the IPT system material properties used a bilinear kinematic hardening model, as presented in Table 4.8.

4.4.5 Analysis and Solution Control

In ANSYS program, the initial Newton-Raphson method was used in a nonlinear static structural analysis to allow the structure to carry the maximum load until failure occurred. The load limit was determined from non-convergence of the global Newton-Raphson solution. In the load limit analysis of Panel 1, the auto time stepping was defined by sub step: 50 initial sub steps and 1,000 maximum sub steps to capture the failure point of the panel. For Panel 2, the initial time-step size of 0.05 seconds was defined for structural failure with 50 equilibrium iterations. The minimum time step was 0.001 seconds with 50 iterations.

4.5 Summary

This chapter demonstrates the modeling of full-size EPCPs in ANSYS through material properties, element types, boundary conditions, and applied loads. In thermal analysis, the concrete used a default element of solid 278. This element had plasticity, large deflection, and large strain capabilities with eight nodes and three degrees of freedom. In cyclic loading and ultimate strength analysis, the CPT 215 element was used for concrete to support the nonlinear solution for damage and failure load results. The CPT 215 was assigned to the plasticity-damage microplane model, and it contained the same capabilities as the solid 278. A mesh size of 1.5 in. for all material was used by considering mesh sensitivity checking.

5. MODEL VALIDATION

The results of the experiment explain the physical phenomenon of electrified concrete pavements. The thermal-structural numerical models were calibrated to realistically render the models. In thermal analysis, some unknown parameters of the IPT, such as the internal heat, were estimated based on the test results. Ultimate failure load was analyzed for structural design safety. ANSYS finite element software was used to investigate the mechanical behavior and damage for all the EPCPs. The comparison between the experimental and simulation results is presented in this chapter.

5.1 Validation of Heat Transfer Analysis

The panels were subjected to transient thermal analysis using ANSYS. During the transient heat transfer, the temperature of the EPCPs fluctuated because the coil was powered for one hour and then turned off for one hour. Only the internal heat loads of the IPT were applied to the structure. The temperature load of the entire structure was then imported into the structural analysis. In the experiment, the embedded IPT coils of the two panels were heated to observe thermal load in the EPCPs. The internal heat load of the IPT system was determined from the FEA modeling based on the experimental results. The validated model was considered for parametric investigation of the entire EPCP structure.

5.1.1 Thermal Analysis

The temperature data from the experiment were obtained from Barnes (2020). As illustrated in Figure 5.1 (a) – (b) and Figure 5.3 (a) – (b), the most critical temperatures were from T2, T1, and T3 because they were located at the center of the IPT coil (the centerline area of two D-shaped windings aligned back to back), which generated the highest heat. For Panel 1, when the coil stopped heating after 68 minutes, the temperature of T2, T1, and T3 increased to 20°C – 23°C in the model, but the heat in the experiment increased to 20°C – 26°C.

For Panel 3, in both the model and the experiment, T2, T1, and T3 reached the same range of 30°C – 38°C after the coil heated for 120 minutes. Thus, the experiment and simulation coincided for Panels 1 and 3. In Panels 1 and 3, temperatures from T6, T4, and T5 were lower because those points were located farther from the center of the IPT coil.

For Panel 2 (Figure 5.2), the coil ran for approximately 37 minutes, but the power stopped due to the steel reinforcement. This issue was identified when the power supply used a current of 6 amperes. The 6 amperes were 40% higher than the expected currents of 3.6 – 3.7 amperes for running Panels 1 and 3. All three panels used 600 volts to run the power in the coils. The heat generated by the Litz wire in the FEA model was increased by 40% to align the model with the experimental data. Even though the coil was powered for 37 minutes, the temperature in the center of the coil [Figure 5.2 (a)] increased to approximately 30°C, which was higher than Panel 1 after powering for one hour.

Some temperature data in the experiment did not correspond with the model. This discrepancy occurred because the temperature sensors were stuck into the holes on the concrete top face and did not reach the desired spots of the IPT coil.

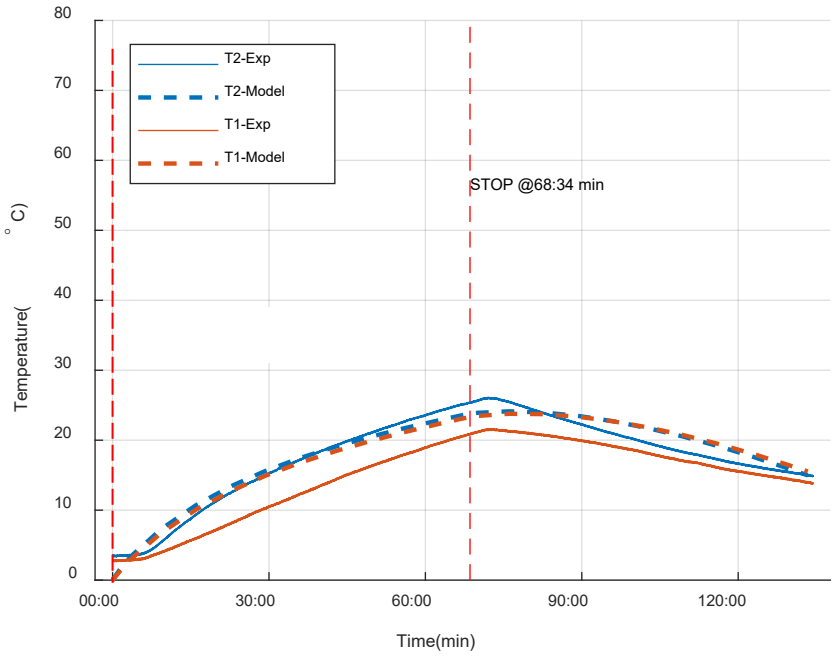
T2-Exp
T2-Model
T1-Exp
T1-Model
STOP @68:34 min
Temperature(° C)
Time(min)
00:00
30:00
60:00
90:00
120:00
0
10
20
30
40
50
60
70
80

(a)

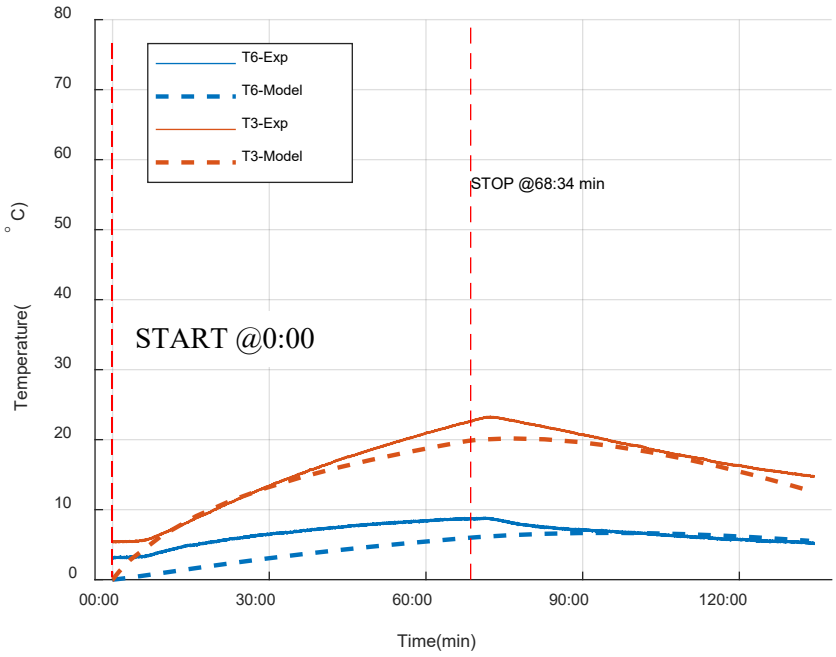
T6-Exp
T6-Model
T3-Exp
T3-Model
STOP @68:34 min
START @0:00
Temperature(° C)
Time(min)
00:00
30:00
60:00
90:00
120:00
0
10
20
30
40
50
60
70
80

(b)

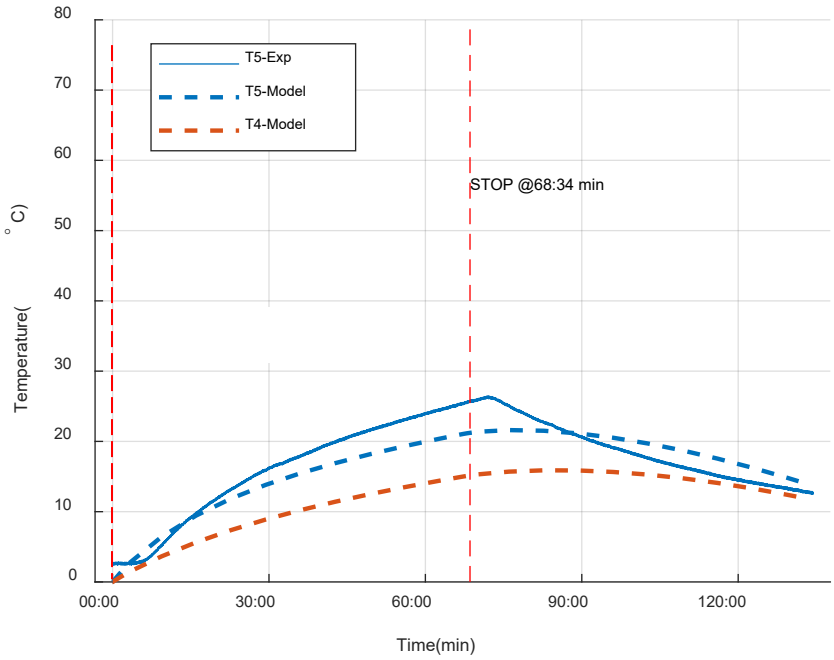

(c)

Figure 5.1 Comparison of experimental and modeling temperature Panel 1: (a) T1 and T2 temperature, (b) T3 and T6 temperature, and (c) T4 and T5 temperature

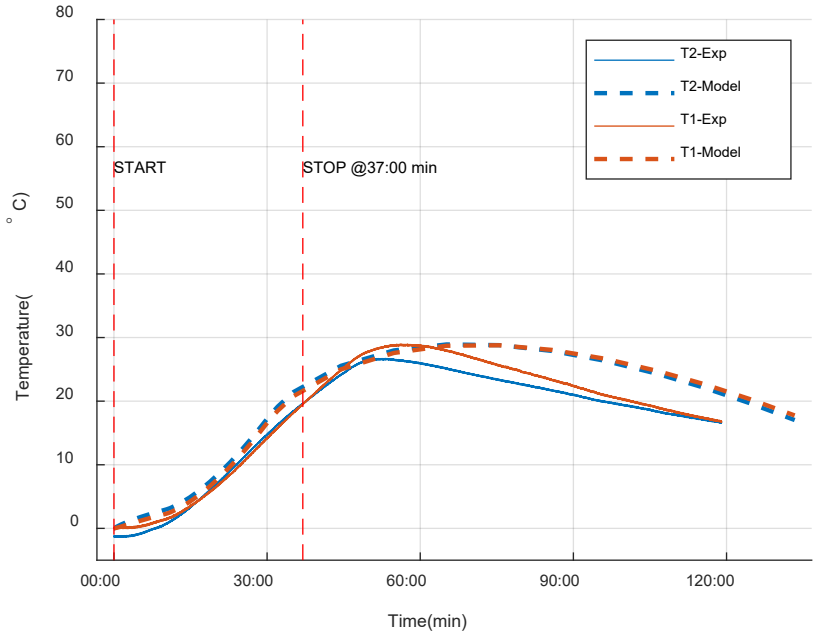
T2-Exp
T2-Model
T1-Exp
T1-Model
START
STOP @37:00 min
Temperature(° C)
Time(min)
00:00
30:00
60:00
90:00
120:00
0
10
20
30
40
50
60
70
80

(a)

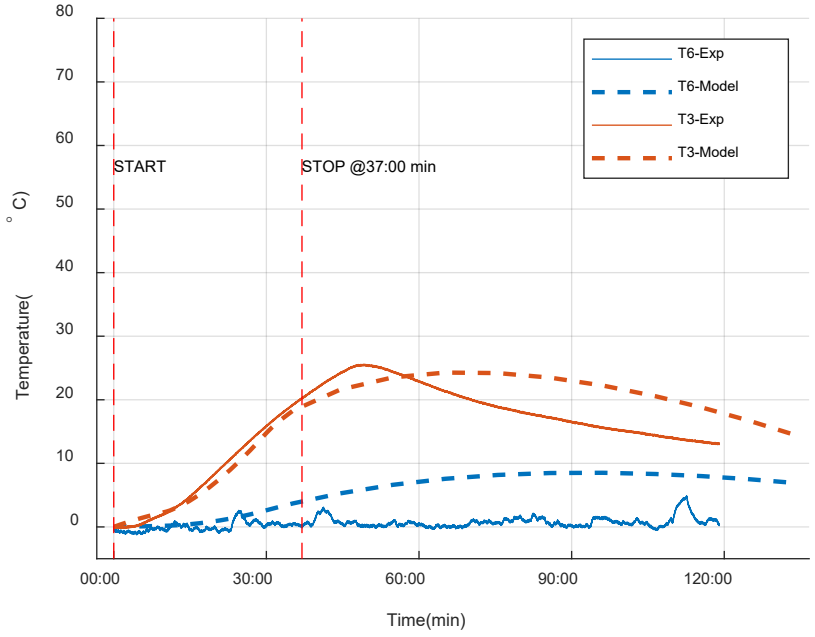
T6-Exp
T6-Model
T3-Exp
T3-Model
START
STOP @37:00 min
Temperature(° C)
Time(min)
00:00
30:00
60:00
90:00
120:00
0
10
20
30
40
50
60
70
80

(b)

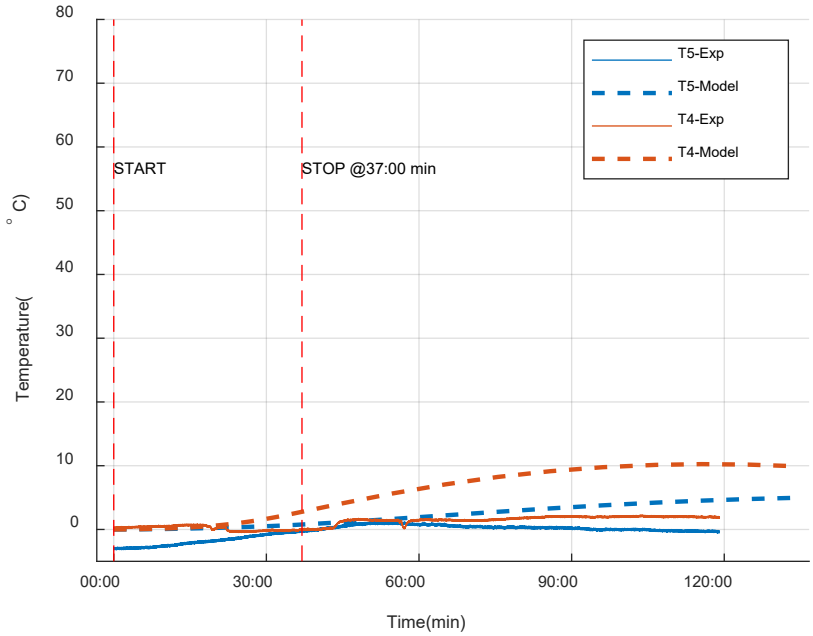

(c)

Figure 5.2 Comparison of experimental and modeling temperature Panel 2: (a) T1 and T2 temperature, (b) T3 and T6 temperature, and (c) T4 and T5 temperature

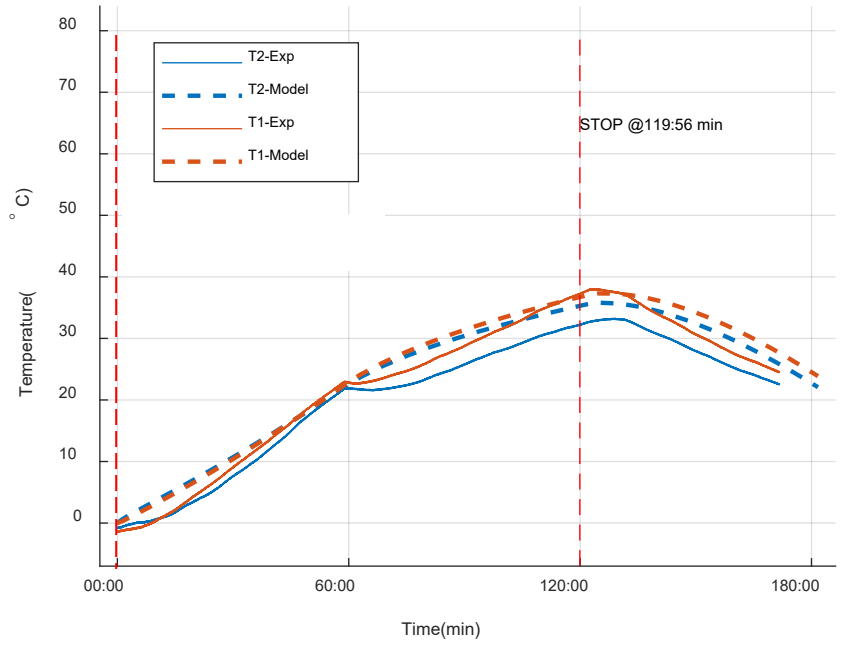
T2-Exp
T2-Model
T1-Exp
T1-Model
STOP @119:56 min
Temperature(° C)
Time(min)
00:00
60:00
120:00
180:00
0
10
20
30
40
50
60
70
80

(a)

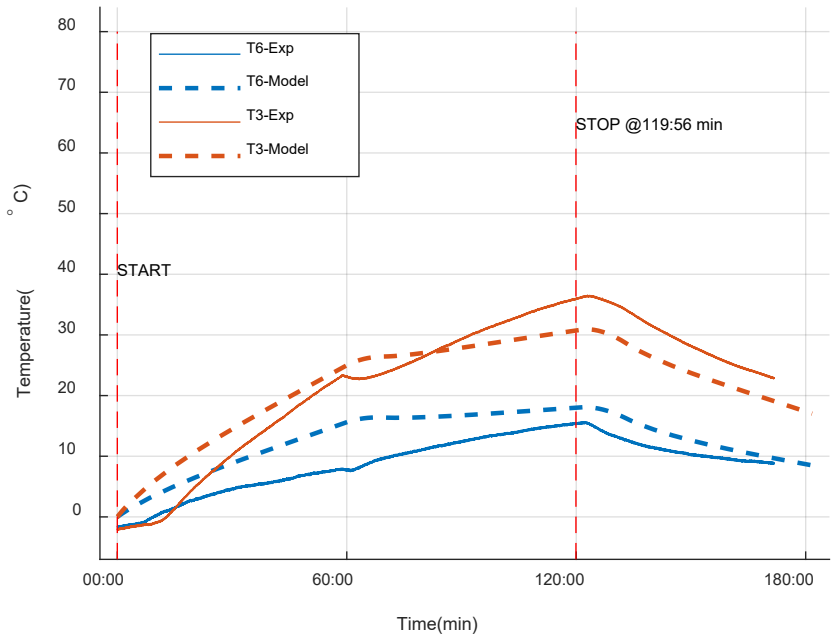
T6-Exp
T6-Model
T3-Exp
T3-Model
STOP @119:56 min
START
Temperature(° C)
Time(min)
00:00
60:00
120:00
180:00
0
10
20
30
40
50
60
70
80

(b)

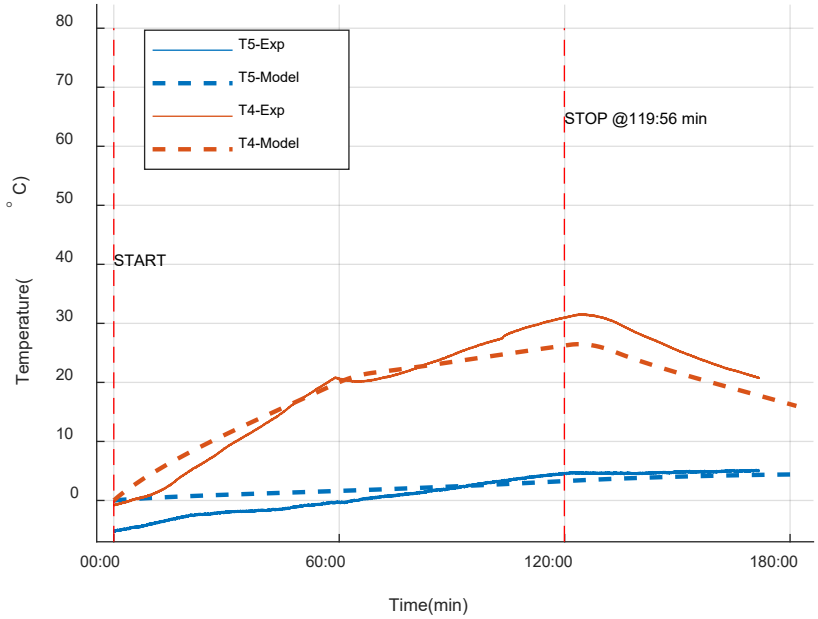

(c)

Figure 5.3 Comparison of experimental and modeling temperature Panel 3: (a) T1 and T2 temperature, (b) T3 and T6 temperature, and (c) T4 and T5 temperature

5.1.2 Structural Analysis

As shown in Figure 5.4 to Figure 5.6, the FEA model is measured in microstrains because the temperature load from the IPT, which was applied to the EPCP model, involved the coefficient of thermal expansion (CTE) of the concrete. In the concrete, the thermally induced extension strains were equal in all directions, so the thermal strain was equal in both x and y directions. The strain data captured by the model corresponded with the strain sensor during the experiment.

Panel 1

As shown in Figure 5.4 (a), the strain sensor (SI2) captured the most critical thermal strain (300 με) at the midspan of the panel, which was 4.5 inches below the top surface and under the center of the IPT coil. SI1 achieved an experimental strain of approximately 180 με and remained slightly off the center coil turns (4.5 inches below the top surface). Figure 5.4 (b) demonstrates that SI5 and SI6 had insignificant strains located 13 inches farther away from the coil on the x direction (4.5 inches below the top surface).

The small strain data of SI7 indicated that the IPT coil heat did not pass through the bottom mat of the reinforcement at the center of the panel [Figure 5.4 (c)]. The FEA results coincided with the test result. However, the numerical results differed from the experiment in the 10% – 67% error range during the one-hour cooling period (68 to 130 minutes). The lowest percentage error of 10% was from the S9 sensor, and the highest percentage was 67% error of S5. After stopping the system for 68 minutes, the measured strain continued to increase, but the model strain suddenly decreased.

Panel 2

As mentioned in the thermal analysis section, the test ran for only 37 minutes because of the power loss from the steel rebar. The strain measurement experienced uncertainty, as presented in Figure 5.5. The steel rebar, where strain sensors were attached, disrupted the heat generated by the coil as seen in the SI1 and SI2 signals. This disruption caused unstable measurements at SI1 and SI2 created from the heat load in the experiment. The SI2 signal fluctuated the most because it was located directly under the coil center area.

Panel 3

The IPT coil was placed a few inches off the centerline of Panel 3 during construction. As a result, strain gauge locations (SI3 and SI4) did not correspond with strain (SI1 and SI2) in Panel 1, as seen in Figure 3.17. However, the thermal strain was equal in horizontal x and y directions. Consequently, SI3 (Panel 3) provided strain data similar to SI2 (Panel 1) because they were located under the coil's center (4.5 inches below the top surface). Figure 5.6 (a) shows that SI3 exhibited the most critical strain, 305 με, in the test.

SI4 was near the edge of the coil's center corresponding to SI1 from Panel 1 (4.5 inches below the top surface). SI4 had a measured strain of 190 με. SI5 and SI6 stayed off from the IPT coil (4.5 inches below the top surface), having the measured strain of 190 με and 135 με, respectively [Figure 5.6 (b)]. However, SI5 and SI6 from Panel 3 did not agree with Panel 1 despite their similar locations. Model results had a percentage error in the 11% – 75% range compared with the test because SI8 was broken in the experiment, but SI8 was simulated in the model, as seen in Figure 5.6 (c). A significant percentage of the errors occurred at SI5 and SI6. SI3 and SI4 in the FEA model corresponded with the experiment.

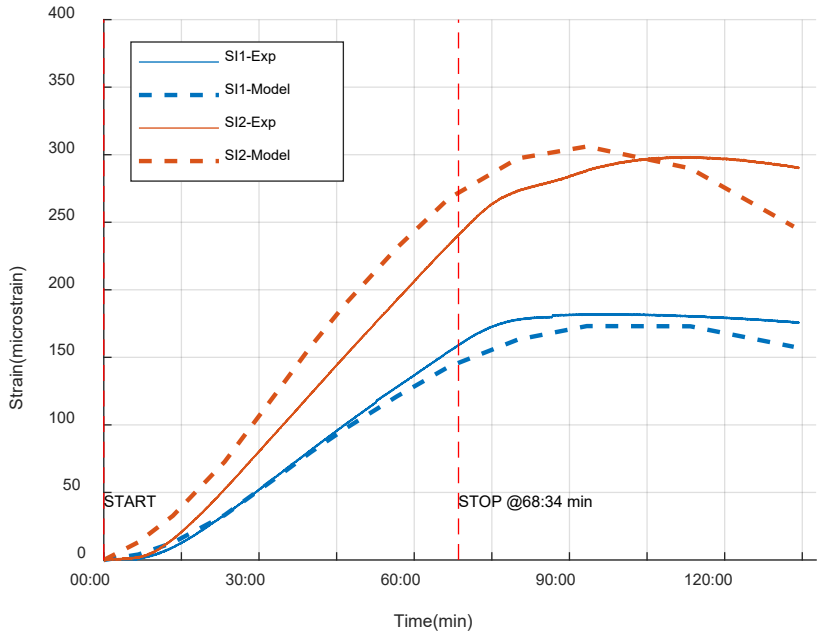
SI1-Exp
SI1-Model
SI2-Exp
SI2-Model
START
STOP @68:34 min
Strain(microstrain)
Time(min)
400
350
300
250
200
150
100
50
0
00:00
30:00
60:00
90:00
120:00

(a)

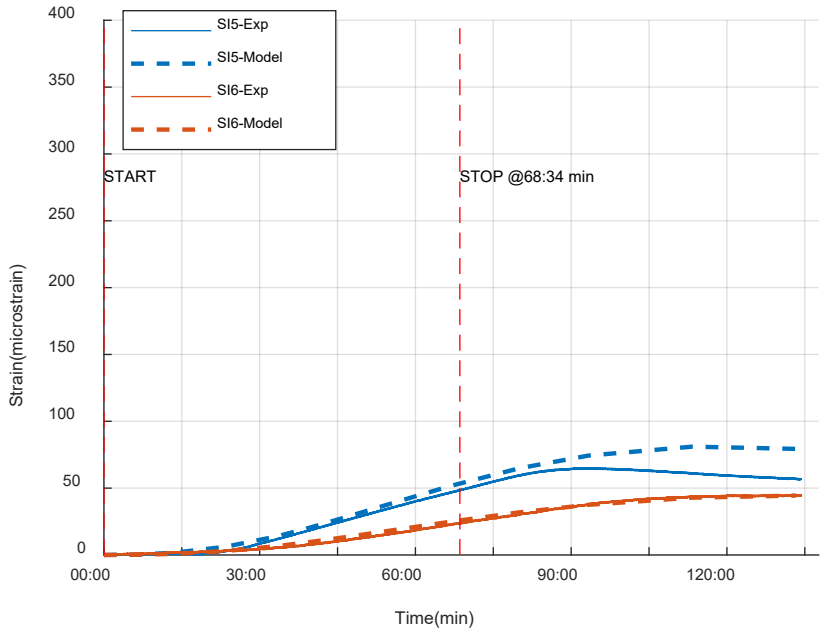
SI5-Exp
SI5-Model
SI6-Exp
SI6-Model
START
STOP @68:34 min
Strain(microstrain)
Time(min)
400
350
300
250
200
150
100
50
0
00:00
30:00
60:00
90:00
120:00

(b)

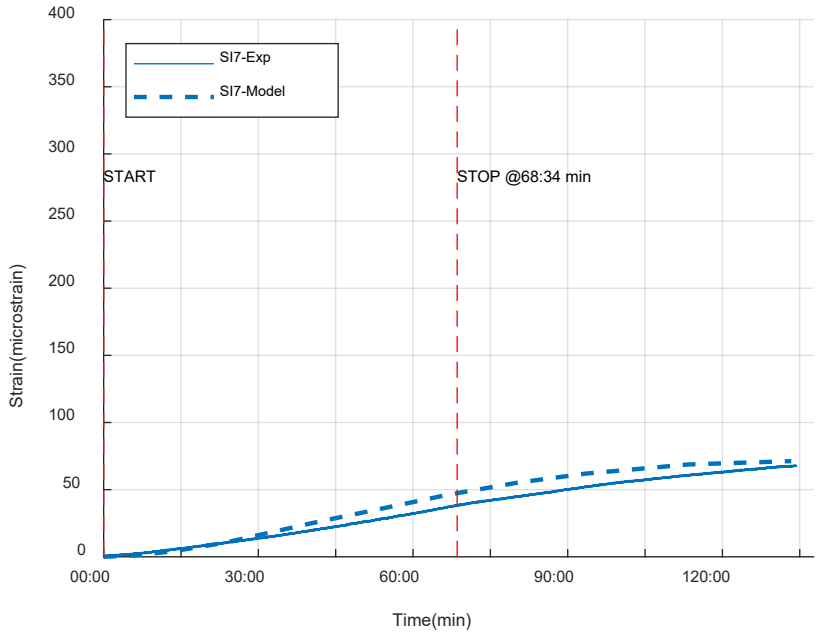

(c)

Figure 5.4 Comparison of experimental and modeling strain Panel 1: (a) SI1 and SI2 strain, (b) SI5 and SI6 strain, and (c) SI7 strain

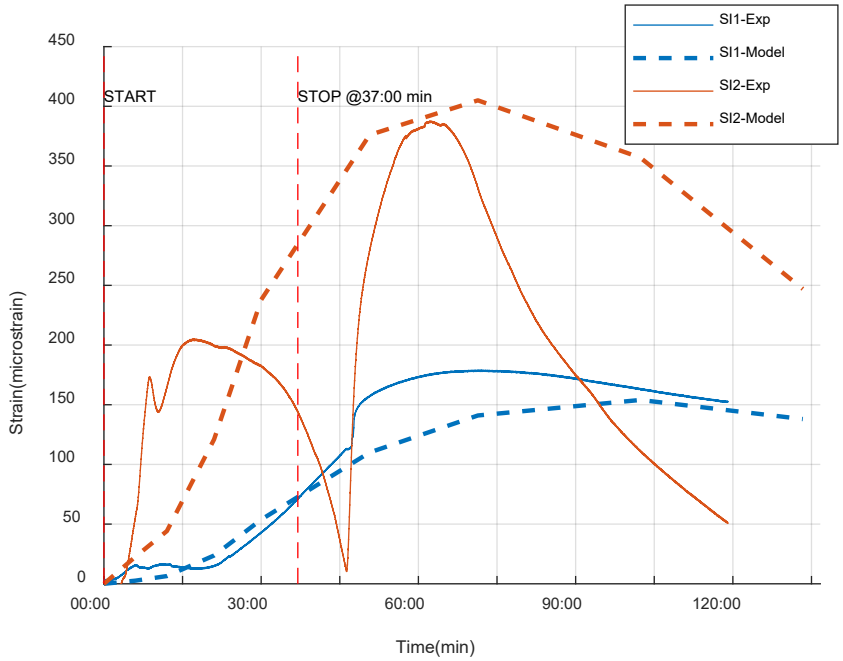

(a)

Figure 5.5 Comparison of experimental and modeling strain Panel 2: (a) SI1 and SI2 strain

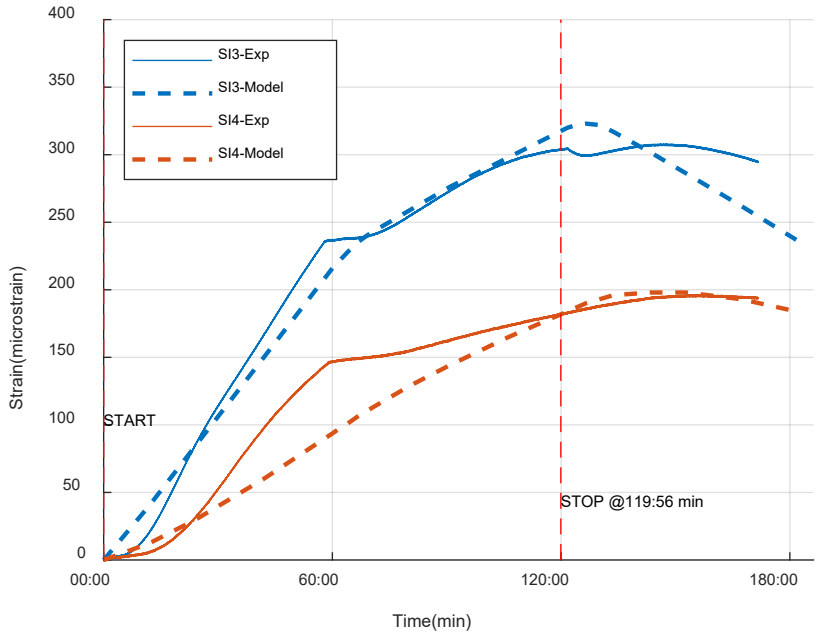
SI3-Exp
SI3-Model
SI4-Exp
SI4-Model
START
STOP @119:56 min
Strain(microstrain)
Time(min)
0
50
100
150
200
250
300
350
400
00:00
60:00
120:00
180:00

(a)

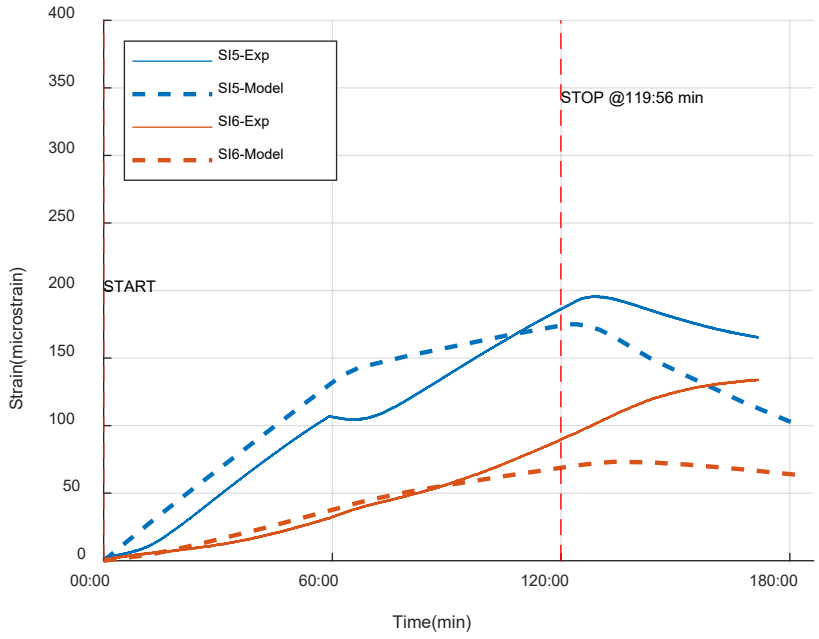
SI5-Exp
SI5-Model
SI6-Exp
SI6-Model
START
STOP @119:56 min
Strain(microstrain)
Time(min)
0
50
100
150
200
250
300
350
400
00:00
60:00
120:00
180:00

(b)

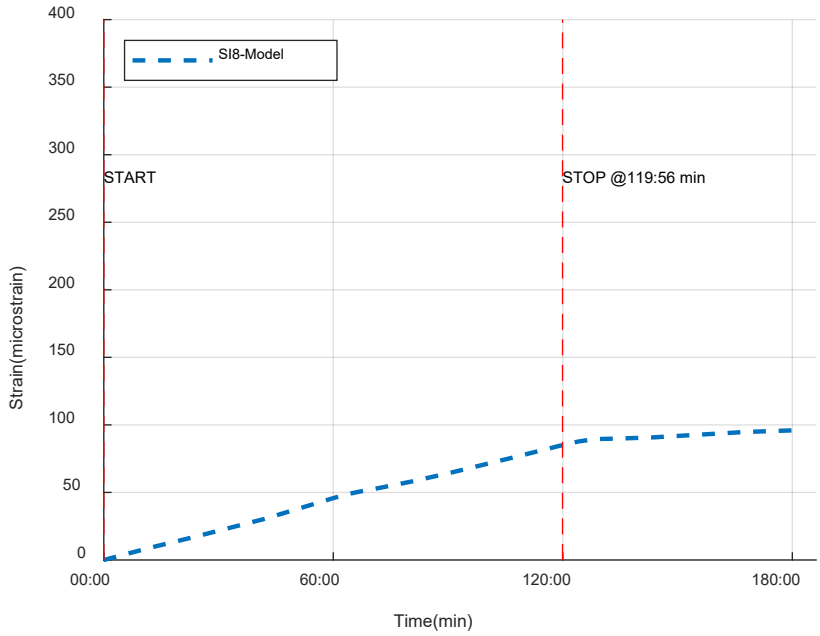

(c)

Figure 5.6 Comparison of experimental and modeling strain Panel 3: (a) SI3 and SI4 strain, (b) SI5 and SI6 strain, and (c) SI8 strain.

5.1.3 Parametric Studies of Electrified Concrete Pavement Panel

After the FEA models were validated and calibrated by the physical experiment, the mechanical behavior of the entire EPCP structure was investigated. Panel 1 was powered for about one hour, and Panel 3 was powered for two hours. Therefore, the parametric studies that affected the mechanical behavior of the concrete were based on different powering times of one hour and two hours.

Effect of Running IPT at Different Times

To investigate the effects of running the IPT for different amounts of time, the time-dependent, transient-thermal analysis was used in the FEA models. Thermal strain and normal stress in x and y directions were the mechanical behaviors to consider.

Thermal Strain

Because the embedded IPT coil generates the internal thermal load, the thermal strain is induced in the concrete structure."As shown in Figure 5.7 to Figure 5.9, the IPT coils in Panels 1, 2, and 3 were heated for one hour, half an hour, and two hours, respectively, then the system was turned off for an hour. Figure 5.7 (a) to Figure 5.9 (a) show the thermal strain gradient at the top face of the EPCP. The high thermal strain of 140 με (Panel 1), 80 με (Panel 2), and 225 με (Panel 3) occurred around the midspan in a y direction (traffic travel direction), which came from the heat at the center area of the IPT coil.

Therefore, for the thermal strain on the top face, the percent difference between Panels 1 and 3 was 46.6%. Figure 5.7 (b) to Figure 5.9 (b) show the maximum thermal strain (250 με, 403 με, and 317 με, respectively) occurred 3 inches away from the top surface of the concrete where the center area of the coil was located. There was a 23.6% difference. Figure 5.7 (c) to Figure 5.9 (c) indicate the difference in concrete thermal strain between two areas of the IPT coil. Figure 5.7 (c) shows that the area of the coil at the side created a concrete thermal strain of 160 με while the strain of 250 με was from the area around the center area of the coil. As demonstrated in Figure 5.9 (c), the strain of the concrete at the coil at the side was 205 με, and it was 317 με for the area around the center area of the coil.

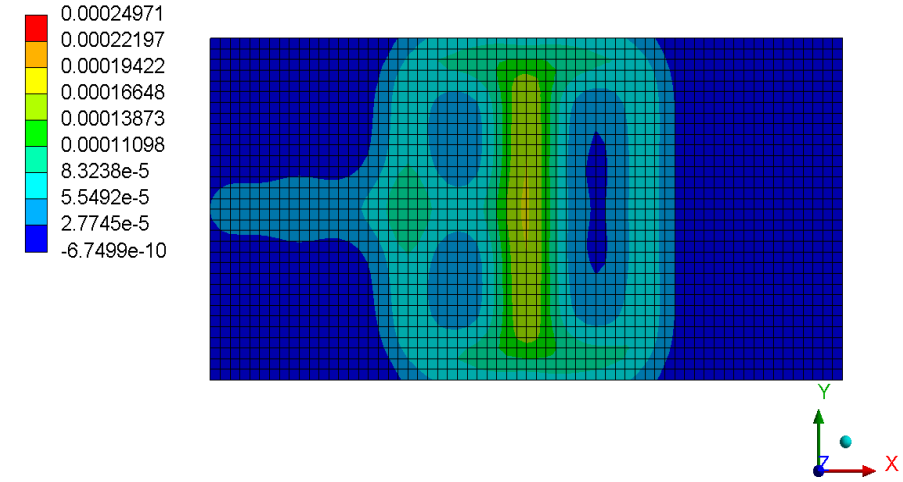

(a)

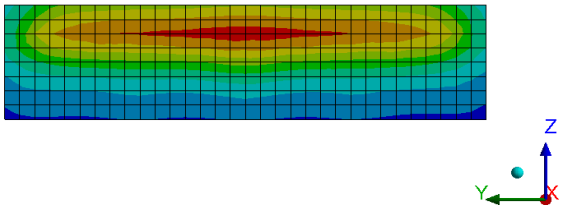

(b)

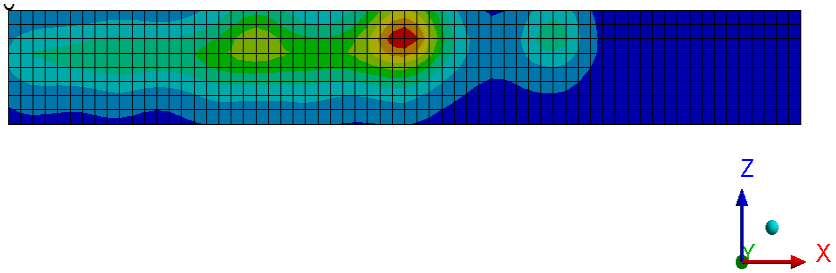

(c)

Figure 5.7 Thermal strain (in ε unit) in concrete of Panel 1: (a) top face, (b) cross-section at mid-span in horizontal y direction, and (c) cross-section at mid-span in horizontal x direction

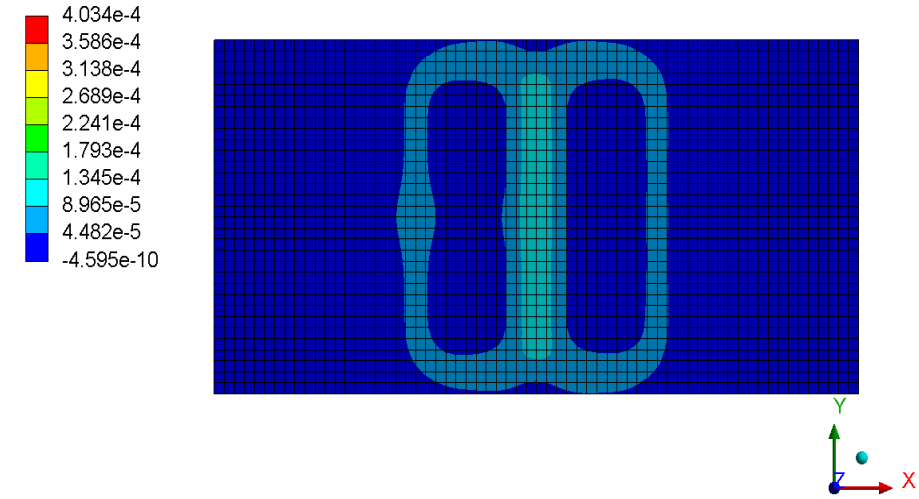

(a)

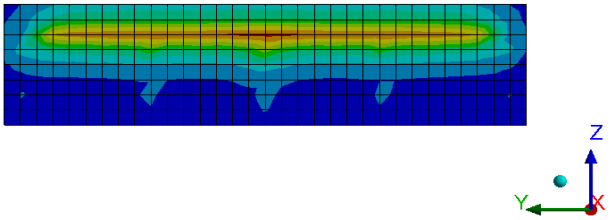

(b)

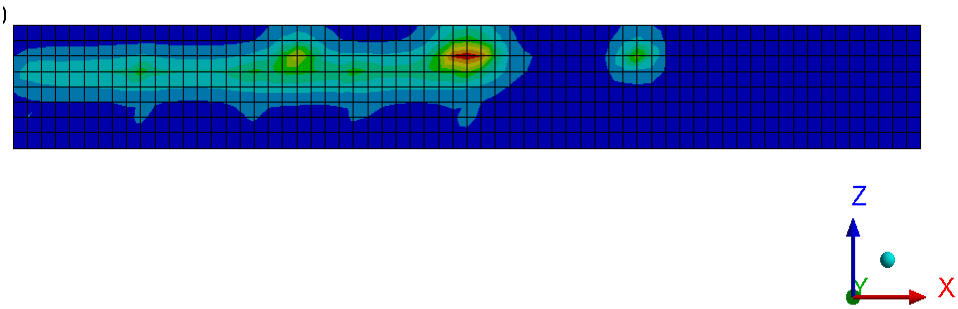

(c)

Figure 5.8 Thermal strain (in ε unit) in concrete of Panel 2: (a) top face, (b) cross-section at mid-span in horizontal y direction, and (c) cross-section at mid-span in horizontal x direction

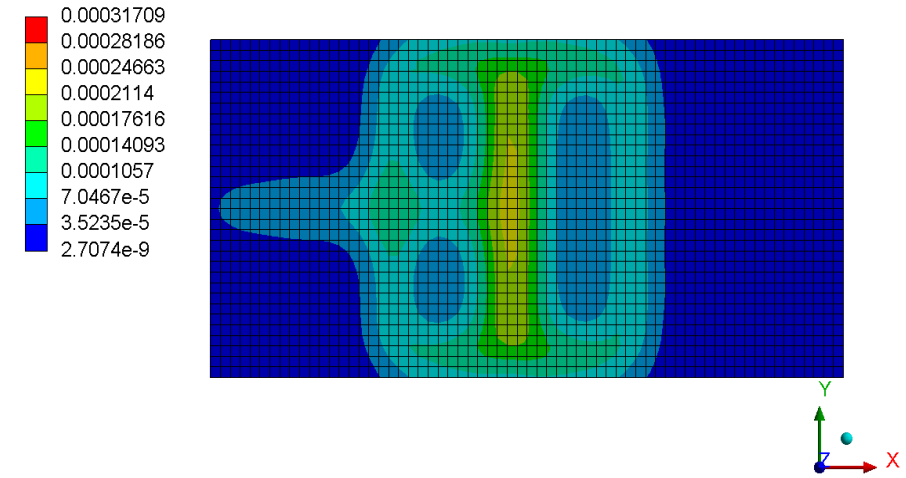

(a)

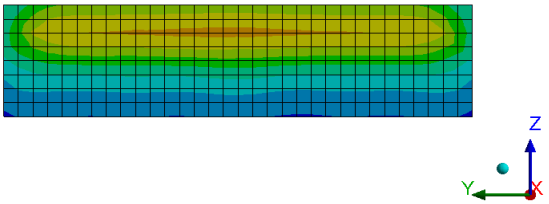

(b)

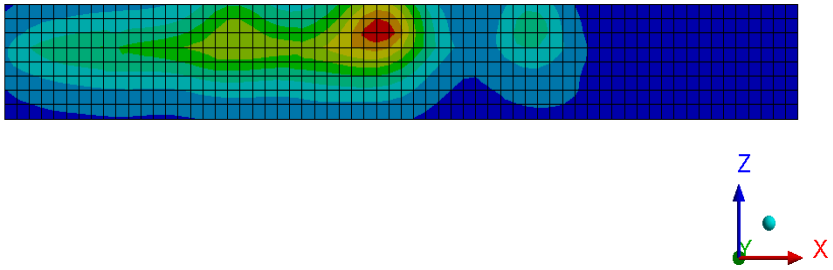

(c)

Figure 5.9 Thermal strain (in ε unit) in concrete of Panel 3: (a) top face, (b) cross-section at mid-span in horizontal y direction, and (c) cross-section at mid-span in horizontal x direction

Normal Stress

Normal stress in the x and y directions could determine the direction of cracking in concrete when stress exceeds the strength of the concrete. In addition, normal stress from thermal analysis could indicate concrete behavior to develop the EPCP designs. Any critical stress areas could be improved by alternative material strengthening and thermal management.

Normal stresses in concrete in the x direction are shown in Figure 5.10, Figure 5.12, and Figure 5.14. The tensile stresses at the top face of the EPCPs, as shown in Figure 5.10 (a), Figure 5.12 (a), and Figure 5.14 (a), were significant in x direction for both panels. The critical tensile stresses were oriented parallel to the pavement centerline (in the horizontal y direction) at the middle panel above the center area of the IPT coil; they were 418 psi, 425 psi, and 497 psi for Panels 1, 2, and 3, respectively. Therefore, the three tensile stresses did not exceed the tensile strength of concrete (424 psi), resulting in no cracking.

Figure 5.10 (c) – (d), Figure 5.12 (c) – (d), and Figure 5.14 (c) – (d) show the stress gradient in the cross-section cut through the mid-panel in the horizontal y and x directions, respectively. As shown in Figure 5.10 (c) and (d), the concrete cover, a 2-in. depth above the center area of the IPT coil, showed stresses in tension between 418 – 72 psi. Also, Figure 5.12 (c) – (d) and Figure 5.14 (c) – (d) indicate that the tensile stresses in the concrete cover area were in the range of 70 – 425 psi and 73 – 497 psi, respectively.

The concrete at the IPT coil location was subjected to compressive stresses. At the bottom faces of the EPCPs, the normal stresses were mainly in compression, whereas the tensile stresses were low [Figure 5.10 (b), Figure 5.12 (b), and Figure 5.14 (b)]. Therefore, the critical tensile stresses in the horizontal x direction predicted the concrete longitudinal cracking at mid-panel across the panel if the stresses exceeded the tensile strength. The compressive stresses were not a major factor in structural damage because the concrete was used to resist compression.

Normal stresses in concrete in the horizontal y direction are shown in Figure 5.11, Figure 5.13, and Figure 5.15. The maximum tensile stresses in the horizontal y direction (298 psi in Panel 1, 310 psi in Panel 2, and 381 psi in Panel 3) were approximately half of the stresses in the horizontal x direction. The maximum stresses in the horizontal y direction were smaller than its tensile strength of 424 psi, which was trivial in concrete failure. The crack pattern (transverse cracking) at the top face of the EPCPs could be determined from the critical tensile stresses where the coil wire reaches out from the concrete panel [Figure 5.11 (a), Figure 5.13 (a), and Figure 5.15 (a)]. The stresses at the bottom face were in both tension and compression, but the tensile stresses were minor [Figure 5.11 (b), Figure 5.13 (b), and Figure 5.15 (b)]. At the cross-section, the stresses at the coil area were in compression [Figure 5.11 (c) – (d), Figure 5.13 (c) – (d), and Figure 5.15 (c) – (d)].

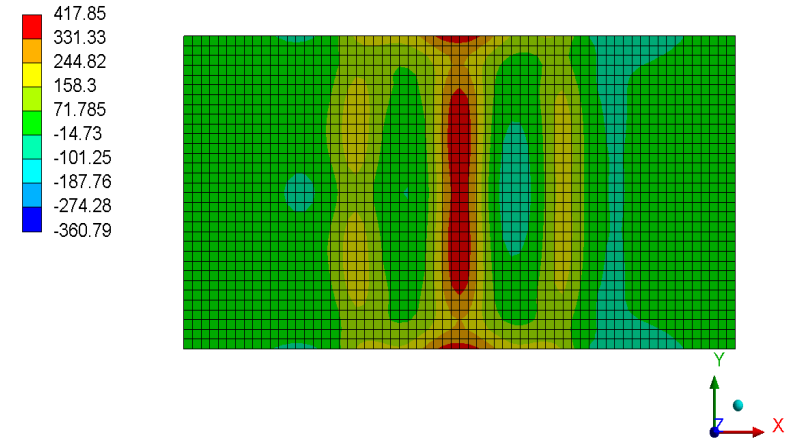

(a)

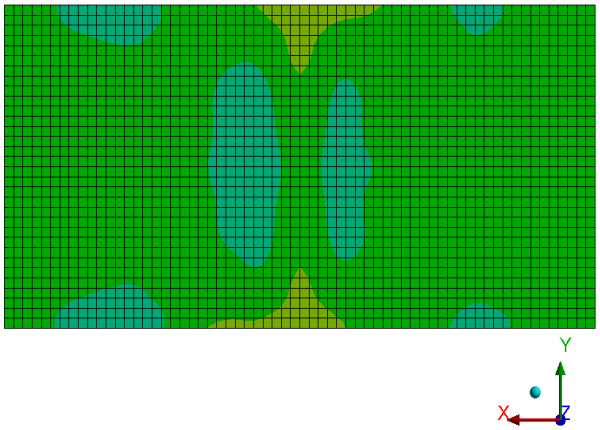

(b)

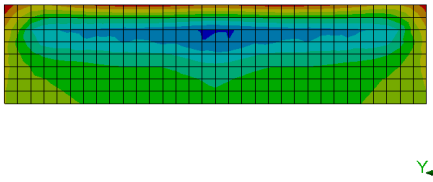

(c)

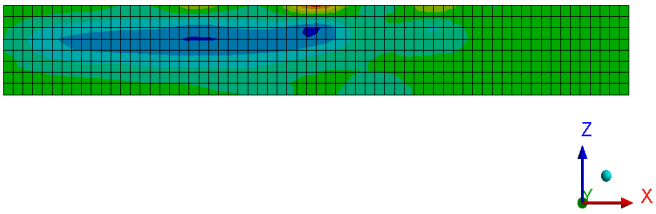

(d)

Figure 5.10 Normal stress (psi) in horizontal x direction in concrete of Panel 1: (a) top face, (b) bottom face, (c) cross-section at mid-span in horizontal y direction, and (d) cross-section at mid-span in horizontal x direction

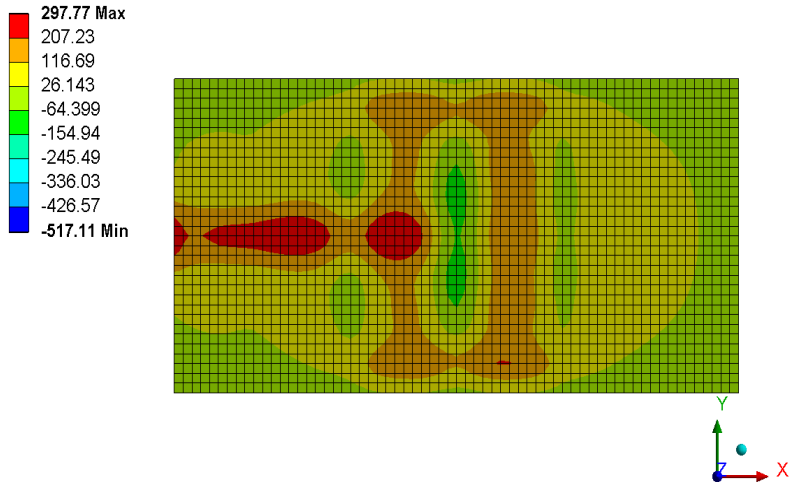

(a)

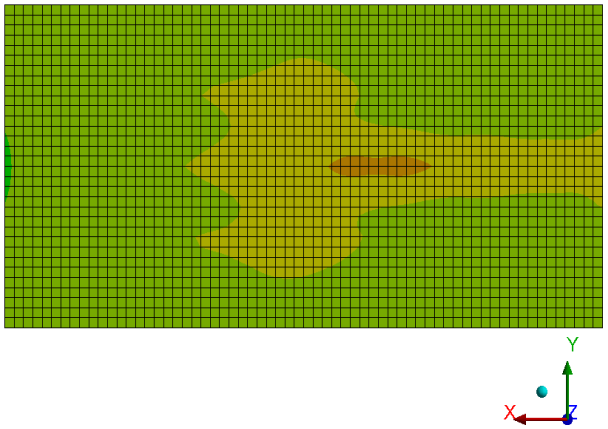

(b)

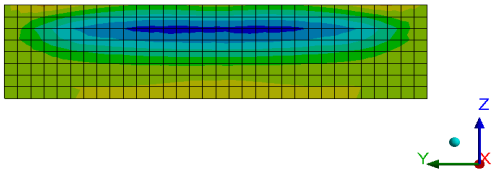

(c)

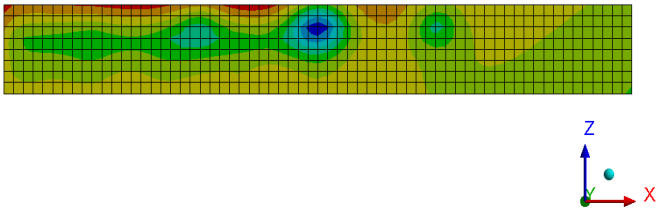

(d)

Figure 5.11 Normal stress (psi) in horizontal y direction in concrete of Panel 1: (a) top face, (b) bottom face, (c) cross-section at mid-span in horizontal y direction, and (d) cross-section at mid-span in horizontal x direction

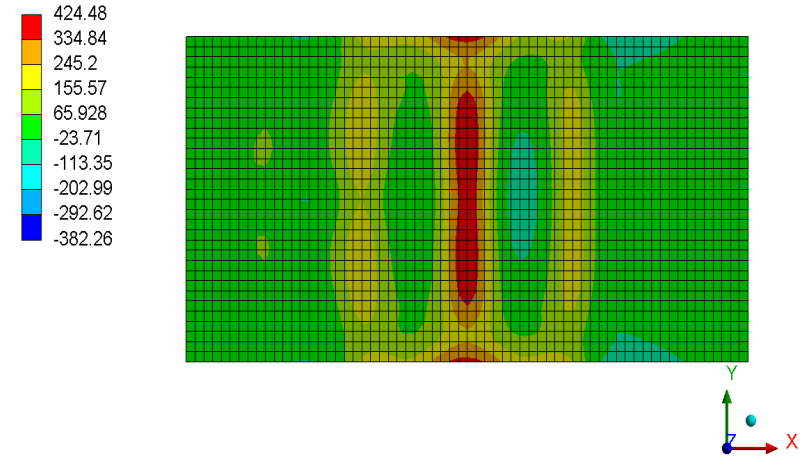

(a)

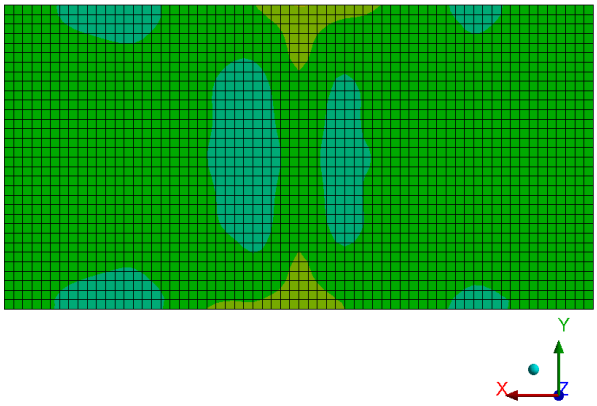

(b)

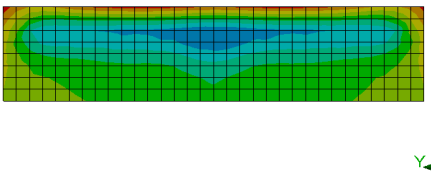

(c)

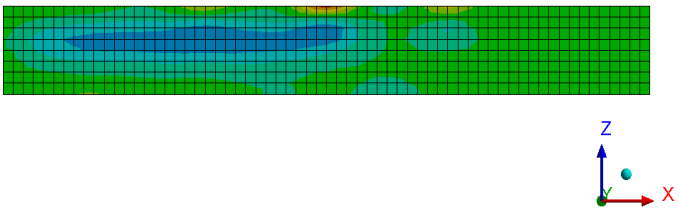

(d)

Figure 5.12 Normal stress (psi) in horizontal x direction in concrete of Panel 2: (a) top face, (b) bottom face, (c) cross-section at mid-span in horizontal y direction, and (d) cross-section at mid-span in horizontal x direction

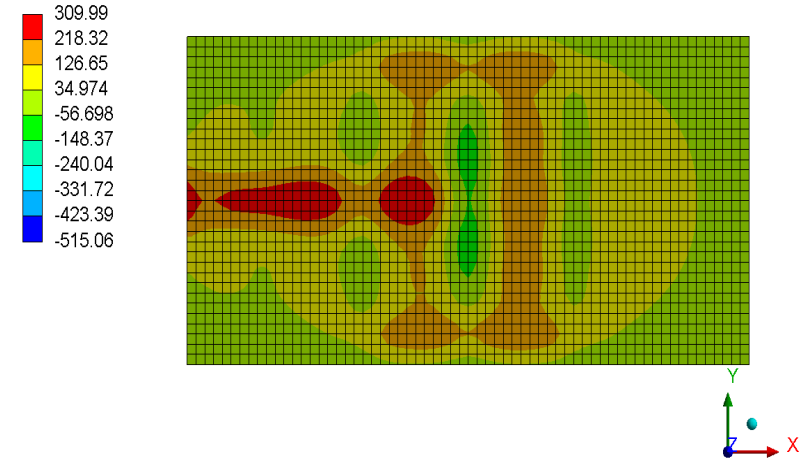

(a)

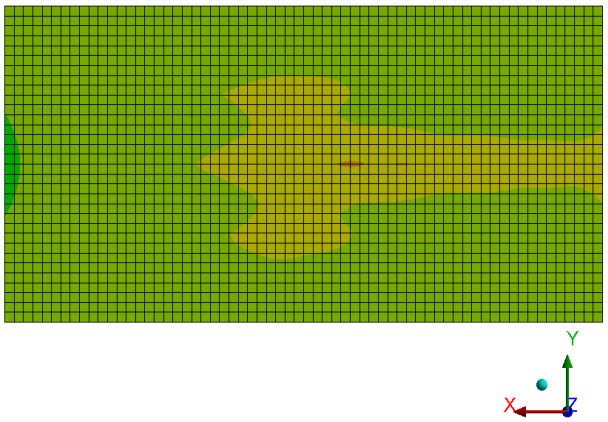

(b)

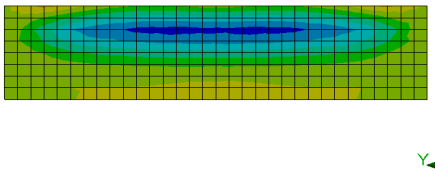

(c)

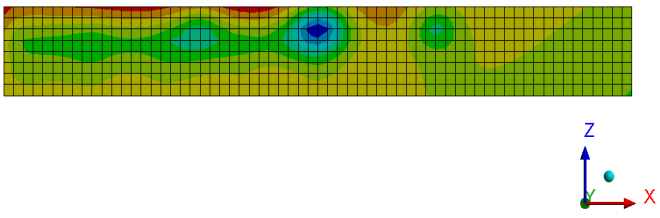

(d)

Figure 5.13 Normal stress (psi) in horizontal y direction in concrete of Panel 2: (a) top face, (b) bottom face, (c) cross-section at mid-span in horizontal y direction, and (d) cross-section at mid-span in horizontal x direction

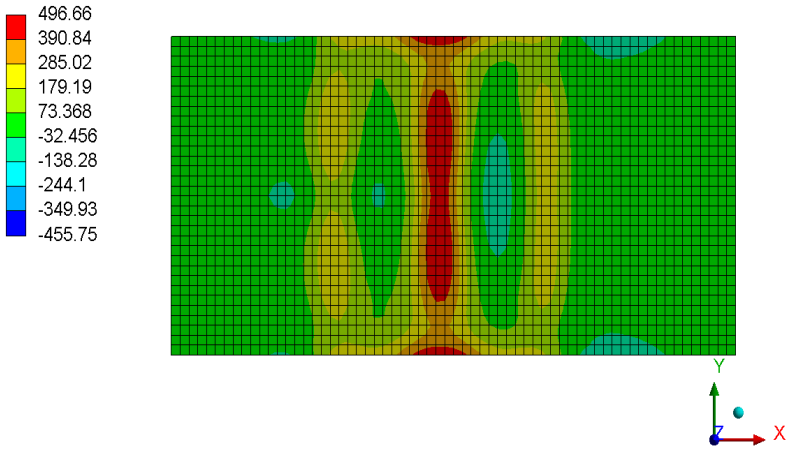

(a)

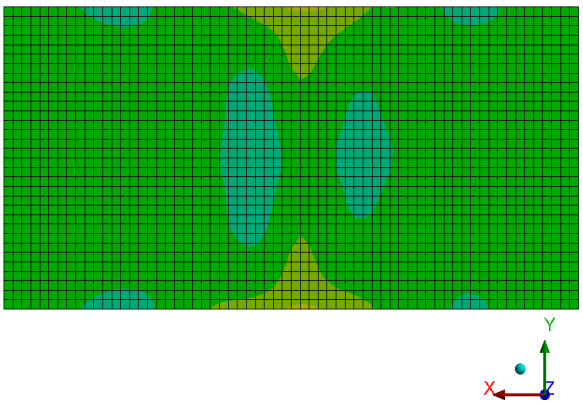

(b)

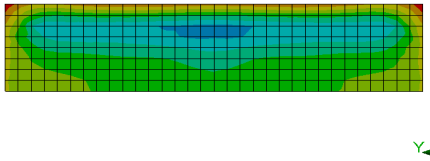

(c)

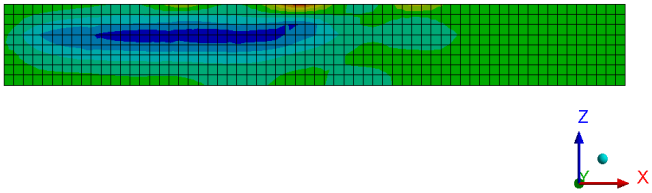

(d)

Figure 5.14 Normal stress (psi) in horizontal x direction in concrete of Panel 3: (a) top face, (b) bottom face, (c) cross-section at mid-span in horizontal y direction, and (d) cross-section at mid-span in horizontal x direction

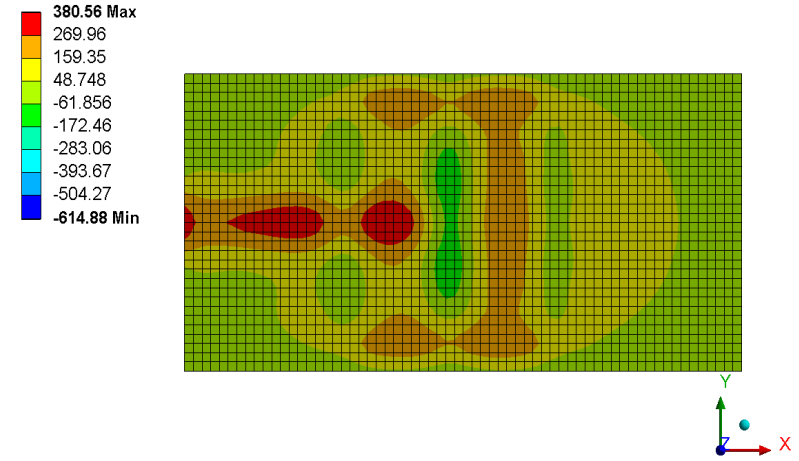

(a)

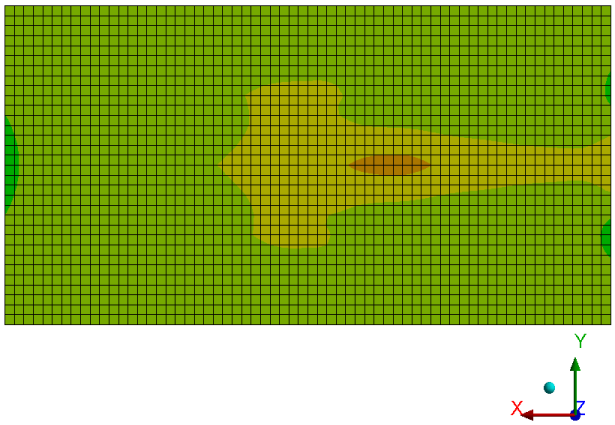

(b)

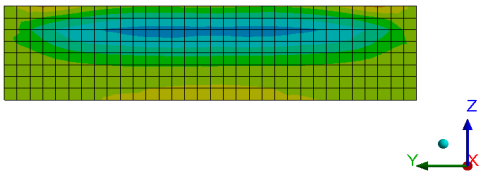

(c)

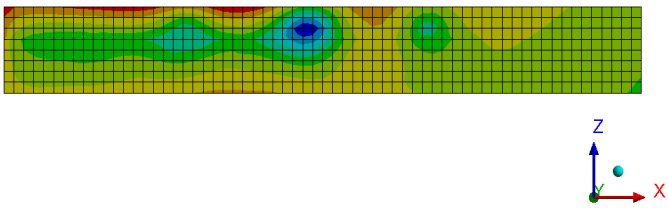

(d)

Figure 5.15 Normal stress (psi) in horizontal y direction in concrete of Panel 3: (a) top face, (b) bottom face, (c) cross-section at mid-span in horizontal y direction, and (d) cross-section at mid-span in horizontal x direction

5.2 Validation of Fatigue Analysis

The FEA fatigue models were calibrated using physical experiments to correct the results, such as crack patterns and stresses. Some unknown physical parameters, such as concrete stiffness and boundary condition, were estimated from reality.

5.2.1 Experimental Results

Top Surface Cracking

Panel 1

The internal and external strain gauges were installed at varying elevations and at high-level strains. They collected the strain data to obtain a damage gradient of the concrete. For example, internal strain (SI2) was compared with external strain (SE2). The gauges measured strain data in the horizontal y direction located at the center of the panel. SE1 and SE4 measured the maximum strain value on the top of the concrete. Maximum and minimum peak strains with the number of cycles from the two types of strain gauges are summarized in Table 5.1. The stress amplitudes are also calculated in the table. The strain amplitude (ε_a) was determined from Eq (5.1),

$$e_a = \frac{e_{max} - e_{min}}{2} \tag{5.1}$$

where ε_{max} = maximum peak strain value and ε_{min} = minimum peak strain value.

The average strain (ε_{avg}) was calculated as follows:

$$e_{avg} = \frac{e_{max} + e_{min}}{2} \tag{5.2}$$

In the experiment, crack initiation occurred at 1,100 cycles on two sides of edge at mid-span, as shown in Figure 5.16. In SE4, the maximum and minimum peak strains were in tensile realm with the values of 268.40 με and 172.64 με, respectively. Thus, the average strain was 220.5 με defined as the maximum tensile strain for the concrete. The initial cracking point was investigated in previous studies. For example, Carmona and Aguado (2012) determined the maximum tensile strain in the concrete, which was in the range of 150 με to 250 με. Laranjeira (2010) defined the average maximum tensile strain as 200 με.

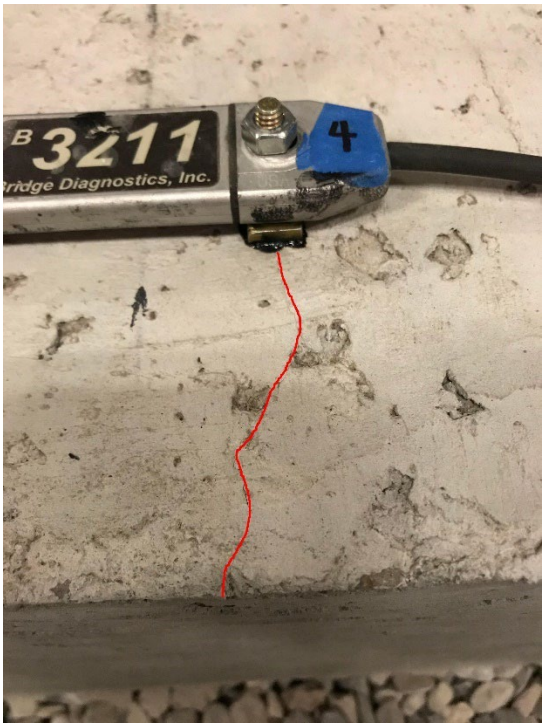

Figure 5.16 Crack initiation occurred at 1,100 cycles (SE4 sensor), Panel 1

Table 5.1 shows the results of the fatigue crack propagation for concrete fracture, which were investigated through the maximum and minimum peak strains with large enough variation or fluctuation. The peak strain could be in tension or compression. The first crack started at the edges on both sides of the concrete slab. The average cyclic strain at failure from SE4 was 220.5 με at 1,100 cycles. The second crack was propagated longitudinally to SE3 sensor next to SE 4 with a cyclic strain of 17.9 με (compression) at 6,275 cycles.

The third crack continued to the mid-slab at 7,772 cycles with 220.48 με cyclic average strain given by SE1. Thus, the cracking extended across the whole slab edge-to-edge in a longitudinal direction (traffic traveling direction). Those average cyclic strains exceeded the maximum tensile strain of 220 με, which implied that the concrete had already completely cracked. The plots of measuring strain data are expressed in Appendix B. The data regarding cracking in Figure 5.17 show that concrete was damaged in tension.

For internal strain gauges, the average cyclic strains of SI1 and SI2 were trivial with the values of 3.16 με and 69.8 με, respectively. The two gauges were attached at the GFRP rebar, which may confirm that Panel 1 failed due to concrete crushing rather than the reinforcement referred to in ACI 440 (2015).

Table 5.1 Maximum and minimum strain values from external and internal strain gauges on Panel 1 (tension positive)

	No. of cycles	$\varepsilon_{upper(max)}$ (με)	$\varepsilon_{lower(min)}$ (με)	ε_a (με)	ε_{avg} (με)
SE1	7,772	+251	+189	31.3	220
SI1	7,894	-6.45	+0.14	3.30	3.16
SE2	7,167	+80.0	+53.0	13.5	66.5
SI2	7,245	-32.4	-47.5	7.55	-39.9
SI5	8,051	+0.352	-6.89	3.62	-3.27
SE3	6,275	-16.8	-19.0	1.08	-17.9
SE4	1,100	+268	+172	48.0	220
SE5	6,243	-14.0	-20.5	3.24	-17.3
SI6	7,553	+5.77	+1.24	2.27	3.51
SE6	6,221	+30.6	-3.07	16.8	13.8
SE7	6,215	-4.51	-7.82	1.66	-6.17
SE8	6,408	+53.8	+16.0	18.9	34.9

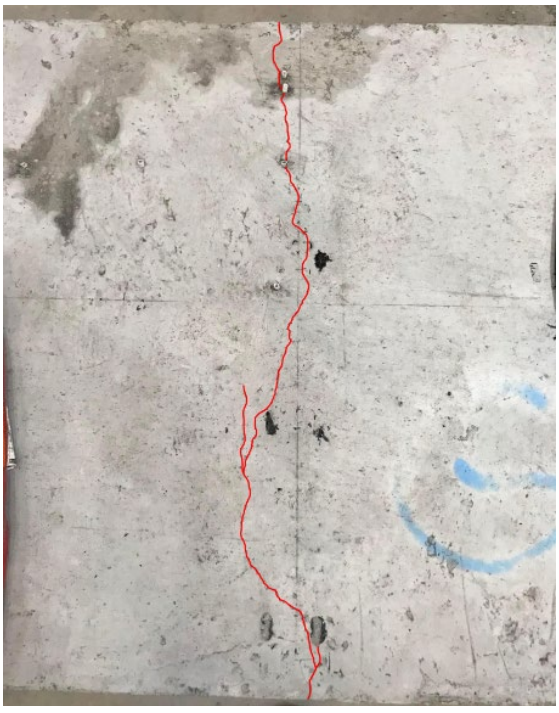

Figure 5.17 Cracking in concrete of Panel 1, at top concrete surface

Panel 2

According to crack propagation, the internal and external strain measured the data in both horizontal x and y directions, as shown in Table 5.2. The critical strain data occurred at SE1, SE3, and SE4. Any critical measured strain data are finalized in Table 5.2. Cyclic strain at failure was determined from strain average (ε_{avg}), as seen in Table 5.2. The first crack occurred around the center of the slab about SE3 location with 349 με average cyclic strain at two cycles.

SE1 captured the second longitudinal cracking with 286 με average strain at 2 cycles. The third cracking occurred at 29 cycles with an average strain of 296 με measuring from the SE4 sensor located at the mid-slab edge. Thus, the cracking propagated across the entire slab by running edge-to-edge in a longitudinal direction (traffic traveling direction). The plots of measuring strain data are shown in Appendix B. As presented in Figure 5.18, the cracking occurred at the center mid-span of the slab in tension similar to Panel 1.

Table 5.2 Maximum and minimum strain values from external and internal strain gauges on the electrified concrete Panel 2 (tension is positive)

	No. of cycles	$\varepsilon_{max(upper)}$ (με)	$\varepsilon_{min(lower)}$ (με)	ε_a (με)	ε_{avg} (με)
SE1	2	+403	+169	117	286
SI1	35	-103	-64.0	19.5	83.5
SE2	29	+16.0	+2.45	6.76	9.21
SI2	48	+118	+51.1	33.7	84.8
SE3	2	+485	+213.	136	349
SE4	29	+375	+217	79.0	296
SE5	29	-0.422	-5.33	2.45	-2.88
SE6	29	+39.8	+0.850	19.5	20.3
SE7	29	+1.68	+0.497	0.591	1.09
SE8	4	+34.6	+7.50	13.6	21.1

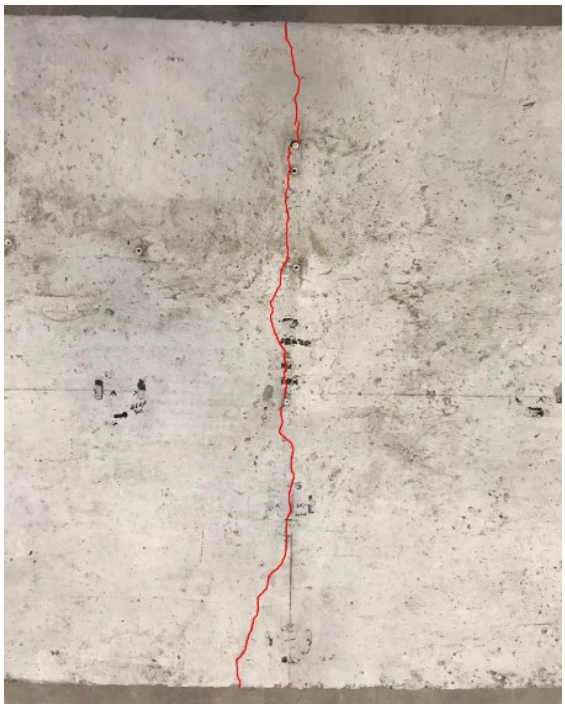

Figure 5.18 Cracking in concrete of Panel 2, at top concrete surface

Side Cracking

Panel 1

In Figure 5.19, the cracking penetrated through cross section of the concrete slab. On one side of the concrete slab, the cracking cut through at the following depths and cycles:

- 4.75 in. depth at 7,500 cycles
- 7 in. depth at 9,700 cycles
- 8.75 in. depth at 11,980 cycles
- 9.75 in. depth at 15,110 cycles
- 10.25 in. depth at 111,200 cycles

On another side, the cracking cut through at the following depths and cycles:

- 6.5 in. depth at 7,500 cycles
- 8 in. depth at 9,700 cycles
- 8.75 in. depth at 11,980 cycles
- 10.25 in. depth at 111,200 cycles

Table 5.2 presents the element elevations of IPT and rebar throughout the thickness of the concrete panel as related to the results shown in Table 5.3 and Table 5.4. In Table 5.3, the top layer of the GFRP reinforcement was able to resist the first cracking until 7,500 cycles of the cyclic loading test at a 4.75 in. to 6.5 in. depth. The second and third cracks were then located between two layers of reinforcement until 11,980 cycles. The last recorded cracking went through the bottom reinforcement mat at 111,200 cycles at a 10.25 in. depth.

Table 5.3 Cracking at the concrete side of the electrified concrete Panel 1

<table>
<tr><th>Depth (in.) measuring from top concrete surface</th><th>Element</th><th>1. Cracking location</th><th>2. Cracking location</th><th>3. Cracking location</th><th>4. Cracking location</th></tr>
<tr><td>0 in. – 2 in.</td><td>concrete covering</td><td rowspan="2"></td><td rowspan="2"></td><td rowspan="2"></td><td rowspan="4"></td></tr>
<tr><td>2 in. – 4 in.</td><td>IPT system</td></tr>
<tr><td>4 in. – 5 in.</td><td>top layer of reinforcement</td><td rowspan="2">4.75 in. – 6.50 in. depth at 7,500 cycles</td></tr>
<tr><td>5 in. – 9 in.</td><td>space between two layers of reinforcement</td><td>7.00 in. – 8.00 in. depth at 9,700 cycles</td><td>8.75 in. depth at 11,980 cycles</td></tr>
<tr><td>9 in. – 10 in.</td><td>bottom layer of reinforcement</td><td rowspan="2"></td><td rowspan="2"></td><td rowspan="2"></td></tr>
<tr><td>10 in. – 12 in.</td><td>concrete covering</td><td>10.25 in. depth at 111,200 cycles</td></tr>
</table>

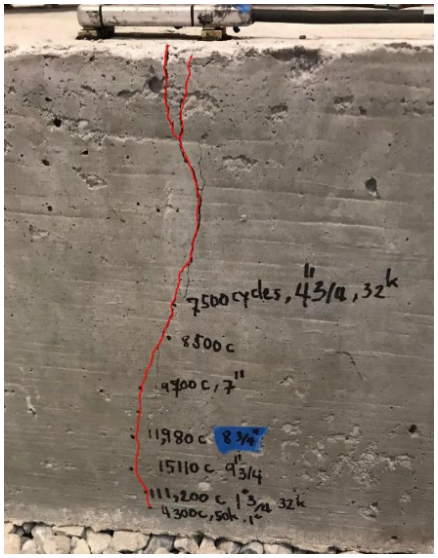

Figure 5.19 Cracking in concrete of Panel 1 at side

Panel 2

In Figure 5.20, the cracking cut through a cross-section of the concrete slab. The cracking was investigated at both of the two cross-section sides. The cracking penetrated through an 8.25 in. depth at 2,680 cycles on one side of the concrete slab. The cutting continued through a 10 in. depth at 10,470 cycles and a 10.25 in. depth at 139,000 cycles. Similarly, another side of the concrete slab cut through an 8 in. depth at 2,680 cycles, an 8.75 in. depth at 10,470 cycles, and a 9.5 in. depth at 139,000 cycles.

As shown in Table 5.4, the first noticeable cracking at the concrete side passed the top layer of steel reinforcement at an 8 in. – 8.25 in. depth at 2,680 cycles, then the second cracking spread to the bottom reinforcement layer at an 8.75 in. – 10 in. depth (10,470 cycles). The bottom reinforcement carried the cracking to 139,000 cycles at a 9.5 in. – 10.25 in. depth.

Table 5.4 Cracking at the concrete side of the electrified concrete Panel 2

<table>
<tr><th>Depth (in) measuring from top concrete surface</th><th>Element</th><th>1. Cracking location</th><th>2. Cracking location</th><th>3. Cracking location</th></tr>
<tr><td>0 in. – 2 in.</td><td>concrete covering</td><td rowspan="3"></td><td rowspan="3"></td><td rowspan="4"></td></tr>
<tr><td>2 in. – 4 in.</td><td>IPT system</td></tr>
<tr><td>4 in. – 5 in.</td><td>top layer of reinforcement</td></tr>
<tr><td>5 in. – 9 in.</td><td>space between two layers of reinforcement</td><td>8.00 in. – 8.25 in. depth at 2,680 cycles</td><td rowspan="2">8.75 in. – 10.00 in. depth at 10,470 cycles</td></tr>
<tr><td>9 in. – 10 in.</td><td>bottom layer of reinforcement</td><td rowspan="2"></td><td rowspan="2">9.50 in. – 10.25 in. depth at 139,000 cycles</td></tr>
<tr><td>10 in. – 12 in.</td><td>concrete covering</td><td></td></tr>
</table>

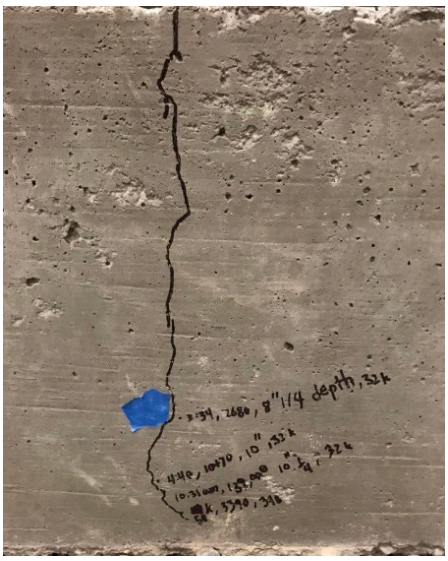

Figure 5.20 Cracking in concrete of Panel 2 at side

5.2.2 Discussion of FEA Modelling and Experimental Results

The FEA results were presented for Panels 1 and 2. From the cyclic load case, normal stresses, equivalent plastic strains, and total deformations in concrete were shown in this section. Normal stresses in the x direction were determined in the IPT's element and reinforcing bar. Furthermore, the failure of the concrete was interpreted as tension damage, compression damage, and total damage.

Panel 1

The cyclic load was applied at a one-time step ending at 1,100 seconds (30 substeps) when the initial cracking for concrete occurred in the experiment. As shown in Figure 5.21 (half scale of the panel), the maximum tensile normal stress at in the horizontal x direction in the concrete was 315 psi, located at the center on the sides of the slab, which caused the initial cracking. The maximum compressive normal stress at the horizontal x direction was 893 psi, located at the center of the bottom face of the slab. Figure 5.22 shows the maximum tensile normal stress in the concrete (the horizontal y direction) of 152 psi, located inside the concrete across a transverse direction. The maximum compressive normal stress was 598 psi at the bottom face's edge. A yield point was a point on the stress-strain curve of the concrete. After the stresses beyond this yield point, the concrete material became nonlinear (plastic and elastic). Plastic deformation, which was permanent, would occur after this point. Therefore, the equivalent plastic strain was the total permanent strain of this plastic deformation and was defined from three-dimensional equivalent strain as:

$$\mathrm{e}_e = \frac{1}{1+\mathrm{n}'}\left(\frac{1}{2}[(\mathrm{e}_1-\mathrm{e}_2)^2+(\mathrm{e}_2-\mathrm{e}_3)^2+(\mathrm{e}_3-\mathrm{e}_1)^2]\right)^{\frac{1}{2}} \tag{5.3}$$

where ν' is effective Poisson's ratio, which is equal to 0.5 for plastic strains.

The macrocrack was defined from the maximum equivalent plastic strain, which occurred at both two sides of the slab running across a longitudinal direction, as seen in Figure 5.24.

As shown in Figure 5.25, the most damage in the concrete failure came from tension. The tensile cracking started at the two center edges and the center at both sides of the slab in Figure 5.25 (b). The compression damage did not cause any concrete cracking, as seen in Figure 5.25 (c). In Figure 5.25 (a), the total damage from the tension and compression damage was able to interpret the microcracking spread over a bigger zone. The crack initiation from the experiment agreed with the damage contour at 1,100 cycles. The initial crack began at the center edges area on both sides leading to a longitudinal crack on the concrete panel.

The FEA model determined the mechanical behavior of the IPT system and reinforcement (Figure 5.26). Panel 1 was reinforced with #4 GFRP rebar. The normal stresses only occurred in the x direction. The maximum tensile normal stress in the rebar in the x direction [Figure 5.26 (a)] was 3,084 psi, located at the mid-length of the top mat transverse rebar. However, the tensile stress was still lower than the yield strength of the GFRP. So, the transverse rebar at the top mat was the main reinforcement to support the cyclic load. For the IPT system, the very small tensile stresses occurred at the corner bends of the double-D Litz wire in Figure 5.26 (b). The edge of the ferrite group contained the maximum tensile normal stress of 2,964 psi in Figure 5.26 (c).

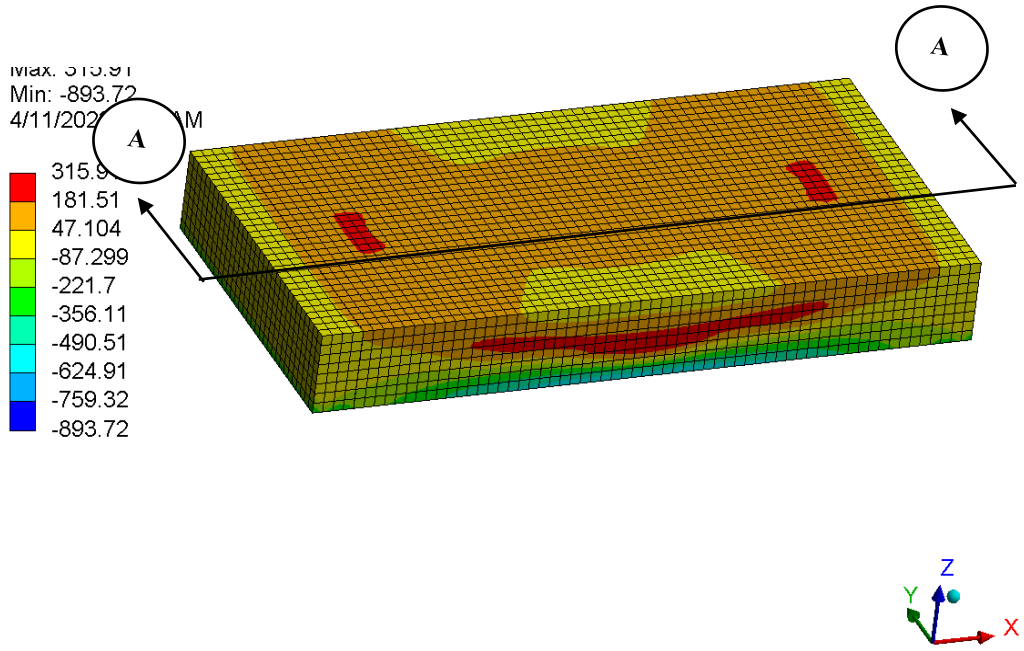

(a)

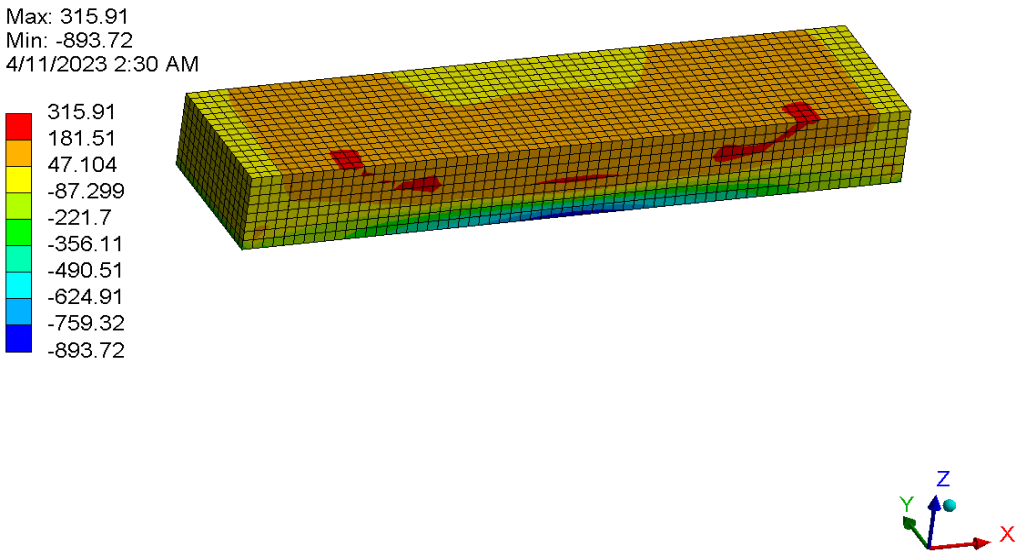

(b)

Figure 5.21 Normal stress (psi) in concrete (Panel 1) at horizontal x direction at the end of simulation (1,100 seconds): (a) top concrete view, and (b) concrete cross section A

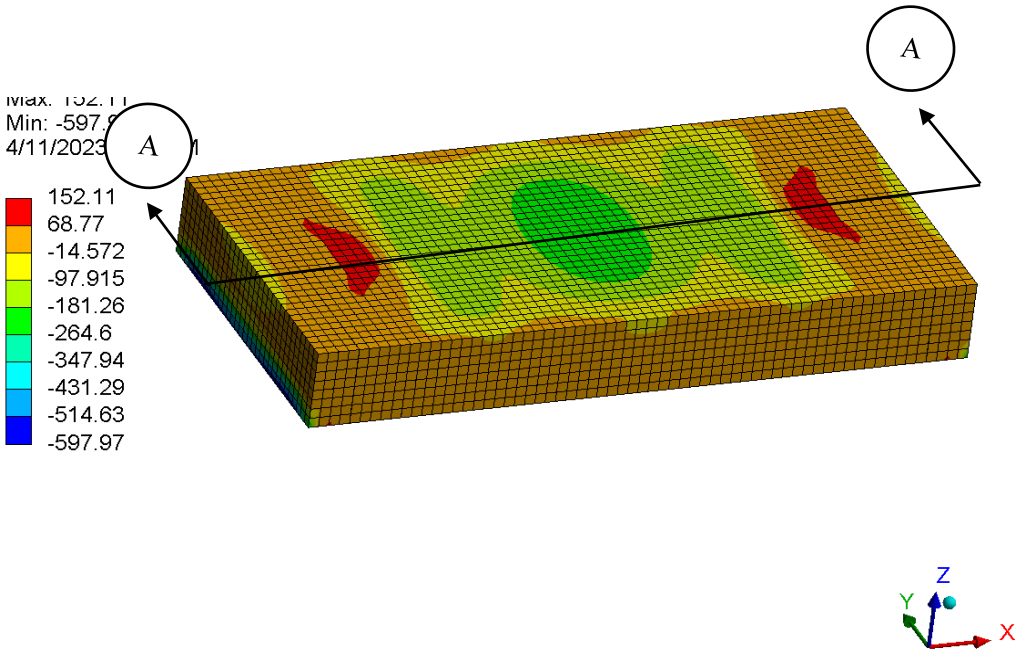

(a)

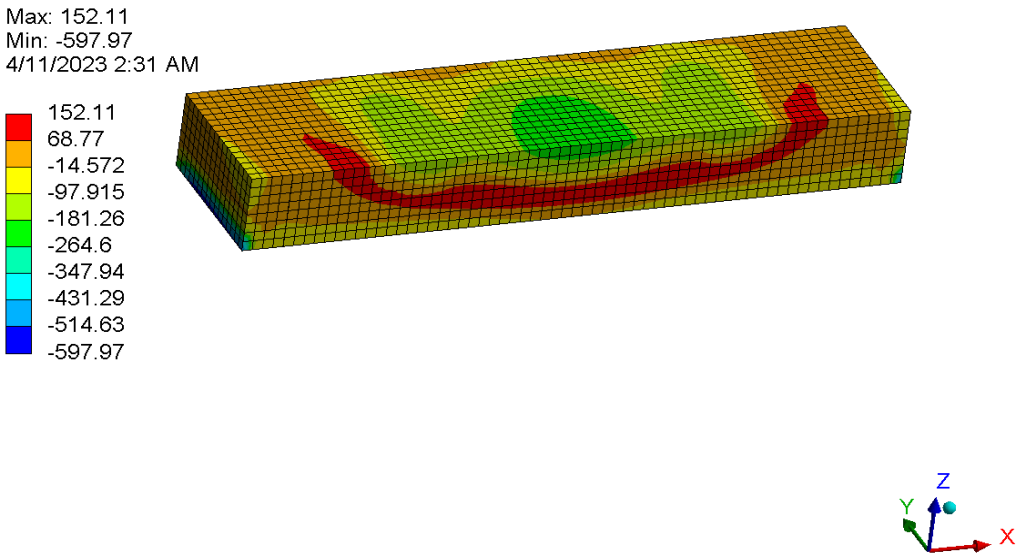

(b)

Figure 5.22 Normal stress (psi) in concrete (Panel 1) at horizontal y direction at the end of simulation (1,100 seconds): (a) top concrete view, and (b) concrete cross section A

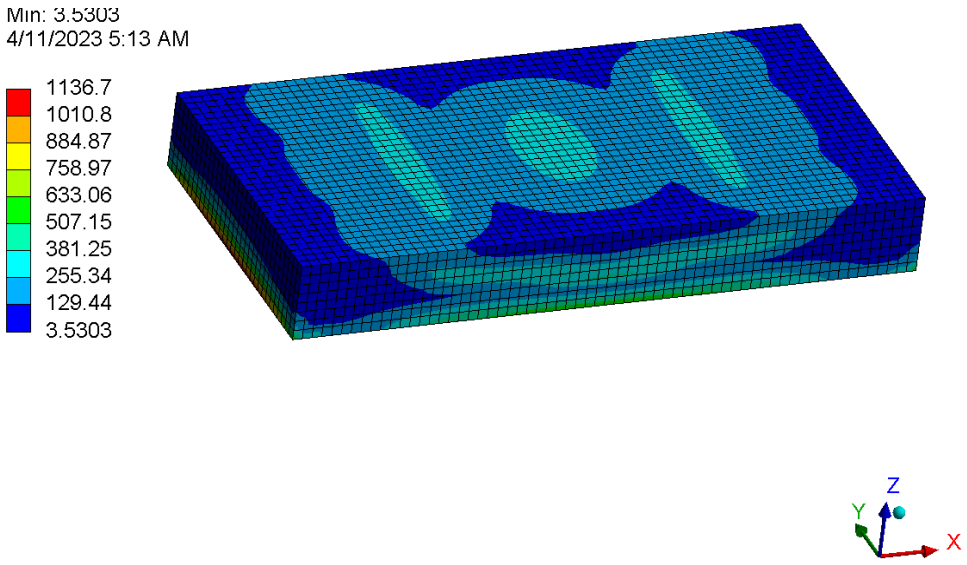

(a)

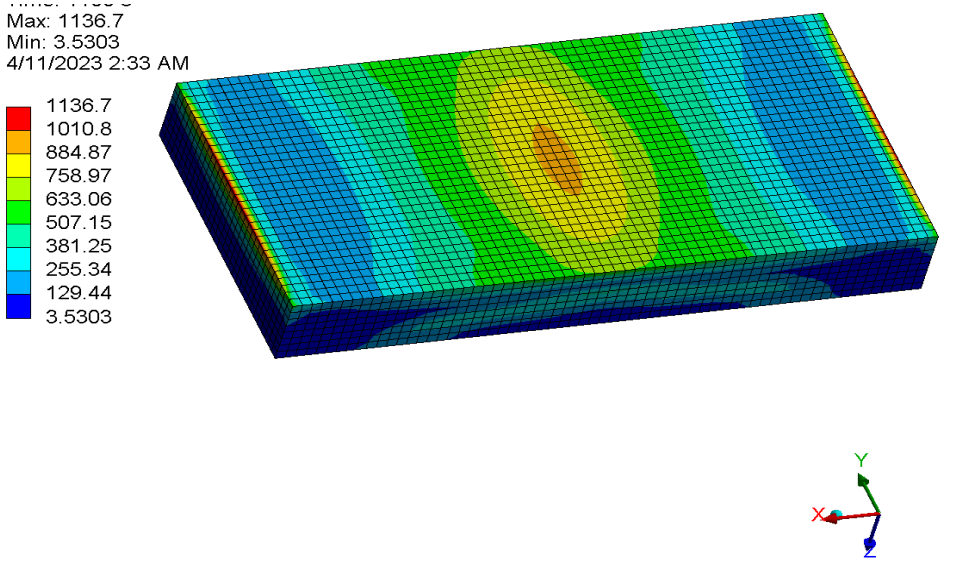

(b)

Figure 5.23 Equivalent von Mises stress (psi) in concrete (Panel 1) at the end of simulation (1,100 seconds): (a) top concrete view, and (b) bottom concrete view

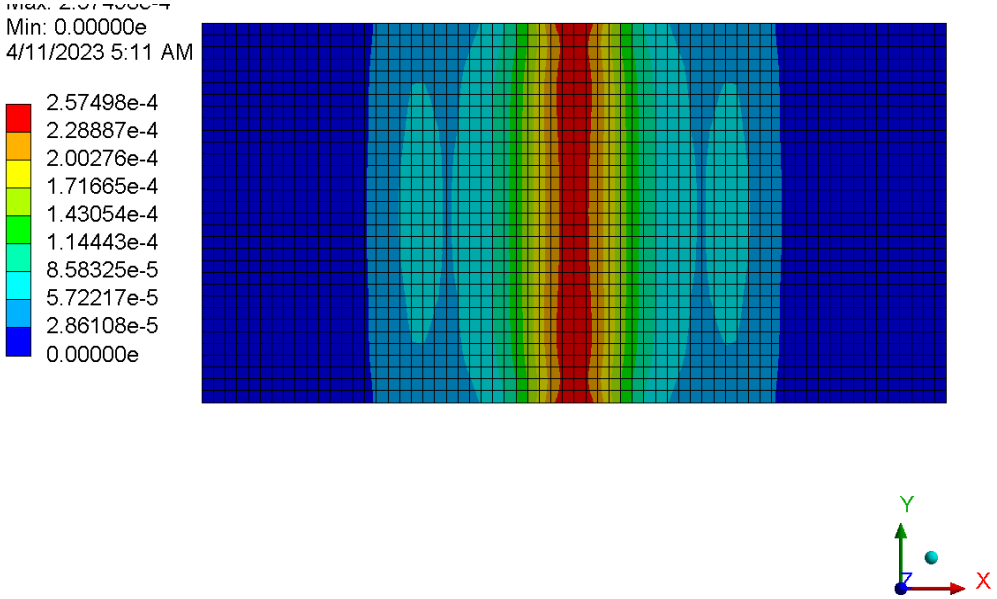

(a)

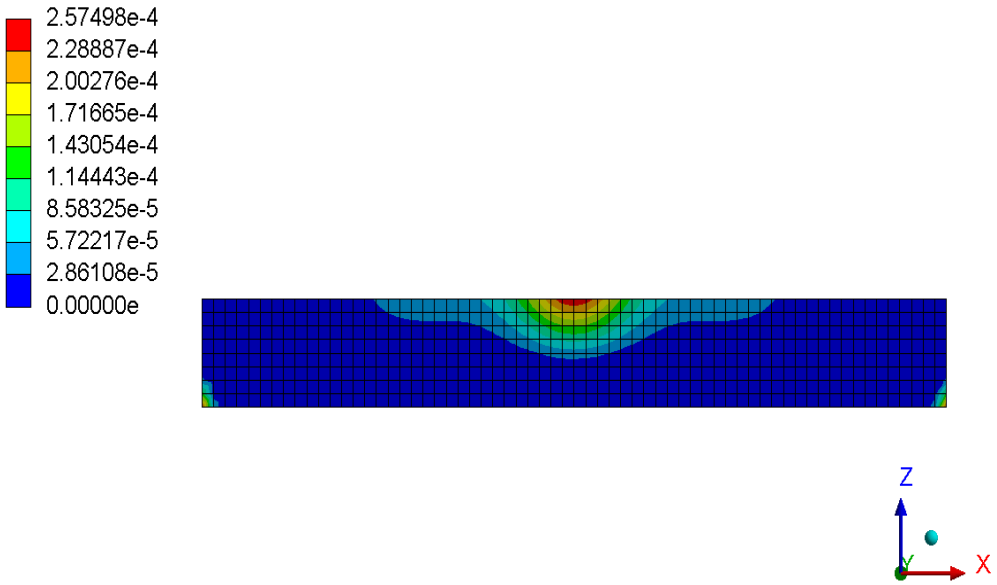

(b)

Figure 5.24 Equivalent plastic strain (strain unit) in concrete (Panel 1) at the end of simulation (1,100 seconds): (a) top concrete view, and (b) concrete at side view

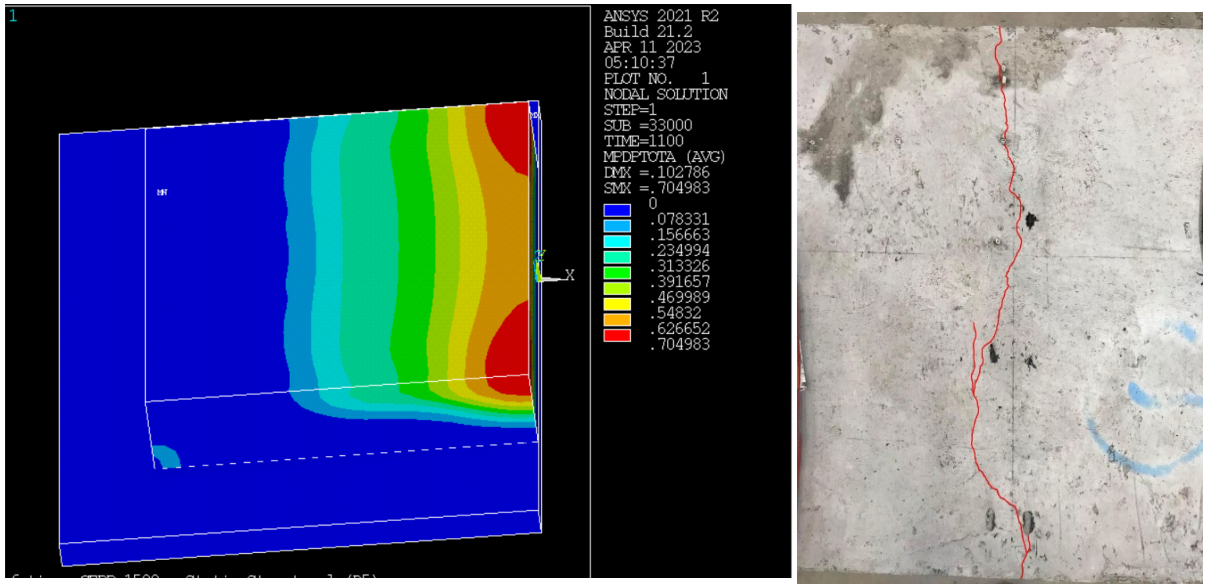
1
ANSYS 2021 R2
Build 21.2
APR 11 2023
05:10:37
PLOT NO. 1
NODAL SOLUTION
STEP=1
SUB =33000
TIME=1100
MPDPTOTA (AVG)
DMX =.102786
SMX =.704983
0
.078331
.156663
.234994
.313326
.391657
.469989
.54832
.626652
.704983
Y
Z
X

(a)

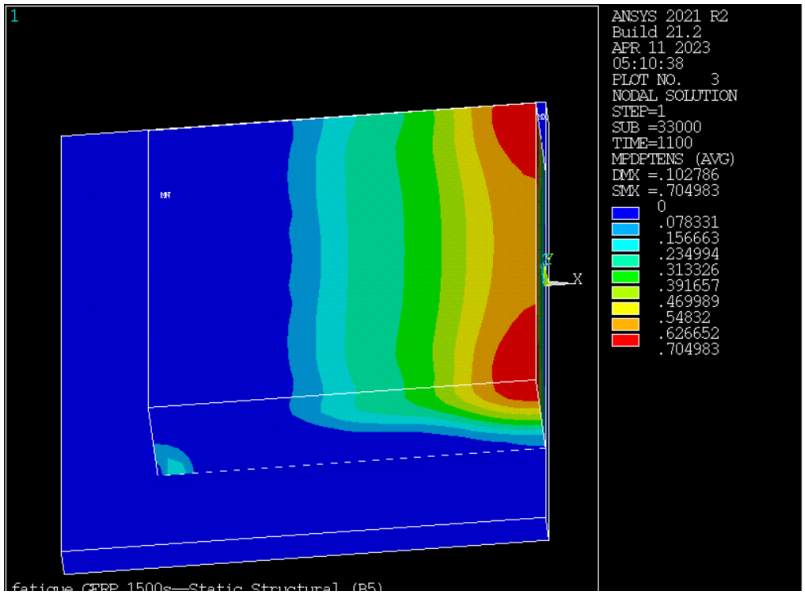
1
ANSYS 2021 R2
Build 21.2
APR 11 2023
05:10:38
PLOT NO. 3
NODAL SOLUTION
STEP=1
SUB =33000
TIME=1100
MPDPTENS (AVG)
DMX =.102786
SMX =.704983
0
.078331
.156663
.234994
.313326
.391657
.469989
.54832
.626652
.704983
Y
Z
X

(b)

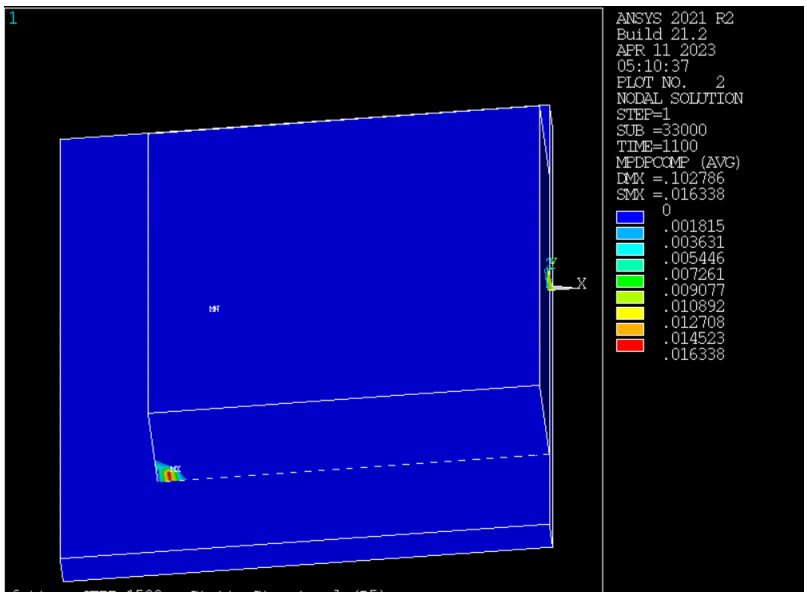

(c)

Figure 5.25 Concrete damage profiles (Panel 1), a half model, at the end of simulation (1,100 seconds): (a) total damage profile, (b) tensile damage profile, and (c) compressive damage profile

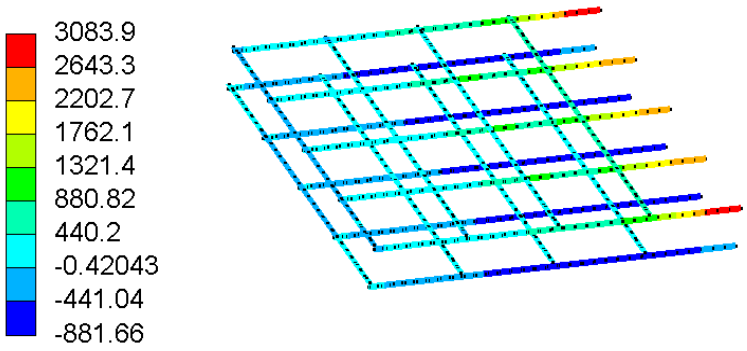
3083.9
2643.3
2202.7
1762.1
1321.4
880.82
440.2
-0.42043
-441.04
-881.66
Z
Y
X

(a)

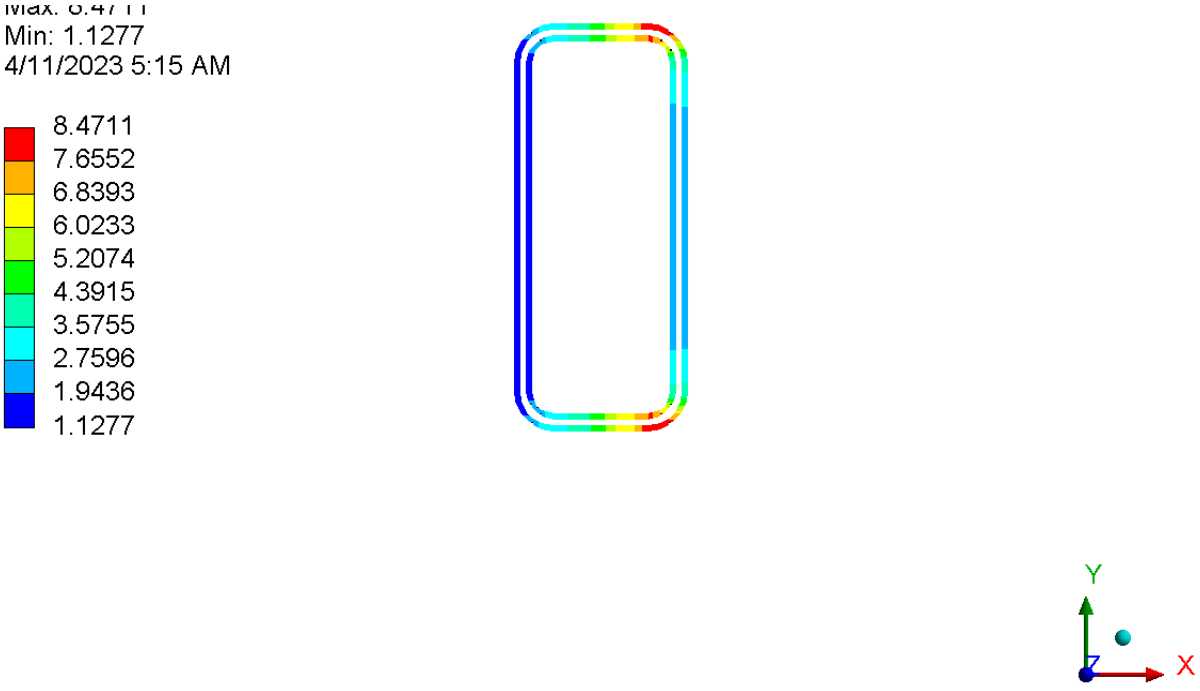
Min: 1.1277
4/11/2023 5:15 AM
8.4711
7.6552
6.8393
6.0233
5.2074
4.3915
3.5755
2.7596
1.9436
1.1277
Y
Z
X

(b)

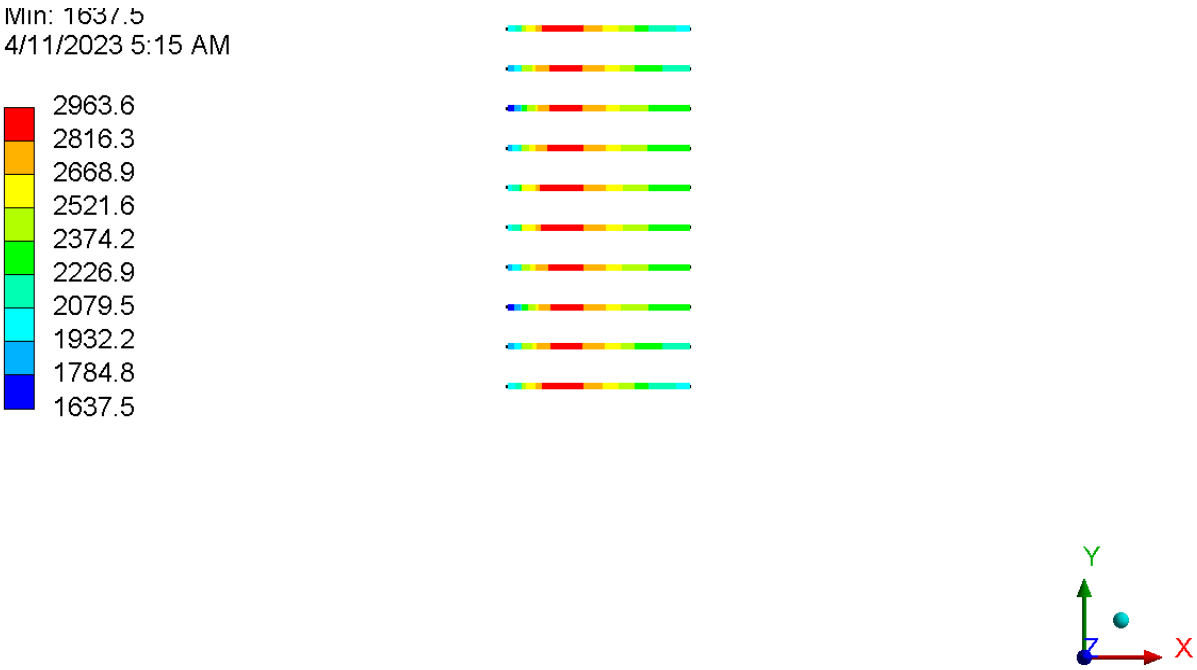

(c)

Figure 5.26 Normal stress (psi) in IPT components at horizontal x direction at the end of simulation: (a) a half rebar model, (b) a half Litz wire model, and (c) a half ferrites model

Panel 2

The FEA model was set to one-time step ending, each step consisting of 40 substeps, for 10 seconds to simulate the cyclic loading (full scale). As shown in Figure 5.27, the maximum tensile stress at the horizontal x direction in the concrete was 291 psi, located at the center on the side of the slab, which caused the initial cracking. The maximum compressive stress at the horizontal x direction, which was 1,090 psi, occurred at the center on the bottom face of the slab. Figure 5.28 presents the maximum tensile stress (the horizontal y direction) in the concrete of 166 psi, located near the area of the applied cyclic load on top of the slab. The maximum compressive stress (the horizontal y direction) was 703 psi at the edge of the bottom slab. However, those stresses caused insignificant damage to the concrete structure.

The equivalent plastic strain (Figure 5.30) represented macrocrack forming in the center and spreading to the outermost edge.

As presented in Figure 5.31, the damage to the concrete at 10 cycles was mainly from tension. The microcracking ran over the larger center zone in the longitudinal direction. The cracking penetrated through the thickness of the slab for two sides. Compressive damage was insignificant at the corners of the concrete, referred to in Figure 5.31 (c). In Figure 5.31 (a), the crack pattern was determined from the total damage, which was the combination of the tensile and compressive damage as mentioned above. The initial crack occurred at the center area running through both sides of the concrete slab. The total damage and plasticity were used to compare with the cracking from physical cyclic load testing, which was in a good agreement.

Figure 5.32 shows the mechanical behavior of the IPT system and reinforcement. Panel 2 was reinforced with #4 steel rebar. The normal stresses only occurred in the x direction. As presented in Figure 5.32 (a), the maximum tensile stress in the rebar in the horizontal x direction was 26,898 psi (lower than yield strength) located at the mid-length of the top mat transverse rebar. So, the top mat transverse rebar was the primary reinforcement to resist the cyclic load. For the IPT system, the maximum tensile stress was minor (17 psi) at the corner bends of the double-D Litz wire in Figure 5.31 (b). The edge of the ferrite group received the maximum tensile normal stress of 2,585 psi in Figure 5.32 (c).

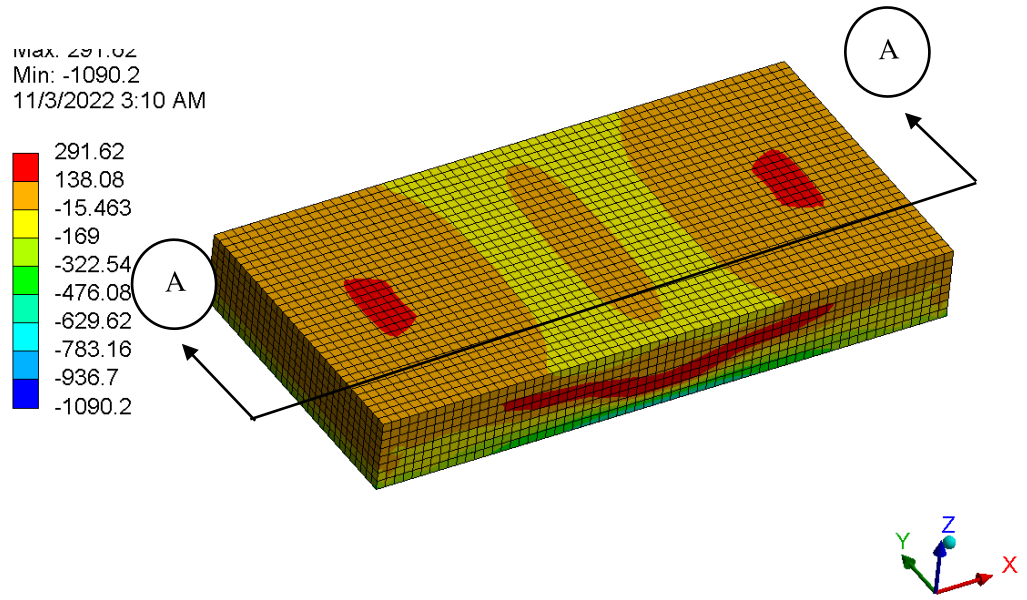

(a)

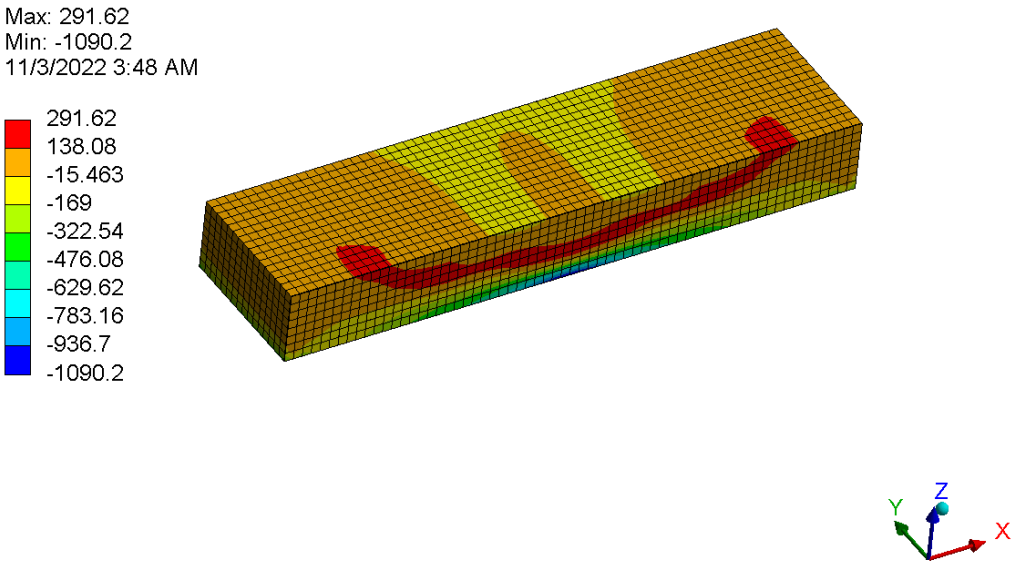

(b)

Figure 5.27 Normal stress (psi) in concrete (Panel 2) at horizontal x direction at the end of simulation (10 seconds): (a) top concrete view, and (b) concrete section A

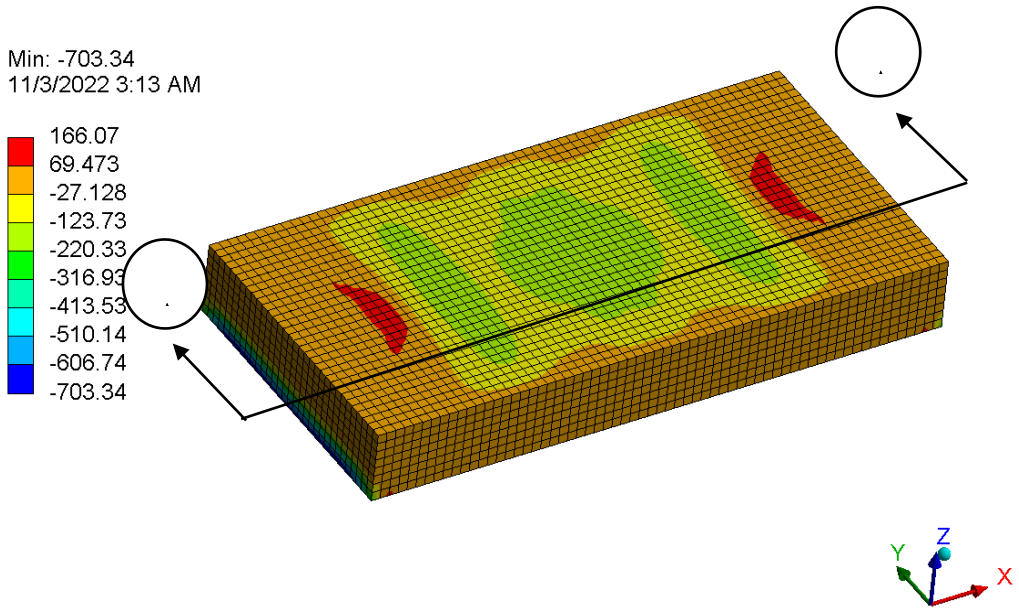

(a)

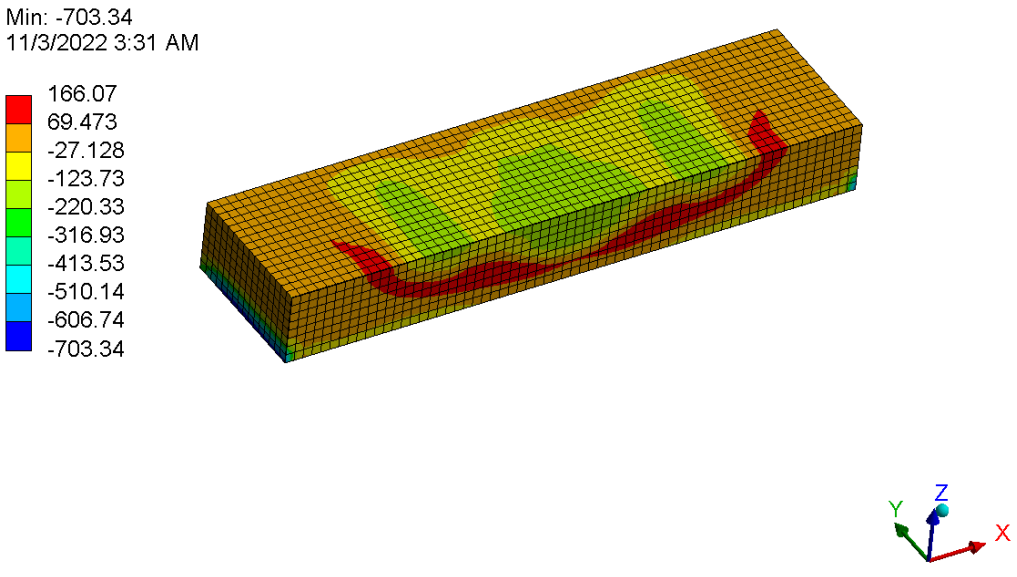

(b)

Figure 5.28 Normal stress (psi) in concrete (Panel 2) at horizontal y direction at the end of simulation (10 seconds): (a) top concrete view, and (b) concrete section A

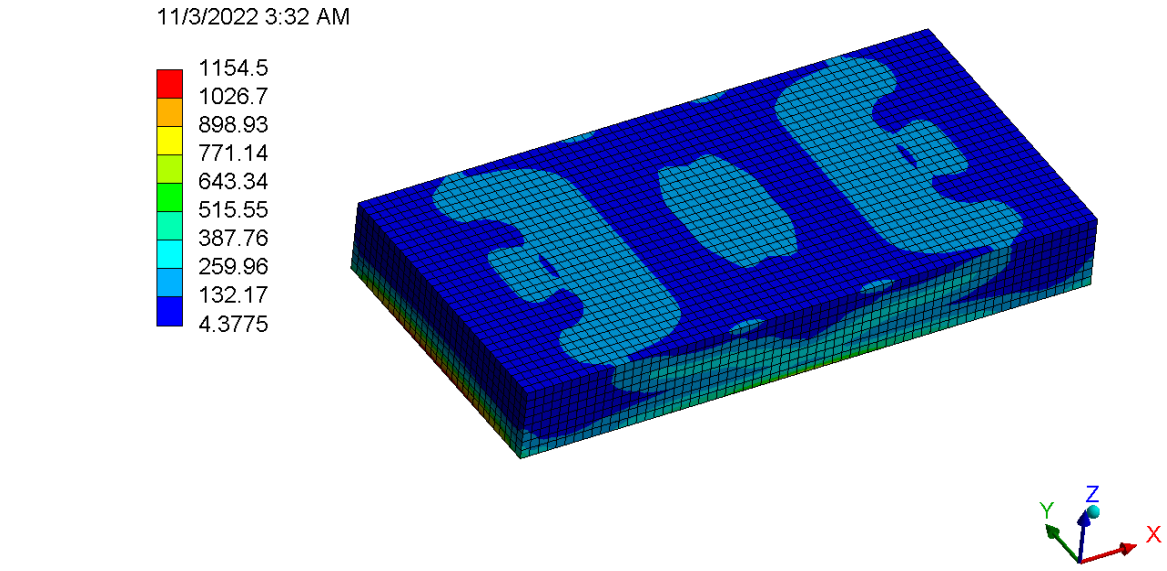

(a)

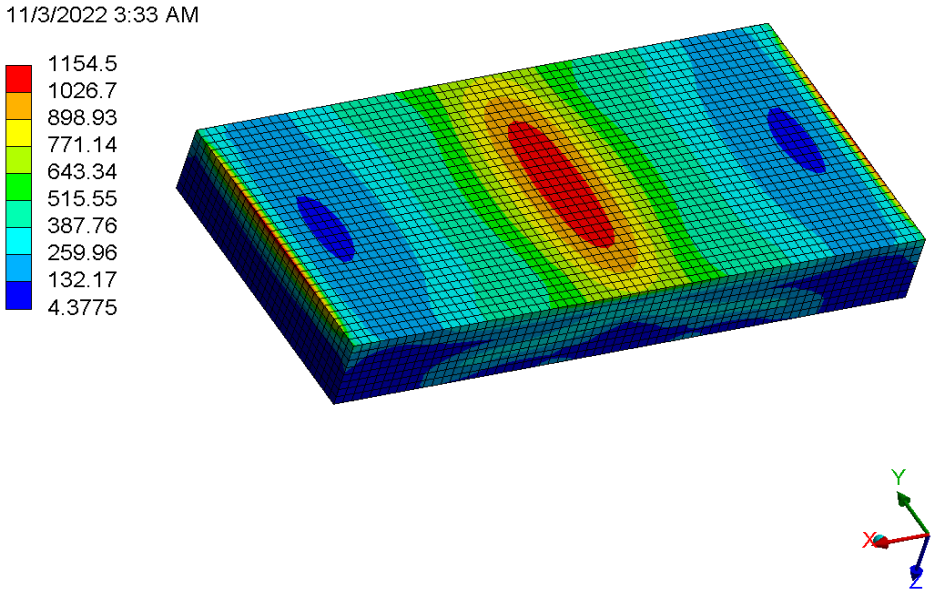

(b)

Figure 5.29 Equivalent von Mises stress (psi) in concrete (Panel 2) at the end of simulation (10 seconds): (a) top concrete view, and (b) bottom concrete view

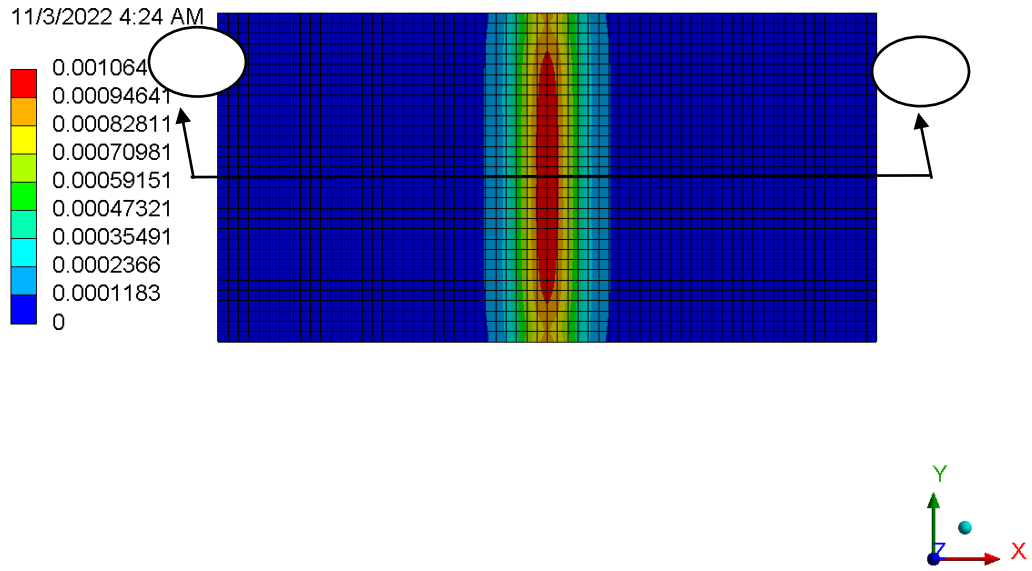

(a)

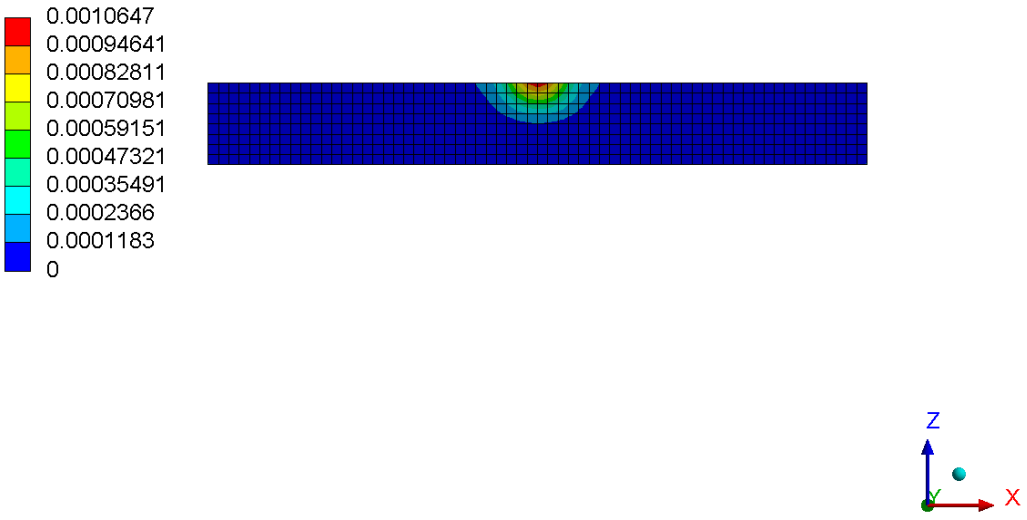

(b)

Figure 5.30 Equivalent plastic strain (strain unit) in concrete (Panel 2) at the end of simulation (10 seconds): (a) top concrete view, and (b) concrete cross section A

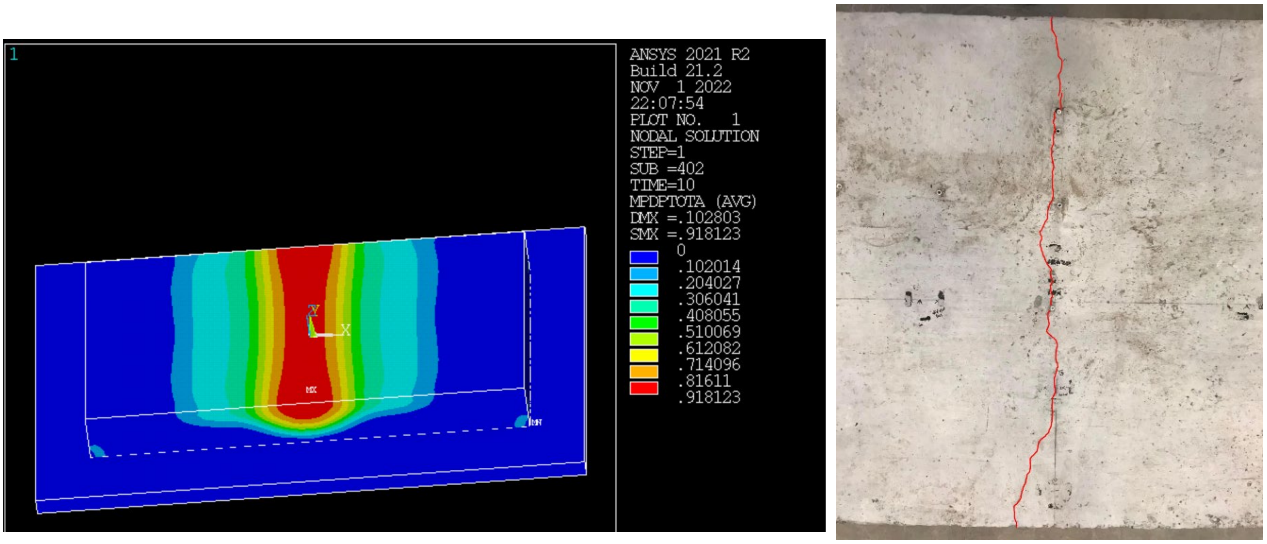
1
ANSYS 2021 R2
Build 21.2
NOV 1 2022
22:07:54
PLOT NO. 1
NODAL SOLUTION
STEP=1
SUB =402
TIME=10
MPDPTOTA (AVG)
DMX =.102803
SMX =.918123
0
.102014
.204027
.306041
.408055
.510069
.612082
.714096
.81611
.918123

(a)

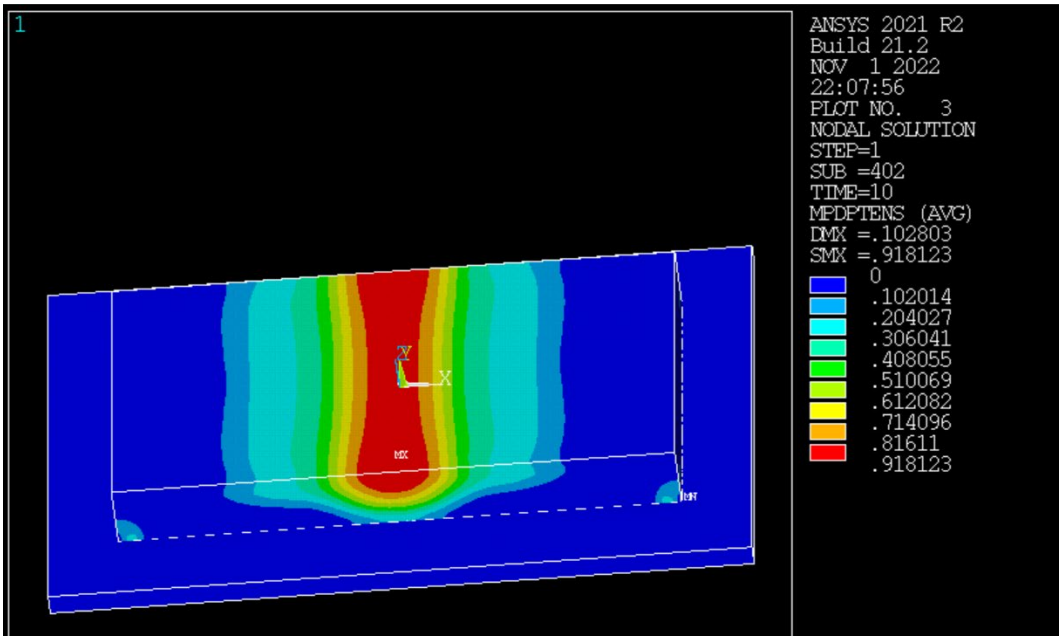
1
ANSYS 2021 R2
Build 21.2
NOV 1 2022
22:07:56
PLOT NO. 3
NODAL SOLUTION
STEP=1
SUB =402
TIME=10
MPDPTENS (AVG)
DMX =.102803
SMX =.918123
0
.102014
.204027
.306041
.408055
.510069
.612082
.714096
.81611
.918123

(b)

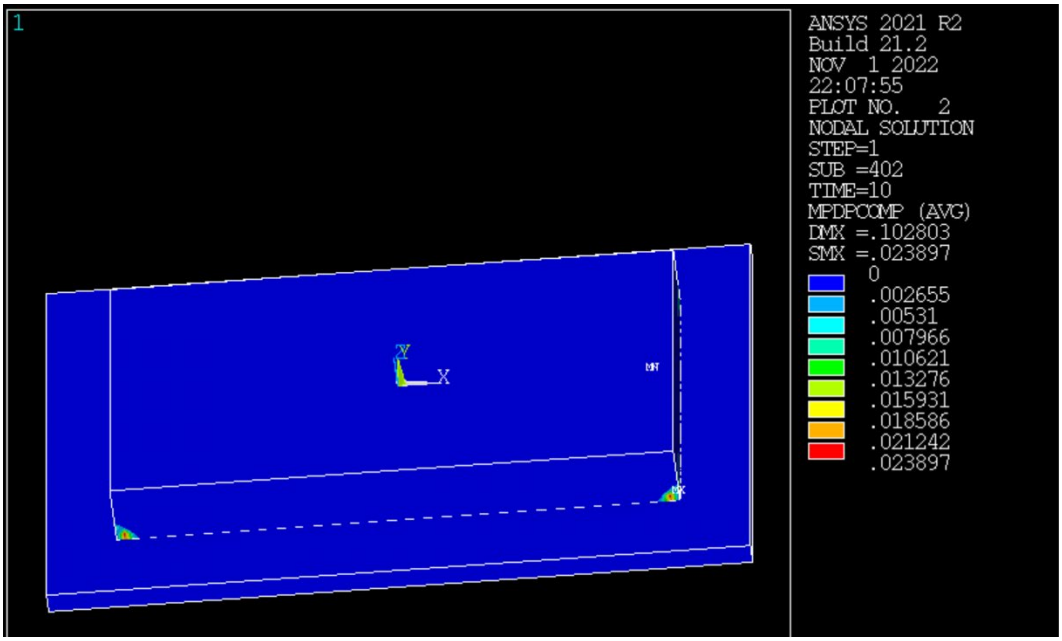

(c)

Figure 5.31 Concrete damage profiles at the end of simulation (Panel 2): (a) total damage profile, (b) tensile damage profile, and (c) compressive damage profile

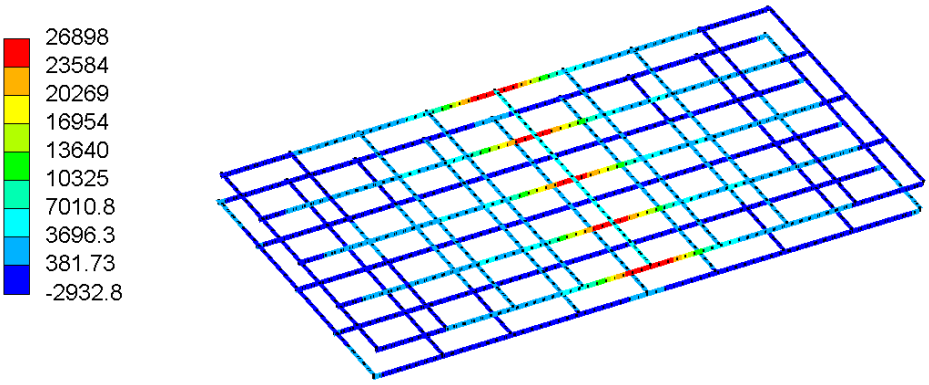
26898
23584
20269
16954
13640
10325
7010.8
3696.3
381.73
-2932.8
Z
Y
X

(a)

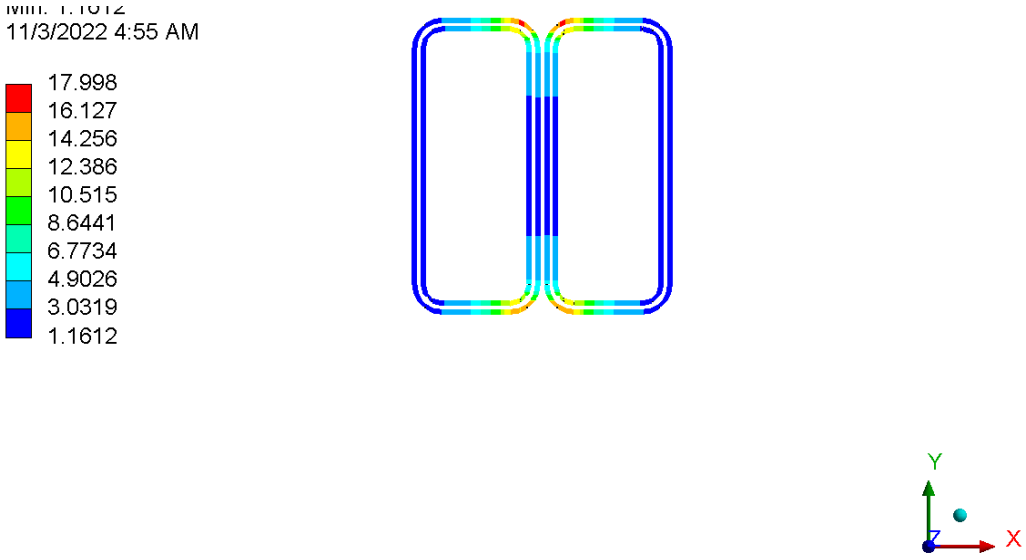
11/3/2022 4:55 AM
17.998
16.127
14.256
12.386
10.515
8.6441
6.7734
4.9026
3.0319
1.1612
Y
X

(b)

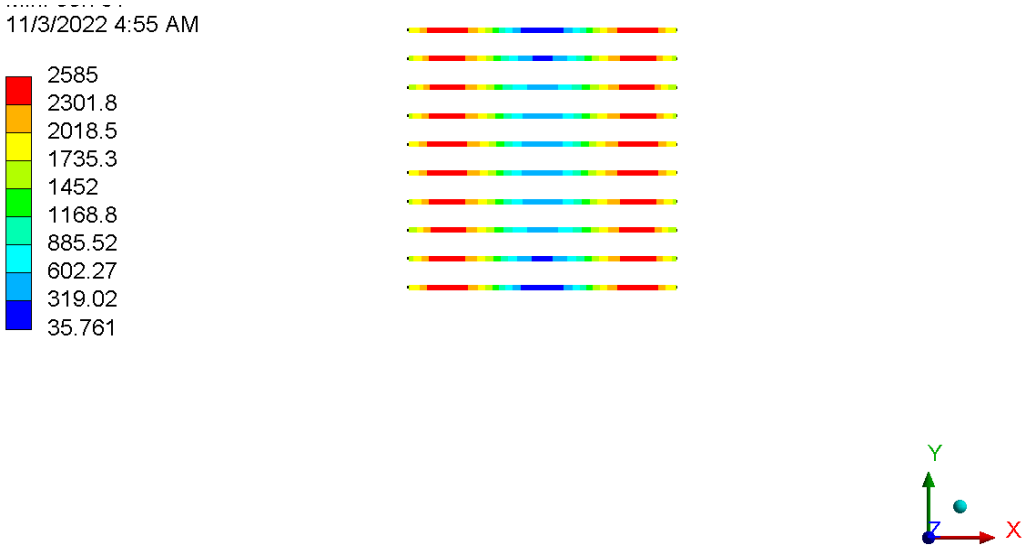

(c)

Figure 5.32 Normal stress (psi) in IPT components at horizontal x direction at the end of simulation: (a) rebar, (b) Litz wire, and (c) ferrite bar

5.3 Validation of Ultimate Capacity for Electrified Concrete Pavement Panel

5.3.1 Load Carrying Capacity

Load carrying capacity for the EPCPs referred to the maximum load under the applied load, which gradually increased until the structure collapsed. In the FEA results, as shown in Figure 5.33 and Figure 5.34, the sum of displacement and fixed support reactions was the total reaction force or maximum failure load for the panels.

Panel 1

Figure 5.33 presents the total reaction force versus the maximum vertical z displacement at the center of the Panel 1 for concrete material from the FEA model. The load-limit analysis determined the result from a loss of numerical convergence with the load/displacement curve. The maximum load of approximately 49,100 lbs. before structural failure was determined from the curve. The maximum deflection of 0.0362 in. was investigated during the load limit.

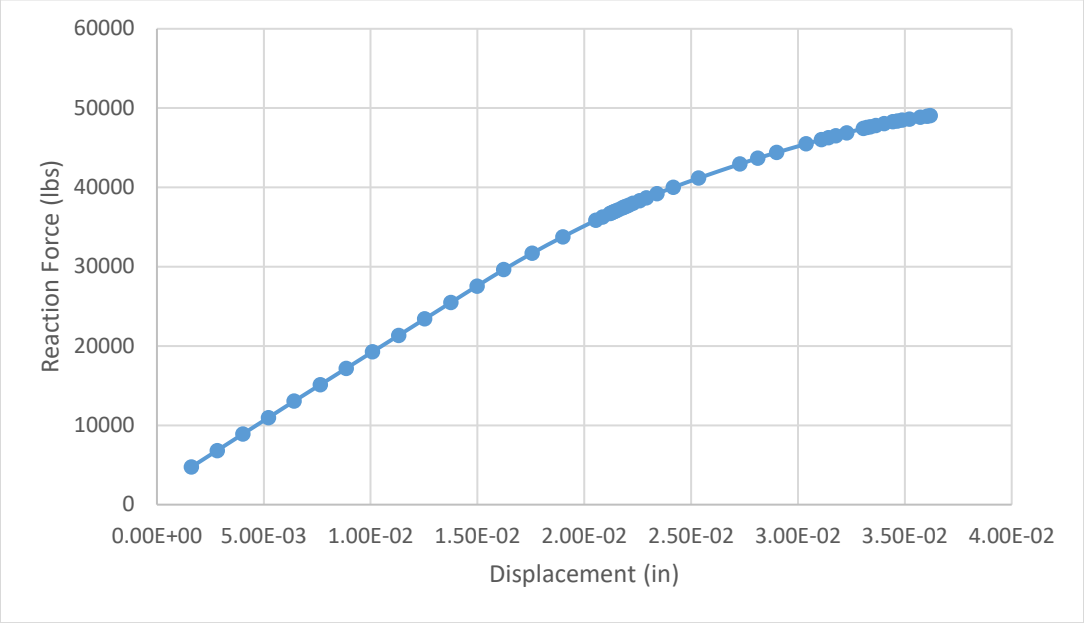

Figure 5.33 Reaction force vs. maximum vertical displacement at the center of Panel 1

Panel 2

The total reaction force versus the maximum vertical z displacement for concrete at the center of the Panel 2 is presented in Figure 5.34 from the FEA model. The maximum failure load of approximately 44,800 lbs. was obtained from the curve. The maximum deflection of 0.0287 in. was determined during the load-limit analysis.

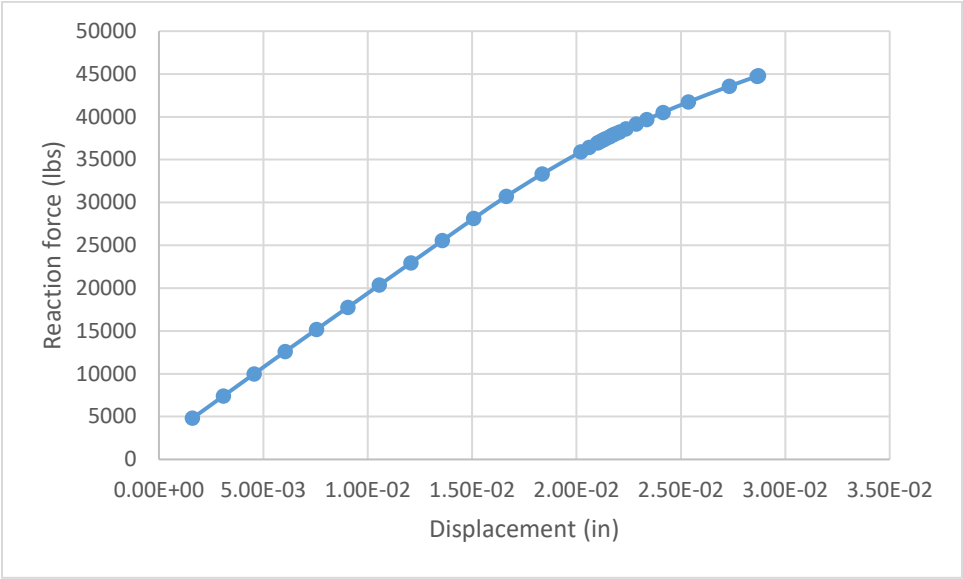

Figure 5.34 Reaction force vs. maximum vertical displacement at the center of Panel 2

The values of the maximum punching shear failure load from the experiment and FEA model are shown in Table 5.5. For Panel 1, the FEA model load limit was lower than the experiment by 4.7%, which could be from toughening mechanisms at the crack faces increasing the failures of the panel before the structure failed. The FEA did not have enough mechanisms compared with the reality. The strength of Panels 1 and 2 from the experiment and ANSYS was in good agreement with acceptable percentage of discrepancy.

Table 5.5 Load limit from experiment and FEA model

Panel	Load limit from experiment (lbs.)	Load limit from FEA model (lbs.)	% Discrepancy
Panel 1	51,475	49,062	4.7
Panel 2	43,730	44,792	2.4

5.3.2 Crack Pattern

For the center point loading test on the panels, the tension face occurred at the bottom (the coil location), and the compression face at the top. Therefore, the fracture started from the bottom in the tensile area.

Panel 1

As presented in Figure 5.35 and Figure 5.36, the crack pattern, at both two side views, from the center point loading test is presented as a red line. The blue line of cracking occurred before from the previous fatigue test. Both sides of the cracking had similar propagations. At the side view, the first cracking was aligned directly under the applied center pressure load. The existing cracking at the center from the fatigue test was larger. The panel then broke apart at the edge of the IPT system location. The failure load was 51,500 lbs. At the top face of the panel, the cracks were distributed around the center of the panel [Figure 5.37 (b)]. The experimental and numerical crack patterns were in good agreement. The fracture location in tension face was within the loading pressure area of an 18-in. width. Many cracks propagated in the center area. The cracks then spread out to the edges in a longitudinal direction.

Figure 5.35 Crack pattern at the front side for Panel 1

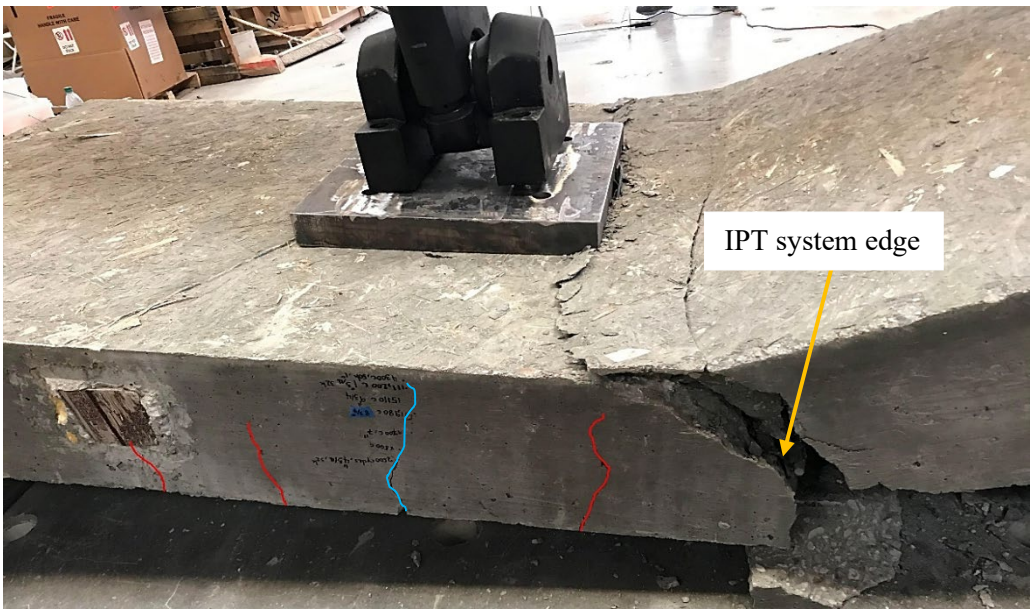

Figure 5.36 Crack pattern at the back side for Panel 1

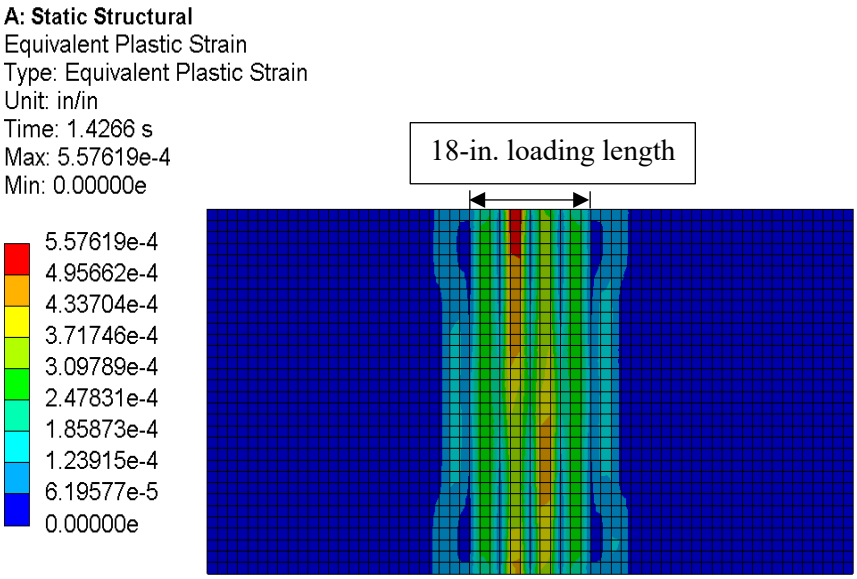

(a)

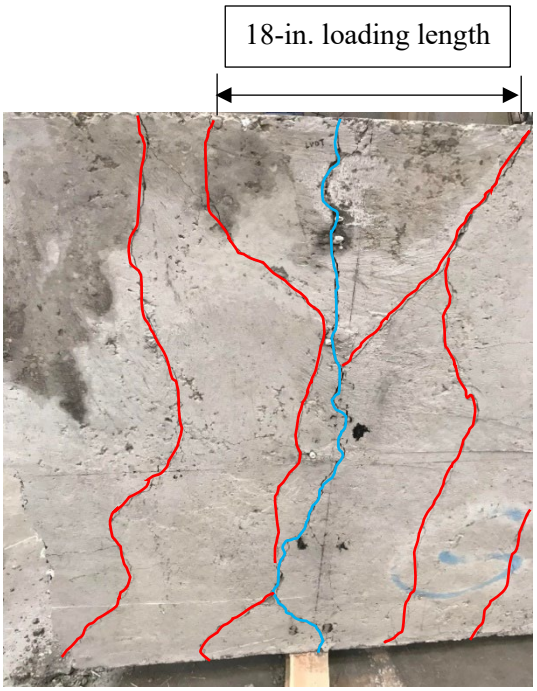

(b)

Figure 5.37 Numerical and experimental crack pattern at the top face for Panel 1: (a) equivalent plastic strains concrete at ultimate limit load, and (b) experimental cracking

Panel 2

Figure 5.37 shows a similar crack formation in the cracking at the side on both front and back views. The blue line cracks were from a previous fatigue load experiment. The first crack was located under the two edges of the center pressure load. At the failure, the panel broke apart at the edge of the IPT system. The maximum load at failure was 43,700 lbs. In Figure 5.40 (b), the fracture happened outside the 18 in. loading length area by 1.5 in. to 3.5 in. The two cracks ran across the panel around the edges of the pressure load area. Also, the center point loading test caused the existing cracking (blue line) to open larger. As seen in Figure 5.40, the experimental crack pattern was consistent with the modeling result. The two cracks then propagated to the edges in a longitudinal direction.

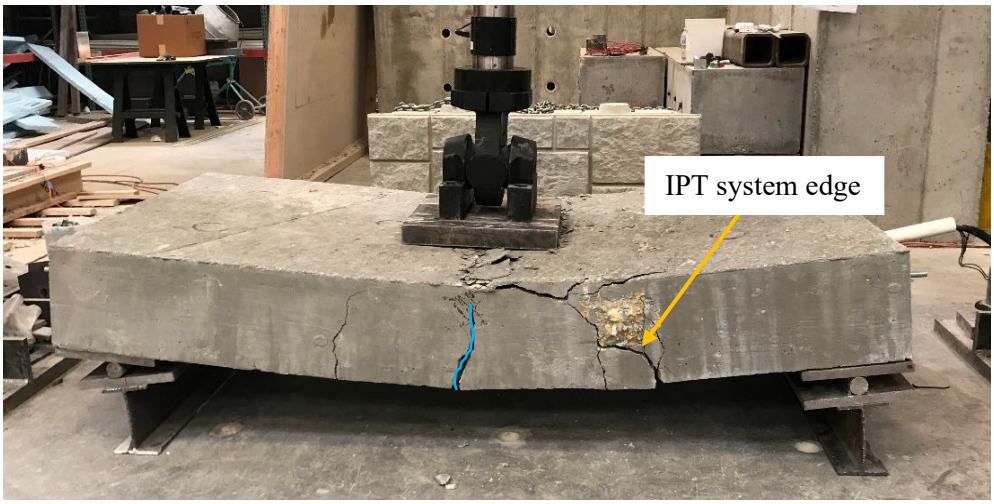

Figure 5.38 Crack pattern at the front side for Panel 2

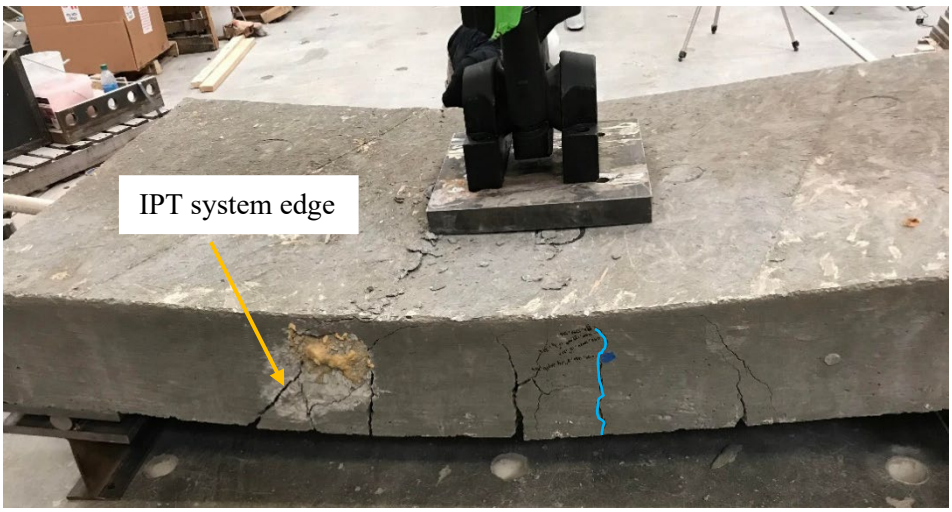

Figure 5.39 Crack pattern at the back side for Panel 2

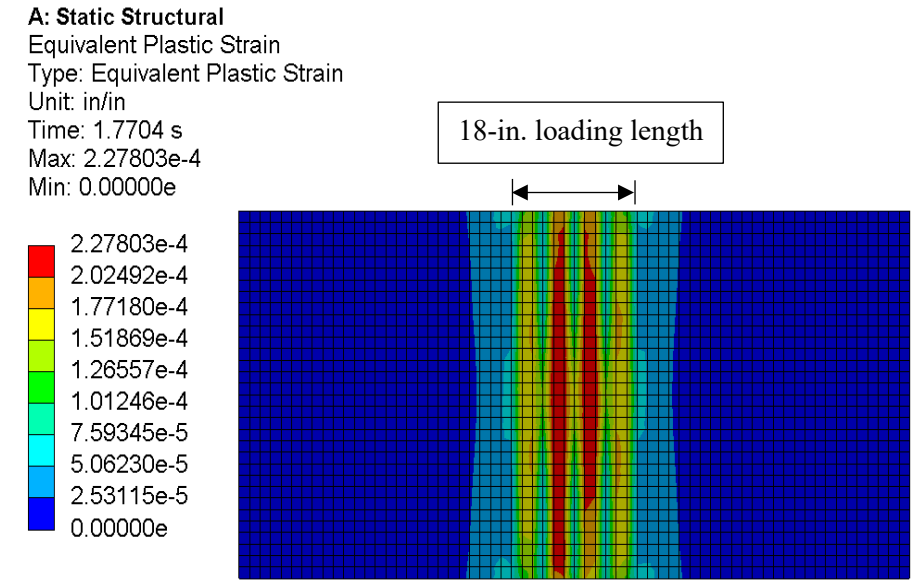

(a)

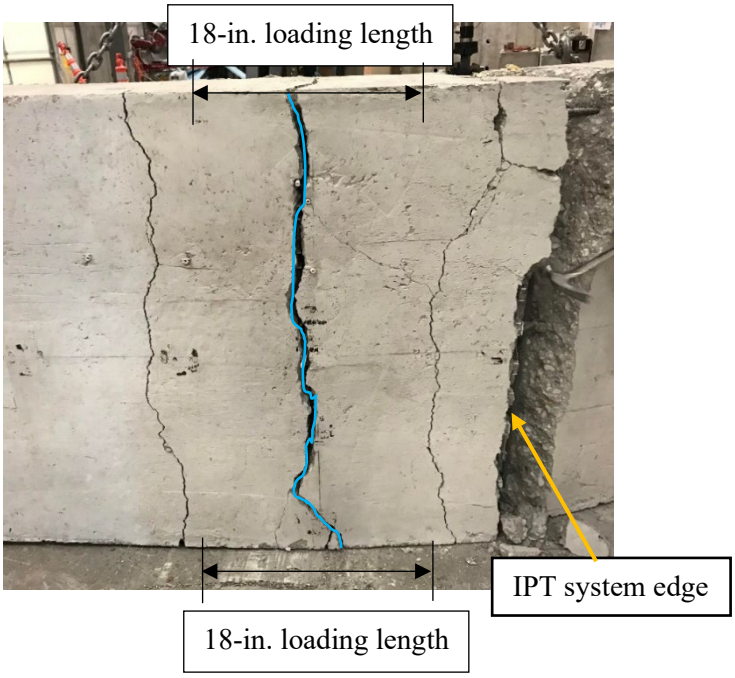

(b)

Figure 5.40 Numerical and experimental crack pattern of Panel 2: (a) equivalent plastic strains concrete at ultimate limit load, and (b) experimental cracking

5.4 Additional FEA Results for Full-Size Electrified Concrete Pavement

5.4.1 Panel 1

In Figure 5.41, the maximum displacement at the ultimate limit load at the mid-span was 22 times larger than the at-rest deflection state. From the FEA model, the maximum displacement (in the vertical z direction) took place at the center, corresponding with the experiment.

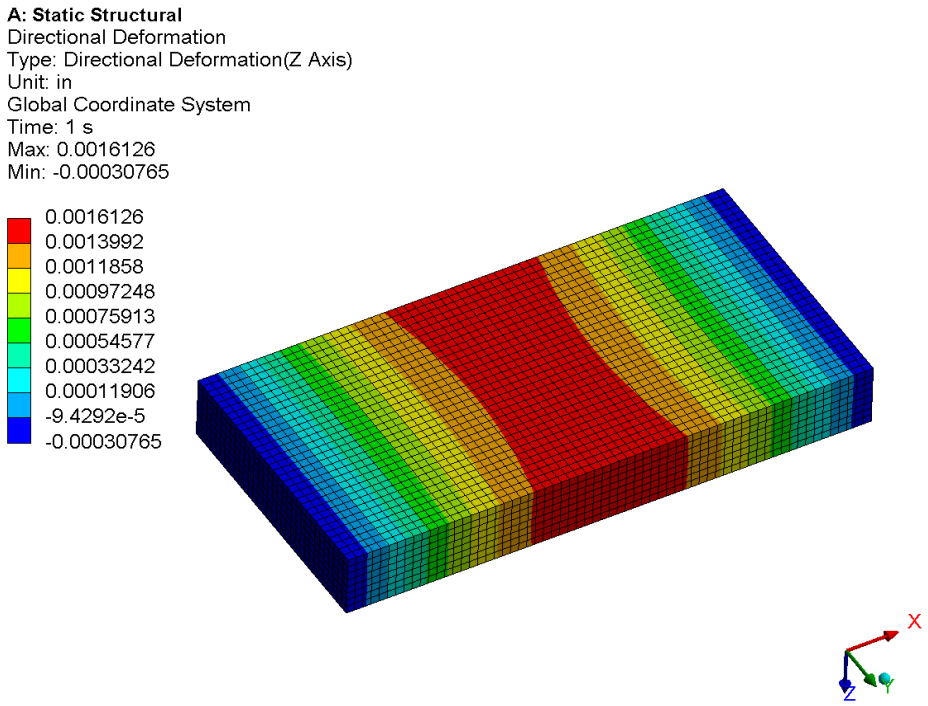

(a)

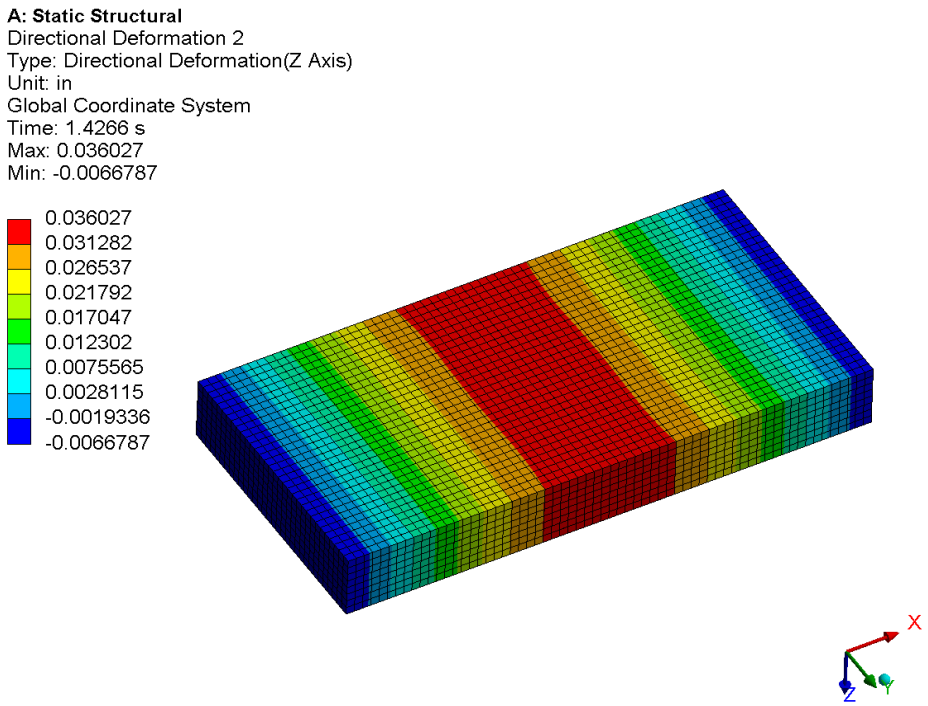

(b)

Figure 5.41 Vertical displacement of Panel 1: (a) after applying dead load, and (b) ultimate limit load

Figure 5.42 and Figure 5.43 demonstrate the stress in the horizontal x and y direction in the concrete material, respectively. The most critical tensile stresses occurred in the horizontal x direction, which predicted the longitudinal cracking perpendicular to the x axis, as indicated by the equivalent plastic strain. The large tensile stresses occurred at the top face of the panel.

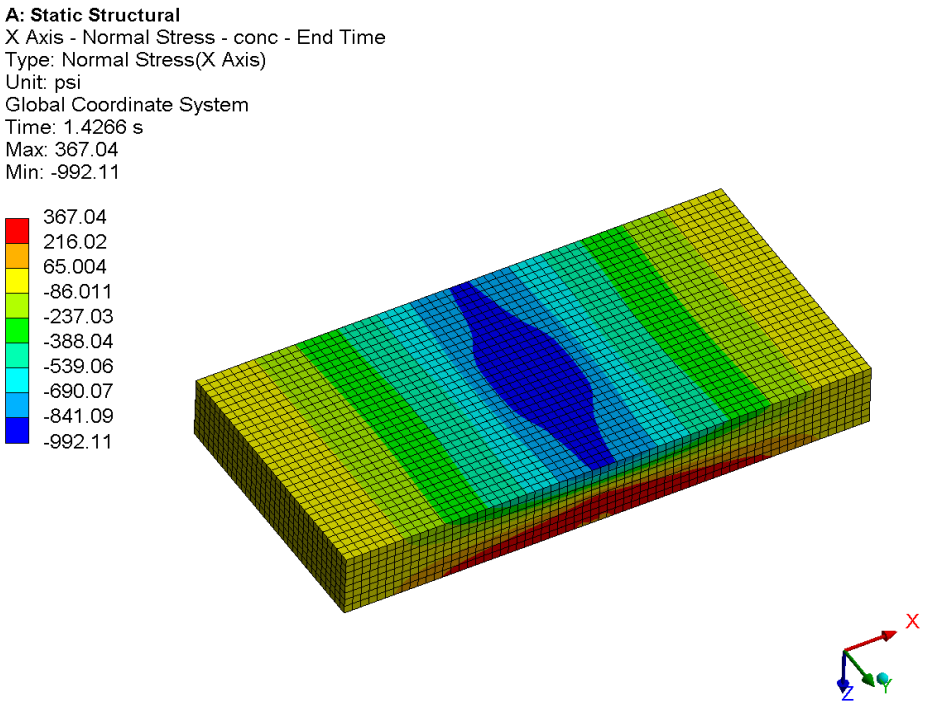

(a)

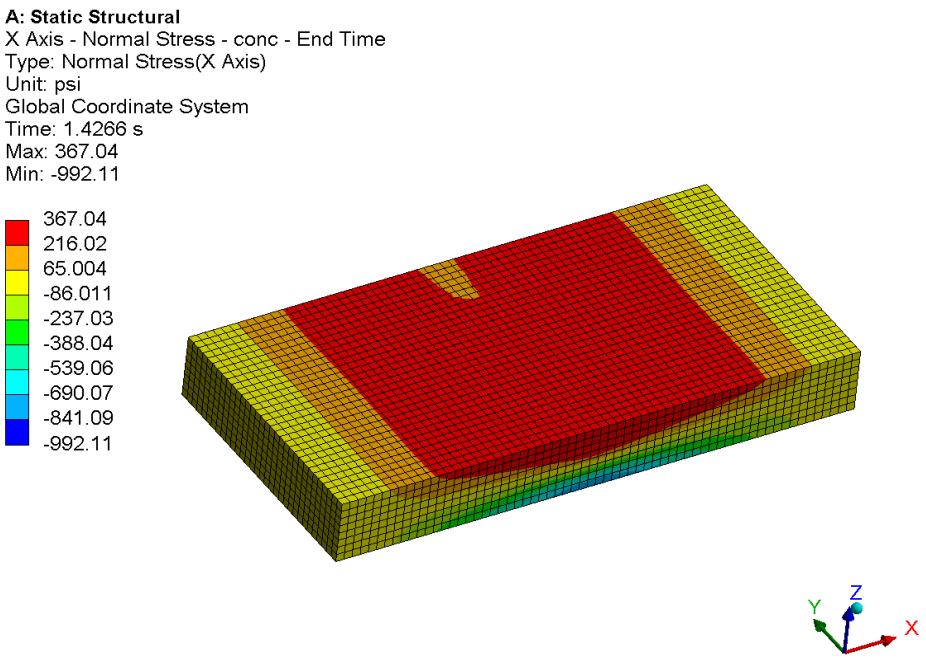

(b)

Figure 5.42 Stress component (SX) concrete of Panel 1 at ultimate limit load: (a) bottom face view, and (b) top face view

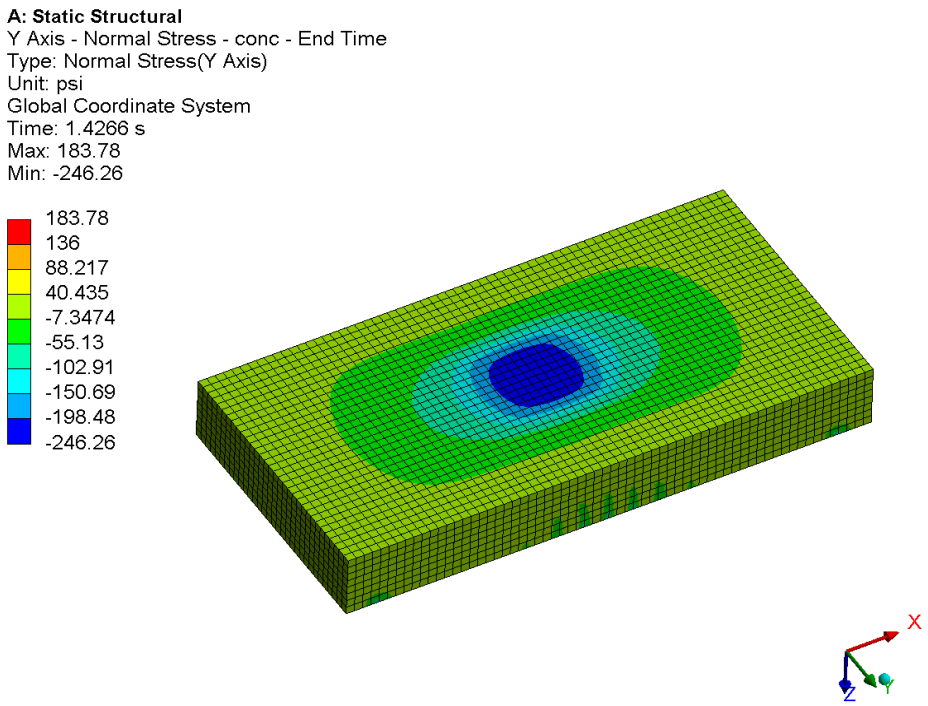

(a)

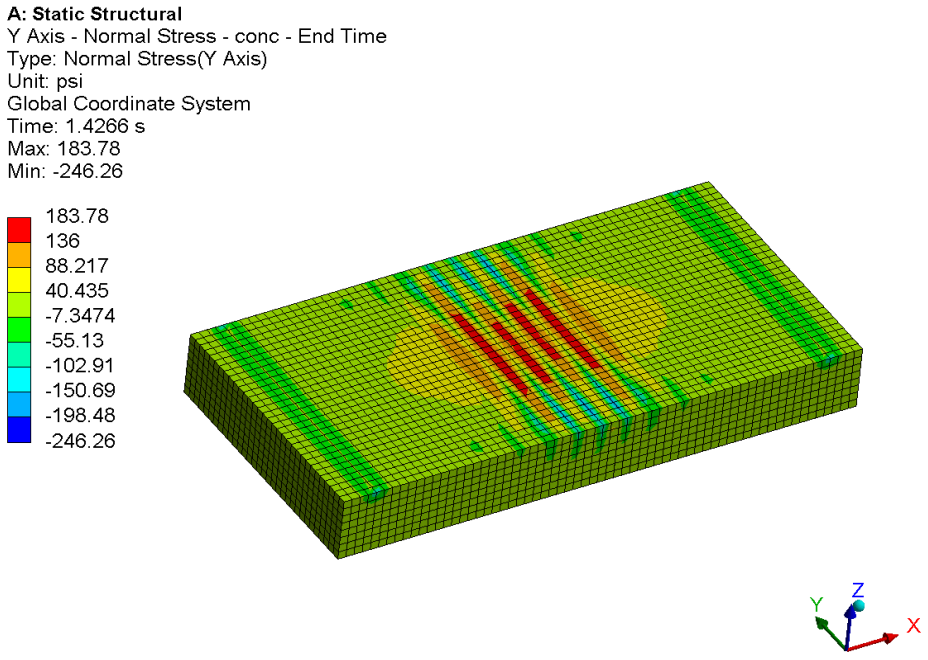

(b)

Figure 5.43 Stress component (SY) concrete of Panel 1 at ultimate limit load: (a) bottom face view, and (b) top face view

The reinforcement carried the ultimate failure load, but the tensile stress (SX) in the GFPR rebar of 1,716 psi was still lower than the yield strength (88,000 psi), as shown in Figure 5.44. The high level of compressive stresses was found at the center of the ferrite area that caused the damage, as presented in Figure 5.45.

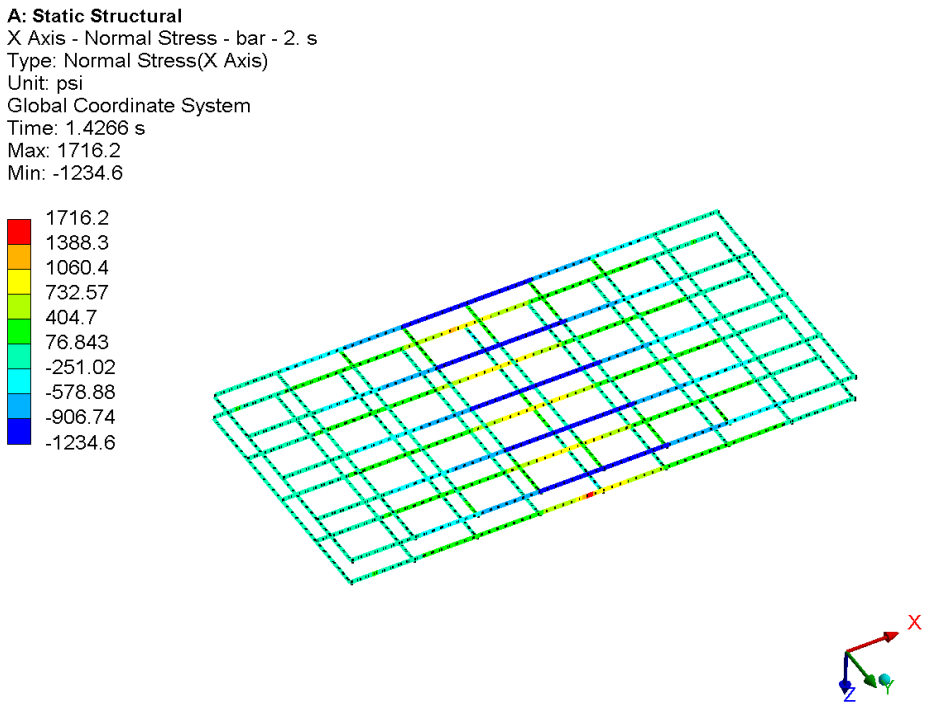

Figure 5.44 Stress component (SX) reinforcement of Panel 1 at ultimate limit load

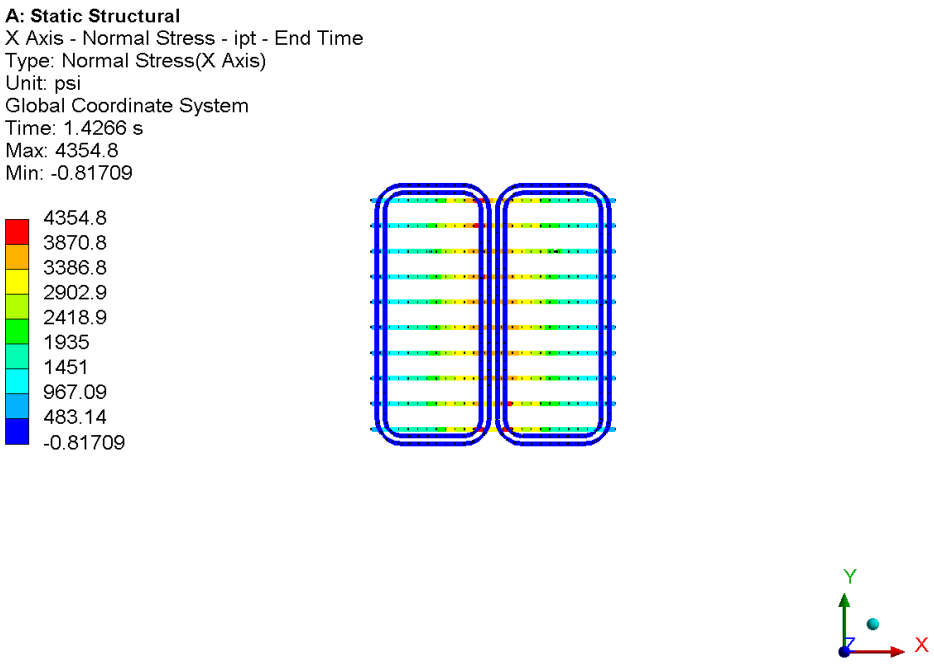

Figure 5.45 Stress component (SX) IPT system of Panel 1 at ultimate limit load

5.4.2 Panel 2

In Figure 5.46, the maximum displacement at the ultimate limit load at mid-span was 18 times larger than the at-rest deformation state. From the FEA model, the maximum displacement (in z direction) happened at the center, corresponding with the experiment.

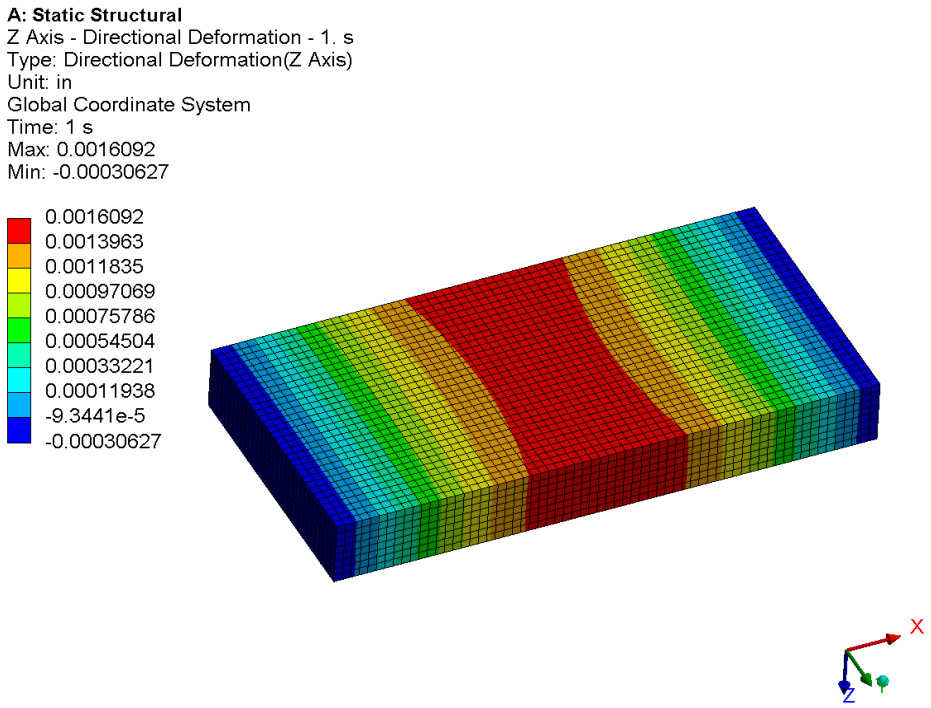

(a)

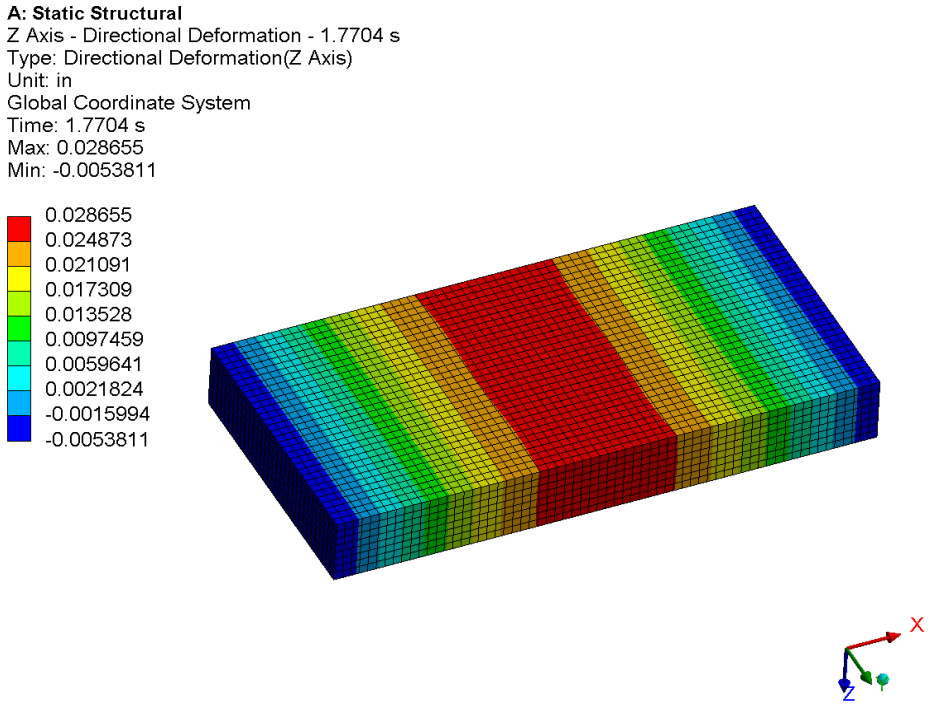

(b)

Figure 5.46 Vertical displacement of Panel 2: (a) after applying dead load, and (b) ultimate limit load

The stresses in the horizontal x and y directions in the concrete material are presented in Figure 5.47 and Figure 5.48, respectively. The high-level tensile stresses were from the horizontal x direction like Panel 1, corresponding to the equivalent plastic strain. Panel 2 carried compressive stresses (793 psi) at the bottom face that were larger than Panel 1. The large tensile stresses were found at the top face of the panel.

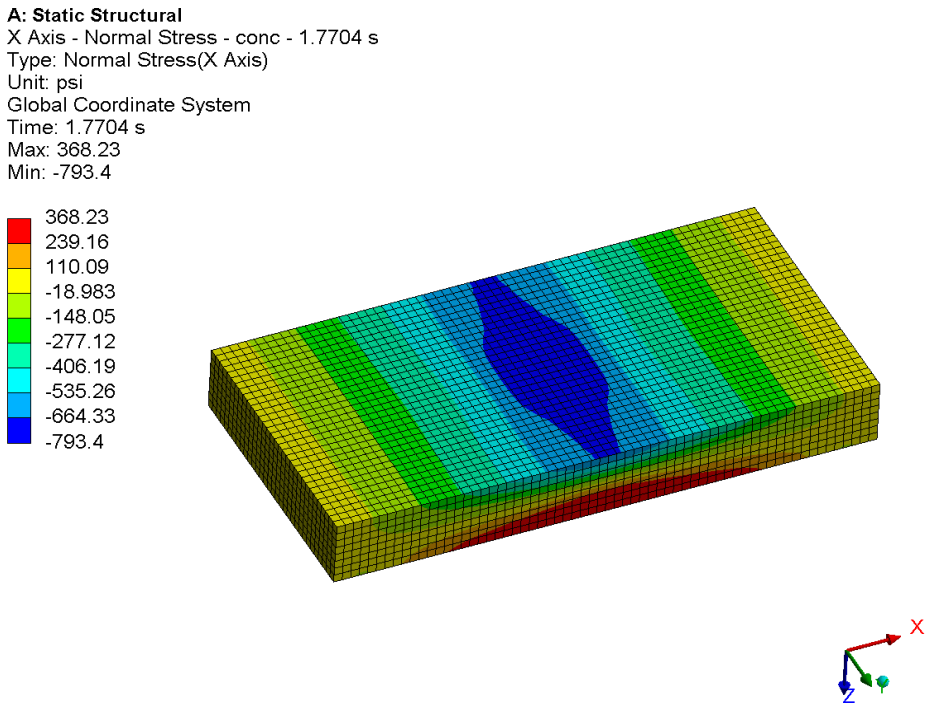

(a)

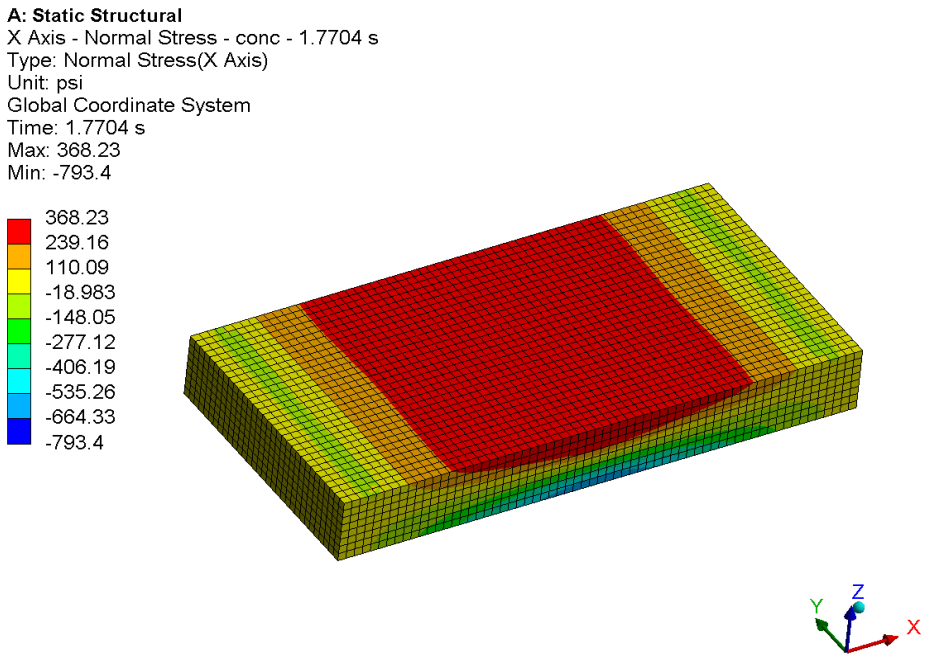

(b)

Figure 5.47 Stress component (SX) concrete of Panel 2 at ultimate limit load: (a) bottom face view, and (b) top face view

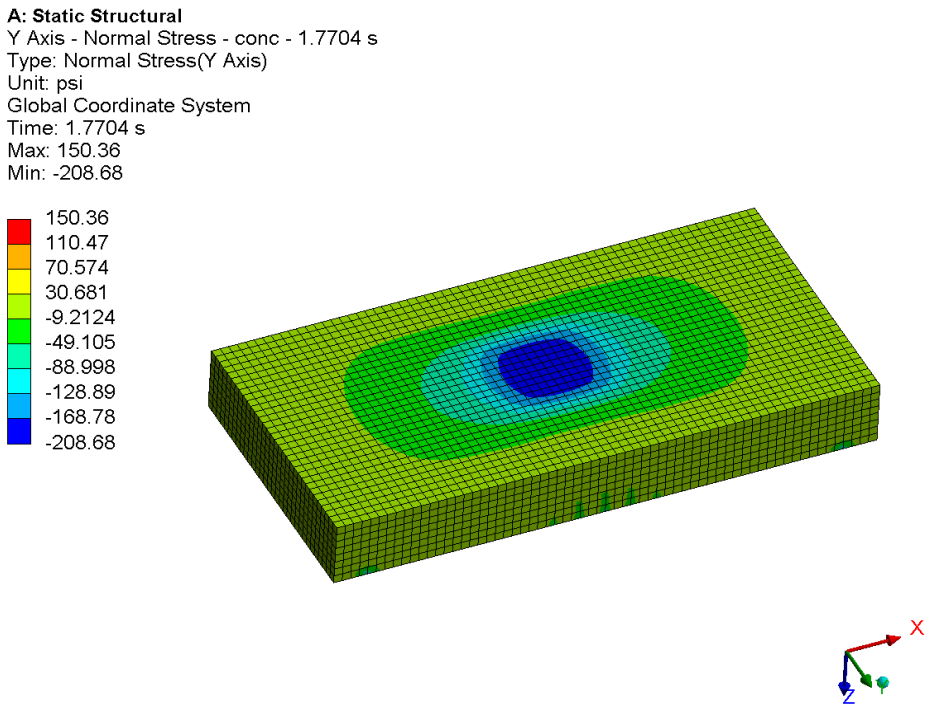

(a)

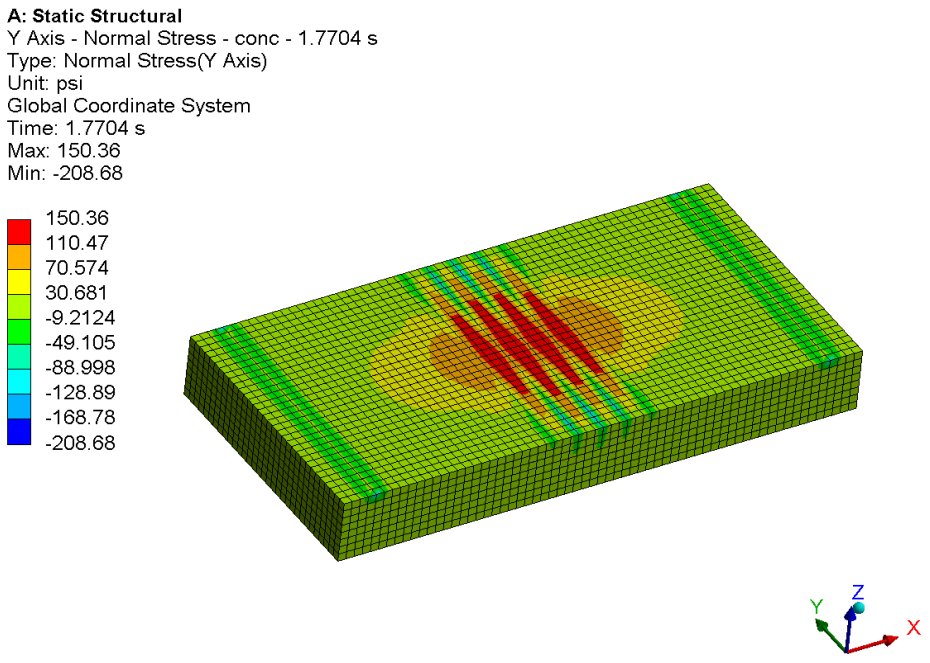

(b)

Figure 5.48 Stress component (SY) concrete of Panel 2 at ultimate limit load: (a) bottom face view, and (b) top face view

The steel reinforcement supported the maximum load, but the tensile stress (SX) in the rebar of 2,450 psi did not exceed the yield strength (40,000 psi), as shown in Figure 5.49. At the ultimate limit load, the high-level compressive stresses occurred at the center of the ferrite area that resulted in the damage, as seen in Figure 5.50.

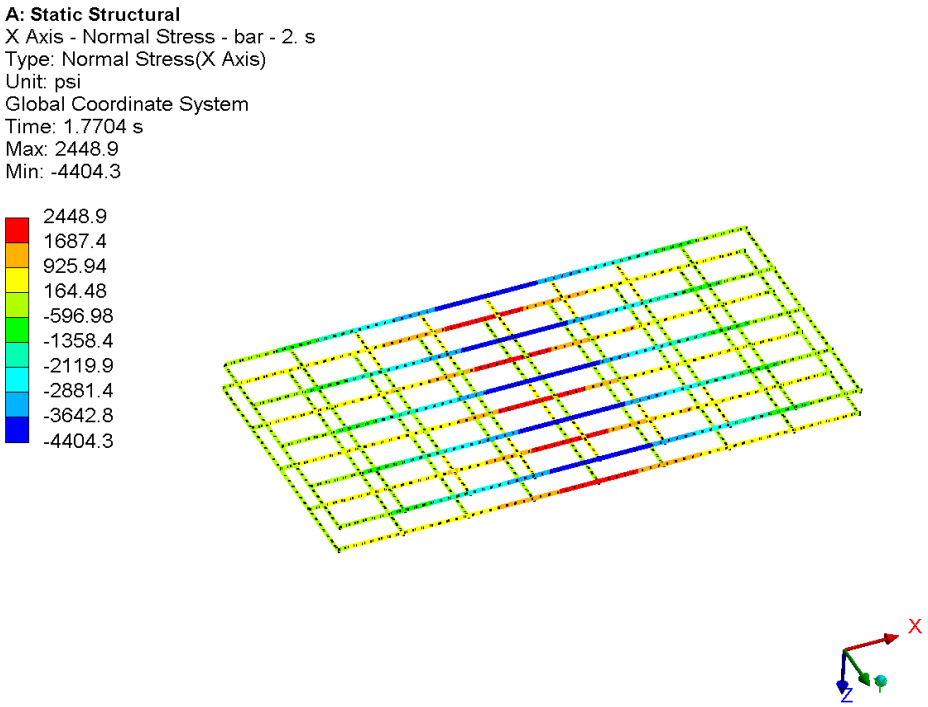

Figure 5.49 Stress component (SX) reinforcement of Panel 2 at ultimate limit load

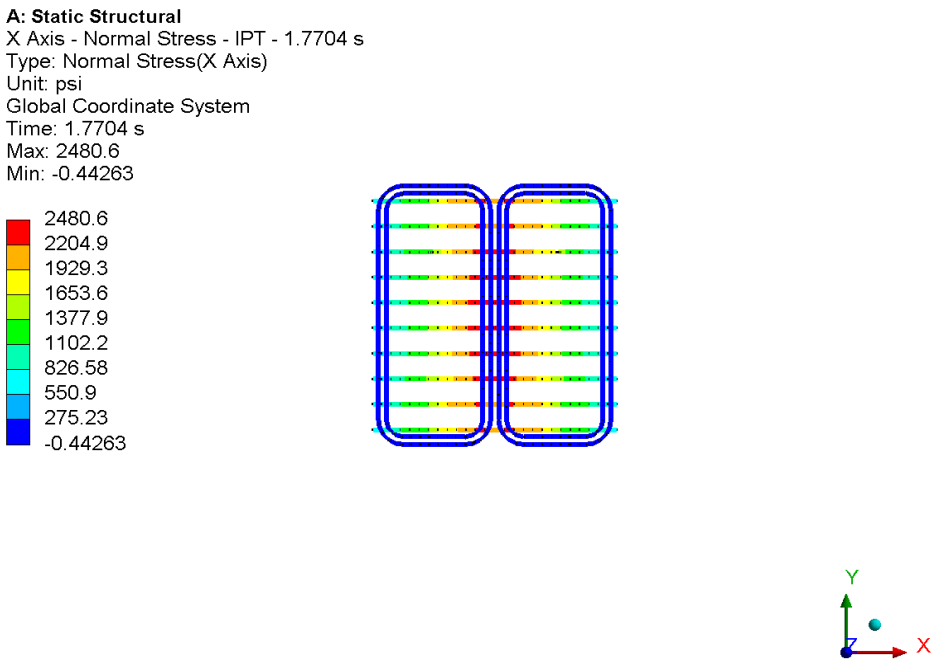

Figure 5.50 Stress component (SX) IPT system of Panel 2 at ultimate limit load

5.5 Discussion

This section discusses the comparison between experimental and modeling results. The FEA models were validated with the testing result. Thus, concrete stiffness and internal heat generation in the models were adjusted to provide reasonable results.

In the heat transfer analysis, T2, T1, and T3 temperature gauges measured the heat at the centerline area of the double-D coil. For Panel 1, the highest temperature (T2) was 23°C in the model and 26°C in the test when the panel was powered for 68 minutes. For Panel 3, the highest temperature (T1) was 38°C after running the coil for two hours in both the experiment and model. Therefore, the temperature of the model was consistent with the experiment. However, Panel 2 had uncertainty due to the power loss caused by the steel reinforcement. Even though the panel was powered for only 37 minutes, the highest temperature at the wire area increased by 30°C in the experiment.

To correct the model result in ANSYS, the heat generation of the Litz wire was increased by 40% compared with the heat load in Panels 1 and 3. The thermal strain in the concrete came from the heat load of the coil. The high-level thermal strain in the concrete was located under the centerline of the coil (4.5 in. below the top surface). The strain readings of 300 με (SI2, Panel 1) and 300 με (SI3, Panel 3) confirmed the critical thermal strain location. The strain results in the experiment agreed with the strain in ANSYS.

For Panel 2, the steel rebar interfered with the coil and affected the result in the strain measurement in the experiment. For all three panels, the large tensile stresses from FEA model were in the horizontal y direction, which led to concrete fracture.

In fatigue analysis, the maximum tensile strain for Panel 1 was 220 με. In the experiment, the crack initiation occurred at 1,100 cycles at the edges along the mid-span. The crack propagated across the whole slab edge-to-edge in a longitudinal direction at 2,800 cycles. For Panel 2, the initial cracking occurred at the center along the mid-span of the panel at two cycles. Then the crack widened quickly at 21 cycles by running edge-to-edge in a longitudinal direction. From the FEA model, the large tensile stress resulted in crack deformation as indicated by the plastic strain. The crack patterns for Panels 1 and 2 were consistent with the plasticity and damage results. The longitudinal cracking running edge-to-edge occurred in both panels.

In the ultimate strength test, the GFRP reinforcement in Panel 1 had a load limit of 49,100 lbs. for the simulation and 51,500 lbs. for the experiment. For Panel 2, steel rebar was used. The steel rebar had a strength of 44,800 lbs. for the modeling and 43,700 lbs. for the physical test. The crack pattern in the experiment agreed with the FEA model.

6. CONCLUSION

This research project investigated the durability of wireless charging concrete pavement based on three types of analyses:

1. Transient thermal analysis dependent upon the IPT running time
2. Structural analysis under cyclic load from heavy traffic
3. Structural analysis under monotonic loading for ultimate panel flexural capacity

Experiments on electrified precast concrete pavement (EPCP) were conducted to determine mechanical behavior, IPT power loss, and thermal management satisfaction. The EPCP construction cost was also taken into consideration. The FEA program was required to accurately predict the structural behavior. The modeling was able to effectively replicate the experimental behavior.

Based on the thermal analysis of the heat generated by IPT, the following conclusions were drawn:

1. The thermal strains in the concrete for one hour or two hours of continuous coil operation did not cause observable damage to the structure.
2. Steel rebar reinforcement, located under the inductive coils, caused increased power losses because the metal interfered with the IPT system.
3. Panels 1, 2, and 3 had the maximum thermal strain of 464 με, 409 με, and 528 με, respectively. The strain was located 3 inches below the concrete top surface at the centerline of double D coil area in the FEA model (Table 6.1). For maximum tensile stress in those three panels (Table 6.1), the high-level stresses in the concrete occurred in the horizontal x direction at the top surface (middle of the panels), resulting in longitudinal cracking (the direction of vehicle travel).

Table 6.1 Maximum thermal strain and tensile stress in concrete

Panel	Configuration	Modeling maximum thermal strain (με)	Modeling maximum tensile stress (psi)
1	GFRP with PCM	464	853
2	Steel	409	757
3	GFRP	528	894

4. According to similar experimental thermal strain data in the concrete, 300 με occurred in Panel 1 (PCM) after the coil operated for 68 minutes. For Panel 3 (Non-PCM), 310 με occurred after the coil operated for 120 minutes. Thus, the coils in those panels needed to be powered for longer than two hours until PCM melted to see the temperature reduction from having PCM.

Repetitive heavy truck loads were applied to Panels 1 and 2. The endurance limit of brittle material like concrete was subjected to the tensile strength, which was 370 psi. The fatigue failure of concrete material was caused by microcracks or brittle failure. The conclusions are drawn as follows:

5. From the measured strain in Panel 1, the cyclic tensile strains under cyclic load were concentrated in the horizontal x direction, leading to longitudinal cracking. The initial cracks formed at the edges mid-span and then propagated to the center of the panel. The experimental result agreed with the FEA model's total damage of the crack pattern. The cracks extended across the entire panel at 2,800 cycles with an average cyclic strain (ε_{avg}) of 220 με. The cyclic strain at failure was converted to stress from equation ($\sigma = E \times \varepsilon = 3x10^6$ psi x 220 x 10^{-6} ε), which was equal to 660 psi. Therefore, the cyclic stress (660 psi) exceeded the endurance limit of 370 psi, resulting in concrete fracture. In modeling, the damage result (microcracks) agreed with the initial cracking in the test at 1,100 cycles.

6. For Panel 2, the tensile cracking began in the center and spread toward edge-to-edge in a longitudinal direction like Panel 1. The experiment's cracking confirmed the crack pattern from the damage and plasticity modeling result. The cracking for Panel 2 ran across the whole slab at 21 cycles with the cyclic strain of 286 με (converting to 858 psi for cyclic tensile stress), exceeding the concrete endurance limit.

The ultimate loading test used the center point loading method to determine the maximum load of the EPCPs. When the structure collapsed, the following outcomes were observed:

7. From the experiment, Panel 1 (reinforced with GFRP) had a flexural load capacity of 51,500 lbs., while Panel 2 (steel rebar) had a strength of 43,700 lbs. There was a 15% difference. The modeling and experimental results agreed.
8. Regarding the crack pattern, the GFRP panel performed well under the applied load by gradually distributing the concrete cracking at the tension face. For steel rebar Panel 2, the cracking did not spread that much. The structure failed due to steel rupture with the two extensive cracks. The fracture of the GFRP panel happened within the 18-in. loading length area, while the steel rebar panel had the fracture outside the loading area.

As a result, Panel 2 with steel reinforcement had lower cycle fatigue than Panel 1 with GFRP reinforcement. Placement of the reinforcement below the IPT could be the cause of early severe concrete fatigue failure of the two panels. The placement of the reinforcement mat decreased the load-carrying capacity of the concrete pavement. This issue needs to be addressed to improve the design of the electrified pavement in the future.

Future research should consider using strengthening material to reinforce the concrete above the IPT system to allow the structure to effectively resist damage. The steel material needs to be eliminated from the electrified concrete pavement panels because it disturbs the magnetic field in the EV battery charging. Additional experimental work should be done on a load combination between the IPT system's thermal and traffic wheel loads. The electrified panels should be installed on the test track to get powered in the IPT while the heavy traffic vehicle moves on the panels.

In this work, the strain and temperature data from sensors embedded in any critical spots could examine the impact of this load combination on the panels in the real situation on the roadway. Moreover, the experimental results will be used to develop the FEA model subjected to this load combination to study the mechanical behavior throughout the entire structure.

7. REFERENCES

Abdualla, H. 2018 “Design, construction, and performance of heated concrete pavements system.” Iowa State University, Digital Repository, 10.31274/etd-180810-5899.

Al-Qadi, I. L., H. Wang, P. J. Yoo, and S. H. Dessouky. 2008. “Dynamic analysis and in situ validation of perpetual pavement response to vehicular loading.” *Transportation Research Record*. 2087 (1): 29–39. https://doi.org/10.3141/2087-04.

American Concrete Institute (ACI). 2001. “Control of cracking in concrete structures.” *ACI 224R-01*, Farmington Hills, MI.

American Concrete Institute (ACI). 2007. “Thermal and volume change effects on cracking of mass concrete.” *ACI207.2R-07*, Farmington Hills, MI.

American Concrete Institute (ACI). 2015. “Guide for the design and construction of concrete reinforced with FRP bars.” *ACI 440.1R-15,* Farmington Hills, MI.

American Society of Heating, Refrigeration and Air-Conditioning Engineer, Inc. (ASHRAE). 2015. *ASHRAE Handbook - HVAC Applications American Society of Heating*, Atlanta, GA, ASHRAE, Snow Melting and Freeze Protection, pp. 51.1–51.20.

ASTM C39. (2012). Standard test method for compressive strength of cylindrical concrete specimens. ASTM C39/C39M-12.

ASTM C469. (2014). Standard Test Method for Static Modulus of Elasticity and Poisson’s Ratio of Concrete in Compression. https://doi.org/10.1520/C0469_C0469M-14

ANSYS, Inc. Products 2021 R2.

American Association of State Highway and Transportation Officials (AASHTO LRFD bridge design specifications). 2021. Washington, D.C.

American Society for Testing and Materials (ASTM C293/C293M-10). 2010. “Standard test method for flexural strength of concrete (using simple beam with center-point loading).” *Annual Book of ASTM Standards*, 04(02):3

Barnes, Arden N. 2020, “Thermal Modeling and Analysis of Roadway Embedded Wireless Power Transfer Modules.” All Graduate Theses and Dissertations. 7808. https://digitalcommons.usu.edu/etd/7808

Bazant, Z. P., and P.G. Gambarova. 1984. “Crack Shear in Concrete: Crack Band Microplane Model.” *Journal of Engineering Mechanics*, 110: 2015–2036.

Bazant, Z. P., and B. H. Oh. 1985. “Microplane Model for Progressive Fracturing.” *Journal of Structural Engineering*, 111: 559–582.

Beskou, N. D., and D. D. Theodorakopoulos. 2011. "Dynamic effects of moving loads on road pavements: A review." *Soil Dynamics and Earthquake Engineering*, 31 (4): 547–567. https://doi.org/10.1016/j.soildyn.2010.11.002.

Bolger, J. G. 1989. "Roadway power and control system for inductively coupled transportation system." US Patent 4 836 344.

Budhia, M., G. A. Covic, and J. T. Boys. 2011. "Design and Optimization of Circular Magnetic Structures for Lumped Inductive Power Transfer Systems." in *IEEE Transactions on Power Electronics*, vol. 26, 11, pp. 3096–3108.

Carmona, S., and A. Aguado. 2012, "New model for the indirect determination of the tensile stress–strain curve of concrete by means of the Brazilian test." *Materials and Structures*, 45, 1473–1485. https://doi.org/10.1617/s11527-012-9851-0

Chen, J. Q., H. Wang, M. Y. Li, and L. Li. 2016. "Evaluation of pavement responses and performance with thermal modified asphalt mixture." *Materials & Design*, 111 (Dec): 88–97. https://doi.org/10.1016/j.matdes.2016

Choi, S. Y., B. W. Gu, S. Y. Jeong, and C. T. Rim. 2015. "Advances in wireless power transfer systems for roadway-powered electric vehicles." *IEEE Journal of Emerging and Selected Topics in Power Electronics*, vol. 3, 1, pp. 18–36.

Covic, G. A., and J. T. Boys. 2013. "Inductive Power Transfer." in *Proceedings of the IEEE*, vol. 101, 6, pp. 1276–1289.

Darestani, M.Y., D. P. Thambiratnam, A. Nataatmadja, and D. Baweja. 2007. "Structural response of concrete pavements under moving truck loads." *Journal of Transportation Engineering*, 133, 670–676.

Dere, Y., A. Asgari, E. Sotelino, and G.C. Archer. 2006. "Failure prediction of skewed jointed plain concrete pavements using 3D FE analysis," *Engine Failure Analysis*,13 898–913.

Eghtesadi, M. 1990. "Inductive power transfer to an electric vehicle-an analytical model." in *Proceedings of the 40th IEEE Conference on Vehicular Technology*, pp. 100–104.

Empey, D. 1994. "Roadway Powered Electric Vehicle Project: Track Construction and Testing Program Phase 3D." California Path Program, Institute of Transportation Studies, University of California, Berkeley.

Endesa. 2015. "Endesa gives electric car batteries a second life in charging points." Accessed September 15, 2021. https://www.endesa.com/en/press/press-room/news/energy-transition/electric-mobility/endesa.

Endesa. 2019. "In Malaga, Endesa, Alstom and Mansel test a cutting-edge system for charging electric buses through a charger integrated into the ground." Accessed September 15, 2021. https://www.endesa.com/en/press/press-room/news/energy-transition/electric-mobility/in-malaga-endesa.

FAA. 2011. "Airside use of heated pavement systems," FAA Advisory Circular (AC) No: 150/5370-17. FAA, US Department of Transportation, Washington, DC.

Gardner, T. 2017. “Wireless Power Transfer Roadway Integration.” All Graduate Theses and Dissertations. 6866.

Gernay, T., A. Millard, and J.M. Franssen. 2013. “A multiaxial constitutive model for concrete in the fire situation: Theoretical formulation.” *International Journal of Solids and Structures,* 50 (22–23) 3659–3673.

Gernay, T., and J. M. Franssen. 2015. “A plastic-damage model for concrete in the fire: Applications in structural fire engineering.” *Fire Safety Journal*, 71 (2015) 268–278.

Hutin, M., and M. Leblanc. 1894. “Transformer system for electric railways.” US Patent 527 857.

INTIS. 2014. “Technical Article eCarTec 2014.” Accessed September 16, 2021. http://www.intis.de/intis/downloads_e.html.

INTIS. n.d. “Imagefolder eShips.” Accessed September 15, 2021. http://www.intis.de/intis/downloads_e.html.

Jeeho, L., and F. Gregory L. 1998. “Plastic-Damage Model for Cyclic Loading of Concrete Structures.” *Journal of Engineering Mechanics*, 124 (8): 892–900.

Joerger, M.D., and F.C. Martinez. 2006. “Electrical heating of I-84 in Land Canyon, Oregon.” Report FHWA-OR-RD06-17. Oregon Department of Transportation, Salem, OR.

Kim, J. H., et al. 2015. “Development of 1-MW Inductive Power Transfer System for a High-Speed Train.” in *IEEE Transactions on Industrial Electronics*, vol. 62, 10, pp. 6242–6250.

Klontz, K. W., D. M. Divan, D. W. Novotny, and R. D. Lorenz. 1992. “Contactless battery charging system.” US Patent 5 157 319.

Kuo, M. C., K.T. Hall, and M. Darter. 1995. “Three-dimensional finite element model for analysis of concrete pavement support.” *Transportation Research Record*. 1505, TRB, National Research Council, Washington, DC, 119–127.

Laranjeira, F. 2010, “Design-Oriented Constitutive Model for Steel Fiber Reinforced Concrete.” Ph.D. Thesis. ETSECCPB, UPC; Barcelona, Spain: p. 318.

Liu, K., H. Xie, S. Huang, and C. Jin, F. Wang. 2017. “The equivalent plasticity strain analysis of heated pavement for snow-melting concrete exposed to inner elevated temperatures.” *Construction and Building Materials*, 137 66–75.

Liu, K., P. Xu, F. Wang, C. Jin, Q. Liu, H. Pang, H. Xie. 2021. “The accumulated stress damage and residual life prediction of unreinforced concrete pavement with electric heating pipes.” *Construction and Building Materials*, 278 122258.

Luccioni, B. M., M. I. Figueroa, and R.F. Danesi. 2003. “Thermo-mechanic model for concrete exposed to elevated temperatures.” *Engineering Structures*, 25 (6) 729–742.

Mackiewicz, P. 2014. “Thermal stress analysis of jointed plane in concrete pavements.” *Applied Thermal Engineering*, 73 (1) 1169–1176.

Mi, C. C., G. Buja, S. Y. Choi, and C. T. Rim. 2016. “Modern advances in wireless power transfer systems for roadway powered electric vehicles.” *IEEE Transactions on Industrial Electronics*, vol. 63, 10, pp. 6533–6545.

Miller, M. A. 1945. “Cumulative Damage in Fatigue.” *Applied Mechanics*. Vol.12 9.

Nechnech, W., F. Meftah, and J.M. Reynouard. 2002. “An elastoplastic damage model for plain concrete subjected to high temperatures.” *Engineering Structures*, 24 (2002)597–611.

Nguyen, M.L., P. Hornych, J.P. Kerzrého, and S. Perez. 2014. “Full scale test on prefabricated slabs for electrical supply by induction of urban transport systems.” Transport Research Arena, Paris.

Nguyen, M. L., P. Hornych, and S. Perez, E. Curran. 2015. “Development of inductive charging pavement for electric buses in urban areas.” Transport Research Arena, Paris.

Pearce, M. G. S., G. A. Covic, and J. T. Boys. 2019. “Robust Ferrite-Less Double D Topology for Roadway IPT Applications.” in *IEEE Transactions on Power Electronics*, vol. 34, 7, pp. 6062-6075.

Schladover, S. E. 1998. “Systems engineering of the roadway powered electric vehicle technology.” presented at the 9th International Electric Vehicle Symposium.

Sharifi, N., S. Askarinejad, and K. Mahboub. 2020. “Fracture performance of a PCM-Rich concrete pavement under thermal stresses.” *International Journal of Pavement Engineering*, https://doi.org/10.1080/10298436.2020.1738436.

Sinai, S., A. Heidarpour, and X. Zhao. 2016 “A micro-mechanical parametric study on the strength degradation of concrete due to temperature exposure using the discrete element method.” *International Journal of Solids and Structures*, 88–89 165–177.

Tejeda, A., C. Carretero, J. T. Boys, and G. A. Covic. 2017. “Ferrite-Less Circular Pad with Controlled Flux Cancelation for EV Wireless Charging.” in *IEEE Transactions on Power Electronics*, vol. 32, 11, pp. 8349–8359.

Varghese, Benny J. 2021, “Roadway-Embedded Transmitters and Multi-Pad Receivers for High Power Dynamic Wireless Power Transfer,” All Graduate Theses and Dissertations. 8232. https://digitalcommons.usu.edu/etd/8232

Wang, H., and I. L. Al-Qadi. 2011. “Impact quantification of wide-base tire loading on secondary road flexible pavements.” *Journal of Transportation Engineering*, 137(9):630–639. https://doi.org/10.1061/(ASCE)TE.1943-5436.0000245.

Wu, C. Y., H. Wang, J. N. Zhao, X. Jiang, Y. J. Qiu, and B. Yusupov. 2020. “Prediction of viscoelastic pavement responses under moving load and different tire contact stresses with 2.5-D finite element method.” *Mathematical Problems in Engineering*, 2020: 1–16. https://doi.org/10.1155/2020/1029089.08.085.

Xotta, G., G. Mazzucco, V.A. Salomoni, C.E. Majorana, and K.J. Willam. “The composite behavior of concrete materials under high temperatures.” *International Journal of Solids and Structures*, 64–65 (2015) 86–99.

Xu, C., and D. Cebon. 2021. “Prediction of Premature Cracking in Jointed Plain Concrete Pavements.” *Journal of Transportation Engineering*, 147.

Yoon, M., G. Kim, G. Choe, Y. Lee, and T. Lee. 2015. “Effect of coarse aggregate type and loading level on the high-temperature properties of concrete.” *Construction and Building Materials*, 78 26–33.

Zhao, J. N., and H. Wang. 2020. “Dynamic pavement response analysis under moving truck loads with random amplitudes.” *Journal of Transportation Engineering*, *Part B: Pavements*, 146(2), 04020020. https://doi.org/10.1061/JPEODX.0000173.

Zreid, I., and M. Kaliske. 2014. “Regularization of microplane damage models using an implicit gradient enhancement.” *International Journal of Solids and Structures*, 51 (19–20): 3480–3489. Elsevier Ltd. https://doi.org/10.1016/j.ijsolstr.2014.06.020.

Zreid, I., and M. Kaliske. 2016. “An implicit gradient formulation for microplane Drucker-Prager plasticity.” *International Journal of Plasticity*, 83: 252–272. Elsevier Ltd. https://doi.org/10.1016/j.ijplas.2016.04.013.

Zreid, I., and M. Kaliske. 2018. “A gradient enhanced plasticity–damage microplane model for concrete.” *Computational Mechanics*, 62 (5): 1239–1257. Springer Berlin Heidelberg. https://doi.org/10.1007/s00466-018-1561-1.

APPENDIX A. RTDAQ code

```
'\Program description

' Measures 1 LVDT and 8 each BDI ST350 strain gages at 10Hz sample rate.

' Added channel assignments table.

'\Program notes:

' (1) before starting, need to calibrate the hysteresis items on a specimen to get an accurate calibration

'\\ Declarations:

'###############################################

' for offset zero of strain sensors

Public FieldcalAvgs

Public Flag(8) As Boolean 'Flag 8 Zeros offset of strain sensor

Public CalFileLoaded As Boolean

Dim R

Public GStrain(8): Units GStrain() = unitless

'\\\\\\\\\\\\\\\\\\\\\\\\\\\\\\\\\\\\\\\\\\\\

'For Mainraw

'          Public ST350_Ref          ={       1,       2,       3,       4,       5,       6,       7,       8 }

'                              ={    1996,    1990,    1982,    3211,    1972,    2611,    2612,    1973 }

'          Public ST350_Mult2(8)       ={  579.50 ,  517.50 ,  422.27 ,  499.20 ,  527.80 ,  539.50 ,  515.90 ,
509.6  }

'          Public ST350_oSet2(8)       ={  000.00 ,  000.00 ,  000.00 ,  000.00 ,  000.00 ,  000.00 ,  000.00 ,
000.00  }

'////////////////////////////////////

Public StrainGF(8) = {  1000/579.50 ,  1000/517.50 ,  1000/422.27  , 1000/499.20 ,  1000/527.80 ,
1000/539.50 ,  1000/515.90 ,  1000/509.6  }

Units StrainGF() = unitless
```

```
Public ScanFlg1x(8) As Boolean

Public GStrainRaw(8): Units GStrainRaw() = unitless

Public CalStartIdx

Public FlagMode8

Public StrainZeroMV(8): Units StrainZeroMV() = unitless

Public CalMode

Public SKnownVar(8)


'###############################################

        Public StorageFlag(2) As Boolean = {  True,  True }

        Alias  StorageFlag(1) = Store_Main 'Alias is used to assign the second name of Public variable

        Alias  StorageFlag(2) = Store_Raw

        Public LVDT_Distance : Units LVDT_Distance = TBD 'To be determined

        Public LVDT_mV 'raw data

        Public LVDT_Mult = -0.01141229*.0387 '0.0387 is a slope in calibration cal

        Public LVDT_oSet = 1.3013


        Public ST350_uStrain(8), ST350_mVPV(8),ST350_uStrainforcali(8)

  Units ST350_uStrain() = microstrain

  Units ST350_mVPV() = mV/V

        Public ST350_Mult(8) ={  0.68344 ,  1.62052 ,  0.70256 ,  0.96906 ,  1.154 ,  1.111 ,  0.695 ,
1.372  } 'from a slope in calibration excel


'\\\ Data Tables:


        DataTable(Main,Store_Main,-1)
```

```
        CardOut(0,-1)' -1 for spending all spaces in a memory card

        DataInterval(0,0,0,10)

        Sample(8,ST350_uStrain(),IEEE4)

        Sample(8,ST350_uStrainforcali(),IEEE4)

        Sample(1,LVDT_Distance(),IEEE4)'\\\\\\\I don't know about which unit it is for the displacement? Pilaiwan

        EndTable


  DataTable(CalHist,NewFieldCal,100) 'Cal table that store Calibration values

        CardOut(0,100)' only 100 data for checking

        SampleFieldCal

        EndTable ' will get zeroMV/V and Gstrain


        DataTable(Raw,Store_Raw,-1)' this contain all raw data of strain and displacement Pilaiwan

        CardOut(0,-1)

        DataInterval(0,0,0,10)

        Sample(1,LVDT_mV       ,IEEE4)

        Sample(8,ST350_mVPV()  ,IEEE4)

        EndTable




        BeginProg


'##########

Flag(8) = True
```

```
For R = 1 To 8                          'Do the following to all of Strain
   GStrain(R) = StrainGF(8)                    'Assign default gauge factor (2) to GStrain
 Next R                                  'Repeat above until finished
 For R = 1 To 8 ' already come up with 8
   ScanFlg1x(R) = True
 Next R
 For R = 1 To 8
   GStrainRaw(R) = GStrain(R)
 Next R


 CalFileLoaded = false
 CalFileLoaded = LoadFieldCal(1)
 FieldcalAvgs = 20
'#############

                Scan(100,mSec,1000,0)'Main scan and set up sample rate (10Hz)


'############
If Flag(8) Then     'Flag 8 zeroing control for the Strain Gages(zeroing calibration).
      If ScanFlg1x(8) Then
        CalStartIdx = 1
        FlagMode8 = 1
        ScanFlg1x(8) = False
      EndIf
```

```
   If (FlagMode8 <= 0) OR (FlagMode8 = 6) Then Flag(8) = 0 ' 6 values current status of calibration
   Else
     ScanFlg1x(8) = True
   EndIf
'#############

                        VoltDiff(LVDT_mV,1,mV5000,2,True,0,250,1.0,0.0)
                        LVDT_Distance = (LVDT_mV*LVDT_Mult)+LVDT_oSet ' Equation for converting raw data to main by multiply with GF

                        BrFull(ST350_mVPV(),8,mV50,7,Vx2,3,5000,False,False,0,250,1.0,0.0)

    CallTable CalHist
'/
                NextScan
        EndProg
```

APPENDIX B. STRAIN PLOTS FROM CYCLIC LOADING TEST

Panel 1 strain reading

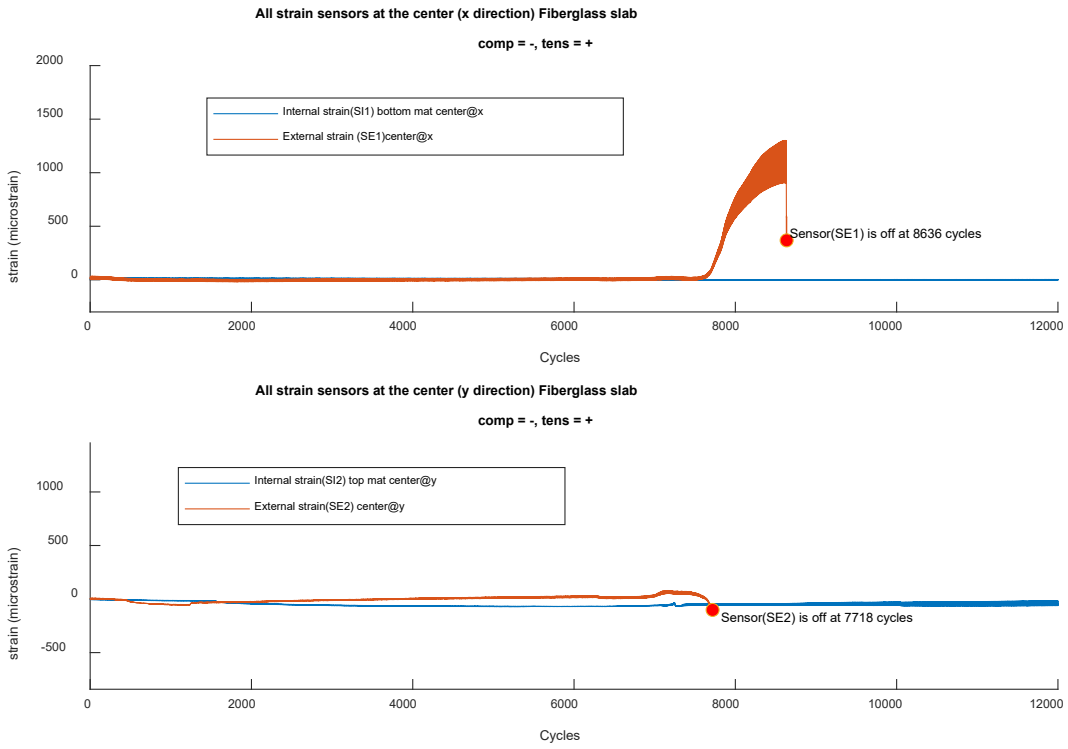

Figure D-1 Comparison of internal and external strain gauges reading (SI1 and SE1) and (SI2 and SE2) for Panel 1

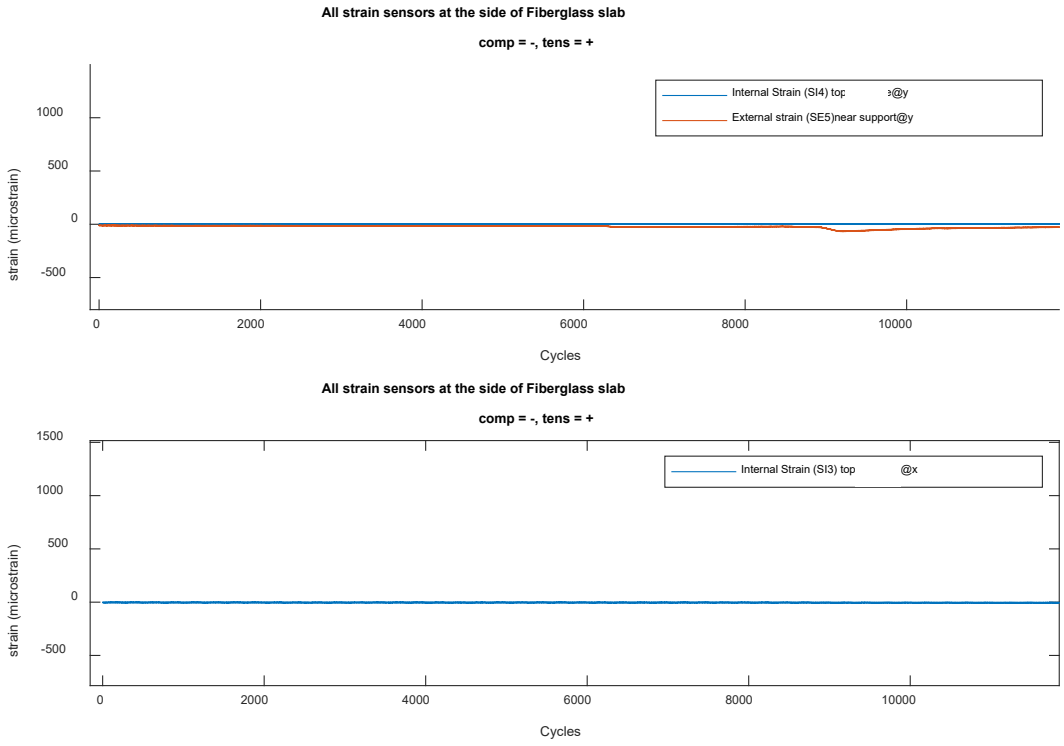

Figure D-2 Comparison of internal and external strain gauges reading (SI6 and SE5) and (SI5 and SE2) for Panel 1

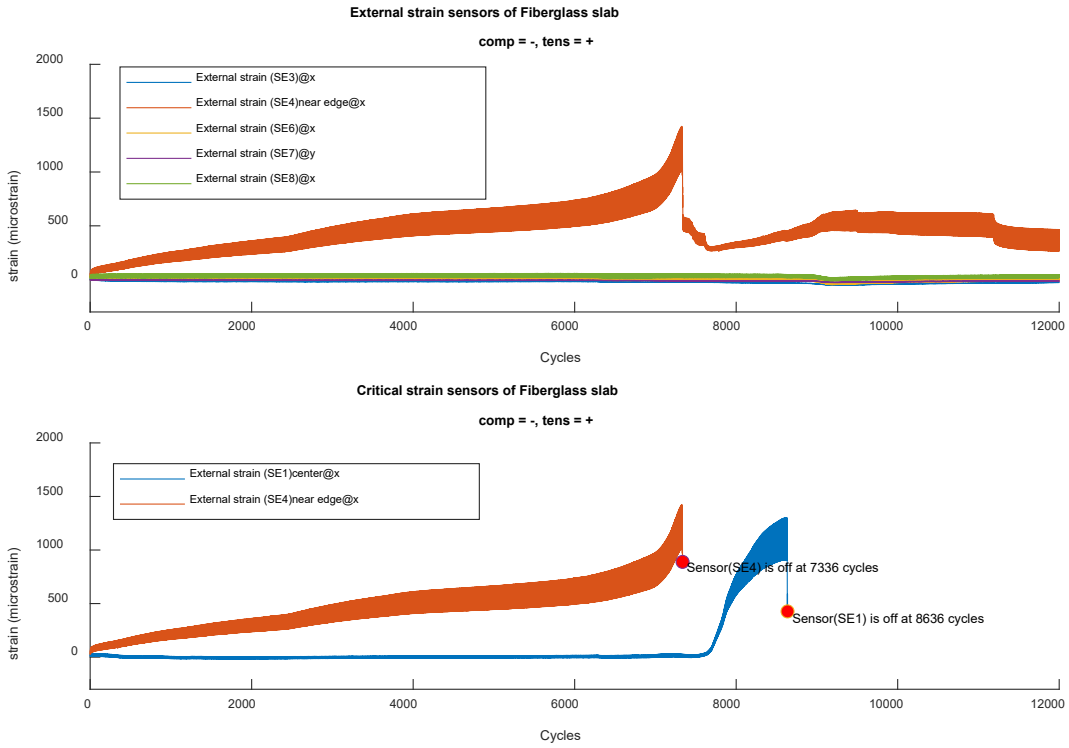

Figure D-3 External strain gauges reading (SE1, SE3, SE4, SE5, SE6, SE7, and SE8) for Panel 1

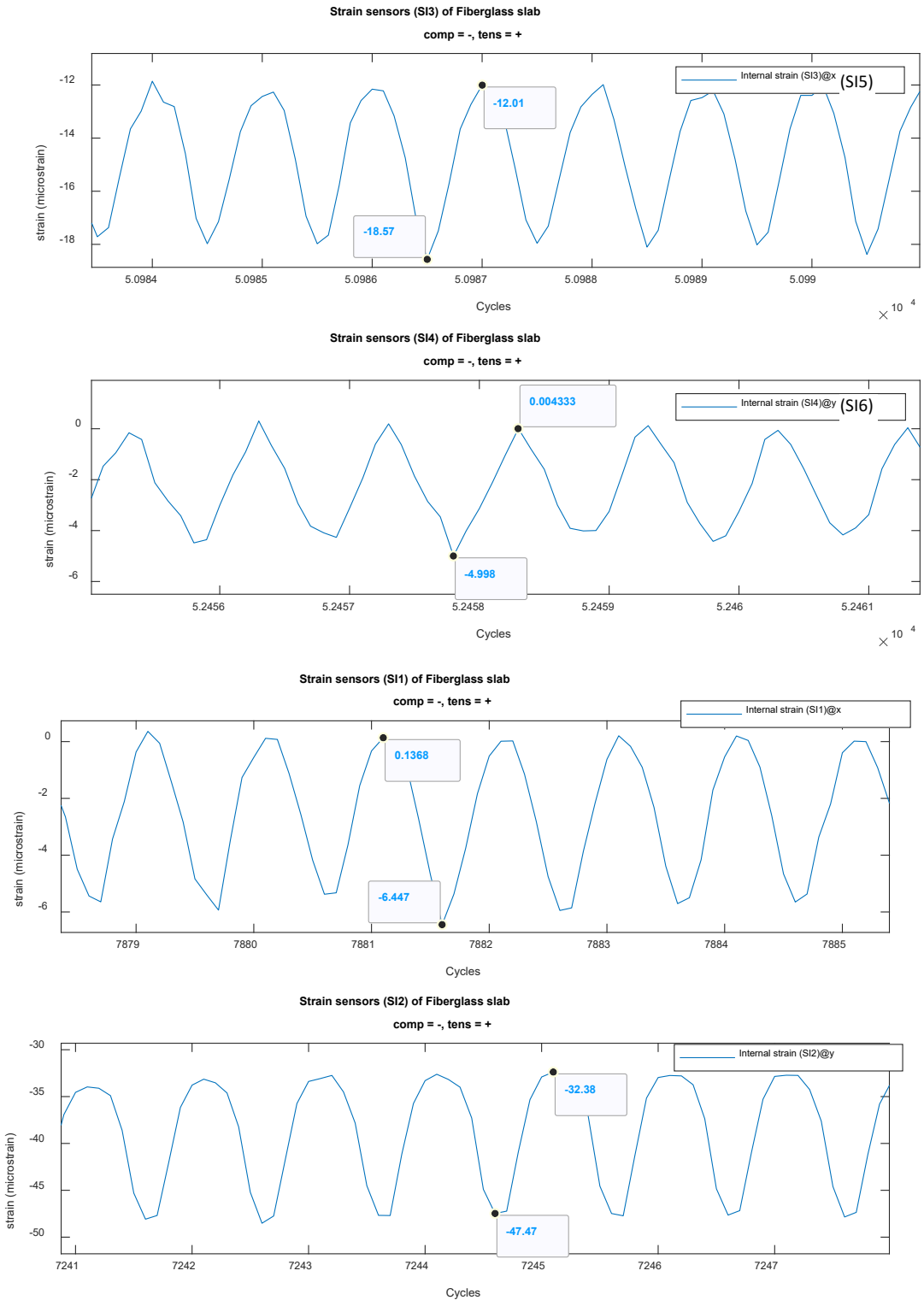

Figure D-4 Internal strain gauges reading (SI5, SI6, SI1, and SI2), closed-up view, for Panel 1

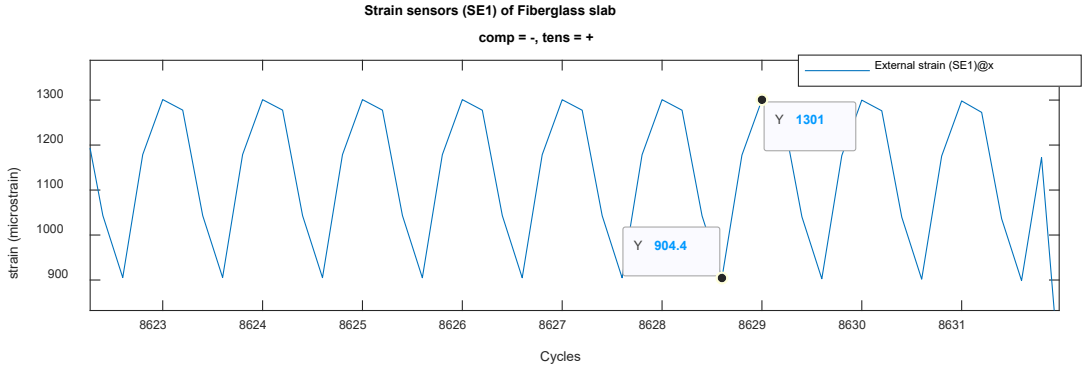
Strain sensors (SE1) of Fiberglass slab
comp = -, tens = +
External strain (SE1)@x
Y 1301
Y 904.4
strain (microstrain)
1300
1200
1100
1000
900
8623
8624
8625
8626
8627
8628
8629
8630
8631
Cycles

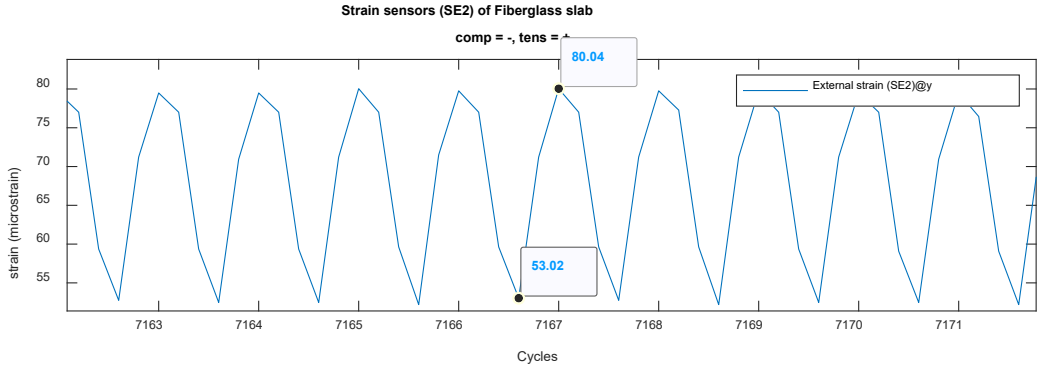
Strain sensors (SE2) of Fiberglass slab
comp = -, tens = +
80.04
External strain (SE2)@y
53.02
strain (microstrain)
80
75
70
65
60
55
7163
7164
7165
7166
7167
7168
7169
7170
7171
Cycles

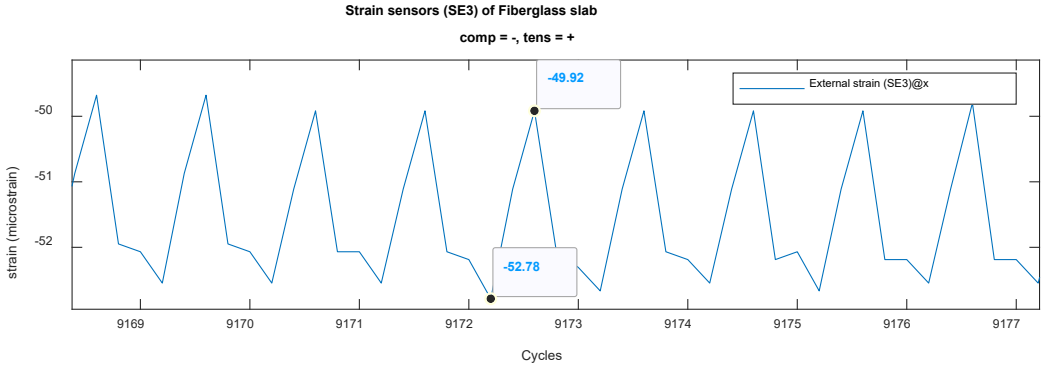
Strain sensors (SE3) of Fiberglass slab
comp = -, tens = +
-49.92
External strain (SE3)@x
-52.78
strain (microstrain)
-50
-51
-52
9169
9170
9171
9172
9173
9174
9175
9176
9177
Cycles

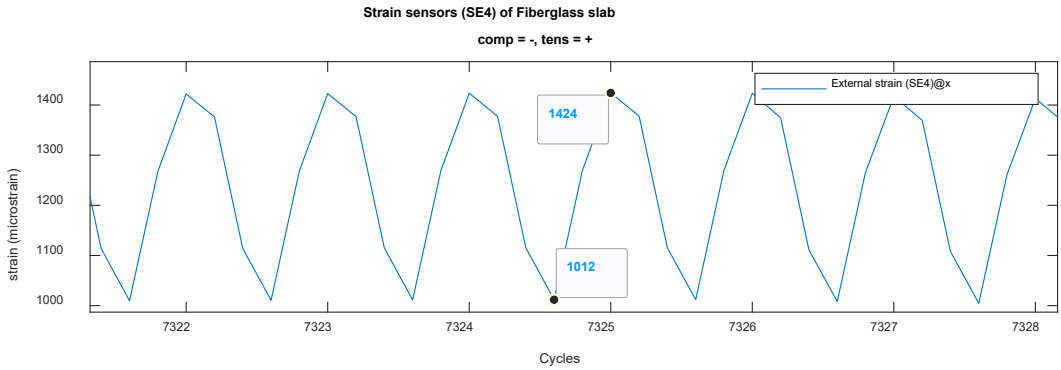
Strain sensors (SE4) of Fiberglass slab
comp = -, tens = +
External strain (SE4)@x
1424
1012
strain (microstrain)
1400
1300
1200
1100
1000
7322
7323
7324
7325
7326
7327
7328
Cycles

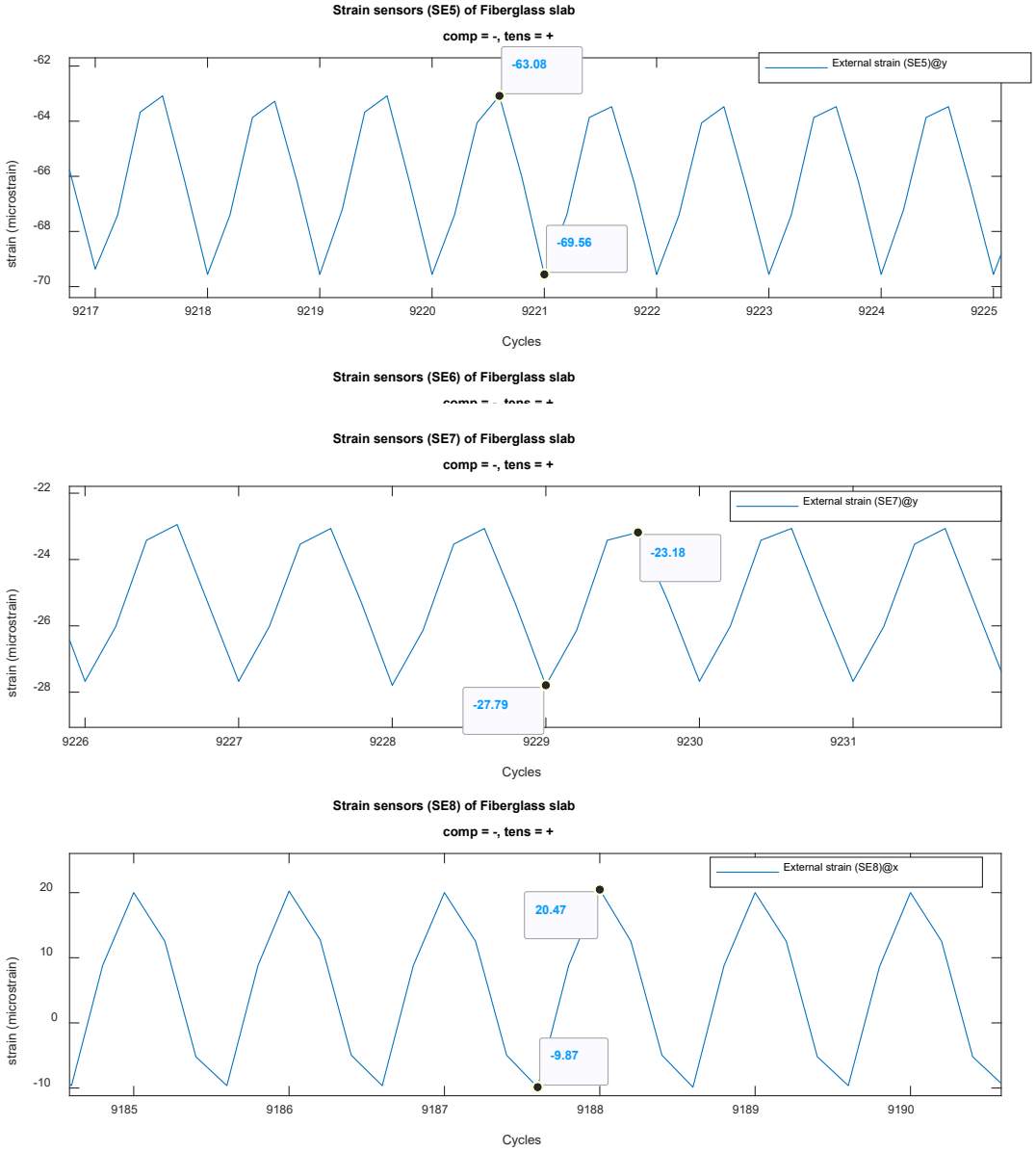

Figure D-5 All external strain gauges reading (SE1 to SE8), closed-up view, for Panel 1

Panel 2 strain reading

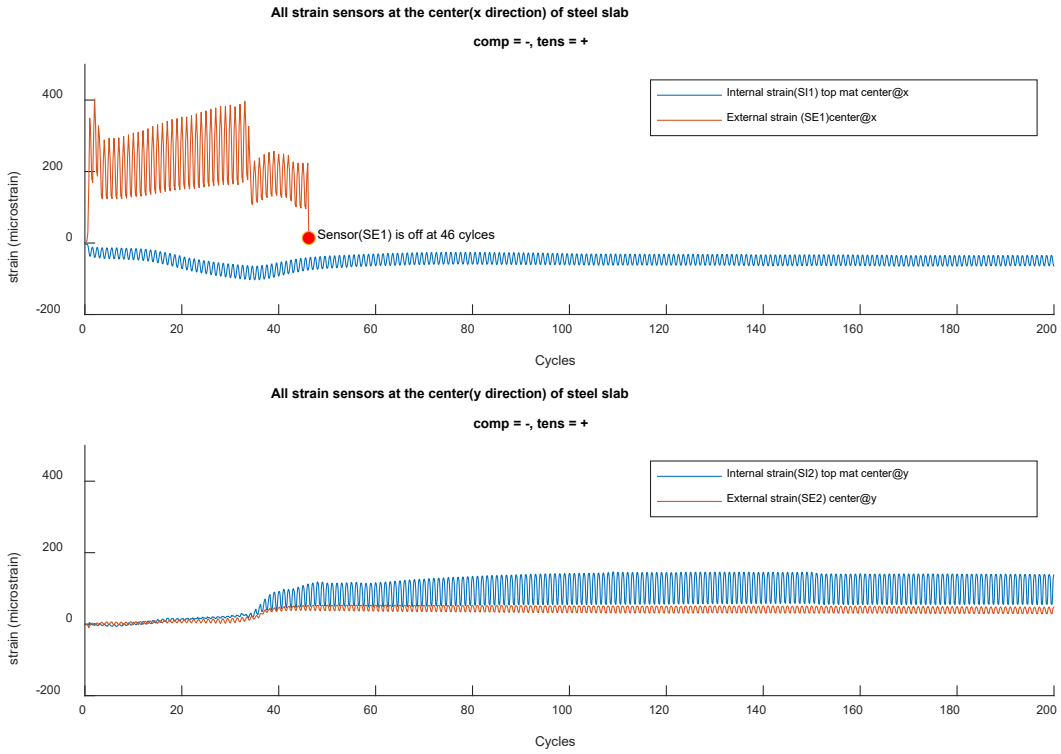

Figure D-6 Comparison of internal and external strain gauges reading (SI1 and SE1) and (SI2 and SE2) for Panel 2

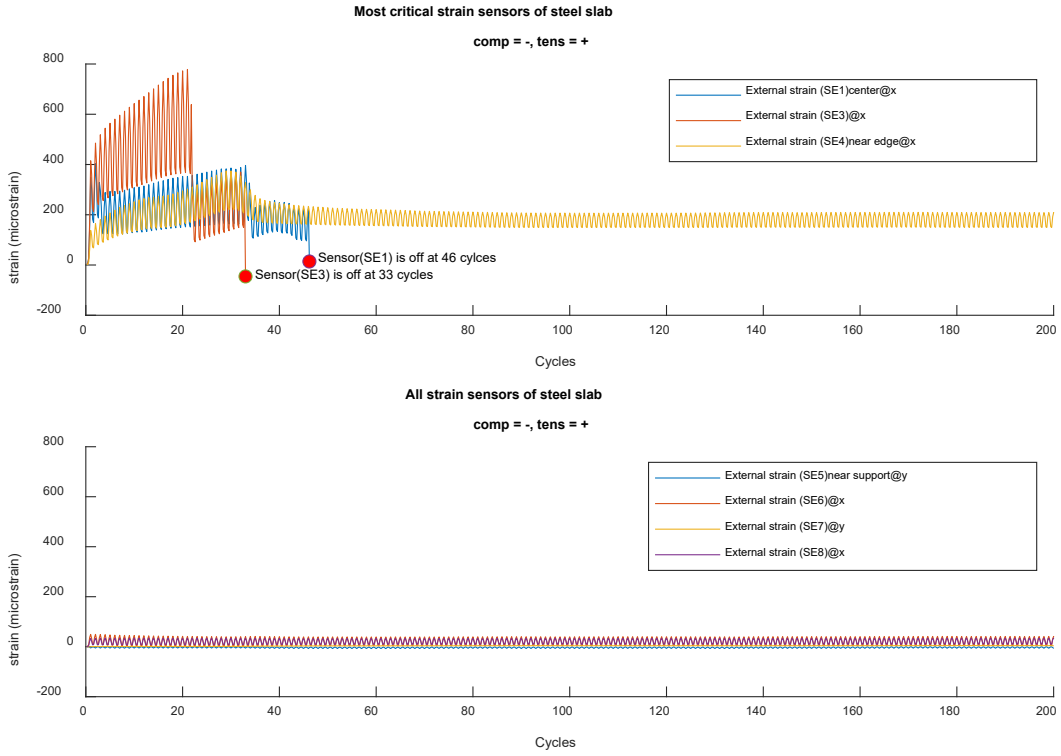

Figure D-7 External strain gauges reading (SE1, SE3, SE4, SE5, SE6, SE7, and SE8) for Panel 2

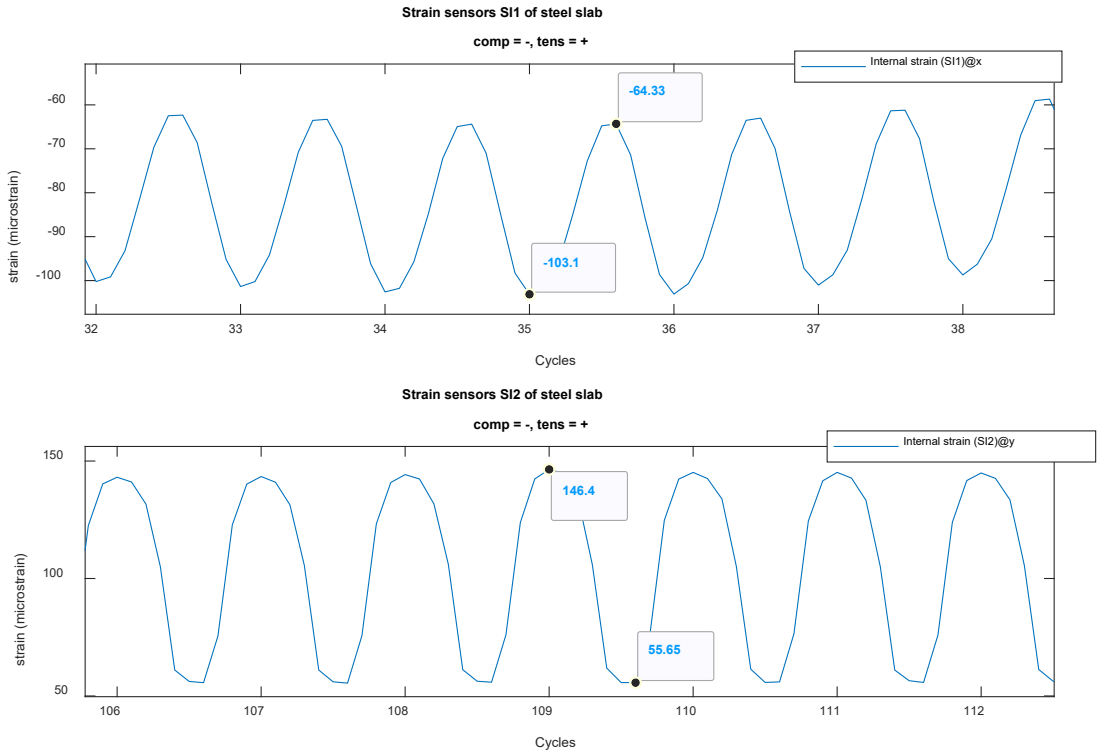

Figure D-8 Internal strain gauges reading (SI1 and SI2), closed-up view, for Panel 2

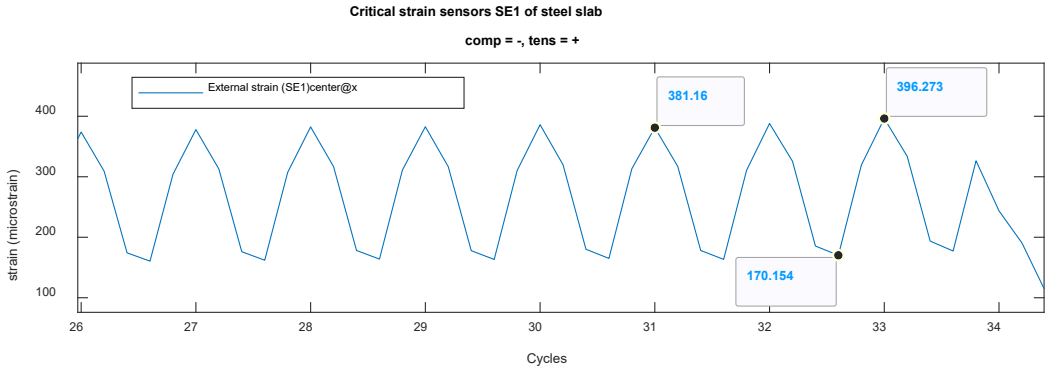
Critical strain sensors SE1 of steel slab
comp = -, tens = +
External strain (SE1)center@x
381.16
396.273
170.154
strain (microstrain)
Cycles

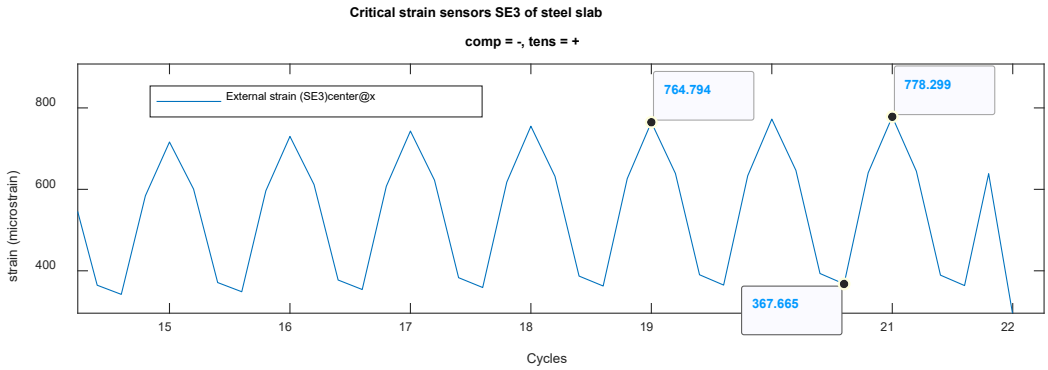
Critical strain sensors SE3 of steel slab
comp = -, tens = +
External strain (SE3)center@x
764.794
778.299
367.665
strain (microstrain)
Cycles

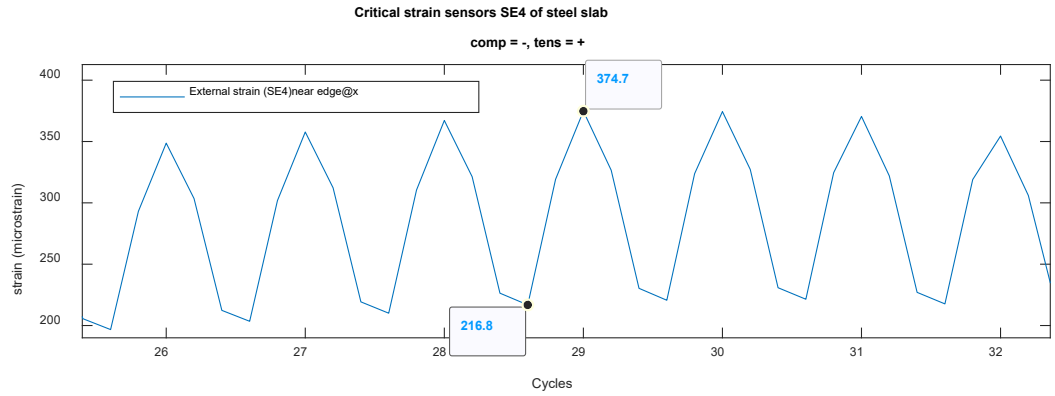
Critical strain sensors SE4 of steel slab
comp = -, tens = +
External strain (SE4)near edge@x
374.7
216.8
strain (microstrain)
Cycles

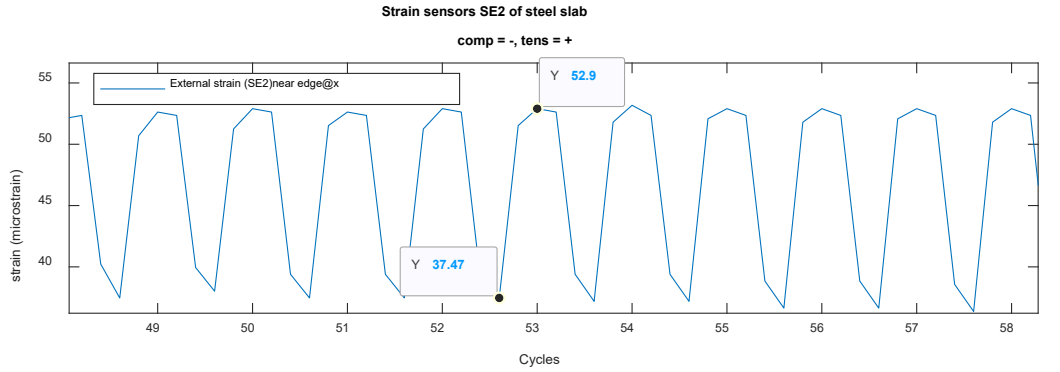
Strain sensors SE2 of steel slab
comp = -, tens = +
External strain (SE2)near edge@x
Y 52.9
Y 37.47
strain (microstrain)
Cycles

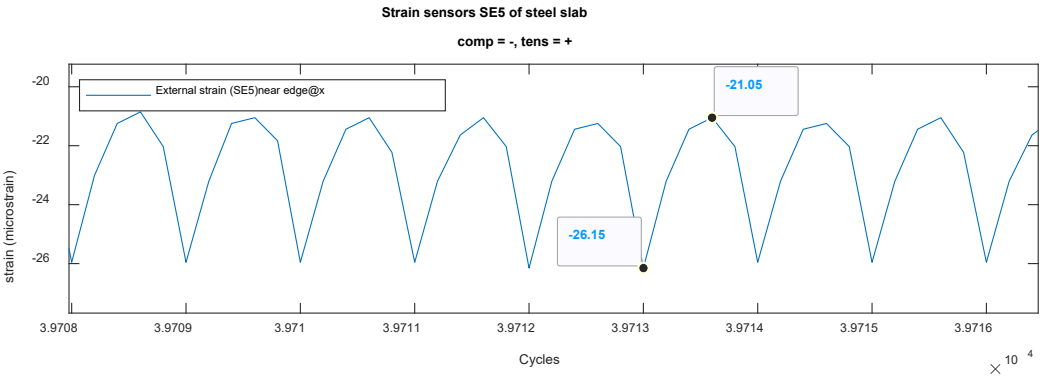
Strain sensors SE5 of steel slab
comp = -, tens = +
External strain (SE5)near edge@x
-21.05
-26.15
strain (microstrain)
Cycles
10 4

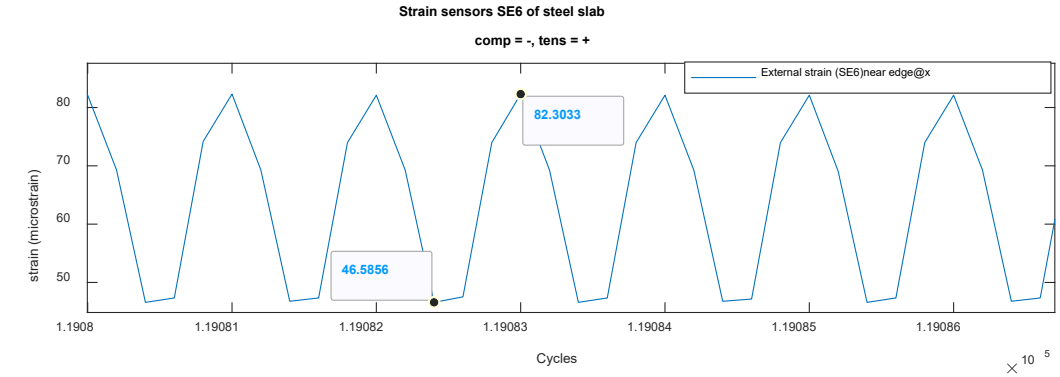
Strain sensors SE6 of steel slab
comp = -, tens = +
External strain (SE6)near edge@x
82.3033
46.5856
strain (microstrain)
Cycles
10 5

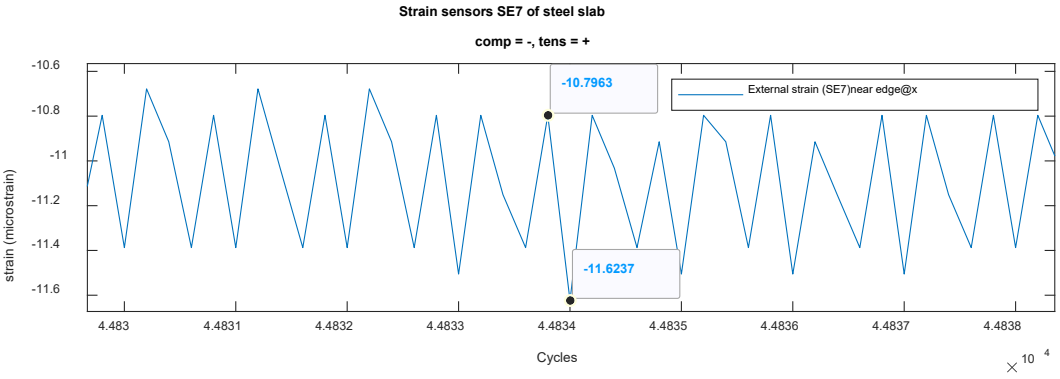
Strain sensors SE7 of steel slab
comp = -, tens = +
External strain (SE7)near edge@x
-10.7963
-11.6237
strain (microstrain)
Cycles
10 4

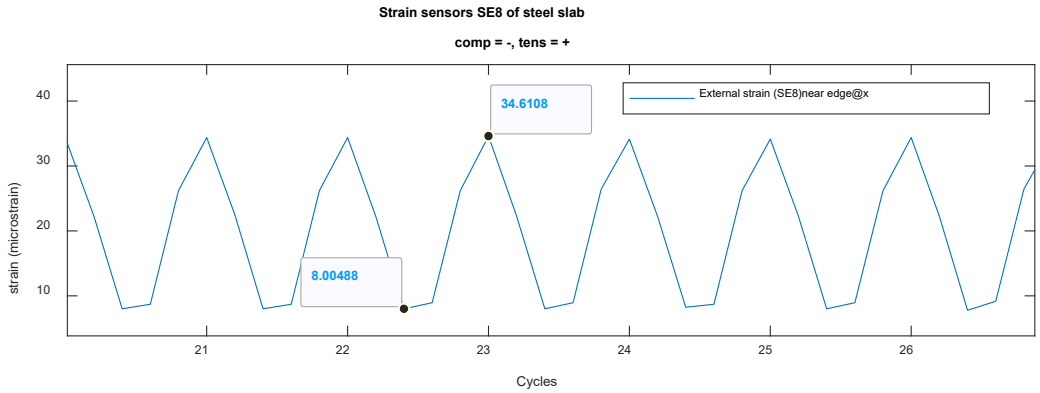

Figure D-9 All external strain gauges reading (SE1 to SE8), closed-up view, for Panel 1

APPENDIX C. MATLAB CODE FOR CYCLIC LOADING TEST

Panel 1 - Strain reading (external and internal strain gauges)

```
clc;
clear;
fclose('all');

infile = '11216_Main_2021-03-11T14-46.dat'; %%%%%need to change according to file
name
FileID = fopen(infile);

    exp1   =  '[^ \f\n\r\t\v,;:]*'; %expression--non-white-space character [^
\f\n\r\t\v]
    exp2    = '(?<=")[^"]+(?=")'; % remove double qoute
    for i=1:4 % extract only first 4 lines in the .dat file
        aline1         = fgetl(FileID); %read first line
        extract1       = regexp(aline1,exp1,'match'); %regexp = match regular
expression, read first 4 lines
        Finfo{i}       = string(extract1);
    end

% No. Column
Datncol= length(Finfo{2}); % line no. 2 has the content of each column

% Dformat           = '%{yyyy-MM-dd HH:mm:ss.SSS}D';
extract2            = textscan(FileID,['%s %f' repmat('%f ',1,Datncol-
2)],'Delimiter',',');% data in each column
datest              = string(regexp(extract2{1},exp2,'match')); %remove "
datetim             = datetime(datest,'InputFormat','yyyy-MM-dd HH:mm:ss.SSS');
log1                = isnat(datetim); %isnat = determine not a time data(NaT)
datetim(log1)       = datetime(datest(log1),'InputFormat','yyyy-MM-dd HH:mm:ss');

tabname             = string(regexp(Finfo{2},exp2,'match')); %set content of each
column from info in line 2
numdata             = cell2mat(extract2(2:end)); %showing all data not including
date
tabdat              = [table(datetim) array2table(numdata)]; %create table of data
tabdat.Properties.VariableNames = tabname; %%%%%%%

% fclose('all');  %close an open file %%%%%%%%
%% Fiber optic sensors
infile2 = {'fatigue_GFRP PanelREV02_S1_M5_Ch1.txt','fatigue_GFRP
PanelREV02_S1_M6_Ch1.txt',....
'fatigue_GFRP PanelREV02_S1_M4_Ch2.txt','fatigue_GFRP PanelREV02_S1_M4_Ch1.txt'};
% {bottom x, top y, top left x, top left y}
for p = 1:4
Filename = fopen(infile2{p});
exp1    = '[^ \f\n\r\t\v,;:]*';
exp2    = '(?<=")[^"]+(?=")'; % remove double quote

  for r=1:6 %extract first 6 lines
      line1 = fgetl(Filename);
```

```
      extract1_data = regexp(line1,exp1,'match'); %titles
      info{p}{r} = string(extract1_data);
  end

 extract2_data = textscan(Filename,'%f %f');
extdata{p}             = [extract2_data{1} extract2_data{2}];

end

numfiles = numel(infile2);
data = cell(1,numfiles);
strain = cell(1,numfiles);
%start count at 739 @5:49pm
for p=1:4
dd{p} = [extdata{p}(:,2)];
time_fiber{p} = [extdata{p}(:,1)];
time_GMT{p} = datetime(time_fiber{p}/10000,
'ConvertFrom','posixTime','TimeZone'....
,'America/Denver','Format','HH:mm:ss.SSS'); %HH:mm:ss.SSS
n2{p} = (1:length(dd{p}))'/10.;
end

dd{2}(277477)=dd{2}(277478); % one data occurs unusual peak

%% ## Plot Section ##
figure(1)
% all sensors
% {bottom x, top y, top left x, top left y}
hold on;
%plot internal sensors
% for p=1:4
% plot(n2{p}(1:length(dd{p}(739:end))),dd{p}(739:end))%start count at 739 @5:49pm
% end
%plot external sensors
cycle_external = (1:length(tabdat.RECORD))/5.;
plot(cycle_external(1:1500000),tabdat{(16560:1516559),tabname(3:end)}*-1)
%1,500,000 is first 300,000 cycle
% plot(tabdat.TIMESTAMP,sgolayfilt(tabdat{:,tabname(2+sensno)},1,33))
hold off;

title({'Internal fiber optic strain sensors(+ is tension)&External strain (+ is
tension)','fatigue test GFRP Panel(32kips)'});
xlabel('Cycles');
ylabel('strain (microstrain)');
legend((strcat('External',tabname(3:end))));
% xlim([0 300000]);
%'Strain#1 bottom mat center@x','Strain#2 top mat center@y','Strain#3 top mat
side@x','Strain#4 top mat side@y',
c1 = {[0.9290, 0.6940, 0.1250],[0.4940, 0.1840, 0.5560]};

%%
figure(2)
```

```
subplot(2,1,1);
% strain #1 bottom center@x and external strain1 center@x
hold on;
%plot internal sensors
plot(n2{1}(1:length(dd{1}(2127:end))),dd{1}(2127:end)*-1)
%plot external sensors
plot(cycle_external(1:43180),tabdat{(16554:59733),tabname(3)}*-1)
plot(cycle_external(43180),tabdat{(59741),tabname(3)}*-
1,'o','MarkerFaceColor','r'); % o = circle, r = read, get red circle
text(8675,400,'Sensor(SE1) is off at 8636 cycles');
xlim([0 12000]);
ylim([-300 2000]);
hold off;
title({'All strain sensors at the center (x direction) Fiberglass slab','comp = -,
tens = +'})
xlabel('Cycles');
ylabel('strain (microstrain)');
legend('Internal strain(SI1) bottom mat center@x','External strain (SE1)center@x');
% legend(['Internal strain(SI1) bottom mat
center@x',(strcat('External',tabname(3),'center@x'))]);
subplot(2,1,2);
% strain #2 top center@y and external strain2 center@y
hold on;
%plot internal sensors
plot(n2{2}(1:length(dd{2}(2127:end))),dd{2}(2127:end)*-1)
%plot external sensors
plot(cycle_external(1:38590),tabdat{(16554:55143),tabname(4)}*-1)
plot(cycle_external(38590),tabdat{(55160),tabname(4)}*-
1,'o','MarkerFaceColor','r'); % o = circle, r = read, get red circle
text(7825,-200,'Sensor(SE2) is off at 7718 cycles');
xlim([0 12000]);
ylim([-300 2000]);

hold off;
title({'All strain sensors at the center (y direction) Fiberglass slab','comp = -,
tens = +'})
xlabel('Cycles');
ylabel('strain (microstrain)');
legend('Internal strain(SI2) top mat center@y','External strain(SE2) center@y');

%%
% {bottom x, top y, top left x, top left y}
figure(3)
subplot(2,1,1);
hold on;
%plot internal sensors%internal Strain#4 top left@y
plot(n2{4}(1:length(dd{4}(2127:end))),dd{4}(2127:end)*-1)
%External sensor SE5
plot(cycle_external(1:1500000),tabdat{(16554:1516553),tabname(2+5)}*-1)%%%OK
hold off;

title({'All strain sensors at the side of Fiberglass slab','comp = -, tens = +'})
```

```
xlabel('Cycles');
ylabel('strain (microstrain)');
legend('Internal Strain (SI4) top mat side@y','External strain (SE5)near
support@y');
ylim([-300 2000]);
xlim([0 12000]);

subplot(2,1,2);
%internal sensor SI3
plot(n2{3}(1:length(dd{3}(2127:end))),dd{3}(2127:end)*-1)
title({'All strain sensors at the side of Fiberglass slab','comp = -, tens = +'})
xlabel('Cycles');
ylabel('strain (microstrain)');
legend('Internal Strain (SI3) top mat side@x');
ylim([-300 2000]);
xlim([0 12000]);


%%
figure(4)
subplot(2,1,1);
hold on;
% external ST350 strain5@y, external ST350 strain7@y
%plot external sensors 16554
for j = 3:4
plot(cycle_external(1:1500000),tabdat{(16554:1516553),tabname(2+j)}*-1)
end
for k = 6:8
plot(cycle_external(1:1500000),tabdat{(16554:1516553),tabname(2+k)}*-1)
end
hold off;
title({'External strain sensors of Fiberglass slab','comp = -, tens = +'})
xlabel('Cycles');
ylabel('strain (microstrain)');
legend('External strain (SE3)@x','External strain (SE4)near edge@x',.....
'External strain (SE6)@x','External strain (SE7)@y','External strain (SE8)@x');
xlim([0 12000]);
ylim([-300 2000]);

subplot(2,1,2);
hold on;
% external ST350 strain3@x, external ST350 strain4@x
%start count 16311 @5:49pm
%plot external sensors
plot(cycle_external(1:43180),tabdat{(16554:59733),tabname(2+1)}*-1)
plot(cycle_external(1:36682),tabdat{(16554:53235),tabname(2+4)}*-1)

plot(cycle_external(43180),tabdat{(59795),tabname(3)}*-
1,'o','MarkerFaceColor','r'); % o = circle, r = read, get red circle
text(8696,330,'Sensor(SE1) is off at 8636 cycles');
```

```
plot(cycle_external(36682),tabdat{(53235),tabname(2+4)}*-
1,'o','MarkerFaceColor','r'); % o = circle, r = read, get red circle
text(7390,800,'Sensor(SE4) is off at 7336 cycles');

hold off;
title({'Critical strain sensors of Fiberglass slab','comp = -, tens = +'})
xlabel('Cycles');
ylabel('strain (microstrain)');
legend('External strain (SE1)center@x','External strain (SE4)near edge@x');
ylim([-300 2000]);
xlim([0 12000]);
% subplot(2,1,1);
% hold on;
% % external ST350 strain5@y, external ST350 strain6@x, external ST350 strain8@x
% %start count 16311 @5:49pm
% %plot external sensors
% for j = 6:2:8
% plot(cycle_external(1:1500000),tabdat{(16560:1516559),tabname(2+j)}*-1)
% end
% hold off;
% title({'All strain sensors of Fiberglass slab','comp = -, tens = +'})
% xlabel('Cycles');
% ylabel('strain (microstrain)');
% legend('External strain (SE6)@x','External strain (SE8)@x');
% % ylim([-400 400]);
% xlim([0 60000]);


%%
figure(5)
subplot(2,1,1);
% plot(n2{1}(1:length(dd{1}(2127:end))),dd{1}(2127:end)*-1)
plot(n2{1}(1:length(dd{1}(2000:end))),dd{1}(2000:end)*-1)
title({'Strain sensors (SI1) of Fiberglass slab','comp = -, tens = +'})
xlabel('Cycles');
ylabel('strain (microstrain)');
legend('Internal strain (SI1)@x');
subplot(2,1,2);
plot(n2{2}(1:length(dd{2}(2127:end))),dd{2}(2127:end)*-1)
title({'Strain sensors (SI2) of Fiberglass slab','comp = -, tens = +'})
xlabel('Cycles');
ylabel('strain (microstrain)');
legend('Internal strain (SI2)@y');
%%
figure(6)
subplot(2,1,1);
plot(n2{3}(1:length(dd{3}(2127:end))),dd{3}(2127:end)*-1)
title({'Strain sensors (SI3) of Fiberglass slab','comp = -, tens = +'})
xlabel('Cycles');
ylabel('strain (microstrain)');
legend('Internal strain (SI3)@x');
subplot(2,1,2);
```

```
plot(n2{4}(1:length(dd{4}(2127:end))),dd{4}(2127:end)*-1)
title({'Strain sensors (SI4) of Fiberglass slab','comp = -, tens = +'})
xlabel('Cycles');
ylabel('strain (microstrain)');
legend('Internal strain (SI4)@y');
%%
figure(7)
subplot(2,1,1);
plot(cycle_external(1:43180),tabdat{(16554:59733),tabname(2+1)}*-1)
title({'Strain sensors (SE1) of Fiberglass slab','comp = -, tens = +'})
xlabel('Cycles');
ylabel('strain (microstrain)');
legend('External strain (SE1)@x');
subplot(2,1,2);
plot(cycle_external(1:38590),tabdat{(16554:55143),tabname(4)}*-1)
title({'Strain sensors (SE2) of Fiberglass slab','comp = -, tens = +'})
xlabel('Cycles');
ylabel('strain (microstrain)');
legend('External strain (SE2)@y');
%%
figure(8)
subplot(2,1,1);
plot(cycle_external(1:1500000),tabdat{(16554:1516553),tabname(2+3)}*-1)
title({'Strain sensors (SE3) of Fiberglass slab','comp = -, tens = +'})
xlabel('Cycles');
ylabel('strain (microstrain)');
legend('External strain (SE3)@x');
subplot(2,1,2);
plot(cycle_external(1:1500000),tabdat{(16554:1516553),tabname(2+4)}*-1)
title({'Strain sensors (SE4) of Fiberglass slab','comp = -, tens = +'})
xlabel('Cycles');
ylabel('strain (microstrain)');
legend('External strain (SE4)@x');
%%
figure(9)
subplot(2,1,1);
plot(cycle_external(1:1500000),tabdat{(16554:1516553),tabname(2+5)}*-1)
title({'Strain sensors (SE5) of Fiberglass slab','comp = -, tens = +'})
xlabel('Cycles');
ylabel('strain (microstrain)');
legend('External strain (SE5)@y');
subplot(2,1,2);
plot(cycle_external(1:1500000),tabdat{(16554:1516553),tabname(2+6)}*-1)
title({'Strain sensors (SE6) of Fiberglass slab','comp = -, tens = +'})
xlabel('Cycles');
ylabel('strain (microstrain)');
legend('External strain (SE6)@x');
%%
figure(10)
subplot(2,1,1);
plot(cycle_external(1:1500000),tabdat{(16554:1516553),tabname(2+7)}*-1)
title({'Strain sensors (SE7) of Fiberglass slab','comp = -, tens = +'})
```

```
xlabel('Cycles');
ylabel('strain (microstrain)');
legend('External strain (SE7)@y');
subplot(2,1,2);
plot(cycle_external(1:1500000),tabdat{(16554:1516553),tabname(2+8)}*-1)
title({'Strain sensors (SE8) of Fiberglass slab','comp = -, tens = +'})
xlabel('Cycles');
ylabel('strain (microstrain)');
legend('External strain (SE8)@x');
```

Panel 2 - Strain reading (external and internal strain gauges)

```
clc;
clear;
fclose('all');

infile = '11216_Main_2021-03-08T17-44.dat'; %%%%%need to change according to file
name
FileID = fopen(infile);
% Finfo = {1,4};

    exp1   =  '[^ \f\n\r\t\v,;:]*'; %expression--non-white-space character [^
\f\n\r\t\v]
    exp2    = '(?<=")[^"]+(?=")'; % remove double qoute
    for i=1:4 % extract only first 4 lines in the .dat file
        aline1         = fgetl(FileID); %read first line
        extract1       = regexp(aline1,exp1,'match'); %regexp = match regular
expression, read first 4 lines
        Finfo{i}       = string(extract1);
    end

% No. Column
Datncol= length(Finfo{2}); % line no. 2 has the content of each column

% Dformat           = '%{yyyy-MM-dd HH:mm:ss.SSS}D';
extract2            = textscan(FileID,['%s %f' repmat('%f ',1,Datncol-
2)],'Delimiter',',');% data in each column
datest              = string(regexp(extract2{1},exp2,'match')); %remove "
datetim             = datetime(datest,'InputFormat','yyyy-MM-dd HH:mm:ss.SSS');
log1                = isnat(datetim); %isnat = determine not a time data(NaT)
datetim(log1)       = datetime(datest(log1),'InputFormat','yyyy-MM-dd HH:mm:ss');

tabname             = string(regexp(Finfo{2},exp2,'match')); %set content of each
column from info in line 2
numdata             = cell2mat(extract2(2:end)); %showing all data not including
date
tabdat              = [table(datetim) array2table(numdata)]; %creat table of data
tabdat.Properties.VariableNames = tabname; %%%%%%%

fclose('all');  %close an open file
%%
infile = {'fatigue_steel Panel_S1_M4_Ch1_GF2001(32kips).txt','fatigue_steel
Panel_S1_M4_Ch2_GF2037(32kips).txt'};
infile2 = {
'fatigue_steelREV02_S1_M4_Ch1(32kips).txt','fatigue_steelREV02_S1_M4_Ch2(32kips).tx
t'};
%'fatgue_50_64kips steel 10000_REV02_S1_M4_Ch1.txt','fatgue_50_64kips steel
10000_REV02_S1_M4_Ch2.txt'};
% Ch1 GF=2001 in x direction top mat
% Ch2 GF=2037 in y direction top mat
numfiles = numel(infile);
numfiles2 = numel(infile2);
data = cell(1,numfiles);
```

```
data2 = cell(1,numfiles2);
strain = cell(1,numfiles);

for j = 1:numfiles2
for k = 1:numfiles
data{k} = load(infile{k},'r');
data2{j} = load(infile2{j},'r');
end
end

dd = [data{1}(:,2); data2{1}(:,2)]; % Module 4 channel 1 x direction top mat
n = (1:length(dd))/10.; %cycle

dd2 = [data{2}(:,2); data2{2}(:,2)];% Module 4 channel 2 y direction top mat
dd2(79435) = dd2(79434) ;
n2 = (1:length(dd2))/10.; %cycle
%%%%%%%%

% dd{p} = [extdata{p}(:,2)];
time_fiber = [data{1}(:,1); data2{1}(:,1)];
time_GMT =
datetime(time_fiber/10000,'ConvertFrom','posixTime','Format','HH:mm:ss.SSS');
%HH:mm:ss.SSS
% n2{p} = (1:length(dd{p}))'/10.;

%% ## Plot Section ##
% hold on
%fiber optic starting record at 16536
figure(1)
subplot(2,1,1);
% Internal strains
hold on;
plot(n(1:length(dd(16894:end))),dd(16894:end)*-1) %strain 1@x
cycle_external = (1:length(tabdat.RECORD))/5.; %MTS 2Hz and external sensor 10Hz
% External strains SE1 @65 cycles sensor fail off
plot(cycle_external(1:231),tabdat{(115:345),tabname(3)}*-1)

plot(cycle_external(231),tabdat{(345),tabname(3)}*-1,'o','MarkerFaceColor','r'); %
o = circle, r = read, get red circle
text(48,15,'Sensor(SE1) is off at 46 cylces');

hold off;
title({'All strain sensors at the center(x direction) of steel slab','comp = -,
tens = +'})
xlabel('Cycles');
ylabel('strain (microstrain)');
legend('Internal strain(SI1) top mat center@x','External strain (SE1)center@x');
xlim([0 200]);
ylim([-200 500]);

subplot(2,1,2);
hold on;
```

```
% Internal strains
plot(n2(1:length(dd2(16894:end))),dd2(16894:end)*-1)%strain 2@y
cycle_external = (1:length(tabdat.RECORD))/5.;
% External strains SE2
plot(cycle_external(1:1500000),tabdat{(115:1500114),tabname(4)}*-1)

hold off;
title({'All strain sensors at the center(y direction) of steel slab','comp = -,
tens = +'})
xlabel('Cycles');
ylabel('strain (microstrain)');
legend('Internal strain(SI2) top mat center@y','External strain(SE2) center@y');
xlim([0 200]);
ylim([-200 500]);
%%
figure(2)
subplot(2,1,1);
hold on;
% External strains SE1 @65 cycles sensor fail off
plot(cycle_external(1:231),tabdat{(115:345),tabname(3)}*-1)

% External strains SE3 @52 cycles sensor fail off
plot(cycle_external(1:165),tabdat{(115:279),tabname(5)}*-1)
% External strains SE4
plot(cycle_external(1:1500000),tabdat{(115:1500114),tabname(6)}*-1)

plot(cycle_external(231),tabdat{(345),tabname(3)}*-1,'o','MarkerFaceColor','r'); %
o = circle, r = read, get red circle
text(48,15,'Sensor(SE1) is off at 46 cylces');
plot(cycle_external(165),tabdat{(279),tabname(5)}*-1,'o','MarkerFaceColor','r'); %
o = circle, r = read, get red circle
text(35,-50,'Sensor(SE3) is off at 33 cycles');

hold off;
title({'Most critical strain sensors of steel slab','comp = -, tens = +'})
xlabel('Cycles');
ylabel('strain (microstrain)');
legend('External strain (SE1)center@x','External strain (SE3)@x','External strain
(SE4)near edge@x');
xlim([0 200]);
ylim([-200 800]);

subplot(2,1,2);
hold on;
% External strains
for j = 5:8
plot(cycle_external(1:1500000),tabdat{(115:1500114),tabname(2+j)}*-1)%%%21to1
end
hold off;
title({'All strain sensors of steel slab','comp = -, tens = +'})
xlabel('Cycles');
ylabel('strain (microstrain)');
```

```
legend('External strain (SE5)near support@y','External strain (SE6)@x','External
strain (SE7)@y','External strain (SE8)@x');
xlim([0 200]);
ylim([-200 800]);

%%
figure(3)
subplot(2,1,1);
% External strains SE1 @65 cycles sensor fail off
plot(cycle_external(1:231),tabdat{(115:345),tabname(3)}*-1)
title({'Critical strain sensors SE1 of steel slab','comp = -, tens = +'})
xlabel('Cycles');
ylabel('strain (microstrain)');
legend('External strain (SE1)center@x');
xlim([0 200]);
ylim([-200 800]);

subplot(2,1,2);
% External strains SE3 @52 cycles sensor fail off
plot(cycle_external(1:165),tabdat{(115:279),tabname(5)}*-1)
title({'Critical strain sensors SE3 of steel slab','comp = -, tens = +'})
xlabel('Cycles');
ylabel('strain (microstrain)');
legend('External strain (SE3)center@x');
xlim([0 200]);
ylim([-200 800]);
%%
figure(4)
subplot(2,1,1);
% External strains SE4
plot(cycle_external(1:1500000),tabdat{(115:1500114),tabname(6)}*-1)
title({'Critical strain sensors SE4 of steel slab','comp = -, tens = +'})
xlabel('Cycles');
ylabel('strain (microstrain)');
legend('External strain (SE4)near edge@x');
xlim([0 200]);
ylim([-200 800]);
%%
figure(5)%%%%%%%%%%%%%
subplot(2,1,1);
% External strains SE2
plot(cycle_external(1:1500000),tabdat{(115:1500114),tabname(4)}*-1)
title({'Strain sensors SE2 of steel slab','comp = -, tens = +'})
xlabel('Cycles');
ylabel('strain (microstrain)');
legend('External strain (SE2)near edge@x');
% xlim([0 200]);
% ylim([-200 800]);
subplot(2,1,2);
% External strains SE5
plot(cycle_external(1:1500000),tabdat{(115:1500114),tabname(7)}*-1)
title({'Strain sensors SE5 of steel slab','comp = -, tens = +'})
```

```
xlabel('Cycles');
ylabel('strain (microstrain)');
legend('External strain (SE5)near edge@x');
%%
figure(6)
subplot(2,1,1);
% External strains SE6
plot(cycle_external(1:1500000),tabdat{(115:1500114),tabname(8)}*-1)
title({'Strain sensors SE6 of steel slab','comp = -, tens = +'})
xlabel('Cycles');
ylabel('strain (microstrain)');
legend('External strain (SE6)near edge@x');
% xlim([0 200]);
% ylim([-200 800]);
subplot(2,1,2);
% External strains SE7
plot(cycle_external(1:1500000),tabdat{(115:1500114),tabname(9)}*-1)
title({'Strain sensors SE7 of steel slab','comp = -, tens = +'})
xlabel('Cycles');
ylabel('strain (microstrain)');
legend('External strain (SE7)near edge@x');
%%
figure(7)
subplot(2,1,1);
% External strains SE8
plot(cycle_external(1:1500000),tabdat{(115:1500114),tabname(10)}*-1)
title({'Strain sensors SE8 of steel slab','comp = -, tens = +'})
xlabel('Cycles');
ylabel('strain (microstrain)');
legend('External strain (SE8)near edge@x');
% xlim([0 200]);
% ylim([-200 800]);
%%
figure(8)
subplot(2,1,1);
% internal strains SI1
plot(n(1:length(dd(16894:end))),dd(16894:end)*-1) %strain 1@x
title({'Strain sensors SI1 of steel slab','comp = -, tens = +'})
xlabel('Cycles');
ylabel('strain (microstrain)');
legend('Internal strain (SI1)@x');
% xlim([0 200]);
% ylim([-200 800]);
subplot(2,1,2);
% internal strains SI2
plot(n2(1:length(dd2(16894:end))),dd2(16894:end)*-1)%strain 2@y
title({'Strain sensors SI2 of steel slab','comp = -, tens = +'})
xlabel('Cycles');
ylabel('strain (microstrain)');
legend('Internal strain (SI2)@y');
```

APPENDIX D. MATLAB CODE FOR THERMAL TEST

Panel 1 - Temperature

```
%% Temperature
close all;
clc;
clear;


infile = {'tmp_Data_System1_Module_1Channel1 (8)_TS1.txt',.....
'tmp_Data_System1_Module_2Channel1 (5)_TS3.txt','tmp_Data_System1_Module_2Channel2
(5)_TS2.txt',....
'tmp_Data_System1_Module_3Channel1 (4)_TS6.txt','tmp_Data_System1_Module_3Channel2
(4)_TS4.txt',....
'tmp_Data_System1_Module_4Channel1 (4)_TS7.txt'};

numfiles = numel(infile);
data = cell(1,numfiles);
time = cell(1,numfiles);
tmp = cell(1,numfiles);

for k = 1:numfiles
    data{k} = load(infile{k},'r');
    time{k} = data{k}(:,1); % epoch ms*10  unixmillis
    tmp{k} = data{k}(:,2);
end

%% convert time

% Panel 1
time_sec = cell(1, numfiles);
time_GMT = cell(1, numfiles);
time_mmss = cell(1, numfiles);
for i = 1:numfiles

    f_time = time{i}(1);
    time_sec{i} = (time{i} - f_time)./10000; % to seconds
    time_mmss{i} = seconds(time_sec{i});
    time_mmss{i}.Format = 'mm:ss';
    % convert time to datetime format
    time_GMT{i} = datetime(time{i}./10000, 'ConvertFrom','posixTime','TimeZone'....
    ,'America/Denver','Format','HH:mm:ss.SSS'); %HH:mm:ss.SSS

end

%% Ansys results

% Panel 1
infile_ansys = 'temp_thermal_PCM08.txt'; %%%%%%%
fid = fopen(infile_ansys,'r');
data_ansys = textscan(fid, '%*f %*f %f %f %f %f %f %f %f', 'HeaderLines',1 ,
'Delimiter', '\t');
```

```
fclose(fid);
% convert to seconds and miniutes
data_ansys_mmss = seconds(data_ansys{1});
data_ansys_mmss.Format = 'mm:ss';

%% plot Panel #1 all
figure();

% plot experiment data
for i = 1:numfiles
    hold on
    plot(time_mmss{i}, tmp{i});
end

for i = 2:length(data_ansys)
    plot(data_ansys_mmss, data_ansys{i}(:), '--', 'linew', 2);
end


% plot text
time_stop = datetime('2020-02-14
16:43','TimeZone','America/Denver','Format','HH:mm');
[~, idx] = min(abs(time_GMT{1} - time_stop));
time_stop_sec = time_mmss{1}(idx);
y_lim = get(gca,'ylim');
plot([1, 1]*time_stop_sec, get(gca,'ylim'),'r--');

% adjust text STOP
text(time_stop_sec, y_lim(2)*0.1,{'STOP @' + string(round(time_stop_sec)) + '
min'});

legend('Exp-TS01', 'Exp-TS03', 'Exp-TS02', 'Exp-TS06', 'Exp-TS04', 'Exp-TS07',...
        'Model-TS01', 'Model-TS03', 'Model-TS06', 'Model-TS04', 'Model-TS07');
title('Strain of PCM with GFRP bars Panel no.1');
xlabel('Time(min)');
ylabel('Temperature(\circC)'); %Celcius
xlim(get(gca,'xlim'));
ylim([0 max(get(gca,'ylim'))]);
grid;

%% plot Panel #1 pair

colors = {'#0072BD', '#D95319'};
legend_p1 = {'T5-Exp', 'T2-Exp', 'TS02-Exp', 'T6-Exp', 'T1-Exp', 'T3-Exp'};
legend_ansys_p1 = {'Time','T5-Model', 'T2-Model', 'T6-Model', 'T1-Model', 'T3-
Model', 'T4-Model'};


% plot experiment data

% TS03 & 04 renumber to be T2 & 1
figure();
```

```
p = [2, 5];
q = [3, 5];

c_idx = 1;
for i = 1:length(p)
    hold on
    plot(time_mmss{p(i)}, tmp{p(i)}, 'Color', colors{c_idx}, 'DisplayName',
legend_p1{p(i)});
    plot(data_ansys_mmss, data_ansys{q(i)}(:), '--', 'linew', 1.65, 'Color',
colors{c_idx}, 'DisplayName', legend_ansys_p1{q(i)});
    c_idx = c_idx + 1;
end
legend;
% plot text
time_stop = datetime('2020-02-14
16:43','TimeZone','America/Denver','Format','HH:mm');
[~, idx] = min(abs(time_GMT{1} - time_stop));
time_stop_sec = time_mmss{1}(idx);
ylim([0 80]);
y_lim = get(gca,'ylim');
plot([1, 1]*time_stop_sec, get(gca,'ylim'),'r--', 'HandleVisibility', 'off');

% adjust text STOP
text(time_stop_sec, y_lim(2)*0.7,{'STOP @' + string(round(time_stop_sec)) + '
min'}); %%%%

% title('Strain of PCM with GFRP bars Panel no.1');
xlabel('Time(min)');
ylabel('Temperature(\circC)');
xlim(get(gca,'xlim'));
ylim([0 max(get(gca,'ylim'))]);
grid;


% TS06 & 07 renumber to be T6 & 3
figure();
p = [4, 6];
q = [4, 6];

c_idx = 1;
for i = 1:length(p)
    hold on
    plot(time_mmss{p(i)}, tmp{p(i)}, 'Color', colors{c_idx}, 'DisplayName',
legend_p1{p(i)});
    plot(data_ansys_mmss, data_ansys{q(i)}(:), '--', 'linew', 1.65, 'Color',
colors{c_idx}, 'DisplayName', legend_ansys_p1{q(i)});
    c_idx = c_idx + 1;
end
legend;
% plot text
time_stop = datetime('2020-02-14
16:43','TimeZone','America/Denver','Format','HH:mm');
```

```
[~, idx] = min(abs(time_GMT{1} - time_stop));
time_stop_sec = time_mmss{1}(idx);
ylim([0 80]);
y_lim = get(gca,'ylim');
plot([1, 1]*time_stop_sec, get(gca,'ylim'),'r--', 'HandleVisibility', 'off');

% adjust text STOP
text(time_stop_sec, y_lim(2)*0.7,{'STOP @' + string(round(time_stop_sec)) + '
min'}); %%%%


xlabel('Time(min)');
ylabel('Temperature(\circC)');
xlim(get(gca,'xlim'));
ylim([0 max(get(gca,'ylim'))]);
grid;


% TS01 & 02 renumber to be T5 & TS02 was removed & T4 %%%%%
figure();
p = 1;
q = 2;

c_idx = 1;
for i = 1:length(p)

    hold on
    plot(time_mmss{p(i)}, tmp{p(i)}, 'Color', colors{c_idx}, 'DisplayName',
legend_p1{p(i)});
    plot(data_ansys_mmss, data_ansys{q(i)}(:), '--', 'linew', 1.65, 'Color',
colors{c_idx}, 'DisplayName', legend_ansys_p1{q(i)});

    c_idx = c_idx + 1;
end
%plot(time_mmss{3}, tmp{3}, 'Color', 'k', 'DisplayName', legend_p1{3}); ambient
temp

plot(data_ansys_mmss, data_ansys{7}(:), '--', 'linew', 1.65, 'Color',
colors{c_idx}, 'DisplayName', legend_ansys_p1{7});

legend;
% plot text
time_stop = datetime('2020-02-14
16:43','TimeZone','America/Denver','Format','HH:mm');
[~, idx] = min(abs(time_GMT{1} - time_stop));
time_stop_sec = time_mmss{1}(idx);
ylim([0 80]);
y_lim = get(gca,'ylim');
plot([1, 1]*time_stop_sec, get(gca,'ylim'),'r--', 'HandleVisibility', 'off');

% adjust text STOP
```

```
text(time_stop_sec, y_lim(2)*0.7,{'STOP @' + string(round(time_stop_sec)) + '
min'}); %%%%


xlabel('Time(min)');
ylabel('Temperature(\circC)');
xlim(get(gca,'xlim'));
ylim([0 max(get(gca,'ylim'))]);
grid;
```

Panel 2 - Temperature

```
%% Temperature
close all;
clc;
clear;

infile = {'tmp_Data_System1_Module_1Channel1 (5)_TS1_p2.txt',.....
'tmp_Data_System1_Module_2Channel1
(2)_TS3_p2.txt','tmp_Data_System1_Module_2Channel2 (2)_TS2_p2.txt',....
'tmp_Data_System1_Module_3Channel1
(1)_TS6_p2.txt','tmp_Data_System1_Module_3Channel2 (1)_TS4_p2.txt',....
'tmp_Data_System1_Module_4Channel1
(1)_TS7_p2.txt','tmp_Data_System1_Module_4Channel2 (1)_TS8_p2.txt'};

numfiles = numel(infile);
data = cell(1,numfiles);
time = cell(1,numfiles);
tmp = cell(1,numfiles);

for k = 1:numfiles
    data{k} = load(infile{k},'r');
    time{k} = data{k}(:,1); % epoch ms*10  unixmillis
    tmp{k} = data{k}(:,2);
end

%% convert time

% Panel 1
time_sec = cell(1, numfiles);
time_GMT = cell(1, numfiles);
time_mmss = cell(1, numfiles);
for i = 1:numfiles

    f_time = time{i}(1);
    time_sec{i} = (time{i} - f_time)./10000; % to seconds
    time_mmss{i} = seconds(time_sec{i});
    time_mmss{i}.Format = 'mm:ss';
    % convert time to datetime format
    time_GMT{i} = datetime(time{i}./10000, 'ConvertFrom','posixTime','TimeZone'....
    ,'America/Denver','Format','HH:mm:ss.SSS'); %HH:mm:ss.SSS

end

%% Ansys results

% Panel 1
infile_ansys = 'temp_thermal_steel2.txt'; %%%%%%%
fid = fopen(infile_ansys,'r');
data_ansys = textscan(fid, '%*f %*f %f %f %f %f %f %f %f', 'HeaderLines',1 ,
'Delimiter', '\t');
fclose(fid);
% convert to seconds and miniutes
```

```
data_ansys_mmss = seconds(data_ansys{1});
data_ansys_mmss.Format = 'mm:ss';



%% plot Panel #1 pair %%%%%%%%%

colors = {'#0072BD', '#D95319'};
legend_p2 = {'T5-Exp', 'T2-Exp', 'TS02-Exp', 'T6-Exp', 'T1-Exp', 'T3-Exp', 'T4-
Exp'};
legend_ansys_p2 = {'Time','T5-Model', 'T2-Model', 'T6-Model', 'T1-Model', 'T3-
Model', 'T4-Model'};


% plot experiment datalegend_p2

% TS03 & 04 renumber to be T2 & 1
figure();
p = [2, 5];
q = [3, 5];

c_idx = 1;
for i = 1:length(p)
    hold on
    plot(time_mmss{p(i)}, tmp{p(i)}, 'Color', colors{c_idx}, 'DisplayName',
legend_p2{p(i)});
    plot(data_ansys_mmss, data_ansys{q(i)}(:), '--', 'linew', 1.65, 'Color',
colors{c_idx}, 'DisplayName', legend_ansys_p2{q(i)});
    c_idx = c_idx + 1;
end
legend;
% plot text
time_stop = datetime('2020-02-12
13:18','TimeZone','America/Denver','Format','HH:mm');
[~, idx] = min(abs(time_GMT{1} - time_stop));
time_stop_sec = time_mmss{1}(idx);
ylim([-5 80]);
y_lim = get(gca,'ylim');
plot([1, 1]*time_stop_sec, get(gca,'ylim'),'r--', 'HandleVisibility', 'off');

% adjust text STOP
text(time_stop_sec, y_lim(2)*0.7,{'STOP @' + string(round(time_stop_sec)) + '
min'}); %%%%

 time_start_sec = 0:0;
    ylim([-5 80]);%%%
    y_lim = get(gca,'ylim');
    plot([0, 0]*time_stop_sec, get(gca,'ylim'),'r--', 'HandleVisibility', 'off');

    % adjust text STart
    text(time_start_sec, y_lim(2)*0.7,{'START'});
```

```
% title('Strain of PCM with GFRP bars Panel no.1');
xlabel('Time(min)');
ylabel('Temperature(\circC)');
xlim(get(gca,'xlim'));
ylim([-5 max(get(gca,'ylim'))]);
grid;


% TS06 & 07 renumber to be T6 & 3
figure();
p = [4, 6];
q = [4, 6];

c_idx = 1;
for i = 1:length(p)
    hold on
    plot(time_mmss{p(i)}, tmp{p(i)}, 'Color', colors{c_idx}, 'DisplayName',
legend_p2{p(i)});
    plot(data_ansys_mmss, data_ansys{q(i)}(:), '--', 'linew', 1.65, 'Color',
colors{c_idx}, 'DisplayName', legend_ansys_p2{q(i)});
    c_idx = c_idx + 1;
end
legend;
% plot text
time_stop = datetime('2020-02-12
13:18','TimeZone','America/Denver','Format','HH:mm');
[~, idx] = min(abs(time_GMT{1} - time_stop));
time_stop_sec = time_mmss{1}(idx);
ylim([-5 80]);
y_lim = get(gca,'ylim');
plot([1, 1]*time_stop_sec, get(gca,'ylim'),'r--', 'HandleVisibility', 'off');

% adjust text STOP
text(time_stop_sec, y_lim(2)*0.7,{'STOP @' + string(round(time_stop_sec)) + '
min'}); %%%%

 time_start_sec = 0:0;
    ylim([-5 80]);%%%
    y_lim = get(gca,'ylim');
    plot([0, 0]*time_stop_sec, get(gca,'ylim'),'r--', 'HandleVisibility', 'off');

    % adjust text STart
    text(time_start_sec, y_lim(2)*0.7,{'START'});


xlabel('Time(min)');
ylabel('Temperature(\circC)');
xlim(get(gca,'xlim'));
ylim([-5 max(get(gca,'ylim'))]);
grid;
```

```
% TS01 & 02 renumber to be T5 & TS02 was removed & T4 %%%%%
figure();

p = [1,7];
q = [2,7];

c_idx = 1;
for i = 1:length(p)

    hold on
    plot(time_mmss{p(i)}, tmp{p(i)}, 'Color', colors{c_idx}, 'DisplayName',
legend_p2{p(i)});
    plot(data_ansys_mmss, data_ansys{q(i)}(:), '--', 'linew', 1.65, 'Color',
colors{c_idx}, 'DisplayName', legend_ansys_p2{q(i)});

    c_idx = c_idx + 1;
end
%plot(time_mmss{7}, tmp{7}, 'Color', 'k', 'DisplayName', legend_p2{7});

%plot(data_ansys_mmss, data_ansys{7}(:), '--', 'linew', 1.65, 'Color',
colors{c_idx}, 'DisplayName', legend_ansys_p2{7});

legend;
% plot text
time_stop = datetime('2020-02-12
13:18','TimeZone','America/Denver','Format','HH:mm');
[~, idx] = min(abs(time_GMT{1} - time_stop));
time_stop_sec = time_mmss{1}(idx);
ylim([-5 80]);
y_lim = get(gca,'ylim');
plot([1, 1]*time_stop_sec, get(gca,'ylim'),'r--', 'HandleVisibility', 'off');

% adjust text STOP
text(time_stop_sec, y_lim(2)*0.7,{'STOP @' + string(round(time_stop_sec)) + '
min'}); %%%%

time_start_sec = 0:0;
    ylim([-5 80]);%%%
    y_lim = get(gca,'ylim');
    plot([0, 0]*time_stop_sec, get(gca,'ylim'),'r--', 'HandleVisibility', 'off');

    % adjust text STart
    text(time_start_sec, y_lim(2)*0.7,{'START'});


xlabel('Time(min)');
ylabel('Temperature(\circC)');
xlim(get(gca,'xlim'));
ylim([-5 max(get(gca,'ylim'))]);
grid;
```

Panel 3 - Temperature

```
%% Temperature
close all;
clc;
clear;


infile_p3 = {
'tmp_Data_System1_Module_1Channel1 (7)_TS1_p3.txt',
'tmp_Data_System1_Module_1Channel1 (6)_TS1_p3.txt',....
'tmp_Data_System1_Module_2Channel1 (4)_TS3_p3.txt',
'tmp_Data_System1_Module_2Channel1 (3)_TS3_p3.txt',....
'tmp_Data_System1_Module_2Channel2 (4)_TS2_p3.txt',
'tmp_Data_System1_Module_2Channel2 (3)_TS2_p3.txt',....
'tmp_Data_System1_Module_3Channel1 (3)_TS6_p3.txt',
'tmp_Data_System1_Module_3Channel1 (2)_TS6_p3.txt',....
'tmp_Data_System1_Module_3Channel2 (3)_TS4_p3.txt',
'tmp_Data_System1_Module_3Channel2 (2)_TS4_p3.txt',....
'tmp_Data_System1_Module_4Channel1 (3)_TS7_p3.txt',
'tmp_Data_System1_Module_4Channel1 (2)_TS7_p3.txt',....
'tmp_Data_System1_Module_4Channel2 (3)_TS8_p3.txt',
'tmp_Data_System1_Module_4Channel2 (2)_TS8_p3.txt'
};

numfiles_p3 = numel(infile_p3);
data_p3_1 = cell(1,numfiles_p3/2);
data_p3_2 = cell(1,numfiles_p3/2);
time_p3 = cell(1,numfiles_p3/2);
tmp_p3 = cell(1,numfiles_p3/2);
i = 1;

for k = 1:2:numfiles_p3

    data_p3_1{i} = load(infile_p3{k},'r');
    data_p3_2{i} = load(infile_p3{k+1},'r');

    % shift time to connect set 2
    last_time_p3_1 = data_p3_1{i}(end,1);
    first_time_p3_2 =  data_p3_2{i}(1,1);
    diff_time = first_time_p3_2 - last_time_p3_1;
    time_p3_2 = data_p3_2{i}(:,1) - diff_time;

    time_p3{i} = vertcat( data_p3_1{i}(:,1), time_p3_2 );

    % compute set 2
    last_strain_p3_1 = data_p3_1{i}(end,2);
    first_strain_p3_2 =  data_p3_2{i}(1,2) + last_strain_p3_1;
    diff_strain = first_strain_p3_2 - last_strain_p3_1;

    tmp_p3_2 = data_p3_2{i}(:,2) + last_strain_p3_1 - diff_strain;  % plus the last
vaule strain of set 1
```

```
    tmp_p3{i} = vertcat( data_p3_1{i}(:,2), tmp_p3_2);

    i=i+1;
end

%% convert time

% Panel 3
time_sec_p3 = cell(1, numfiles_p3/2);
time_GMT_p3 = cell(1, numfiles_p3/2);
time_mmss_p3 = cell(1, numfiles_p3/2);

for i = 1:numfiles_p3/2

    f_time_p3 = time_p3{i}(1);
    time_sec_p3{i} = (time_p3{i} - f_time_p3)./10000; % to seconds
    time_mmss_p3{i} = seconds(time_sec_p3{i});
    time_mmss_p3{i}.Format = 'mm:ss';

    % convert time to datetime format
    time_GMT_p3{i} = datetime(time_p3{i}./10000,
'ConvertFrom','posixTime','TimeZone'....
    ,'America/Denver','Format','HH:mm:ss.SSS'); %HH:mm:ss.SSS

end

%% Ansys results

% Panel 3
infile_ansys_p3 = 'temp_thermal_nonPCM08.txt'; %%%%%%%%%%
fid = fopen(infile_ansys_p3,'r');
data_ansys_p3 = textscan(fid, '%*f %*f %f %f %f %f %f %f %f',
'HeaderLines',1,'Delimiter', '\t');
fclose(fid);
% convert to seconds and miniutes
data_ansys_mmss_p3 = seconds(data_ansys_p3{1});
data_ansys_mmss_p3.Format = 'mm:ss';

%% Panel #3 all
figure()

% plot experiment data
for i = 1:1:numfiles_p3/2
    hold on
    plot(time_mmss_p3{i}, tmp_p3{i});
end

% plot text
time_stop_p3 = datetime('2020-02-14
13:16','TimeZone','America/Denver','Format','HH:mm');
[~, idx] = min(abs(time_GMT_p3{1} - time_stop_p3));
time_stop_sec_p3 = time_mmss_p3{1}(idx);
```

```
y_lim = get(gca,'ylim');
plot([1, 1]*time_stop_sec_p3, get(gca,'ylim'),'r--');

% adjust text STOP
text(time_stop_sec_p3, y_lim(2)*0.05,{'STOP @' + string(round(time_stop_sec_p3)) +
' min'});



legend('Exp-T5', 'Exp-T2', 'Exp-TS02','Exp-T6', 'Exp-T1', 'Exp-T3', 'Exp-T4'); %%%%
title('Temperature of Non-PCM with GFRP bars Panel no.3');
xlabel('Time(min)');
ylabel('Temperature(\circC)');
xlim(get(gca,'xlim'));
grid;

%% plot Panel #3 pair

colors = {'#0072BD', '#D95319'};
legend_p3 = {'T5-Exp', 'T2-Exp', 'TS02-Exp', 'T6-Exp', 'T1-Exp', 'T3-Exp', 'T4-
Exp'};
legend_ansys_p3 = {'Time', 'T5-Model', 'T2-Model', 'T6-Model', 'T1-Model', 'T3-
Model', 'T4-Model'};

% plot experiment data

% T03 & 04
figure();
p = [2, 5];
q = [3, 5];

c_idx = 1;
for i = 1:length(p)
    hold on
    plot(time_mmss_p3{p(i)}, tmp_p3{p(i)}, 'Color', colors{c_idx}, 'DisplayName',
legend_p3{p(i)});
    plot(data_ansys_mmss_p3, data_ansys_p3{q(i)}(:), '--', 'linew', 1.65, 'Color',
colors{c_idx}, 'DisplayName', legend_ansys_p3{q(i)});
    c_idx = c_idx + 1;
end
legend;
% plot text
time_stop_p3 = datetime('2020-02-14
13:16','TimeZone','America/Denver','Format','HH:mm');
[~, idx] = min(abs(time_GMT_p3{1} - time_stop_p3));
time_stop_sec = time_mmss_p3{1}(idx);
ylim([-7 80]);
y_lim = get(gca,'ylim');
plot([1, 1]*time_stop_sec, get(gca,'ylim'),'r--', 'HandleVisibility', 'off');

% adjust text STOP
```

```
text(time_stop_sec, y_lim(2)*0.8,{'STOP @' + string(round(time_stop_sec)) + '
min'});

 time_start_sec = 0:0;
 ylim([-7 80]);
 y_lim = get(gca,'ylim');
 plot([0, 0]*time_stop_sec, get(gca,'ylim'),'r--', 'HandleVisibility', 'off');

  % adjust text STart
 text(time_start_sec, y_lim(2)*0.5,{'START'});

% title('Strain of PCM with GFRP bars Panel no.1');
xlabel('Time(min)');
ylabel('Temperature(\circC)');
xlim(get(gca,'xlim'));
ylim([-7 1.05*max(get(gca,'ylim'))]);
grid;


% T06 & 07
figure();
p = [4, 6];
q = [4, 6];

c_idx = 1;
for i = 1:length(p)
    hold on
    plot(time_mmss_p3{p(i)}, tmp_p3{p(i)}, 'Color', colors{c_idx}, 'DisplayName',
legend_p3{p(i)});
    plot(data_ansys_mmss_p3, data_ansys_p3{q(i)}(:), '--', 'linew', 1.65, 'Color',
colors{c_idx}, 'DisplayName', legend_ansys_p3{q(i)});
    c_idx = c_idx + 1;
end
legend;
% plot text
time_stop_p3 = datetime('2020-02-14
13:16','TimeZone','America/Denver','Format','HH:mm');
[~, idx] = min(abs(time_GMT_p3{1} - time_stop_p3));
time_stop_sec = time_mmss_p3{1}(idx);
ylim([-7 80]);
y_lim = get(gca,'ylim');
plot([1, 1]*time_stop_sec, get(gca,'ylim'),'r--', 'HandleVisibility', 'off');

% adjust text STOP
text(time_stop_sec, y_lim(2)*0.8,{'STOP @' + string(round(time_stop_sec)) + '
min'});

 time_start_sec = 0:0;
 ylim([-7 80]);
 y_lim = get(gca,'ylim');
 plot([0, 0]*time_stop_sec, get(gca,'ylim'),'r--', 'HandleVisibility', 'off');
```

```
  % adjust text STart
 text(time_start_sec, y_lim(2)*0.5,{'START'});

% title('Strain of PCM with GFRP bars Panel no.1');
xlabel('Time(min)');
ylabel('Temperature(\circC)');
xlim(get(gca,'xlim'));
ylim([-7 1.05*max(get(gca,'ylim'))]);
grid;


% T01 & 02 renumber to be
figure();
p = [1, 7];
q = [2, 7];

c_idx = 1;
for i = 1:length(p)
    hold on
    plot(time_mmss_p3{p(i)}, tmp_p3{p(i)}, 'Color', colors{c_idx}, 'DisplayName',
legend_p3{p(i)});
    plot(data_ansys_mmss_p3, data_ansys_p3{q(i)}(:), '--', 'linew', 1.65, 'Color',
colors{c_idx}, 'DisplayName', legend_ansys_p3{q(i)});
    c_idx = c_idx + 1;
end
%plot(time_mmss_p3{3}, tmp_p3{3}, 'Color', 'k', 'DisplayName', legend_p3{3});

legend;
% plot text
time_stop_p3 = datetime('2020-02-14
13:16','TimeZone','America/Denver','Format','HH:mm');
[~, idx] = min(abs(time_GMT_p3{1} - time_stop_p3));
time_stop_sec = time_mmss_p3{1}(idx);
ylim([-7 80]);
y_lim = get(gca,'ylim');
plot([1, 1]*time_stop_sec, get(gca,'ylim'),'r--', 'HandleVisibility', 'off');

% adjust text STOP
text(time_stop_sec, y_lim(2)*0.8,{'STOP @' + string(round(time_stop_sec)) + '
min'});%%%%

 time_start_sec = 0:0;
 ylim([-7 80]);
 y_lim = get(gca,'ylim');
 plot([0, 0]*time_stop_sec, get(gca,'ylim'),'r--', 'HandleVisibility', 'off');

  % adjust text STart
 text(time_start_sec, y_lim(2)*0.5,{'START'});

xlabel('Time(min)');
ylabel('Temperature(\circC)');
xlim(get(gca,'xlim'));
```

```
ylim([-7 1.05*max(get(gca,'ylim'))]);
grid;


figure();
 time_start_sec = 0:0;
 ylim([-7 80]);
 y_lim = get(gca,'ylim');
 plot([0, 0]*time_stop_sec, get(gca,'ylim'),'r--', 'HandleVisibility', 'off');

  % adjust text STart
 text(time_start_sec, y_lim(2)*0.5,{'START'});
```

Panel 1 and 3 – Strain

```
%% Strain
close all;
clc;
clear;

%% Panel 1  %%%%%%%%%%%%%%%%%%%%%%%%%

infile = {'Data_System1_Module_4Channel2 (4)_S4.txt','Data_System1_Module_5Channel1
(4)_S5.txt',....
'Data_System1_Module_5Channel2 (5)_S1.txt','Data_System1_Module_6Channel1
(5)_S8.txt',....
'Data_System1_Module_6Channel2 (5)_S9.txt'};

numfiles = numel(infile);
data = cell(1,numfiles);
time = cell(1,numfiles);
strain = cell(1,numfiles);

for k = 1:numfiles
    data{k} = load(infile{k},'r');
    time{k} = data{k}(:,1); % epoch ms*10  unixmillis
    strain{k} = data{k}(:,2);
end

%%
% Panel 3
infile_p3 = {'Data_System1_Module_6Channel1
(4)_S7_p3.txt','Data_System1_Module_6Channel1 (3)_S12_p3.txt',....
'Data_System1_Module_6Channel2 (4)_S3_p3.txt','Data_System1_Module_6Channel2
(3)_S11_p3.txt',....
'Data_System1_Module_5Channel1 (3)_S12_p3.txt','Data_System1_Module_5Channel1
(2)_S7_p3.txt',....
'Data_System1_Module_5Channel2 (4)_S11_p3.txt','Data_System1_Module_5Channel2
(3)_S3_p3.txt'};

numfiles_p3 = numel(infile_p3);
data_p3_1 = cell(1,numfiles_p3/2);
data_p3_2 = cell(1,numfiles_p3/2);
time_p3 = cell(1,numfiles_p3/2);
strain_p3 = cell(1,numfiles_p3/2);
i = 1;

for k = 1:2:numfiles_p3

    data_p3_1{i} = load(infile_p3{k},'r');
    data_p3_2{i} = load(infile_p3{k+1},'r');

    % shift time to connect set 2
    last_time_p3_1 = data_p3_1{i}(end,1);
    first_time_p3_2 =  data_p3_2{i}(1,1);
    diff_time = first_time_p3_2 - last_time_p3_1;
```

```
    time_p3_2 = data_p3_2{i}(:,1) - diff_time;

    time_p3{i} = vertcat( data_p3_1{i}(:,1), time_p3_2 );

    % compute set 2
    last_strain_p3_1 = data_p3_1{i}(end,2);
    first_strain_p3_2 =  data_p3_2{i}(1,2) + last_strain_p3_1;
    diff_strain = first_strain_p3_2 - last_strain_p3_1;

    strain_p3_2 = data_p3_2{i}(:,2) + last_strain_p3_1 - diff_strain;  % plus the
last vaule strain of set 1

    strain_p3{i} = vertcat( data_p3_1{i}(:,2), strain_p3_2);

    i=i+1;
end

%% convert time

% Panel 1
time_sec = cell(1, numfiles);
time_GMT = cell(1, numfiles);
time_mmss = cell(1, numfiles);
for i = 1:numfiles

    f_time = time{i}(1);
    time_sec{i} = (time{i} - f_time)./10000; % to seconds
    time_mmss{i} = seconds(time_sec{i});
    time_mmss{i}.Format = 'mm:ss';
    % convert time to datetime format
    time_GMT{i} = datetime(time{i}./10000, 'ConvertFrom','posixTime','TimeZone'....
    ,'America/Denver','Format','HH:mm:ss.SSS'); %HH:mm:ss.SSS

end


% Panel 3
time_sec_p3 = cell(1, numfiles_p3/2);
time_GMT_p3 = cell(1, numfiles_p3/2);
time_mmss_p3 = cell(1, numfiles_p3/2);

for i = 1:numfiles_p3/2

    f_time_p3 = time_p3{i}(1);
    time_sec_p3{i} = (time_p3{i} - f_time_p3)./10000; % to seconds
    time_mmss_p3{i} = seconds(time_sec_p3{i});
    time_mmss_p3{i}.Format = 'mm:ss';

    % convert time to datetime format
    time_GMT_p3{i} = datetime(time_p3{i}./10000,
'ConvertFrom','posixTime','TimeZone'....
    ,'America/Denver','Format','HH:mm:ss.SSS'); %HH:mm:ss.SSS
```

```
end

%% plot

% Panel 1
figure(1)
for i = 1:numfiles
    hold on
    plot(time_sec{i}, strain{i});
end

% plot text
time_stop = datetime('2020-02-14
16:43','TimeZone','America/Denver','Format','HH:mm');
[~, idx] = min(abs(time_GMT{1} - time_stop));
time_stop_sec = time_sec{1}(idx);
y_lim = get(gca,'ylim');
plot([1, 1]*time_stop_sec, get(gca,'ylim'),'r--');

% adjust text STOP
text(time_stop_sec, y_lim(2)*0.7,{'STOP @' + string(round(time_stop_sec)) + '
sec'});

legend('S04', 'S05', 'S01', 'S08', 'S09');
%title('Strain of PCM with GFRP bars Panel no.1');
xlabel('Time(sec)');
ylabel('Strain(microstrain)');
xlim(get(gca,'xlim').*0.9);
ylim([0 max(get(gca,'ylim'))]);
grid;

%%%%%%%%%%
% Panel 3
figure(2)
for i = 1:4
    hold on
    plot(time_sec_p3{i}, strain_p3{i});
end

% plot text
time_stop_p3 = datetime('2020-02-14
13:16','TimeZone','America/Denver','Format','HH:mm');
[~, idx] = min(abs(time_GMT_p3{1} - time_stop_p3));
time_stop_sec_p3 = time_sec_p3{1}(idx);
y_lim = get(gca,'ylim');
plot([1, 1]*time_stop_sec_p3, get(gca,'ylim'),'r--');

% adjust text STOP
text(time_stop_sec_p3, y_lim(2)*0.7,{'STOP @' + string(round(time_stop_sec_p3)) + '
sec'});
```

```
legend('S12', 'S11', 'S07', 'S03');
title('Strain of Non-PCM with GFRP bars Panel no.3');
xlabel('Time(sec)');
ylabel('Strain(microstrain)');
xlim(get(gca,'xlim').*0.9);
grid;

%% Ansys results

% Panel 1 with PCM
infile_ansys = 'strain_thermal_PCM07.txt'; %%%%%%%%%%
fid = fopen(infile_ansys,'r');
data_ansys = textscan(fid, '%*f %*f %f %f %f %f %f %f', 'HeaderLines',1 ,
'Delimiter', '\t');
fclose(fid);
% convert to seconds and miniutes
data_ansys_mmss = seconds(data_ansys{1});
data_ansys_mmss.Format = 'mm:ss';


% Panel 3 nonPCM
infile_ansys_p3 = 'strain_thermal_nonPCM07.txt'; %%%%%%%%%%
fid = fopen(infile_ansys_p3,'r');
data_ansys_p3 = textscan(fid, '%*f %*f %f %f %f %f %f %f', 'HeaderLines',1 ,
'Delimiter', '\t');
fclose(fid);
% convert to seconds and miniutes
data_ansys_mmss_p3 = seconds(data_ansys_p3{1});
data_ansys_mmss_p3.Format = 'mm:ss';


%% plot Panel vs ansys

colors = {'#0072BD', '#D95319'};

% Panel 1

legend_p1 = {'SI7-Exp', 'SI5-Exp', 'SI6-Exp', 'SI1-Exp', 'SI2-Exp'};
legend_ansys_p1 = {'SI7-Model', 'SI5-Model', 'SI6-Model', 'SI1-Model', 'SI2-
Model'};

% S04 renumber to S07
figure()
c_idx = 1;
for i = 1

    hold on
    plot(time_mmss{i}, strain{i}, '-', 'Color', colors{c_idx});
    plot(data_ansys_mmss, data_ansys{i+1}(:)./10^-6, '--', 'linew', 1.65, 'Color',
colors{c_idx});
    c_idx = c_idx + 1;
```

```
    % plot text
    time_stop = datetime('2020-02-14
16:43','TimeZone','America/Denver','Format','HH:mm');
    [~, idx] = min(abs(time_GMT{1} - time_stop));
    time_stop_sec = time_mmss{1}(idx);
    ylim([0 400]);
    y_lim = get(gca,'ylim');
    plot([1, 1]*time_stop_sec, get(gca,'ylim'),'r--');

    % adjust text STOP
    text(time_stop_sec, y_lim(2)*0.7,{'STOP @' + string(round(time_stop_sec)) + '
min'});

    time_start_sec = 0:0;
    ylim([0 400]);%%%
    y_lim = get(gca,'ylim');
    plot([0, 0]*time_stop_sec, get(gca,'ylim'),'r--');

    % adjust text STart
    text(time_start_sec, y_lim(2)*0.7,{'START'});


    legend({legend_p1{i}, legend_ansys_p1{i}})
    %title('Strain of PCM with GFRP bars Panel no.1');
    xlabel('Time(min)');
    ylabel('Strain(microstrain)');
    xlim([0 max(get(gca,'xlim'))]);
%     ylim([0 max(get(gca,'ylim'))]);
    grid;
end


% S05 S08 renumber to be S05 S01
s_no = [4, 5];
c_idx = 1;
figure()
for i = s_no

    hold on
    plot(time_mmss{i}, strain{i}, '-', 'Color', colors{c_idx});
    plot(data_ansys_mmss, data_ansys{i+1}(:)./10^-6, '--', 'linew', 1.65, 'Color',
colors{c_idx});
    c_idx = c_idx + 1;

    if i==s_no(end)
    % plot text
    time_stop = datetime('2020-02-14
16:43','TimeZone','America/Denver','Format','HH:mm');
    [~, idx] = min(abs(time_GMT{1} - time_stop));
    time_stop_sec = time_mmss{1}(idx);
    ylim([0 400]);
    y_lim = get(gca,'ylim');
```

```
    plot([1, 1]*time_stop_sec, get(gca,'ylim'),'r--');

    % adjust text STOP
    text(time_stop_sec, y_lim(2)*0.1,{'STOP @' + string(round(time_stop_sec)) + '
min'});

   time_start_sec = 0:0;
    ylim([0 400]);%%%
    y_lim = get(gca,'ylim');
    plot([0, 0]*time_stop_sec, get(gca,'ylim'),'r--');

    % adjust text STart
    text(time_start_sec, y_lim(2)*0.1,{'START'});

    legend(legend_p1{s_no(1)}, legend_ansys_p1{s_no(1)}, legend_p1{s_no(2)},
legend_ansys_p1{s_no(2)})
    %title('Strain of PCM with GFRP bars Panel no.1');
    xlabel('Time(min)');
    ylabel('Strain(microstrain)');
    xlim([0 max(get(gca,'xlim'))]);
%     ylim([0 max(get(gca,'ylim'))]);
    grid;
    end

end


% S01 S05 renumber to be S06 S05
s_no = [2, 3];
c_idx = 1;
figure()
for i = s_no

    hold on
    plot(time_mmss{i}, strain{i}, '-', 'Color', colors{c_idx});
    plot(data_ansys_mmss, data_ansys{i+1}(:)./10^-6, '--', 'linew', 1.65, 'Color',
colors{c_idx});
    c_idx = c_idx + 1;

    if i==s_no(end)
    % plot text
    time_stop = datetime('2020-02-14
16:43','TimeZone','America/Denver','Format','HH:mm');
    [~, idx] = min(abs(time_GMT{1} - time_stop));
    time_stop_sec = time_mmss{1}(idx);
    ylim([0 400]);
    y_lim = get(gca,'ylim');
    plot([1, 1]*time_stop_sec, get(gca,'ylim'),'r--');

    % adjust text STOP
    text(time_stop_sec, y_lim(2)*0.7,{'STOP @' + string(round(time_stop_sec)) + '
min'});
```

```
    time_start_sec = 0:0;
    ylim([0 400]);%%%
    y_lim = get(gca,'ylim');
    plot([0, 0]*time_stop_sec, get(gca,'ylim'),'r--');

    % adjust text STart
    text(time_start_sec, y_lim(2)*0.7,{'START'});

    legend(legend_p1{s_no(1)}, legend_ansys_p1{s_no(1)}, legend_p1{s_no(2)},
legend_ansys_p1{s_no(2)})
    %title('Strain of PCM with GFRP bars Panel no.1');
    xlabel('Time(min)');
    ylabel('Strain(microstrain)');
    xlim([0 max(get(gca,'xlim'))]);
%     ylim([0 max(get(gca,'ylim'))]);
    grid;
    end

end

%% plot Panel vs ansys

colors = {'#0072BD', '#D95319'};


% Panel 3
legend_p3 = {'SI3-Exp', 'SI4-Exp', 'SI5-Exp', 'SI6-Exp'};
legend_ansys_p3 = {'SI3-Model', 'SI4-Model', 'SI5-Model', 'SI6-Model', 'SI8-
Model'};

% S11 S12 renumber s04 03
s_no = [1, 2];
c_idx = 1;
figure()
for i = s_no

    hold on
    plot(time_mmss_p3{i}, strain_p3{i}, '-', 'Color', colors{c_idx});
    plot(data_ansys_mmss_p3, data_ansys_p3{i+1}(:)./10^-6, '--', 'linew', 1.65,
'Color', colors{c_idx});
    c_idx = c_idx + 1;

    if i==s_no(end)
    % plot text
    time_stop = datetime('2020-02-14
13:16','TimeZone','America/Denver','Format','HH:mm');
    [~, idx] = min(abs(time_GMT_p3{1} - time_stop));
    time_stop_sec = time_mmss_p3{1}(idx);
    ylim([0 400]);
    y_lim = get(gca,'ylim');
    plot([1, 1]*time_stop_sec, get(gca,'ylim'),'r--');
```

```
    % adjust text STOP
    text(time_stop_sec, y_lim(2)*0.1,{'STOP @' + string(round(time_stop_sec)) + '
min'});

     time_start_sec = 0:0;
    ylim([0 400]);%%%
    y_lim = get(gca,'ylim');
    plot([0, 0]*time_stop_sec, get(gca,'ylim'),'r--');

    % adjust text STart
    text(time_start_sec, y_lim(2)*0.25,{'START'});

    legend(legend_p3{s_no(1)}, legend_ansys_p3{s_no(1)}, legend_p3{s_no(2)},
legend_ansys_p3{s_no(2)}, 'Location', 'northwest')
    %title('Strain of Non-PCM with GFRP bars Panel no.1');
    xlabel('Time(min)');
    ylabel('Strain(microstrain)');
    xlim([0 max(get(gca,'xlim'))]);
%     ylim([0 max(get(gca,'ylim'))]);
    grid;
    end

end


% S07 S03
s_no = [3, 4];
c_idx = 1;
figure()
for i = s_no

    hold on
    plot(time_mmss_p3{i}, strain_p3{i}, '-', 'Color', colors{c_idx});
    plot(data_ansys_mmss_p3, data_ansys_p3{i+1}(:)./10^-6, '--', 'linew', 1.65,
'Color', colors{c_idx});
    c_idx = c_idx + 1;

    if i==s_no(end)
    % plot text
    time_stop = datetime('2020-02-14
13:16','TimeZone','America/Denver','Format','HH:mm');
    [~, idx] = min(abs(time_GMT_p3{1} - time_stop));
    time_stop_sec = time_mmss_p3{1}(idx);
    ylim([0 400]);
    y_lim = get(gca,'ylim');
    plot([1, 1]*time_stop_sec, get(gca,'ylim'),'r--');

    % adjust text STOP
    text(time_stop_sec, y_lim(2)*0.85,{'STOP @' + string(round(time_stop_sec)) + '
min'});
```

```
 time_start_sec = 0:0;
    ylim([0 400]);%%%
    y_lim = get(gca,'ylim');
    plot([0, 0]*time_stop_sec, get(gca,'ylim'),'r--');

    % adjust text STart
    text(time_start_sec, y_lim(2)*0.5,{'START'});

    legend(legend_p3{s_no(1)}, legend_ansys_p3{s_no(1)}, legend_p3{s_no(2)},
legend_ansys_p3{s_no(2)}, 'Location', 'northwest')
    %title('Strain of Non-PCM with GFRP bars Panel no.1');
    xlabel('Time(min)');
    ylabel('Strain(microstrain)');
    xlim([0 max(get(gca,'xlim'))]);
%     ylim([0 max(get(gca,'ylim'))]);
    grid;
    end

end

% S10 renumber to s08
s_no = 5;
c_idx = 1;
figure()
for i = s_no

    hold on
    %plot(time_mmss_p3{i}, strain_p3{i}, '-', 'Color', colors{c_idx});
    plot(data_ansys_mmss_p3, data_ansys_p3{i+1}(:)./10^-6, '--', 'linew', 1.65,
'Color', colors{c_idx});
    c_idx = c_idx + 1;

    if i==s_no(end)
    % plot text
    time_stop = datetime('2020-02-14
13:16','TimeZone','America/Denver','Format','HH:mm');
    [~, idx] = min(abs(time_GMT_p3{1} - time_stop));
    time_stop_sec = time_mmss_p3{1}(idx);
    ylim([0 400]);
    y_lim = get(gca,'ylim');
    plot([1, 1]*time_stop_sec, get(gca,'ylim'),'r--');

    % adjust text STOP
    text(time_stop_sec, y_lim(2)*0.7,{'STOP @' + string(round(time_stop_sec)) + '
min'});

 time_start_sec = 0:0;
    ylim([0 400]);%%%
    y_lim = get(gca,'ylim');
    plot([0, 0]*time_stop_sec, get(gca,'ylim'),'r--');

    % adjust text STart
```

```
    text(time_start_sec, y_lim(2)*0.7,{'START'});

    legend( legend_ansys_p3{5}, 'Location', 'northwest')
    %title('Strain of Non-PCM with GFRP bars Panel no.1');
    xlabel('Time(min)');
    ylabel('Strain(microstrain)');
    xlim([0 max(get(gca,'xlim'))]);
%     ylim([0 max(get(gca,'ylim'))]);
    grid;
    end
%
end
```

Panel 2 – Strain

```
%% Strain
close all;
clc;
clear;


%% Panel 2 S6 & S2 = S8 & S9 in ansys model
infile = {'Data_System1_Module_6Channel1
(2)_S6_p2.txt','Data_System1_Module_6Channel2 (2)_S2_p2.txt'};

numfiles = numel(infile);
data = cell(1,numfiles);
time = cell(1,numfiles);
strain = cell(1,numfiles);

for k = 1:numfiles
    data{k} = load(infile{k},'r');
    time{k} = data{k}(:,1); % epoch ms*10  unixmillis
    strain{k} = data{k}(:,2);
end
%% convert time

% Panel 1
time_sec = cell(1, numfiles);
time_GMT = cell(1, numfiles);
time_mmss = cell(1, numfiles);
for i = 1:numfiles

    f_time = time{i}(1);
    time_sec{i} = (time{i} - f_time)./10000; % to seconds
    time_mmss{i} = seconds(time_sec{i});
    time_mmss{i}.Format = 'mm:ss';
    % convert time to datetime format
    time_GMT{i} = datetime(time{i}./10000, 'ConvertFrom','posixTime','TimeZone'....
    ,'America/Denver','Format','HH:mm:ss.SSS'); %HH:mm:ss.SSS

end

% Panel 2
infile_ansys = 'strain_thermal_steel03.txt'; %%%%%%%%%% strain_thermal_steel02
(previous)
fid = fopen(infile_ansys,'r');
data_ansys = textscan(fid, '%*f %*f %f %f %f', 'HeaderLines',1 , 'Delimiter',
'\t');
fclose(fid);
% convert to seconds and miniutes
data_ansys_mmss = seconds(data_ansys{1});
data_ansys_mmss.Format = 'mm:ss';

%% plot Panel vs ansys
```

```
colors = {'#0072BD', '#D95319'};

% Panel 2

legend_p2 = {'SI1-Exp', 'SI2-Exp'};
legend_ansys_p2 = {'SI1-Model', 'SI2-Model'};


% S06 S02
s_no = [1, 2];
c_idx = 1;
figure()
for i = s_no

    hold on
    plot(time_mmss{i}, strain{i}, '-', 'Color', colors{c_idx});
    plot(data_ansys_mmss, data_ansys{i+1}(:)./10^-6, '--', 'linew', 1.65, 'Color',
colors{c_idx});
    c_idx = c_idx + 1;

    if i==s_no(end)
    % plot text
    time_stop = datetime('2020-02-12
13:18','TimeZone','America/Denver','Format','HH:mm');
    [~, idx] = min(abs(time_GMT{1} - time_stop));
    time_stop_sec = time_mmss{1}(idx);
    ylim([0 450]);%%%
    y_lim = get(gca,'ylim');
    plot([1, 1]*time_stop_sec, get(gca,'ylim'),'r--');

    % adjust text STop
    text(time_stop_sec, y_lim(2)*0.9,{'STOP @' + string(round(time_stop_sec)) + '
min'});

    time_start_sec = 0:0;
    ylim([0 450]);%%%
    y_lim = get(gca,'ylim');
    plot([0, 0]*time_stop_sec, get(gca,'ylim'),'r--');

    % adjust text STart
    text(time_start_sec, y_lim(2)*0.9,{'START'});



    legend(legend_p2{s_no(1)}, legend_ansys_p2{s_no(1)}, legend_p2{s_no(2)},
legend_ansys_p2{s_no(2)})
    %title('Strain of PCM with GFRP bars Panel no.1');
    xlabel('Time(min)');
    ylabel('Strain(microstrain)');
    xlim([0 max(get(gca,'xlim'))]);
%     ylim([0 max(get(gca,'ylim'))]);
    grid;
```

```
    end

end
```